Predicting and Locating Fracture in Bone using Acoustic Emission

John O’Toole

Doctor of Philosophy

Supervisors:

Dr. Leo Creedon and Dr. John Hession

Institute of Technology Sligo

Submitted to the Institute of Technology, Sligo, March, 2015

Declaration

This work has been carried out while registered at the Institute of Technology Sligo, Sligo for the degree of Doctor of Philosophy. It is entirely my own work. No part of this thesis has been submitted for any other degree at this or any other institution. Portions of this work have been submitted as two journal papers and 3 conference papers. These are listed below.

I give permission for the Library at Institute of Technology Sligo to lend or copy the thesis upon request. This work was carried out in the School of Engineering and Design at Institute of Technology Sligo from September 2008 to November 2014.

This research was funded by the Programme for Research in Third-Level Institutes, Technology Sector Research, Strand 3.

Publications

Journal Papers:

O'Toole, J., Creedon, L., Hession, J., and Muir, G. (2012). Hyperbolic Source Location of Crack Related Acoustic Emission in Bone. *Journal of Biomechanical Engineering,* 135(1), pp.011006.

O'Toole, J., Creedon, L., Hession, J., and Muir, G. (2012). Acoustic Emission Source Localisation On Bone Using Multiple Regression. *International Journal of Nano and Biomaterials,* 4(2), pp.128-147.

Conference Abstracts:

O’Toole, J., Creedon, L., Hession, J., Muir, G. The Use of Acoustic Emission to Prevent Intra-operative Fractures (Bioengineering In Ireland 18 Conference, Belfast, United Kingdom, January 2012).

O’Toole, J., Hession, J., Creedon, L. and Muir, G. Source Location of Cracks in Bone using Acoustic Emission (Bioengineering In Ireland 17 Conference, Galway, Ireland, January 2011).

J. O’Toole, G. Reilly, J. Hession, and G. Muir. Source Localization of cracks and the propagation of cracks in bone using Acoustic Emission (Bioengineering In Ireland 15 Conference, Limerick, Ireland, January 2009).

Dedication

To Monika

and our two children Martha and David

Acknowledgements

I would like to thank my supervisors: Dr. Leo Creedon for his dedicated help, his enthusiasm which inspired me to continue when I was losing faith and his encouragement to achieve journal publication, Dr. John Hession without whom I would not have started this research and who gave me the freedom to explore the fascinating field of bone fracture.

I would like to thank Gordon Muir who gave me much help and many ideas in the laboratory.

I would like to thank all the postgraduate students who shared our office and were a joy to work with and around, in particular those of the Biomedical Engineering Research Group: Rob Carroll, Padraig Varley, Michael Cafferty, and Tom Burke.

I would also like to thank Dr. Brendan McCormack, Mr. Mulhall and Mr. Macey for their help on the subject of Hip Arthroplasty.

Finally, I would like to thank my lovely Monika for her support and belief in me that I could finish this work.

Abstract

Predicting and Locating Fracture in Bone using Acoustic Emission

John O'Toole

A novel way to predict intra-operative fracture during Total Hip Arthroplasty (THA) using acoustic emission (AE) has been tentatively discovered. AE has also been shown to be able to predict the location of such fracture. This work has potential benefit for the THA surgeon as it gives him a warning of when fracture is imminent and secondly where on the bone it is likely to occur. Eight bovine femora were tested using a Materials Testing Machine. Mock implants were forced into the specially prepared femora until the femora fractured. Both strain guages and AE sensors were mounted on the femora. Strain was used as a control to indicate when the femur fractured. The data from the AE sensors was analyzed post test to determine a parameter that could be used to predict when fracture was imminent and indeed when it had occurred. It was discovered that the peak frequency of the AE waves reduced significantly just before fracture occurred. It is theorized that as the bone material undergoes microcracking, the properties of the materials alter resulting in this change in peak frequency.

Two AE source location algorithms were tested on rectangular samples of bone harvested from the mid diaphysis of bovine bone to determine the feasibility of predicting the location of the fracture by locating in real time the microcracks that occur as their prelude. The source location algorithms detected artificial AE sources (pencil lead breaks) to just over 1 mm (on average) of their true location. Then three samples were loaded in three point bending until they fractured. The source location algorithms located the microcracks using AE data collected during the tests. The computed locations showed that there was a close correlation between where the microcracks were detected and where the fractured occurred.

Table of Contents

List of Tables

List of Figures

1. Introduction

1.1 Bone, the Fracture Process and Acoustic Emission

Bone is a natural composite material. It is irregular in shape and composition. It varies between species and within species. Indeed within one animal there are many types of bone. A human vertebrae is very different from a human femur. Elephant femora are almost completely devoid of marrow, while some bird bones have cavities filled with gas to reduce weight. The upside of this variation is that bone is supremely adapted to its function. An elephant needs solid bones to support its immense weight and if bird's bones were too heavy they would struggle to fly. Furthermore bones vary throughout the life of the animal, again to suit its environmental experience. The variation and complexities of bone is what make it a very interesting but challenging material to study.

Even within one type of bone the structure and composition is complicated. Take for example bovine cortical bone in a femur. Without the aid of a microscope it appears to be a dense uniform material with the occasionally channel through it for veins and arteries. Also visible is a cartilaginous skin encasing the bone. However at a microscopic level, mature human bone is arranged in sheets called lamellae, burrowing through the lamellae are osteons, each of which consists of concentric lamellae rings. Blood vessels and nerves run down through the haversian canals which are at centre of the osteon. Volksmann's canals join osteons together and to the periosteum. A variety of cells are present, ranging from osteoblasts that form bone to osteoclasts that destroy bone. At a still lower level bone consists of collagen fibrils, themselves made up of microfibrils. A type of calcium phosphate crystals are distributed between and within the fribrils. This combination of collagen and mineral crystal gives bone its stiffness (mineral), and toughness (collagen). This very brief description is intended to give the reader a flavour for the complexity of bone material. In addition there is much about bone that is not understood. The reader is referred to (Currey 2006; Cowin 2001) for a more detailed description of the composition and structure of bone.

This complexity translates into a complex fracture process when bone is stressed to the point of failure. The fracture process in bone is divided into three phases, (Gupta and Zioupos 2008; Currey 2006). In Phase 1 the material deforms, but when the load is lifted the material returns to its natural condition with little or no obvious damage. However in Phase 2 while the material is still in one piece it absorbs the energy in the form of diffuse microcracks and the material becomes less stiff and loses some of its strength. Phase 3 consists of more severe microcracking, absorbing more energy and the final failure of the material. There are a number of bone characteristics which slow the fracture process. The osteons and lamellae will deflect the growth of a crack, spreading the force over a greater area and/or away from the direction of applied force. On a lower level the collagen fibres prevent or slow down the cracking of the calcium phosphate crystals by holding them together. The microcracks range in size from a couple of microns across to 50 µm across (Currey 2006). In Phase 3 these microcracks coalesce into larger cracks known as macrocracks and these very quickly propagate to cause bone failure.

This dissertation primarily deals with the detection and localisation of these microcracks, as their location and indeed their formation indicate the initiation and the continuation of the fracture process. When a microcrack occurs, it vibrates the molecules in its immediate vicinity. These molecules vibrate others next to them. This translates into mechanical waves which propagate out from the microcrack. These waves continue to travel out from the source reducing in amplitude, until they have lost all their energy. If a piece of piezoelectric material is placed on the bone material close to where the microcrack occurs, the mechanical waves will vibrate the piezoelectric substance which translates into a proportional voltage signal. This phenomenon is known as Acoustic Emission (AE). An acoustic emission sensor is a piece of piezoelectric material housed in a metal shielding which reduces interference from noise. It is important to realise that the microcracking is a transient event and thus the resulting bursts of AE waves are transient, rising quickly to a peak, and dropping off more slowly until they fade away into the background noise. This burst of AE is known as an AE hit. The characteristics of the AE hit are related to the type of microcrack that has occurred, for example a large microcrack will produce a large AE hit. Furthermore the greater the distance the microcrack is from the sensor the more attenuated the AE wave will be. Therefore it is important to be able to locate the source of the AE (the microcrack), when using the amplitude of the AE hit to determine the size of the crack. AE can be used in a number of ways: it can be used to locate where the microcrack has happened, give some information about the type of event, and by looking at the accumulation of AE hits over time, information pertaining to the fracture event can be gleamed.

1.2 The Hypotheses

The main overriding hypothesis of this research project is that acoustic emission can be used to look inside bone and observe fracture unfold and in doing so discover something useful to medicine, veterinary science and biomedical engineering. To break it down into more defined hypotheses:

1) Fracture of bone can be predicted using acoustic emission, in particular intra-operative fracture during Total Hip Arthroplasty can be predicted.
2) Microcracks can be accurately located in bone using acoustic emission.

1) This work discovers a technique to determine when bone is going to fracture. This technique employs acoustic emission as the tool for prediction. Acoustic emission can allow one to effectively peer inside the bone on a microscopic as well as on a macroscopic level and 'see' how the fracture process is unfolding. The hypothesis is that the acoustic emission signals contain information about the microcracks that are occurring and if this information can be interpreted correctly, reading the acoustic emission from the microcrack is like observing in real time the fracture process. This should permit prediction of fracture, consequently allowing its prevention. However this work does more than just try to predict fracture. It attempts to predict a particular type of fracture for a particular medical application. This is intra-operative fracture during Total Hip Arthroplasty and this type of fracture prediction is particularly challenging.

2) Using acoustic emission to predict fracture is part one of a potentially two part technique. It would be useful and desirable to see where fracture is occurring as well

as how it is progressing. Being able to locate the microcrack also allows the filtering out of other unwanted acoustic emission sources. Despite being potentially very useful, little work on localisation of microcracks in bone by acoustic emission has been found in the literature. Beyond the scope of this thesis is the potential use of microcrack localisaiton to a surgeon; if they know where microcracking is taking place, they can relieve the stress at that location and still get a stable prosthesis.

1.3 Preventing Intra-operative Fractures using Acoustic Emission

1.3.1 Background

Total Hip Arthroplasty involves the replacement of the diseased hip with a prosthetic one. The first attempts were in the 1890s where ivory and metal were used. A Burmese surgeon reported 88% success rate with 300 hip replacements using ivory prosthetic hips in the 1960s (Net Doctor 2012). However it was John Charnley, a British surgeon from Wrightington Hospital near Manchester in the U.K. who made the greatest advances and is hailed as the pioneer of hip replacement (Net Doctor 2012). Total hip Arthroplasty is a two part operation: the femur and the acetabulum. The top end of the femur is replaced with an artificial implant and the socket part of the acetabulum is replaced with an artificial socket. The first step is the removal of the femoral head. A slot is then reamed down the medullary canal of the femur (this is where the marrow resides). When the slot is reamed to a sufficient size, the femoral prosthesis is inserted. The top part of the prosthesis consists of a femoral head similar to the natural one. Next the surgeon rasps away the damaged part of the acetabulum to form a space suitable for the acetabular component (prosthetic socket). This can be held in place with friction or with screws. Figures 1.1, 1.2 and 1.3, show respectively the prosthetic components, the process of implanting an artificial hip and the end result as seen in an X-ray image. The prosthetic femoral implant can be attached to the femur in two ways. The more common and older method (John Charnley used this method) is the use of bone cement (PMMA) which quickly bonds to the bone and to the prosthesis. A more modern (cementless) method is to use friction and bone in-growth to secure the prosthetic component. These cementless prosthetic implants are covered in micro pores which permit the bone to grow into them and thus solidify the interface. They can also be coated in hydroxyapapite which again encourages bone in-growth and bonding (Bharati et al. 2005). The cementless approach is becoming more common as they tend to last longer (Shiel 2010). A requirement for the cementless approach is a tight fit, thus they are also known as “press fit” prostheses. If the femoral component does not fit snugly into the femur, it can easily move relative to the femur causing the artificial joint to become unstable. Furthermore if there is too much of a void between the prosthesis and the bone, bone in-growth will not occur. Therefore the femora are generally under reamed (drilled) and a broach (the same shape as the implant with a rough surface to rasp away mostly cancellous bone and marrow) is used to create a slot for the implant. During the impaction of the broach and the insertion of the implant significant stress is placed on the femur. If this stress is too high, it can cause a femoral fracture during the surgery. This is known as intra-operative fracture. It can be the implant perforating through the wall of the femur if the implant is not inserted at the correct angle. It can also cause a spiral fracture which starts at the cut edge where the femoral head had been removed and propagates down the femur.

According to Davidson et al. (2008) the rate of intra-operative fractures ranges from 0.3% to 20.9% and Mabry et al. (2006) reported 1% to 3% when just considering primary total hip arthroplasty. When cemented prosthetic stems are used Davidson et al. (2008) reported rates of 0.3% to 1.2% and Khan and O'Driscoll (1977) reported a rate of just under 1%. But when cementless stems are used an intra-operative fracture rate of 5.4% was found (Davidson et al. 2008). By far the highest intra-operative fracture rates occur during revision surgery where the old prosthetic implant is removed and a new one (normally cementless) is inserted. Fracture rates during revision THA range from 19% to 20.9% (Davidson et al. 2008) and up to 30% according to Meek et al. (2004). Thillemann et al. (2008) found that intra-operative fractures increase the risk of revision surgery during the first 6 months postoperatively. Therefore is can be concluded that the literature shows that intra-operative fractures during THA occur at significant rates, can lead to revision surgery and are most prevalent when the surgeon uses cementless implants. The fracture rate during revision is much higher than primary surgery. Furthermore, Mabry et al. (2006) stated that with the advent of minimally invasive THA surgery there is an increase in intra-operative fractures.

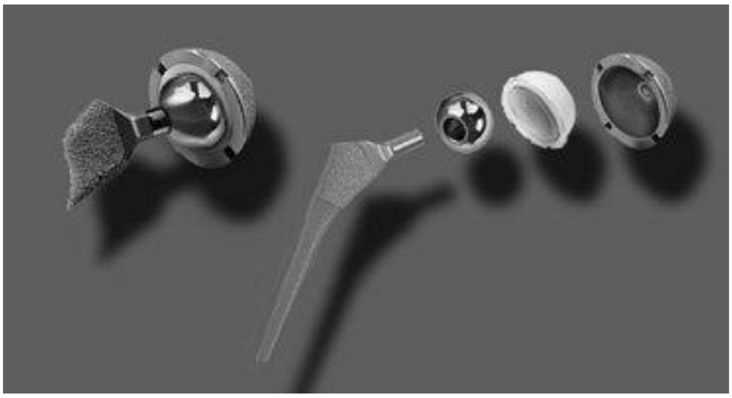

Fig. 1.1 The components of a prosthetic hip. The bowl shaped component fits into the hip socket (acetuabulum) while the longer, slightly curved component inserts into the femur.

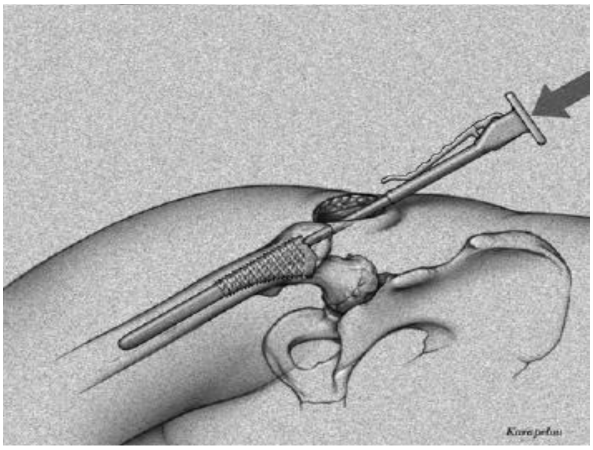

Fig. 1.2 An implant is being inserted with impaction into the femur.

Fig. 1.3 The left hip joint has been replaced with a prosthetic hip. The radiograph shows the prosthetic hip in white.

Davidson et al. (2008) gives details of the types of fractures that can occur during THA surgery. He makes reference to the Vancouver classification system for intra-operative femur fracture. Intra-operative fractures are classified as type A if they involve the proximal metaphysis, type B if they are in the disphyseal region and type C if they are distal of the implant tip. Intra-operative fractures are further classified into subtype 1 for a cortical perforation, subtype 2 for a non-displaced fracture and subtype 3 for a displaced unstable fracture. Davidson et al. (2008) describes the advised treatment of the different types of fractures. The subtype 3 (unstable displaced fractures) are the most serious especially if they are type B and C. The treatment usually involves the use of a longer stem that would bypass the fracture location. Type A3 is near the proximal end of the femur and a typical implant can still have enough length to acquire a secure fix. Davidson et al (2008) also stated that often types B and C are often not diagnosed till a post-operative radiograph is taken as this part of the bone is not exposed during the surgery. The current proposed solution to intra-operative fractures should ideally predict all types of intra-operative fractures. But focus should be on subtype 3 fractures i.e. displaced fractures.

1.3.2 Proposed Solution to Intra-operative Fractures

This research proposes to investigate the application of the acoustic emission technique to detect and predict to intra-operative fracture. With this information a surgeon can then avoid the fracture and still achieve a stable implant.

Little work has been found in the literature regarding trying to predict femoral intra-operative fracture during Total Hip Arthroplasty. Rowlands et al. (2008) used a vibration technique called vibrometry to detect and quantify hip prosthesis loosening.

The basic principle involves applying a vibration signal to the femoral condyle and an accelerometer picks up the driving frequency through the greater trochanter of the femur. The authors stated that the difficulty with this approach was that the soft tissue between the bone and the sensor greatly attenuated the received signal. In an effort to overcome that shortcoming they proposed the use of an ultrasound probe that used the Doppler shift phenomenon. This, they successfully demonstrated was more sensitive than an accelerometer. Lannocca et al. (2007) used a vibration technique not to detect or predict intra-operative fracture but to determine good initial stability of the implant in the femur by achieving optimal press-fitting. If good stability can be determined then the surgeon does not risk a fracture through the application of excessive force to the femur. In their proposed technique, the surgeon applies a small torsion force to the implant for ten seconds. An accelerometer monitors the resonant frequency of the bone-implant system. A stable implant exhibited a constant resonant frequency over the ten seconds while an unstable implant exhibited a marked decrease in the resonant frequency over time. Marvrogordato et al. (2011) used acoustic emission to monitor microdamage in a simplified total hip stem model. They embedded the AE sensors in the implant and found that these embedded sensors gave a closer approximation of the damage observed with a micro-CT scan than externally mounted sensors. While this approach may be effective in monitoring damage accumulation post operation or for new implant testing, it may not be usable during surgery as the impaction noises and the subsequent implant borne AE would most likely obscure any AE emanating from the femur. Only Sakai et al. (2011) attempted to predict fracture during THA Surgery. They tested three femora models with properties equivalent to that of living bone and used a microphone to listen to the hammering sound during the impaction process from one meter away. They discovered that close to the fracture event the frequency of the sound reduced. They reported that this frequency reduction could be used as an indicator of impending intra-operative fracture. Instead of listening to the hammering sounds, the present work proposes to listen to the acoustic emission generated by microcrack formation in cortical bone before an intra-operative fracture occurs, and use one or more acoustic emission parameter to predict intra-operative fracture.

Previous researchers have used acoustic emission to understand the fracture process in bone. Zioupos et al. (1994) used acoustic emission and Laser Scanning Confocal Microscopy to examine the failure mechanisms in antler and in bone. They found that the AE hits corresponded with damage accumulation at the knee and post-knee regions of the stress curve in both materials but more so with antler. Thus AE is a good indicator of microdamage in these materials. Similarly Rajachar et al. (1999A) showed how the AE technique could be used to demonstrate damage at yield and just before facture. Toen et al. (2012) examined the AE produced by vertebrae under compression and ligaments under tensile forces. They found that they could be distinguished because the AE hits emanating from the vertebrae had higher amplitudes and frequencies than those from the ligaments. Akkus et al. (2000) used AE to understand the fracture process in longitudinal and transverse human bone specimen. They showed that the pattern of AE was different in the two loading orientations.

It is clear from the literature that AE can provide a lot of information about what is happening within bone during the fracture process, and therefore it may be able to give the surgeon a warning of when fracture is about to occur. In practice it is envisaged that the surgeon could mount an AE sensor onto an exposed part of the femur during surgery and connect this sensor to a monitoring system which would analyze the AE signals as they are detected. If and when intra-operative fracture becomes imminent, the characteristics of the AE signals being analyzed would become different in some manner and this would be a warning to the surgeon of impending fracture and he could thus avoid this fracture.

The second hypothesis of the present work is that microcracks in bone and thus where fracture is occurring can be located using acoustic emission. Being informed of where fracture is going to occur as well as the fact that fracture is imminent, the surgeon may be able to avoid this fracture. Suppose an implant is being inserted with impaction at an incorrect angle and is placing a dangerous amount of stress at a particular part of the femur: the proposed AE warning system would indicate that fracture is imminent. Knowing the location of impending fracture would allow the surgeon to re-orient the implant at the correct angle and thus achieve stability without fracture.

To supplement the literature review of Total Hip Artroplasty and in particular intra-operative fracture, two active hip surgeons were interviewed to determine to what extent intra-operative fracture prediction would be useful to them, the types of fracture they have encountered and if predicting the site of fracture would be useful.

1.3.3 Consultation with Surgeons

Two surgeons were interviewed: Mr. Macey who practices in Sligo General Hospital and Mr. Kevin Mulhall who practices in Beaumount Hospital, Dublin and in the Sports Surgery Clinic, Dublin.

Both surgeons confirmed that intra-operative fracture does occur during Total Hip Arthroplasty. They said that the rates of intra-operative fracture in their experience were low. Mr. Mulhall even stated that an intra-operative fracture has yet to occur to one of his patients. Mr. Macey said that an intra-operative fracture occurred in a revision setting for him recently. Both agreed that a device to warn the surgeon of intra-opertive fracture would be a useful tool with Mr. Mulhall emphasing that revision surgery is the most viable application for the proposed technique. He proceeded to say that occasional surgeons are more likely to cause an intra-operative fracture as well as those in training. So while the experienced surgeon may in very rare cases cause an intra-opertive fracture, not every hospital has enough work for a surgeon dedicated solely to THA surgery and every surgeon has to be trained before they reach a level of proficiency where they can comfortably avoid intra-operative fracture. Mr. Mulhall and Mr. Macey saw the benefit in locating the site of impending fracture but said that the prediction is useful on its own and locating should come as a secondary priority. Furthermore Mr. Mulhall expressed concern that it would be difficult to mount multiple sensors (as would be required for locating microcracks) on the femur since such a small area of the bone is exposed during surgery. Both he and Mr. Macey stated that any detection device that comes in contact with the femur or any patient tissue needs to be sterlised and the connection to the monitoring computer would have to be wireless. Mr. Mulhall stated that during surgery, it is normal for cancellous bone to be compressd and removed from the femur, while no cortical bone should be damaged or removed. This would suggest that any acoustic emission emanating from cancellous bone would have to be distinguished from cortical bone in order to predict cortical bone fracture.

Mr. Mulhall described a typical situation where intra-operative fracture can occur. It is the over sizing of broaches. A range of different sized broaches are used to enlarge and form the correct slot for the final implant. A possible scenario could happen as follows: The surgeon uses broaches 1 and 2 without incident with broach 2 providing a good fit, but he thinks that maybe broach 3 would give a tighter fit ensuring optimum bone ingrowth. However as he impacts in broach 3, the femur becomes over stressed and a sprial fracture propagates distally from where the femoral head was removed. If the proposed warning system had been in place, the AE sensor would detect the dangerous microcracks that would occur before fracture and warn the surgeon of impending fracture. Thus he could retract broach 3 before facture occurred and save the patient increased trama and avoid increased patient rehabiliation time.

1.3.4 Summary

After reviewing the literature and consulting with the two afore mentioned surgeons the following conclusions can be drawn.

1. Intra-operative fracture is a concern for surgeons and warning surgeons of impending fracture would be very useful in particular for revision THA

surgeries, occasional surgeons, trainee surgeons and indeed during their education.

2. While locating microcracks and thus the site of impending fracture is beneficial, it is not essential. Furthermore it may prove difficult in practice.
3. There is a need to filter out the acoustic emission of cancellous bone cracking during its compression and removal from the femur.
4. The impaction sound will also produce acoustic emission. This will have to be filtered from the received AE signals.

Therefore the following form for the dissertation was decided on: firstly test both cortical bone and cancellous bone samples to see if there is a way to distinguish the acoustic emission signals from each other. Next, see how fracture of cortical bone can be predicted and simulate a THA surgery in the laboratory to determine if an intra-operative fracture can be predicted. Then test and develop ways to find the location of microcracks in bone using acoustic emission and discover if the location of fracture can be predicted before the fracture happens.

2. Acoustic Emission Instrumentation

2.1 The Acoustic Emission System

A typical acoustic emission system consists of four components: the AE sensors, the preamplifiers, the analogue to digital converter and the software that measures, records and analyses the AE waveforms.

The AE sensor converts the acoustic wave propagating through the test material into an electrical signal. The most common type of AE sensor is a piezoelectric sensor. It consists of a disc of piezoelectric crystal that fits inside a metal housing. The part of the metal housing that is between the piezoelectric disc and the test sample is known as the wear plate. Usually a couplant is needed between the sensor wear plate and the test material to ensure no air gaps exist between them. Couplants include anything from natural wax to super glue.

The purpose of a preamplifier is to amplify the very small amplitude signal to a suitable magnitude for analogue to digital conversion. Typically preamplifiers with gains of 40 dB are used. A 40 dB gain is where the output is 100 times the input. A wide frequency response is important for the preamplifier typically from 20 kHz to 1 MHz. It is essential that noise introduced by the preamplifier circuitry is minimal.

The most complicated and costly part of the AE system is the data acquisition device whose main component is the analogue to digital converter or digitizer which converts the raw analogue signal into a digital representation. Two characteristics of AE make the electronics of an AE digitizer particularly complicated and costly: a large bandwidth extending into relatively high frequencies and a very large dynamic range (the difference between the smallest the largest signal of interest). The dynamic range can be of the order of 80 dB to 90 dB. It would not be abnormal for an AE device to sample signals ranging from 5 mV up to 10,000 mV and in order to faithfully sample the 5 mV signal amplitude levels of around 0.5 mV would need to be detectable. In order to achieve a bandwidth of up to 1 MHz and a dynamic range of 80 – 90 dB, the analogue to digital convertor needs to have a sampling frequency of at least 10 MHz and a vertical resolution of at least 16 bits giving it 65,536 quantization levels (2^{16} = 65,536). Another concern when performing AE source location on small samples is the time domain resolution: since the source localization is based on time differences, it is essential to precisely measure the time of arrival at each sensor and if the AE signal is not sampled often enough, an unacceptably large error will be introduced.

Software that controls the AE acquisition and analyses the AE waveforms, can come as a turn-key AE system that has all the system controls and analysis options already programmed and easy for the user to operate and analyse. If a purpose built AE system is used, most of the AE control and analysis will have to be programmed by the user.

A turn-key AE system was available at the commencement of this project. It is the PCI-2 (18 bit AE) card from Physical Acoustics Corporation. It has two AE channels and it comes with software called AEwin which performs a range of analysis. Source location on a two dimensional surface requires a minimum of three sensors and thus AE channels, so either a second PCI-2 card is acquired and used in conjunction with this one or a different AE data acquisition card/device is used. A second PCI-2 AE card proved too costly, so instead a general purpose digitizer was sourced and purchased. It is the PXI 9846 digitizer from Adlink Technologies Corporation. It has four channels of AE with a sampling frequency of 40 MHz and 16 bits dynamic range. The biggest limitation of this device is its input voltage range which is 2 volts (±1 V). With a 40 dB preamplifier it is as sensitive as the PCI-2 card but any AE hit whose amplified amplitude exceeds ±1 V will be clipped (truncated). But since “first threshold crossing” is the method used for determining when an AE hit has arrived at a sensor, this limitation will not affect the source location endeavors. Furthermore the PXI 9846 digitizer comes with a driver for various software packages including NI LabVIEW, a graphical programming language which the author used to acquire and analyze the AE waveforms.

Therefore the PCI-2 AE system was used for fracture prediction as it has an inbuilt capability to extract AE feature data as well as a wide dynamic range data acquisition. The PXI 9846 digitizer was used for the fracture source localization work as it has 4 AE channels.

2.2 Acoustic Emission Components

Acoustic Emission Sensors

While only one or two piezoelectric sensors (AE sensors) are needed for the fracture prediction work, at least three are required for the AE source localization. The distances under test on bone are relatively small on the order of centimeters so a small sensor is preferred. The smallest sensors available are approximately 3mm in diameter from Vallen Systeme Gmbh. However a slightly larger AE sensor at 5mm diameter was chosen as it is more robust and has a broadband frequency response and it is significantly lower in cost. This is the Pico Z AE sensor from Pancom Ltd UK. It has a broadband frequency response ranging from 100 kHz to 850 kHz and a diameter of 5 mm. The calibration sheets of all the sensors used in this work are in the Appendix.

Preamplifiers

The most common gain that an AE preamplifier has is 40 dB and it was envisaged that this would probably be sufficient. However, a switchable gain preamplifier known as "2/4/6" from Physical Acoustics Corporation was chosen to give more flexibility. It has the capability to switch gain between 20 dB, 40 dB and 60 dB, hence its name. Four of these preamplifiers were purchased.

Power Supply and Regulator

The 2/4/6 preamplifier is powered by a phantom DC supply from the PCI 2 AE system (Physical Acoustics Corporation). However when using the PXI 9846 digitizer, no such facility exists, so an electronic unit had to be developed to provide this power supply to the preamplifiers. This unit needs to supply 28 volts DC to the output of preamplifier without interfering with the AC signal travelling from the preamplifier to the PXI 9846 digitizer. This solution together with the required circuit diagram was taken from the *Acoustic Emission Preamplifiers* catalogue from Vallen Systeme GmbH. A copy of this circuit diagram is in the Appendix and it is reproduced in Figure 2.1 as a *Circuit Maker* schematic.

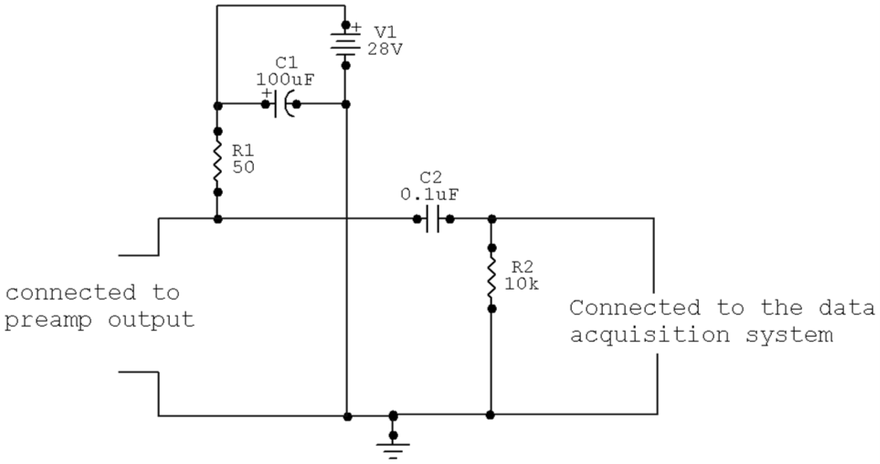

Fig. 2.1 Preamplifier power supply circuit diagram.

The operation of the circuit is as follows: it fits in-line between the output of the preamplifier 2/4/6 and the input of the PXI 9846 digitizer. A bench power supply delivers 28 volts to the circuit. Referring to Figure 2.1, DC current flows from V1, through R1 and then to the positive terminal of the preamplifier output where it supplies the preamplifier with 28 volts. It then returns straight back to the negative terminal of V1. It cannot flow into the input of the digitizer (data acquisition system) as it is a DC voltage and C2 stops it. From an AC perspective the AC signal propagates from the preamplifier unhindered through C2 as capacitors do not stop AC current, and thus the signal reaches the input of the PXI9846 digitizer.

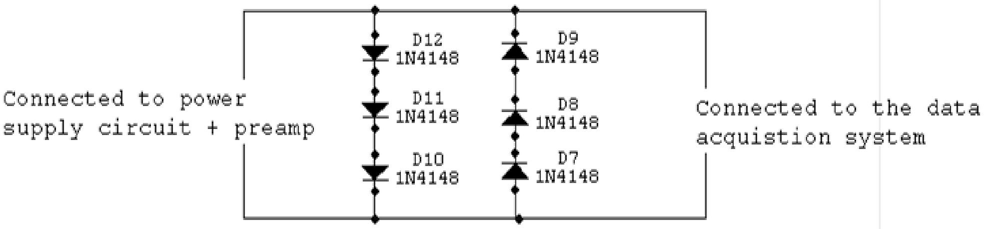

Fig. 2.2 The voltage regulator circuit diagram.

The digitizer for which the 2/4/6 preamplifiers and the PICO-Z AE sensors was designed supports a ±10 volt input but the PXI 9846 features a ±1 volt input. However the PXI 9846 digitizer can withstand at a maximum ±5 volts. Any voltage outside this range has the potential to damage the digitizer, so a voltage regulator needs to be incorporated. A simple diode clipper was selected for its ease of design and operation. The circuit requirements are as follows: any signal between -1 volt and + 1 volt should not be affected by the circuit and the signal needs to be clipped (truncated) before it goes outside the ±5 volt range. Therefore there is a 4 volt margin for the clipping to come in play. Each diode has approximately 0.7 volts across it but the exact level will depend on frequency and current and can in extreme cases vary from 0.5 to 1 volt. Three diodes in series were chosen to give a minimum clipping level of 1.5 volts and a maximum clipping level of 3 volts. A second set of three diodes were also arranged in reverse order to clip the negative half cycle. The diodes selected are special high speed diodes to deal with the high frequency AE waveforms. A circuit diagram is presented in Fig. 2.2.

Therefore there are two circuits required to complete the AE system: the power supply circuit and the voltage regulator circuit. It was decided to incorporate the two circuits in one module encased in a noise shielded aluminum box. This module is called PwrReg (power supply, voltage regulator) and its place within the AE system is illustrated in Fig 2.3. Four modules are required.

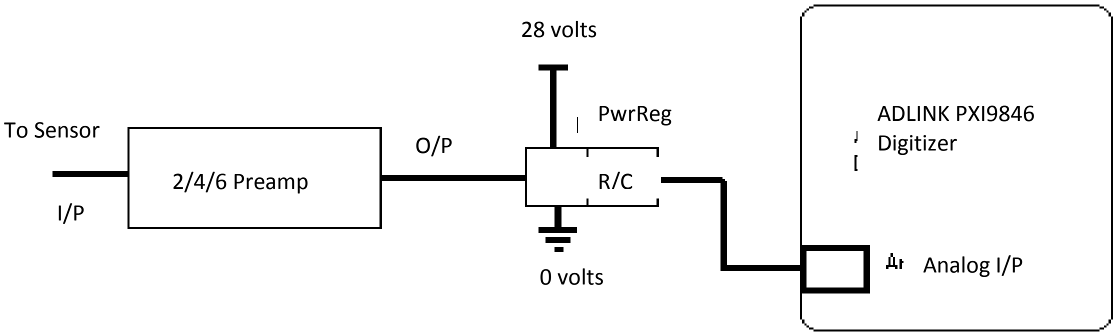

Fig. 2.3 The PwrReg and the AE system.

Design and Assembly of PwrReg

The design and construction of PwrReg consists of three stages: circuit simulator, bread board testing and permanent assembly. The circuit was initially designed and simulated in *Circuit Maker*. Next the PwrReg was built on a breadboard using the physical components and real instrumentation. Then it was built on a strip of *Vero Board* (*Strip Board*) and inserted in an aluminium enclosure. BNC connecters were attached to both ends of the aluminium box for connection via BNC cables from the preamplifier to the digitizer. Power supply terminals were attached on one side and 4mm connectors were used to bring power to the PwrReg. A photograph of the assembled module is shown in Figure 2.4.

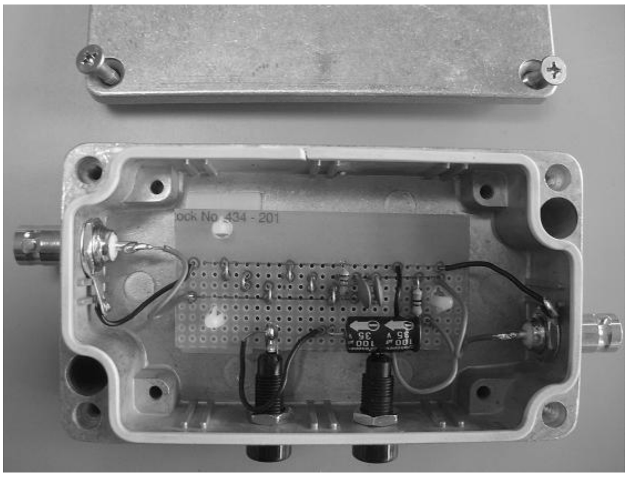

Fig. 2.4 A photograph of the PwrReg (Power Supply Voltage Regulator).

Digital Trigger Module

In order to acquire burst type acoustic emission, the data acquisition needs to be triggered when the analogue AE signal reaches a certain threshold. In the PCI-2 AE system there is a piece of software that can be configured to achieve this. The PXI 9846 digitizer can be triggered in a number of ways. The most straightforward way is the analogue trigger. The user sets the threshold in software with 8 bit resolution and when the input signal rises above this threshold level at the selected channel, the PXI 9846 device records a preset number of samples. Given the 8 bit resolution the lowest level the trigger can be set to is 0.0078 volts. While this is sufficient for most AE applications, in some cases if may be required to detect even smaller AE signals. Furthermore during initial testing of the PXI 9846 device by the author, this trigger technique was found to be unreliable and more than once would only accept signals that reached 0.1 volts. For this reason it was decided to make use of another trigger method, the digital trigger. This works by recording AE on all software selected channels when a digital pulse is received at the TRG IO connector on the PXI 9846 device front panel. The pulse must be at least 20ns long and 3.3 volt TTL (Transistor Transistor Logic) compatible.

The solution was to take a connection from one of the PwrReg's and wire it into a specifically designed module which would convert the very small analogue signal into a TTL compatible digital signal which could in turn be connected directly to the TRG IO of the PXI 9846 digitizer. This module which is called the External Digital Trigger Module would have an adjustable trigger level which could be altered using a screw driver and a voltmeter.

Figure 2.5 shows the circuit as built in *Circuit Maker*. R3 is a variable resistor which can be adjusted with a screw driver to set the trigger voltage. A voltmeter connected at the negative input of the comparator (IN-) displays this trigger voltage. If the input signal rises above this trigger voltage, the comparator output voltage increases to that of the supply voltage (V1 in Figure 2.5). The comparator is configured with hysteresis so that a very brief rise above the trigger voltage is held for a longer period of time even though the input signal may fall more quickly. This hysteresis action is shown in Figure 2.6. The output (A) switches to high when the input AC wave (B) reaches the trigger voltage. But it does not go low until the output (A) falls below the trigger level. This ensures that even a very brief rise above the trigger level will satisfy the minimum 20 ns pulse width requirement. The comparator needs a power supply of 5 V to operate and therefore the output will swing from +5 V to close to 0 V, while the PXI 9846 requires a 3.3 V to 0 V swing. In order to reduce the logic high output to 3.3 V, a transistor amplifier with a gain of less than one is added on to the circuit as seen in Figure 2.5. Figure 2.6 shows the output swinging from close to 0 V to just over 3.2 V.

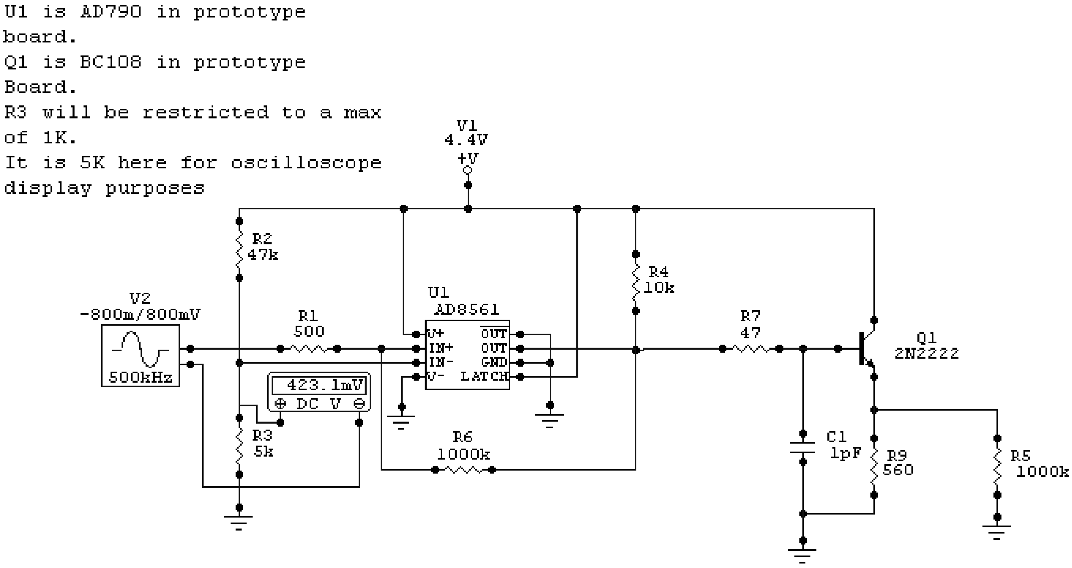

Fig. 2.5 The circuit diagram of the External Digital Trigger Module in *Circuit Maker*.

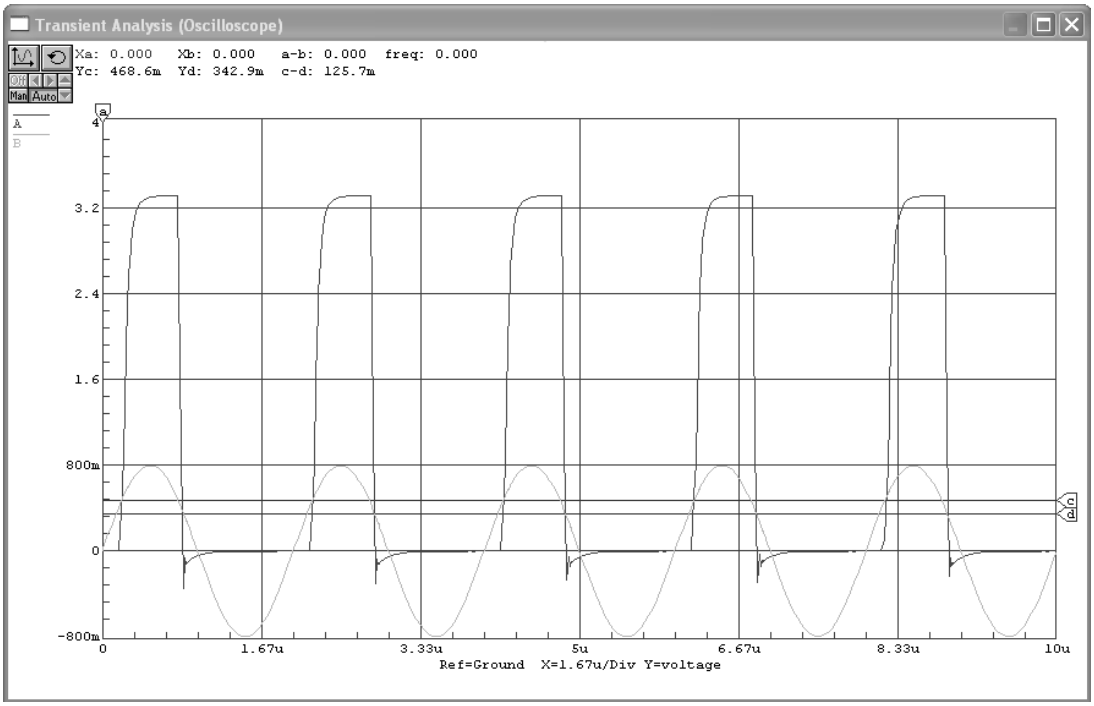

Fig. 2.6 The *Circuit Maker* simulation showing how an analogue AC signal is converted to the digital signal compatible to 3.3 volt TTL.

With the design complete the circuit was constructed on strip board and inserted in an aluminum box with a BNC connector for the analogue input signal and a SMB cable and connector at the output for connection to the TRG IO on the front panel of the PXI 9846 digitizer. A photograph of the complete module is presented in Figure 2.7. Next a test was performed with the PXI 9846. A signal was generated with a function generator and fed directly through the PwrReg with its power turned off and then into channel 0 of the digitizer. The PwrReg was included in the test as it facilitates a tap off the input signal which is then used by the External Digital Trigger Module.

The Module operated reliably with a trigger level set as low as 0.5mV and also at all desired higher voltage levels.

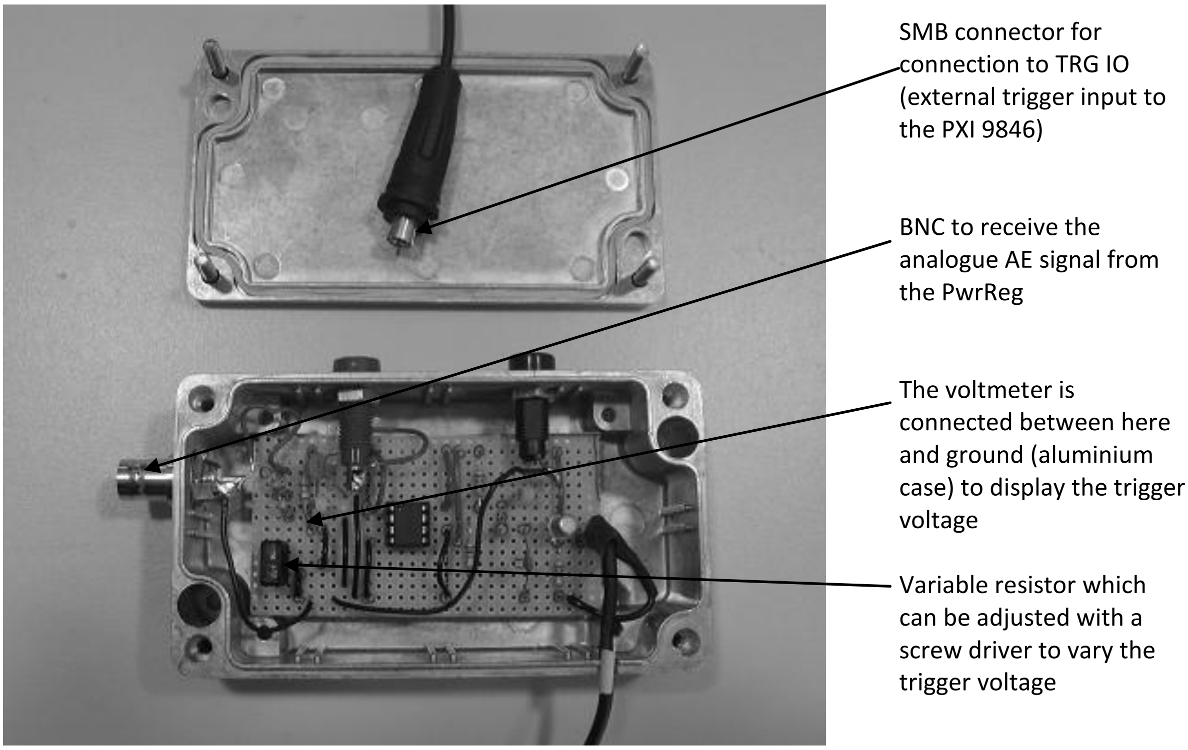

Fig. 2.7. A photograph of the External Digital Trigger Module showing the internal electronics.

Software Settings to Acquire an AE hit with the PXI 9846 Digitizer

The PXI 9846 digitizer is shipped with a software application called DAQ Pilot. This appliation can be use to acquire waveforms on its own or it can be called from another program for example a C++ or LabVIEW program. Either way it has a number of settings which are important to understand before acquiring AE waveforms. The following table explains the more relevant of these.

Setting	Description
Channels	There are four analogue input channels available
Sampling Rate	This can be set anywhere between 1 and 40 million samples per second even when every channel is used. All the channels are sampled at the same rate
Number of Scans (samples)	This is the number of samples the device records every time the trigger is triggered
Trigger source	External digital is to be used in this work
Trigger mode	There are four options, but Middle Trigger is used in this work. This means that the device records samples before (pre-trigger) and after (post-trigger) the trigger event. This allows the whole AE event to be sampled
Pre-trigger count	This is the number of scans allocated for pre-trigger sampling
Post-trigger count	This is the number of scans allocated for post-trigger sampling

It was found most effective to carry out acquisition first and then process the AE waveforms post acquisition. So, two programs were developed. The first is used for acquiring the AE data and the second to analyze the AE data. Figure 2.8 presents the front panel of the AE data acquisition program developed in LabVIEW (National Instruments).

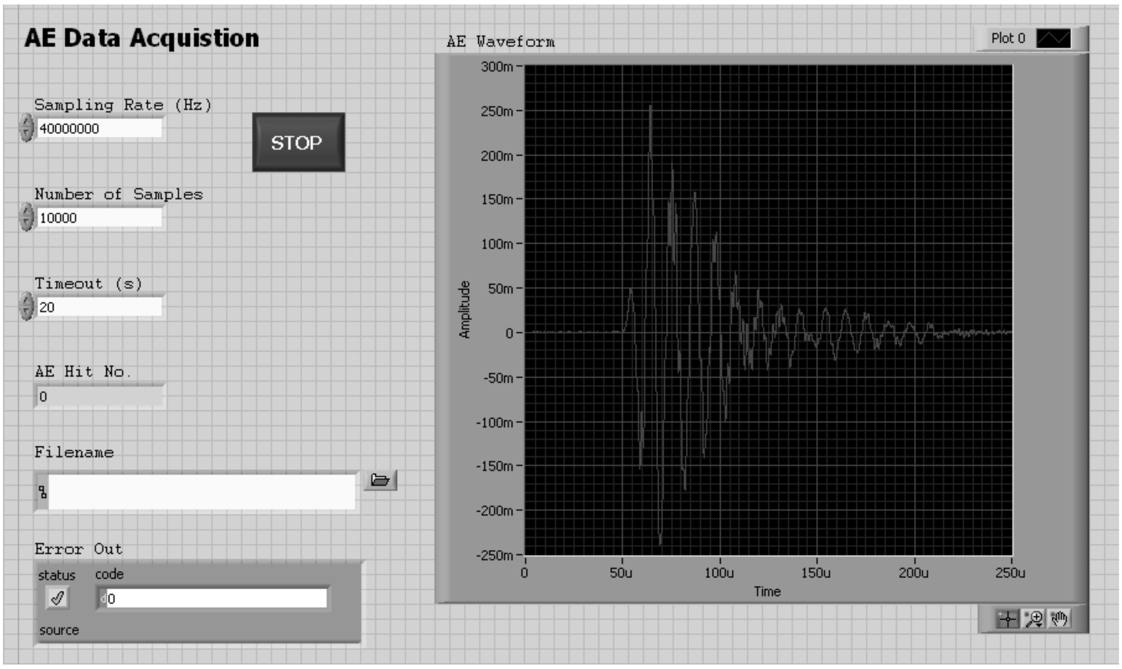
AE Data Acquistion

Sampling Rate (Hz)
40000000

Number of Samples
10000

Timeout (s)
20

AE Hit No.
0

Filename

Error Out
status ✓
code 0
source

Fig. 2.8 The AE data acquisition program developed in NI LabVIEW.

3. Fracture Prediction: Distinguishing Cortical Bone Microcracking from Cancellous Bone Microcracking

3.1 Introduction

A major challenge involved in the prediction of intra-operative fractures during THA (Total Hip Arthroplasty) is discerning which detected acoustic emission hit is the microcracking of cortical bone and which is from another source. The other two main sources of acoustic emission are cancellous bone microcracking and the acoustics of the impaction of the implant or broach. This chapter deals with trying to distinguish between cortical and cancellous bone AE. In THA surgery, the broach is impacted down the medullary canal. It must force cancellous bone out of its way by either compressing it or pushing it into the marrow further along the bone. As this cancellous bone becomes compressed or displaced the broach creates the correct slot for itself and in order to ensure a tight fit some forces are placed on the surrounding cortical bone, but sufficient forces to cause it to fracture should not be experienced. Currey (2006) states that as cortical bone is stressed little or no AE occurs until the bone passes the elastic stage (pre-yield) and enters the plastic stage (post-yield). This is because the microcracks contribute mostly to the plasticity of the bone. So if there was no cancellous bone present in the THA surgery operation and impaction acoustics are ignored, then the onset of AE would indicate imminent fracture and the surgeon should halt impaction thus avoiding fracture. It becomes necessary then to be able to distinguish cortical microcracking AE from cancellous microcracking AE. In order to do this the first step is to get AE data from typical cortical bone microcracking and typical cancellous bone microcracking similar to what might occur in THA surgery.

The cancellous bone experiences compressive forces during the THA surgery. So loading samples of cancellous bone in compressive static tests at a low crosshead speed should produce typical cancellous AE. The cortical bone experiences a mixture of compressive and tensile forces. A typical test that produces both tensile and compressive forces is the three point bend test. The bone samples need to be taken perpendicular to the long axis of the bone. The part of the femur that probably experiences most stress is just below the femoral head. Therefore the cancellous and cortical samples are taken from there.

3.2 Test 1 – First Samples to Collect Cortical and Cancellous AE Data

Aim:

The aim of this test is to see if it is possible to distinguish the acoustic emission emanating from cortical bovine bone from the acoustic emission emanating from cancellous bovine bone.

Materials and Methods

A bovine femur, approximately two years old was acquired from the local butcher (Burns, Grange, Co. Sligo). It is from a *Charolais Cross* female animal. The femur was taken straight to the laboratory where it was cleaned of flesh and cartilage using scalpels. Then using a band saw a 35 mm section (in the longitudinal direction) of the femur is sawn just below the femoral head and was labelled *proximal diaphysis section* as can be seen in Fig. 3.1. During the sawing process, de-ionised water was used to keep the bone cool. Furthermore a slow cutting speed was maintained. Figure 3.2 shows the proximal face of the section. The cortical shell, the cancellous bone and marrow are visible. The cancellous sample is taken from the proximal end of the section as it has the most cancellous bone and the cortical sample is taken from the distal end as the cortical bone is thicker here. A low speed diamond saw as shown in Figure 3.4 is used to cut the cortical and cancellous samples from the proximal diaphysis section. Figure 3.5 and Figure 3.6 show the shape and dimensions of the cortical and cancellous samples respectively.

Fig. 3.1 Proximal diaphysis section cut from femur anterior aspect.

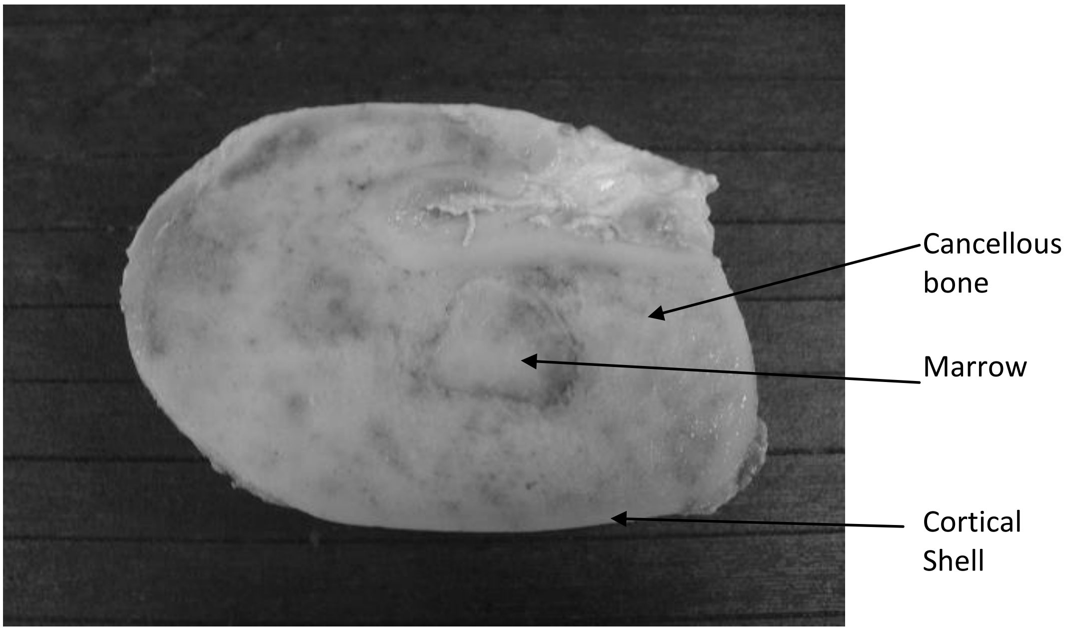

Fig. 3.2 View of the proximal end of the 35 mm section. The bottom of the picture is the anterior aspect of the femur.

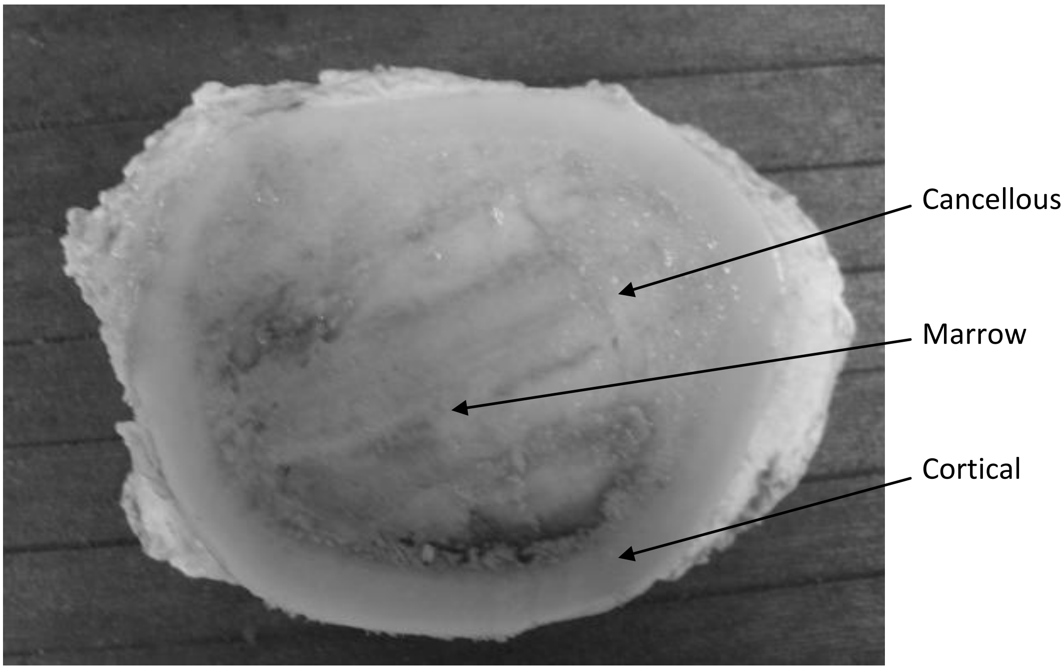

Fig. 3.3 View of the distal end of the 35 mm section. The bottom of the picture is the anterior aspect of the femur.

Fig 3.4 The slow speed diamond (Isomet from Buehler) saw cutting the cortical specimen to size. Water was whipped up by the cutting wheel from the water bath to keep the sample cool. Water was also sprayed from pressurized container to keep parts of the specimen not currently undergoing cutting moist.

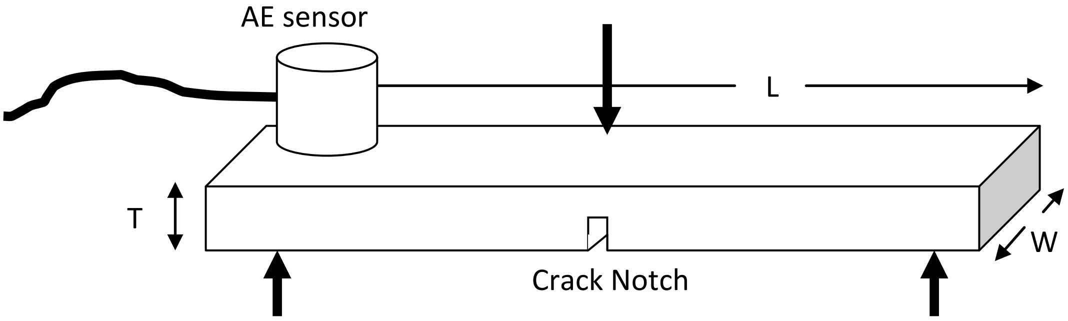

L	41.6mm	Length	Tangential to medullary canal
W	5.0mm	Width	Parallel to medullary canal
T	2.5mm	Thickness	From endosteum to perisoteum
Notch	2.5 x 0.5mm	Notch	Depth by Width of notch

Fig. 3.5 Cortical beam loaded in 3 point bending.

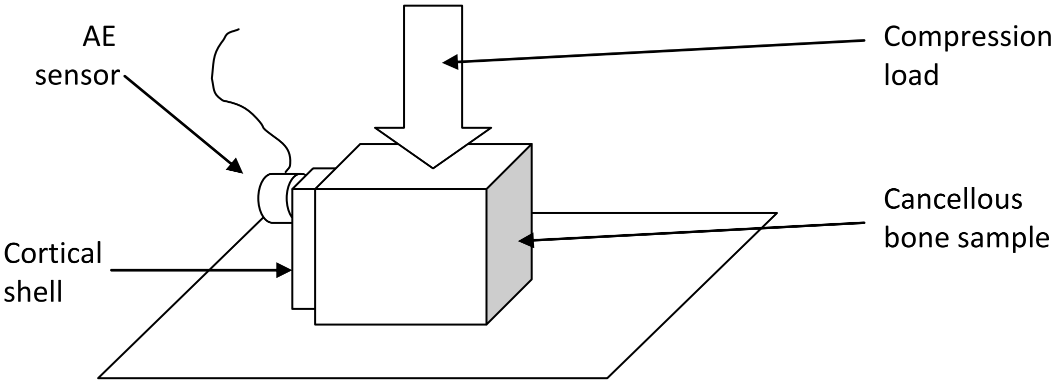

Fig. 3.6 Cancellous bone sample loaded in compression

The cortical bone sample had a length L of 41.6 mm, width W of 5.0 mm and a thickness T of 2.5 mm. A notch was created at the midpoint of the sample. The slow speed diamond saw was used to cut the notch. The depth of the notch was 2.5 mm and it was 0.5 mm wide. The three point bend span was 36 mm and the pins had a diameter of 10 mm. Ultrasound couplant which has the texture of petroleum jelly was used between the 3 point bend pins and the bone specimen to minimise friction noise that could interfere with the acoustic emission.

The cancellous bone sample was 10 mm high and 5 mm wide and thick. A piece of cortical shell was left attached to one side of the cancellous sample for the AE sensor to adhere to. The sample was loaded in compression taking care that no force is placed on the cortical shell. The Acoustic Emission system from Physical Acoustics was used to record and analyze the AE hits that occurred during the tests. A voltage threshold level for accepting valid AE hits from both samples was set at 40dB (with 0 dB equating to 1 μV).

The samples were loaded in the Materials Testing Machine at a cross head speed of 0.05 mm/minute. The cancellous test was stopped after the sample had displaced by 3mm and the cortical bone sample was stopped when the sample broke (10% of peak load).

Results and Analysis

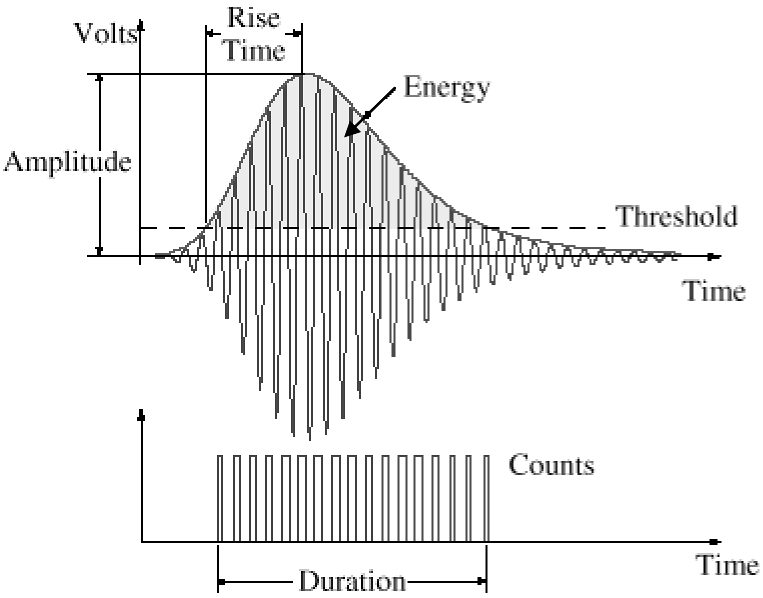

Fig. 3.7 AE Features extracted from a typical AE waveform.

The AE system used to acquire, record and extract acoustic emission feature data was the PCI-2 (2 channels, 18 bits, 40 MHz PCI card) from Physical Acoustics Corporation. The gain of the 2/4/6 preamplifiers was set to 40 dB. In this test a threshold level of 40dB was used meaning that once the voltage signal reached 10 mV the acquisition system started recording the waveform for a preset period of time. Once the AE waveform reaches the PCI-2 AE card, two processes are carried out: firstly the digitized waveforms are transferred into memory and stored on the hard drive. Secondly real time analysis is carried out on the waveforms as they are accepted into the PCI-2 card. This analysis involves generating many time domain and frequency domain parameters such as the peak amplitude and peak frequency of a received AE waveform. This feature data is displayed on screen during the test and also saved to hard disk along with the actual waveforms. This approach allows for real time monitoring of the material under test, easy analysis of AE features post test and further testing of the actual waveforms, if the AE feature data are not extensive enough. Table 3.1 lists the AE features along with a brief explanation.

AE Feature	Description
Rise Time	This the time from when the AE burst or hit first crosses the threshold set to detect the AE hit to the time of the wave peak. After the peak the wave decays until it falls below the threshold again.
Count	The number of times the AE wave burst or hit crosses the threshold in one direction. This is the equivalent to the number of wave peaks in the AE wave burst.
Energy	The integral of the rectified voltage signal over the duration of the AE hit.
Duration	The time of the first threshold crossing to the end of the last threshold crossing in one AE burst or hit.
Peak Amplitude	The maximum amplitude (positive or negative) during an AE hit
Average Frequency	AE Counts divided by Duration of hit
RMS	Root Mean Squared (volts)
ASL	Average Signal Level (dB)
Reverberation Frequency	Average frequency of AE hit after peak amplitude
Initiation Frequency	Average frequency of AE hit before peak amplitude
Signal Strength	Same as Energy except it is independent of gain
Absolute Energy	True energy content. Integral of rectified voltage divided by reference resistance (10 KΩ) over whole waveform
Frequency Centroid	Weighted average frequency and performed using the FFT
Frequency Peak	Point in power spectrum at which the peak magnitude occurs.

Table 3.1. Brief explanation of AE feature data

The Frequency Centroid and the Frequency Peak are calculated using the Fast Fourier Transform (FFT) while the rest of the features are calculated in the time domain. While it is possible to calculate all these AE features directly from the AE wave, it is quicker and easier to use the recorded feature data.

So the first step in analyzing the cortical and cancellous data is to compare the feature data of both samples. There were 556 AE hits in the cortical data set and 91 AE hits in the cancellous data set. Each of these hits had at least 10 counts (threshold crossings). In order to determine the best measures to use in analyzing the data, it is important to establish whether the data is normal or not. The Shapiro-Wilk test is performed using an Excel add-in called “Analyze it”. The test reported all the features of the cortical data to be not normal with P-values less than 0.0001. The test reported two features of the cancellous data to be normal: Reverberation Frequency and the Average Frequency with P-values of 0.1765 and 0.01284 respectively. The rest of the cancellous features were reported as not normal. Because most of the data is not normal, Medians and IQRs (Inter Quartile Ranges) are used to compare the data sets. Figure 3.8 shows the medians and IQRs of all 13 AE features for cortical and cancellous data sets.

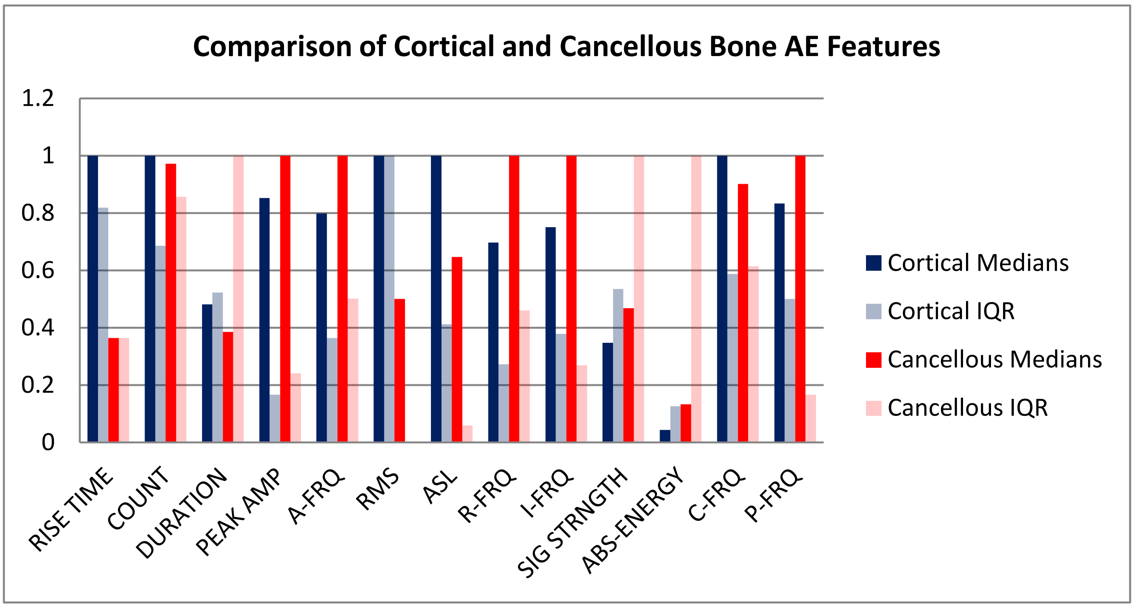

Fig 3.8 Comparing cortical and cancellous data in terms of normalized Medians and IQRs.

Visually analyzing the data, two conditions are used to determine if a particular AE feature is useful or not

1. The median is significantly different between the cortical and cancellous data sets and
2. The IQR is small compared to the median.

While this approach is very subjective, it does give a starting point for analysis. If the IQR is large compared the median there is likely to be a lot of overlap between the data sets, making distinguishing them difficult. At first glance the following parameters appear useful: Rise time, Peak Amplitude, ASL, Average Frequency, RMS, Reverberation Frequency, Initiation Frequency and Peak Frequency. A Single Factor ANOVA test from Excel was used to compare the cortical data with the cancellous data to determine if there is a significant difference at the 5% confidence level. All of the above mentioned AE features show a statistical significant difference except Rise Time. According to the ANOVA data (see Appendix) the Reverberation Frequency shows the best separation with a P-value of 6.73×10^{-18}.

In a surgical setting an average or median of the data can only be calculated after the data has been collected, which is too late for fracture prediction, and it is impossible to know with any high degree of certainty whether any particular value is cortical or cancellous in origin because of the overlap. However by computing a moving average of the data, separation of the data can be achieved without having to wait until all the data has been received. A 15 value moving average was found to give a good separation between the sample of cortical and cancellous bone, as can be seen in Figures 3.9A through to 3.9E. The moving average is calculated by taking the previous 15 values and computing their average. Then when a new value is received the moving average computes the average of this value with the previous 14. Because of the averaging the variation in the data is reduced. But if too many values are used in the averaging the response time is compromised. Through trial and error a 15 value moving average was found to be the optimum. In a surgical setting the surgeon would be warned of the onset of cortical bone microdamage, at the latest, 15 AE hits after the cortical bone started experiencing microdamage. Figure 3.9A through to Figure 3.9E show the moving average for the five AE features that showed a statistically significant difference between the cortical and cancellous data sets.

While ASL showed a significant statistical difference, it can be seen (Figure 3.9A) that this separation is only present for a very small moment in time, probably when the final facture of the sample occurred. Therefore this feature is clearly not suitable for fracture prediction. While the other four parameters show a good separation, caution must be used when interpreting the Peak Amplitude. It is known that value of the Peak Amplitude is very dependent on the sample size. The small cortical bone sample tested here would only produce low amplitude hits while a whole femur microcracking could be expected to produce much larger peak amplitude. It would be preferable if the parameter chosen was independent of the size of the bone sample. The three frequency based features would be expected to be independent of sample size. Separation can be observed in Figures 3.9C, 3.9D and 3.9E, for the Reverberation, Initiation, and Peak Frequency respectively.

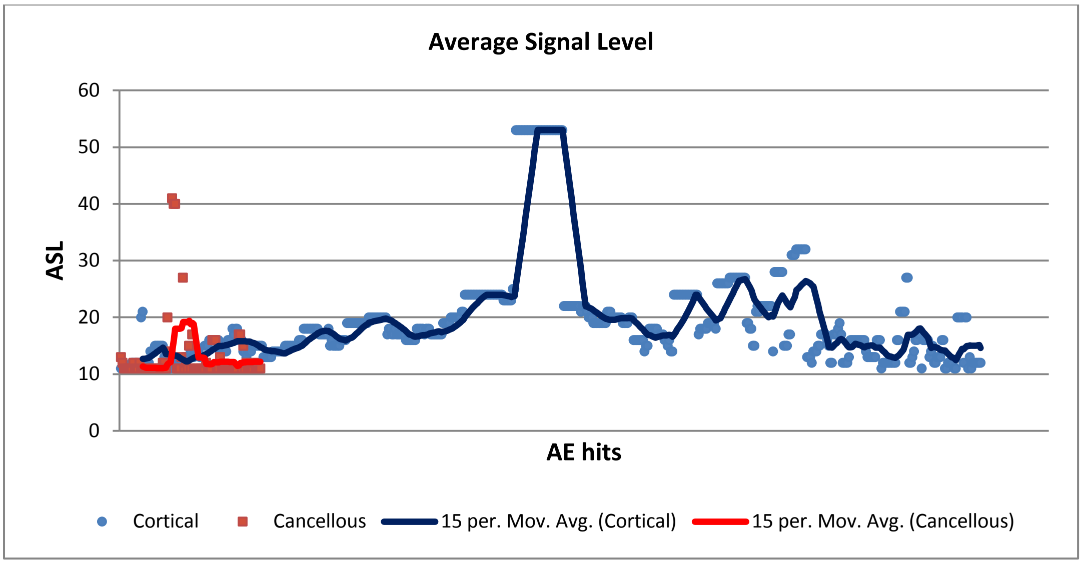

Fig. 3.9A Comparing cortical and cancellous data for AE feature ASL (Average Signal Level).

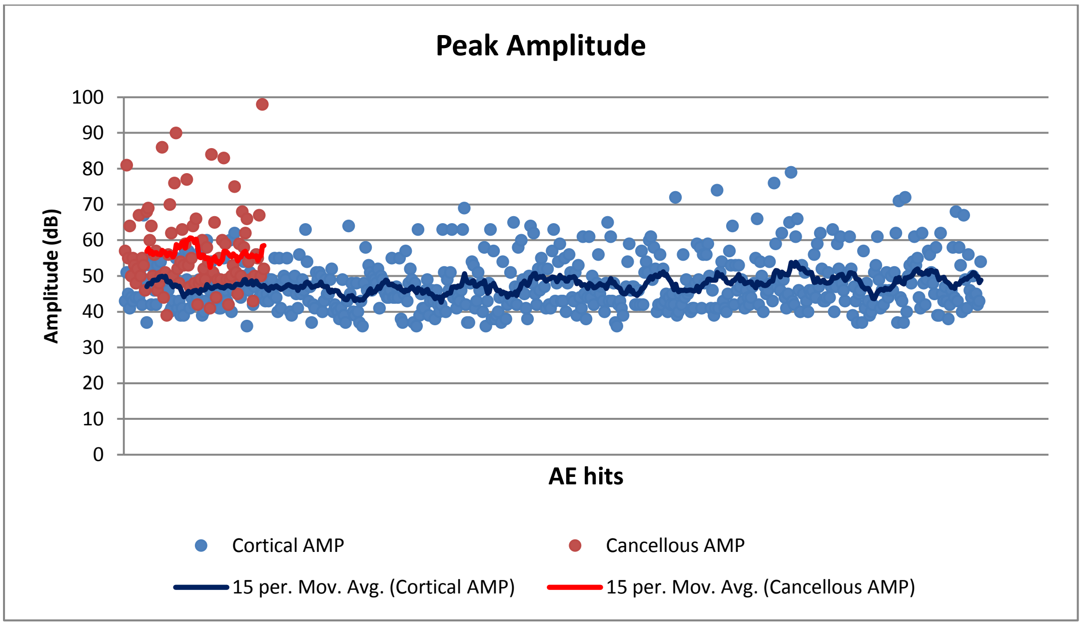

Fig. 3.9B Comparing cortical and cancellous data for AE feature Peak Amplitude.

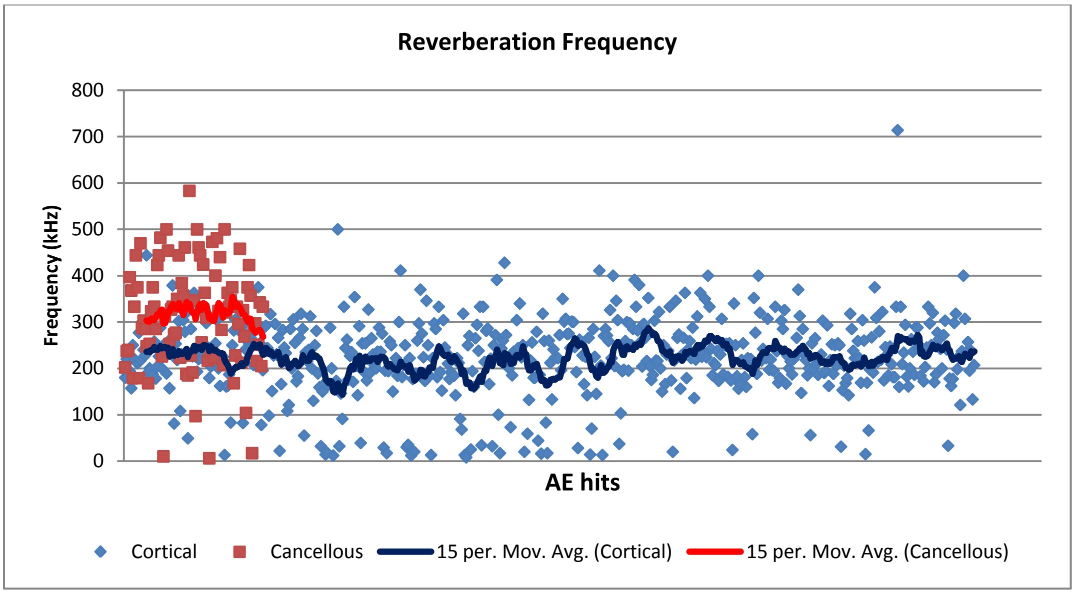

Fig. 3.9C Comparing cortical and cancellous data for AE feature Reverberation Frequency.

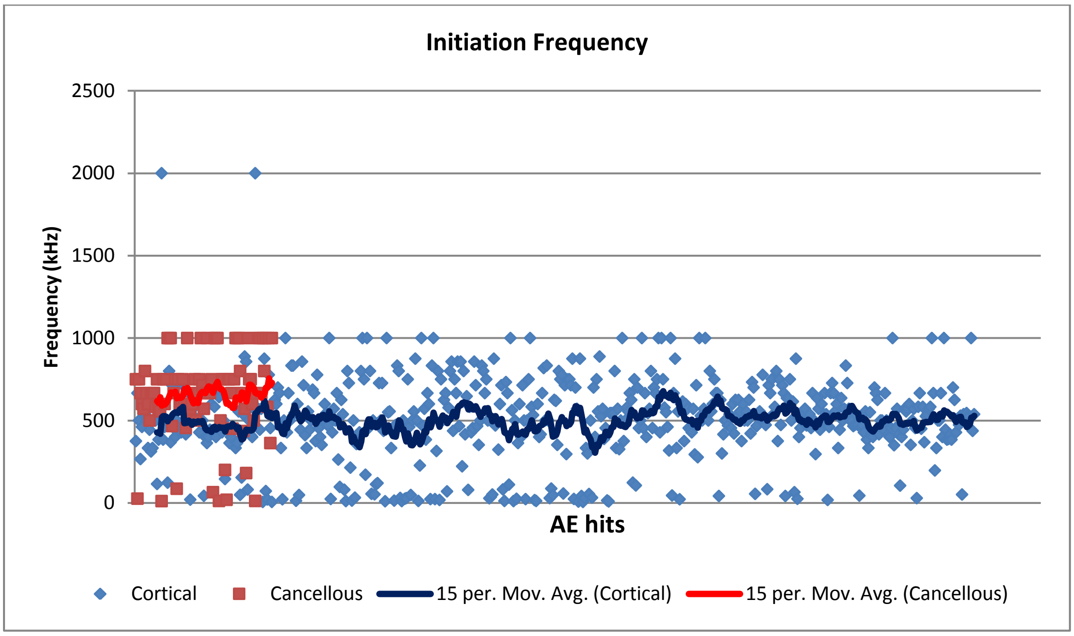

Fig. 3.9D Comparing cortical and cancellous data for AE feature Initiation Frequency.

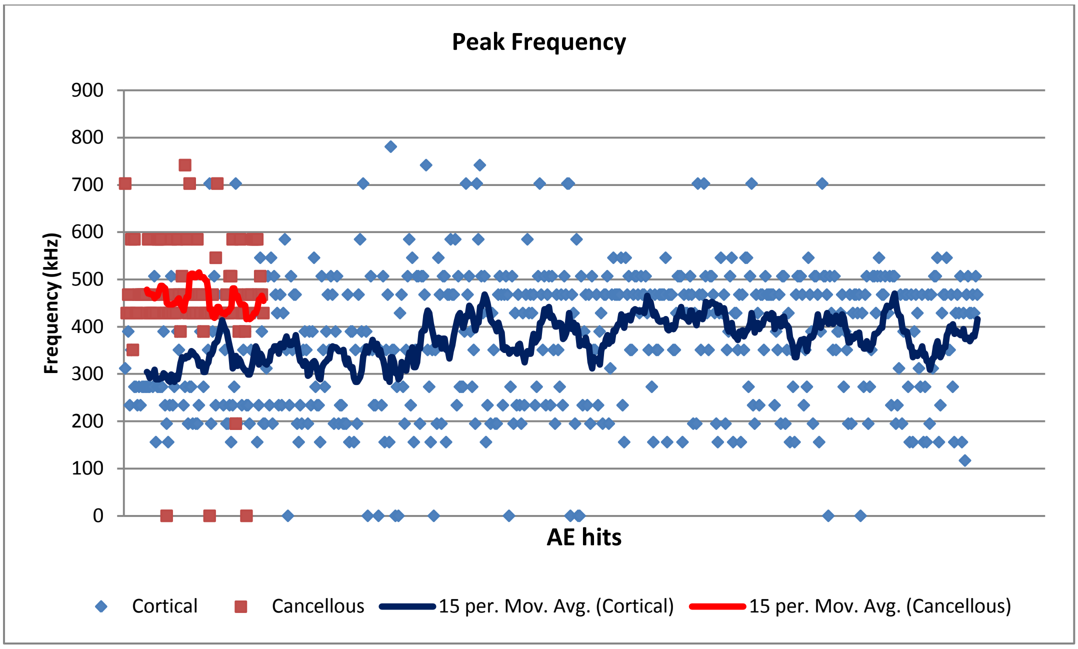

Fig. 3.9E Comparing cortical and cancellous data for AE feature Peak Frequency.

3.3 Test 2 – Testing a Larger Number of Samples

While Test 1 showed significant promise in that not only was it possible to distinguish between cortical and cancellous AE resulting from microcracking typical of a surgical setting, but also despite the overlap of the data it showed how the moving average of the data could be used to warn the surgeon of the onset of cortical bone microcracking. However these findings were based on the results of one cortical bone sample and one cancellous bone sample, so more samples need to be tested to determine if these results are typical and not a once off.

Aim:

This test is designed to collect more cortical and cancellous data to verify the results from Test 1.

Materials and Methods:

Three bovine femora were taken from a local butcher (Burns butcher, Grange, Co. Sligo). All three femora are from right hind legs of 1.5 - 2.5 year old female Charolais Cross cattle. The femora were taken fresh from the butcher, cleaned of any adhering flesh and cartilage and then stored at circa -18°C. Later the femora are taken from the freezer, left for an hour to defrost and then brought to a machine room for cutting. A bandsaw was used to cut two sections from each femur; a mid diaphysis section and an epiphysis section, as in Figure 3.10. Next the mid diaphysis section was cut into three cortical segments: Anterior Lateral, Anterior Medial and Posterior, and the epiphysis section was cut into four cancellous segments: Anterior, Lateral, Medial and Posterior, as in Figure 3.11. The bandsaw was used to create all these segments. De-ionised water was used to keep the samples cool and a low cutting speed was used (24-35 rpm). The samples were further reduced to the desired dimensions using the low speed diamond saw (Isomet from Buehler). Figure 3.12 shows a cortical bone sample in three point bend test. The periosteum of the bone sample is cut flat to facilitate vertical loading in the three point bend test. Also the right end is cut flat to allow good attachment of the AE sensor. However the endosteum of the bone sample is left natural. In this test no notch is cut as the sample is quite thin and the weakest point is naturally near the centre of the sample. The cancellous sample is shown in the same Figure in a compression test. Note that the cortical shell is left intact to facilitate sensor attachment and to more closely represent the probable surgical scenario. The biggest risk with this approach is that the cortical shell would also get loaded and produce some AE that would get mixed in with the cancellous AE. Therefore extreme care was taken to make sure that only the cancellous bone was loaded. As cortical bone is much harder than cancellous bone keeping the loading points of the test away from the cortical shell should prove sufficient. The Tinius Olsen Materials Testing Machine was used to load the samples (settings are listed below). The PCI-2 card from Physical Acoustics Corporation was used to record and analyze the AE data. The software and hardware settings are also listed below.

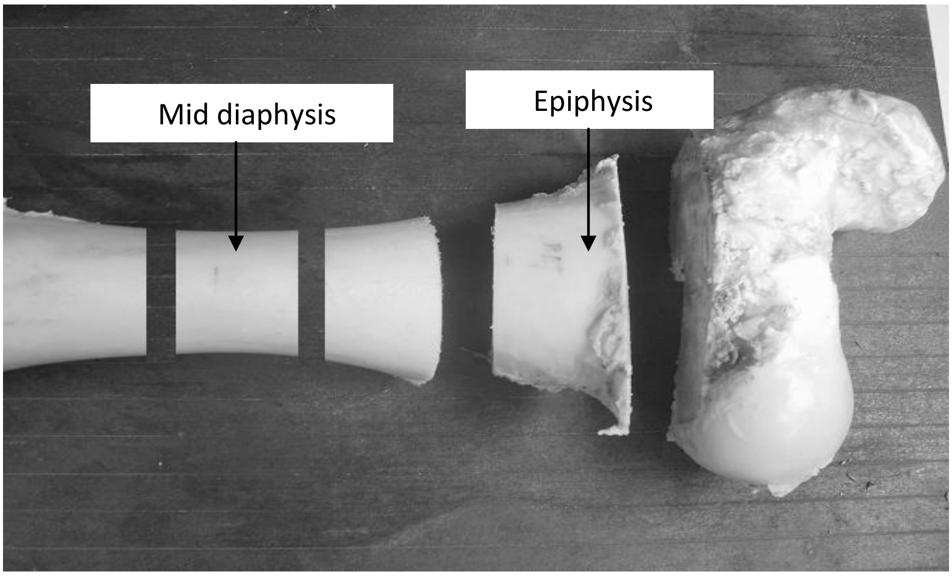

Fig. 3.10. Harvesting the epiphysis and mid diaphysis sections from a bovine femur.

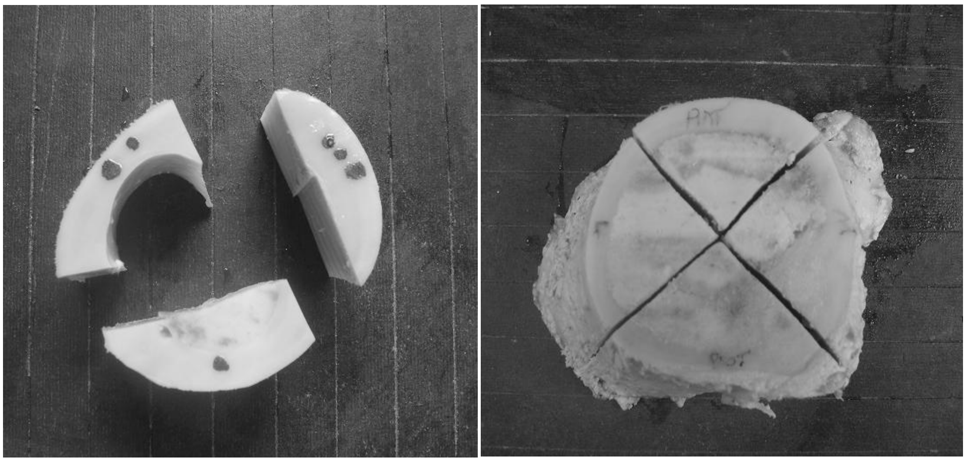

Fig. 3.11. Dividing the sections into segments: three segments for the cortical samples and four segments for the cancellous samples.

Femur	Cortical Samples (mid diaphysis)	Cancellous Samples (Epiphysis)
1	Anterior Lateral	Anterior
	Anterior Medial	Posterior
	Posterior	Medial
		Lateral
2	Anterior Lateral	Anterior
	Anterior Medial	Posterior
	Posterior	Medial
		Lateral
1	Anterior Lateral	Anterior
	Anterior Medial	Posterior
	Posterior	Medial
		Lateral

Table 3.2 Cortical and Cancellous samples from the 3 femora used in Test 2

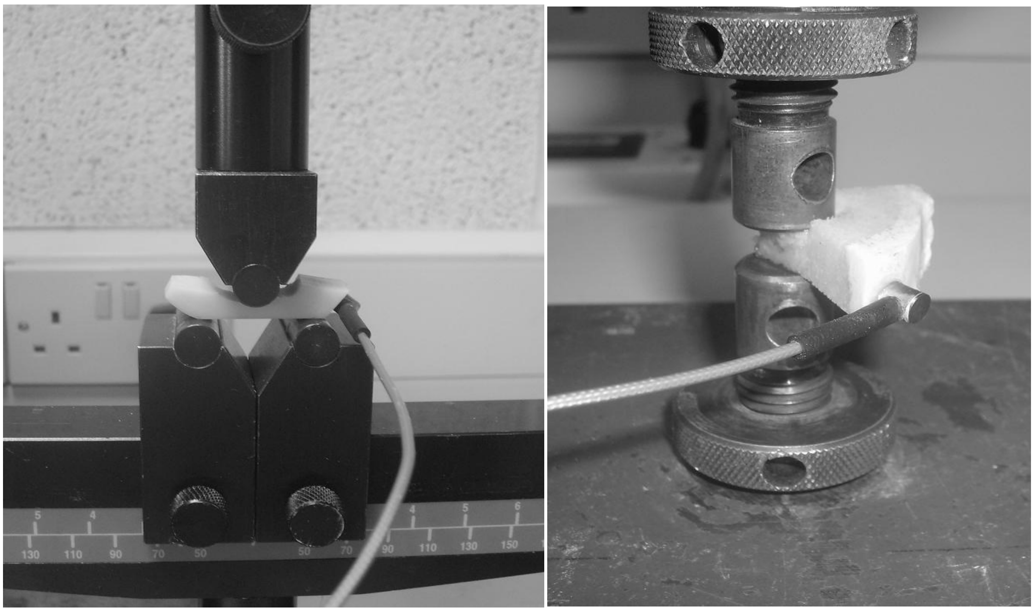

Fig. 3.12 Loading the cortical sample in three point bending and the cancellous sample in compression to generate AE data.

Cortical Mechanical and Acoustic Emission Test Settings

QMAT settings for Tinius Olsen Materials Testing Machine:

Load Range	3000 N
Displacement Range	4 mm
Speed	0.05 mm/minute
Approach Speed	0.5 mm/minute
Preload	50 N
Auto Return	OFF

AEwin Setting for PAC AE system

AE Channels	1
Threshold	30 dB
Preamplifier Gain	40 dB
Analog Filter	100 kHz – 1 MHz
Sampling Frequency	40 MHz
Pre – trigger	30
Acquisition length	8000 samples
PDT	120 µs
HDT	120 µs
HLT	150 µs
Max Duration	1 ms
Front End Filters	5 – 1000 counts
AE sensor	PICO Z s62
Peramplifier	PAC 2/4/6 (preamp 3)

Cancellous Mechanical and Acoustic Emission Test Settings

<u>QMAT settings for Tinius Olsen Materials Testing Machine:</u>

Load Range	10,000 N
Displacement Range	3 mm*
Speed	0.5 mm/minute
Height	10 mm
Extend until	3 mm*
Approach Speed	5 mm/minute
Preload	50 N
Auto Return	OFF
AE system turned on at	100 N

<u>AEwin Setting for PAC AE system</u>

AE Channels	1
Threshold	30 dB
Preamplifier Gain	40 dB
Analog Filter	100 kHz – 1 MHz
Sampling Frequency	40 MHz
Pre – trigger	30
Acquisition length	5000 samples
PDT	60 µs
HDT	80 µs
HLT	100 µs
Max Duration	1 ms
Front End Filters	5 – 1000 counts
AE sensor	PICO Z s62
Peramplifier	PAC 2/4/6 (preamp 3)

*Lateral segment = 3 mm/minute, posterior segment = 2 mm/minute, medial and anterior segment = 2.5 mm/minute

3.4 Test 2 – Results Analysis

The four frequency AE features, the Peak Amplitude and the ASL (Average Signal Level) showed most promise at distinguishing cortical AE data from cancellous AE data. However the frequency based features should be more consistent than the energy based features (peak amplitude, ASL, absolute energy etc). One difficulty with using the energy based features is that the magnitude of these features is a function of the sensor's distance from the source location. The further the sensor is from the source the less energy the signal will contain. This attenuation of the wave is primarily due to geometric attenuation (Egle 1987): AE waves travel outward in all direction from the source, so even in a material where no energy is lost, while the energy in the wave front remains the same it is spread over a larger and larger spherical area. If two microcracks at different distances from one AE sensor produce the same amplitude and energy in terms of AE waves, the AE waves that have travelled further will appear smaller at the sensor. So unless the distance from the source is known for each AE hit the amplitude and energy of different AE hits could vary considerably. In larger samples including whole bone this variation will only increase. Due to this only the frequency components were analysed.

Femur 1

		Average Freq (kHz)	Reverberation Freq (kHz)	Initiation Freq (kHz)	Peak Freq (kHz)
Cortical	**Anterior Lateral**	324	310	571	507
		123.5	121	252	97.5
	Anterior Medial	366	342	583	507
		115	112	228	117
	Posterior	261	219	514.5	507
		123	126	329.75	263.25

Cancellous	**Anterior**	369	327.5	696	585
		166.5	159.75	300	79
	Posterior	316	281	666	468
		116	101	429	39
	Medial	288	200	500	195
		133	116.5	166.5	234
	Lateral	389	354	571	507
		136	136.5	166	58.5

Key:	Medians
	IQRs

Table 3.3 Frequency Analysis of Femur 1.

Femur 2

Cortical		Average Freq (kHz)	Reverberation Freq (kHz)	Initiation Freq (kHz)	Peak Freq (kHz)
	Anterior	314	306	428	507
		206	208	333.5	39
	Posterior Lateral	180.5	168	302	507
		160.5	120.75	391	409.5
	Posterior Medial	358	309	583	507
		110.5	116	203	157

Cancellous	**Anterior**	326	305.5	535.5	468
		113	128.25	210.25	224.25
	Lateral	317.5	288	463.5	526.5

		144.5	165.5	72	322
	Medial	226.5	183	422	234
		89.25	76.25	191.25	312
	Posterior	152	142	307	156
		164	93	560	39

Key	
	Medians
	IQRs

Table 3.4 Frequency Analysis of Femur 2

Femur 3

Cortical		**Average Freq (kHz)**	**Reverberation Freq (kHz)**	**Initiation Freq (kHz)**	**Peak Freq (kHz)**
	Anterior				
	Posterior Lateral	231	251	283.5	507
		145.5	157.25	290	0
	Posterior Medial	367	333	625	546
		106.5	116.5	195	118
Cancellous	**Anterior**	387	360	571	507
		143.5	147.5	208	19.5
	Lateral	341	303	636	507
		203	188	500	156
	Medial	246	195	461	351
		120	103	220	351
	Posterior	336.5	283	625	468
		125.25	140	183	48.75

Key

Medians
IQRs

Table 3.5 Frequency Analysis of Femur 3. Note the Anterior Cortical sample was accidently broken before test could be conducted and therefore the relevant data is not available.

Looking at Tables 3.1, 3.2 and 3.4, the difference observed in Test 1 between the cortical and cancellous bone is not apparent. The only frequency parameter that shows any promise is the Peak Frequency. Consequently the Peak Frequency results are graphed in Figures 3.13A – C. All the cortical samples have a median peak frequency of around 500 kHz, while three cancellous samples have significantly lower peak frequencies around 200 kHz and one (Femur 3 medial) at 351 kHz. These lower frequency samples are highlighted on the tables 3.3, 3.4 and 3.5 and are easily identifiable in the graphs (Fig 13A – C). These results are somewhat surprising, as a significant difference between the cortical and cancellous bone was observed in Test 1 and it was expected a similar difference would be evident in this Test.

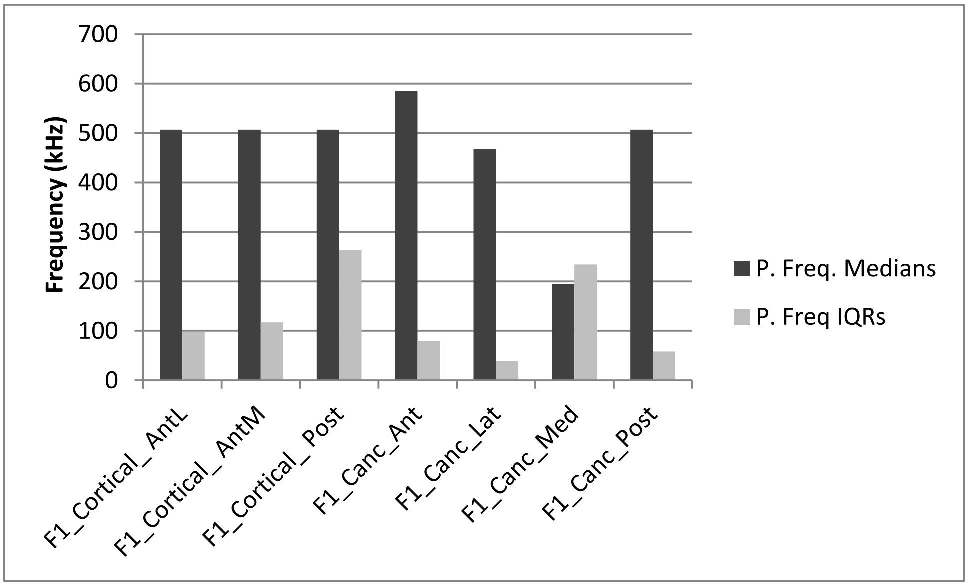

Fig. 3.13A The Peak Frequency (medians and IQRs) of Femur 1.

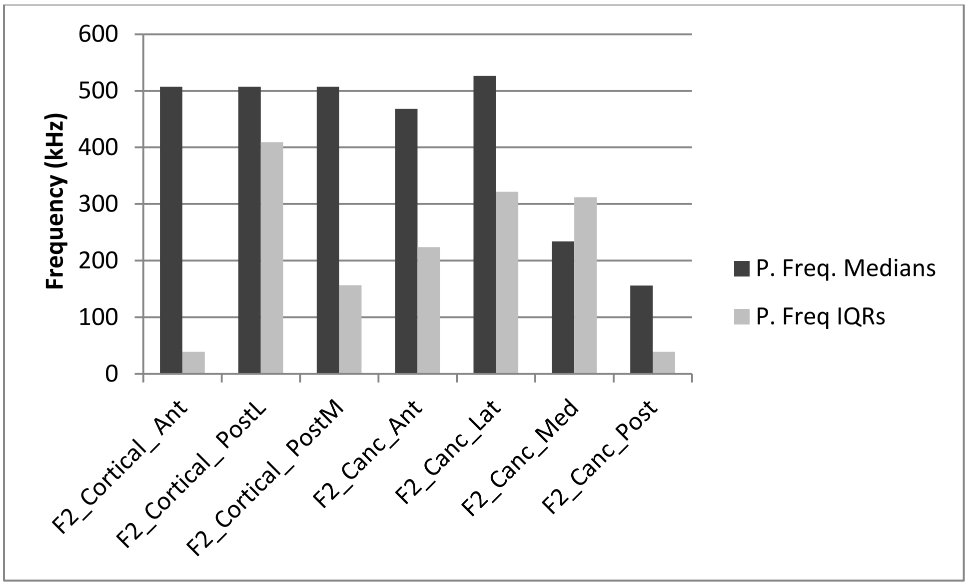

Fig. 3.13B The Peak Frequency (medians and IQRs) of Femur 2.

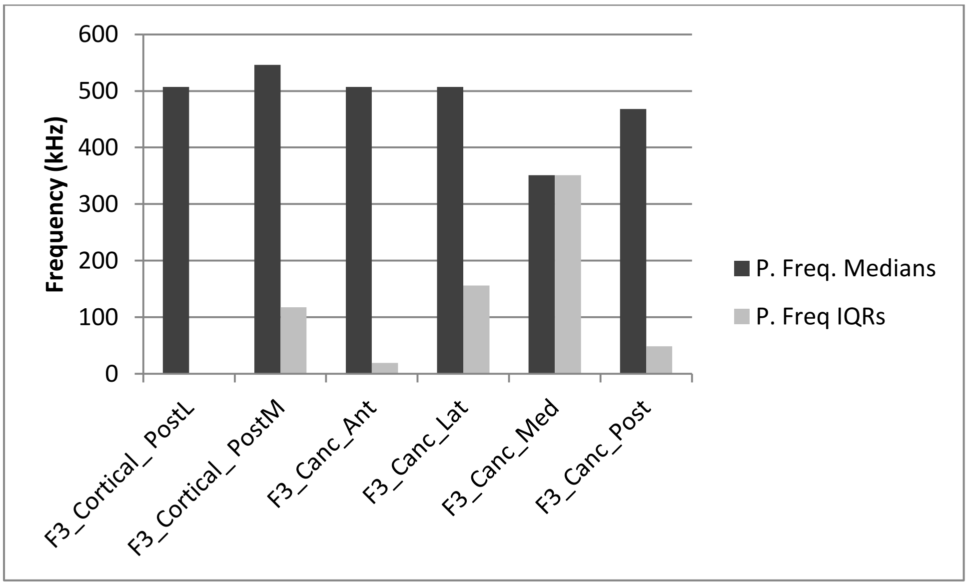

Fig. 3.13C The Peak Frequency (medians and IQRs) of Femur 3).

There are three main differences between Test 1 and Test 2.

1) Different bones are used, even though they are taken from similar animals of similar age and environmental location.

2) While the cancellous bone samples are taken from the same part of the femur (proximal epiphysis) in both Test 1 and Test 2, the cortical bone samples are taken from the mid diaphysis in Test 2 while it is taken from the proximal epiphysis in Test 1.

3) While the same type of AE sensor was used in both tests, two different sensors were used.

While different bones could have contributed to the different results, it would be desirable that AE parameters that reliably distinguish cortical bone AE from cancellous bone AE could be found which are independent of the particular animal selected. Regarding the different sources of cortical bone sample, even if this did contribute to the differing results, it is still necessary to find a parameter or paramenters that distinguish cancellous bone AE from all cortical bone AE in the femur. The sensor difference, if there is a difference between the two sensors is something that can be controlled. Since the frequency content of the AE signal is what is being analysed it would make sense that the frequency response of the two sensors are different and that this is affecting the results. Each AE sensor that was purchased came with a calibration curve (see Appendix). Figures 3.14 and 3.15 present the calibration curves for sensor 50 (used in Test 1) and sensor 62 (used in Test 2) respectively. Both frequency responses range from 100 kHz up to 850 kHz. But sensor 50 has a much flatter response. Looking at the range from 250 kHz to 850 kHz, sensor 50 has a magnitude range of just over 18dB while sensor 62 has a magnitude range of 24 dB. Furthermore sensor 60 has a much better response from 500 kHz to 800 kHz than from 200 kHz to 500 kHz. However sensor 50 has less variation between the above 500 kHz mark and the below 500 kHz mark, for example there is only 6 to 7 dB difference between 450 kHz and 700 kHz, while there is 15 dB difference between the same points on sensor 60. It is very plausible that these substantial differences between two sensors could cause or at least contribute to the differing results between Test 1 and Test 2. Since sensor 50 has a flatter response it suggests that perhaps Test 1 is closer to the truth despite only being one sample.

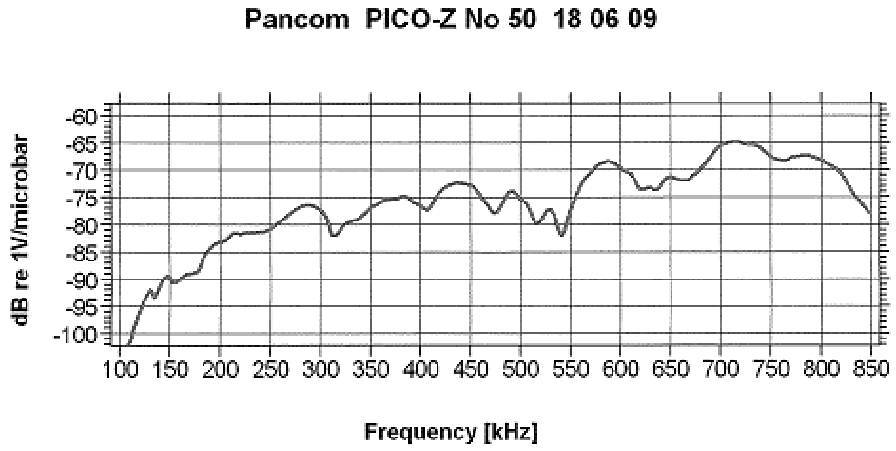

Pancom PICO-Z No 50 18 06 09

Calibration method based upon ASTM standard E976. Face to Face excitation ; 0,1Vrms at V103 (No 546007) 50 ohm loaded , preampifier AEP4 gain 34dB, offset -148dB, Filter bandwidth bypass

Fig. 3.14. The frequency response of AE sensor s50 which was used in Test 1.

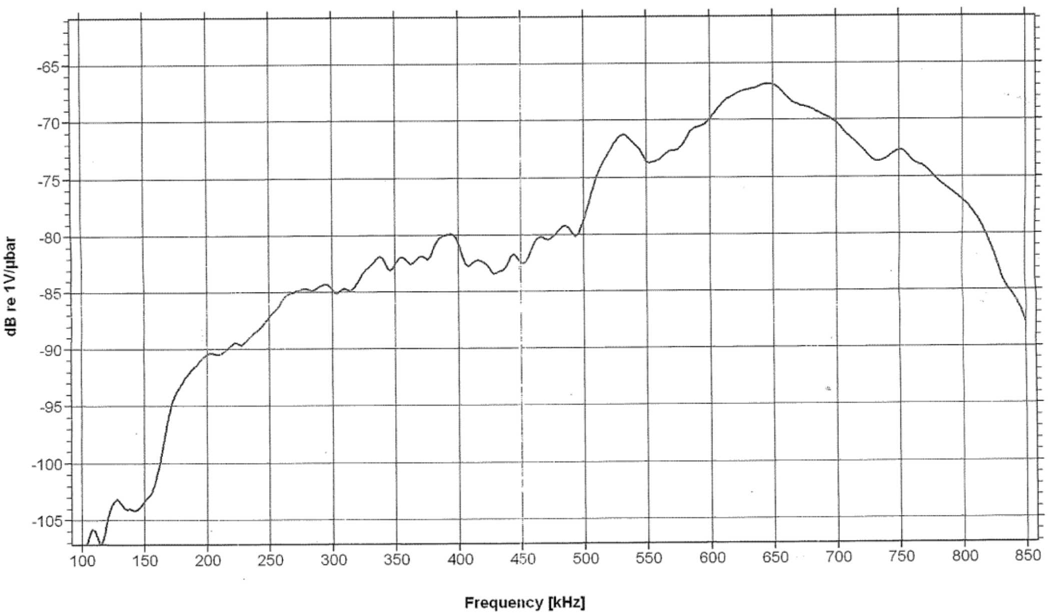

Pancom pico-Z No 62 23 04 2011

Calibration method based on ASTM standard E976. Face to face excitation: 0,1Vrms at V103 (50R), Offset -(114 + Gain)dB, coupling agent: light machine oil. For sensitivity to ANSI S1.2-1988 subtract 15dB.

Fig. 3.15. The frequency response of AE sensor s62 which was used in Test 2.

Also of note are the peak frequency results from Test 2 (Figure 3.13A through to Figure 3.13C) where most of the samples are close to 500 kHz (all cortical samples and some cancellous) coinciding with the higher magnitude response part of sensor 60’s frequency curve (Test 2). But the peak frequency results from Test 1 (Figure 3.9E) are not so concentrated at the 500 kHz band because sensor 50 (Test 1) has a flatter response and thus does not seem to alter the natural location of the peak frequency.

On discovering that the frequency response of the AE sensors may have a significant influence on the results, it becomes necessary to compensate for the sensor’s un-flat response. One reason why this PICO Z sensor was chosen was that it exhibits a relatively broadband frequency response which helps to minimise the sensors effect on the frequency of the AE waveform. However as observed there is still significant variation across its frequency curve (100 kHz to 850 kHz). The proposed solution is frequency compensation. The most convenient way to do this is in software which simply involves multiplying each value in the FFT by a compensation factor. A computer program is developed in LabVIEW (from National Instruments) which will read in text files containing the waveform data, perform a FFT on this waveform data, then multiply each value of the FFT by its appropriate compensation factor, display the result in a graph and measure the different frequency parameters that the AEwin software previously did automatically.

However the compensation factor array must first be measured and this is done using the frequency response curve in Figure 3.15 (sensor 62). In this Figure there are vertical gridlines every 50 kHz from 100 kHz to 850 kHz. So a magnitude measurement (dB) which is the average of the preceding 50 kHz is taken at every 50 kHz mark. These values are entered into a spreadsheet reproducing the curve in Figure 3.15. Next the inverse of this curve is calculated - the compensation curve. If this “compensation curve” is multiplied by the sensor curve the result is the true frequency composition of the AE hit. Both are plotted in Figure 3.16. It was discovered subsequently that increasing the magnitude of frequencies below 200 kHz had the effect of swamping the higher frequencies, so instead these were multiplied by the smallest compensation factor used in the compensation array. The AEwin software calculated four frequency parameters: Average frequency, Reverberation frequency, Initiation frequency and Peak frequency. The first three are calculated in the time domain while the Peak frequency is calculated in the frequency domain (FFT). As frequency compensation of the sensor happens in the frequency domain only the Peak frequency is measured in the LabVIEW program. It would be possible to measure the other frequency parameters with more complex methods than employed in the AEwin software. Also in the LabVIEW program a frequency parameter called Frequency Centroid is calculated. This is a weighted average of the frequency spectrum and is calculated using the following formula.

Frequency Centroid = SUM(magnitude*frequency)/SUM(magnitude).

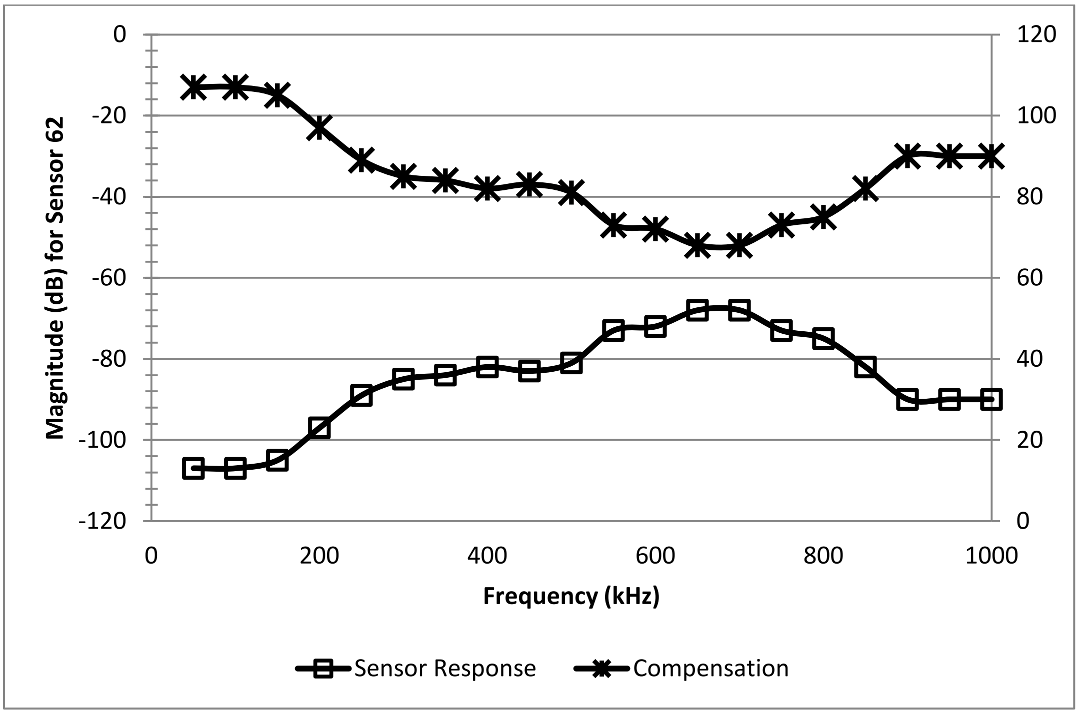

Fig. 3.16 AE sensor 62 frequency response and its compensation curve.

The results are presented in Figure 3.17 to 3.19. Femur 2 (Figure 3.18) shows the most striking results. The three cortical samples have a median peak frequency between 450 kHz and 500 kHz while the four cancellous samples have median peak frequencies between 200 kHz and 300 kHz. All the cortical bone samples and two cancellous bone samples (Medial and Posterior) have IRQs less than 100 kHz. The samples from femur 1 and 3 do not provide such good separation between cortical and cancellous samples. It can be seen though that the medians of the cortical samples are consistently between 420 kHz and 500 kHz for all three femora and the IQRs are less than 100 kHz, some substantially so. However the cancellous samples have very variable medians ranging from 200 kHz to close to 500 kHz and many of their IQRs are much larger than those of the cortical samples. An interesting observation with the cancellous samples is that all the cancellous Medial Segment samples have a median peak frequency of just over 200 kHz and an IQR of less than 100 kHz. Whether this is due to chance or if it is the nature of these Medial Segment samples that are responsible is unknown. Visual inspection of the samples did not reveal a reason for this. Referring back to Fig. 3.13A – C, showing the Peak Frequency before sensor compensation was undertaken, all the cortical samples have a peak frequency of over 500 kHz which agrees with the compensated results, however the IQR's are larger in the results without sensor compensation. The medial and posterior cancellous samples of femur 2 have a peak frequency around 200kHz but the other two do not. Again the cancellous medial sample peak frequency is consistently lower than the cortical bone samples. So in conclusion while similar patterns are evident with and without sensor compensation, the compensation does improve the separation between cortical and cancellous bone.

It can also be theorized that an improved cancellous bone test may give more consistent cancellous results. Perhaps removing the cortical shell on the cancellous samples may achieve this. This is what is attempted in Test 3.

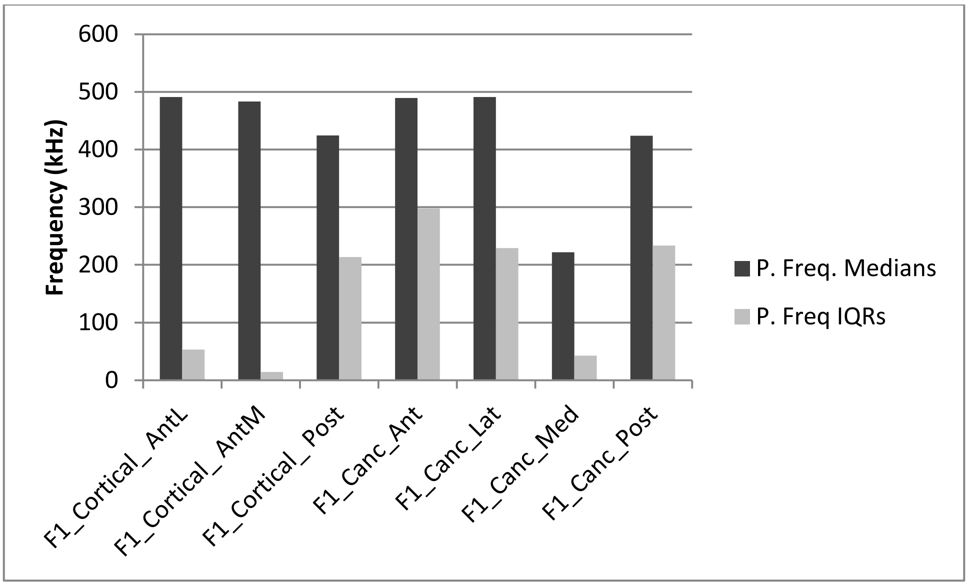

Fig. 3.17 The medians and Inter-quartile ranges of the peak frequency for Femur 1 for both cortical and cancellous bone samples.

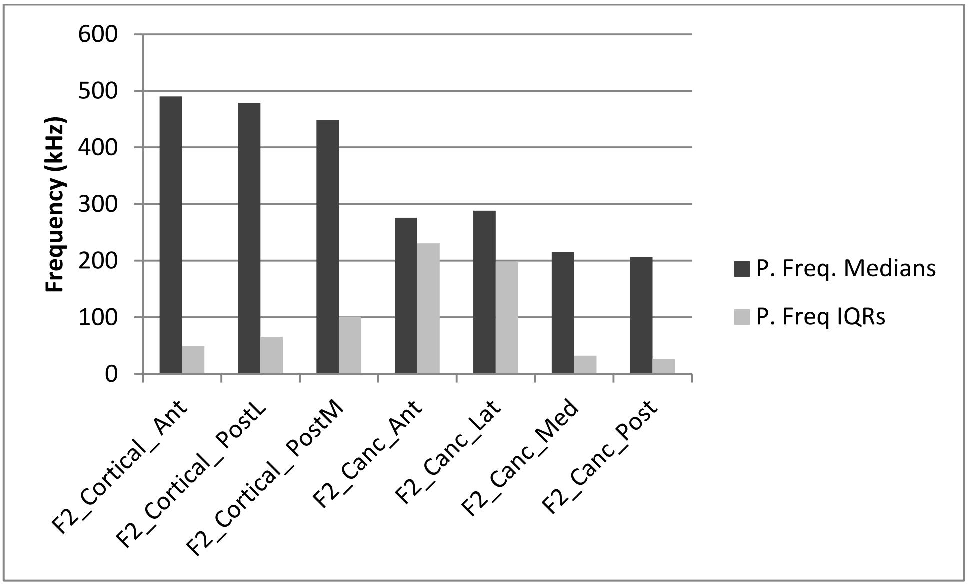

Fig. 3.18 The medians and Inter-quartile ranges of the peak frequency for Femur 2 for both cortical and cancellous bone samples.

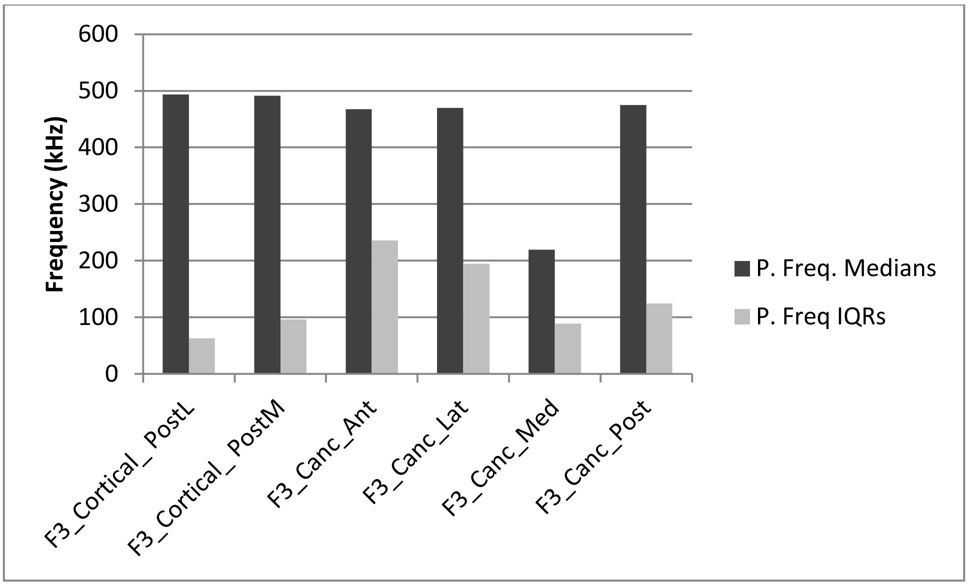

Fig. 3.19 The medians and Inter-quartile ranges of the peak frequency for Femur 3 for both cortical and cancellous bone samples.

Plotting the moving average as was done in Test 1 will show if the separation could be sufficient to indicate the onset of cortical bone micro damage in a Total Hip Arthroplasty surgery. Since only femur 2 showed a substantial difference between medians of the all cortical and cancellous bone samples, the data from this femur is shown here. The graph in Figure 3.20 shows that most of the AE peak frequency values for the cortical bone samples are within the region between 350 kHz and 520 kHz and consequently the moving averages remain between 510 kHz and 370 kHz. While cancellous peak frequency data in Figure 3.21 resides mostly within the range of 200 kHz and 300 kHz, quite a few data values exist on or near the 500 kHz mark. The moving averages however are all below 400 kHz.

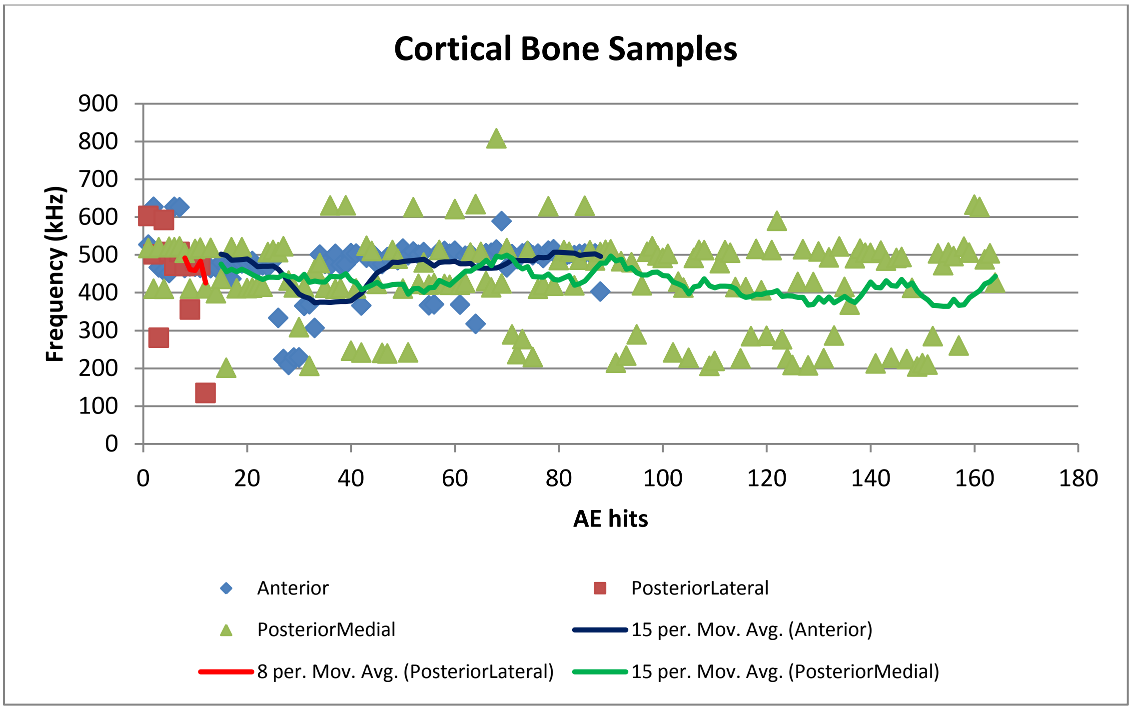

Fig. 3.20 The peak frequencies of the three cortical bone samples from Femur 2. The 15 period moving average of each of these peak frequencies is also plotted. All the moving averages stay above 370 kHz at all times.

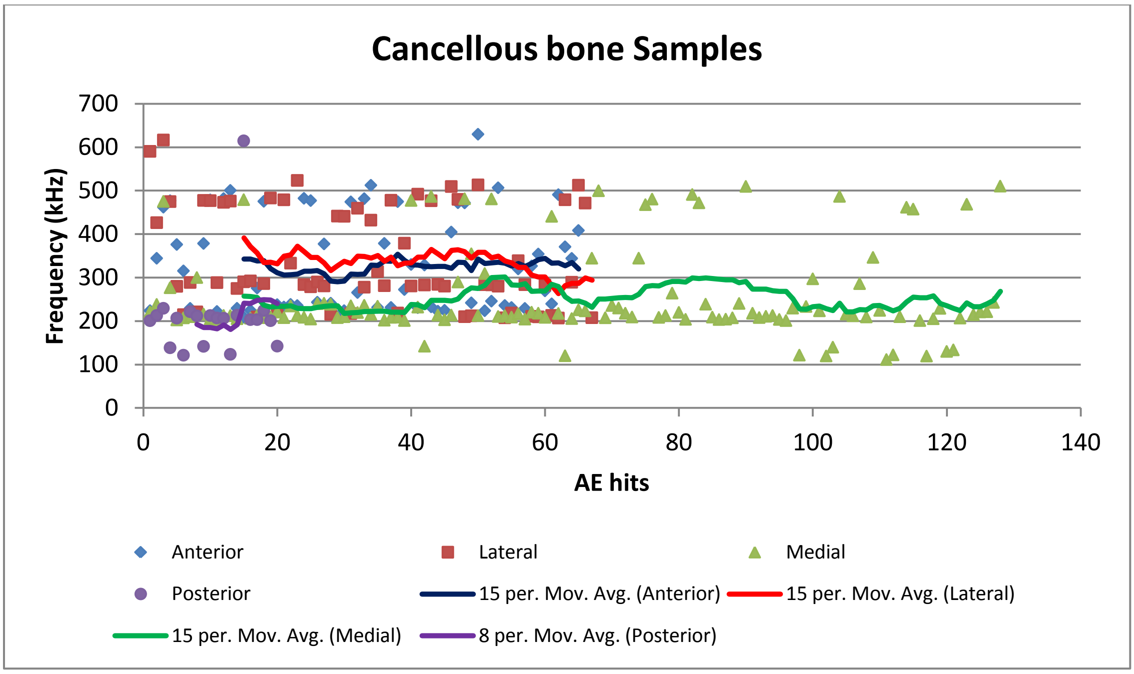

Fig. 3.21 The peak frequencies of the four cancellous bone samples from Femur 2. The 15 period moving average of each of these peak frequencies is also plotted. All the moving averages stay below 370 kHz at all times.

The question needs to be asked whether the higher peak frequency values (those around 500 kHz) in the cancellous results (Fig. 3.21) are really cancellous. Perhaps these values have some cortical origin since they match so well the cortical data. Suppose the cortical shell was stressed somewhat during the loading of the samples and these particular hits are cortical. Alternatively these may be from denser parts of the cancellous bone samples which may be more similar to cortical bone.

Test 1 gave different values for cortical and cancellous bone sample peak frequencies. The cortical bone had peak frequency values between 300 kHz and 400 kHz while the cancellous bone had peak frequency values between 400 kHz and 500 kHz. But the opposite to this was found to be the case in Test 2 with the cortical bone exhibiting a higher peak frequency than the cancellous bone. The AE sensor in Test 1 was not compensated for however, and this may explain the disparity. Carrying out compensation of the AE sensor might confirm this theory. So the process of frequency compensation is now carried out on the data from Test 1. Figure 3.22 shows the sensor’s natural frequency response and the compensation curve which is multiplied by the FFT of each of the detected AE hits in Test 1. Figures 3.23 and 3.24 show the compensated peak frequency for the cortical and cancellous bone samples respectively. However despite the frequency compensation the peak frequencies for the cortical and cancellous bone samples remain consistent with the uncompensated data. Whatever the reason is for the difference between Test 1 and Test 2, the frequency response does not seem to be it.

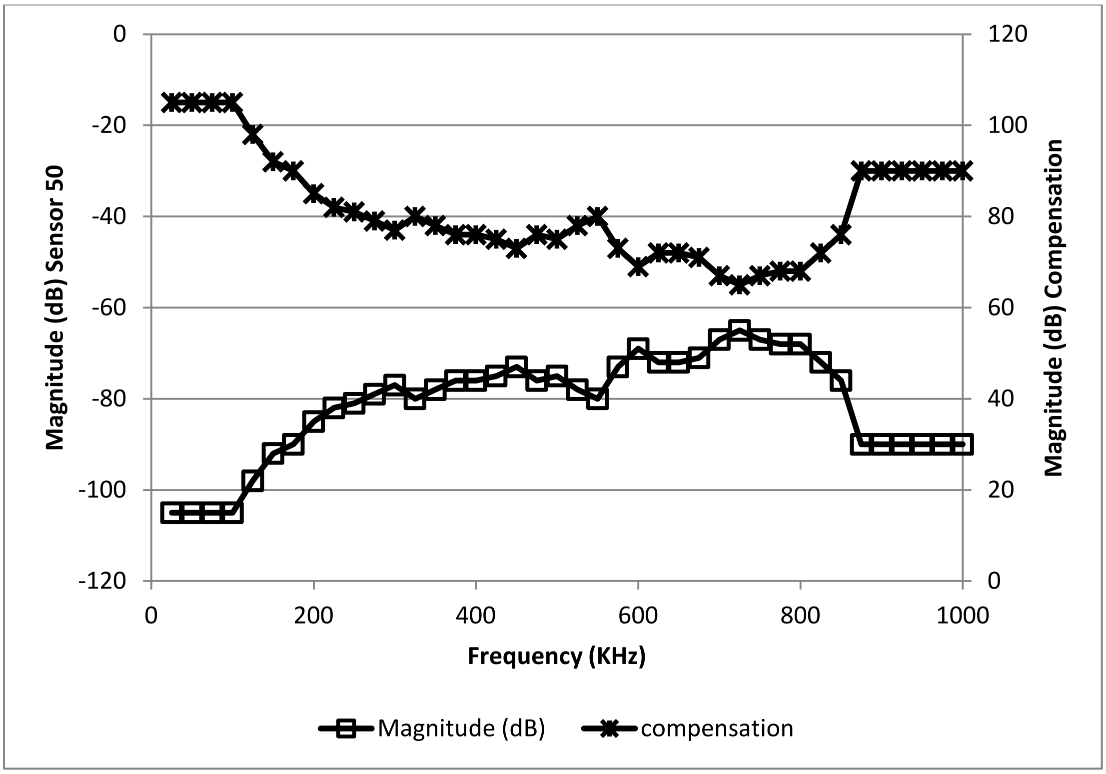

Fig. 3.22 Frequency Compensation for Sensor 50 (used in Test 1).

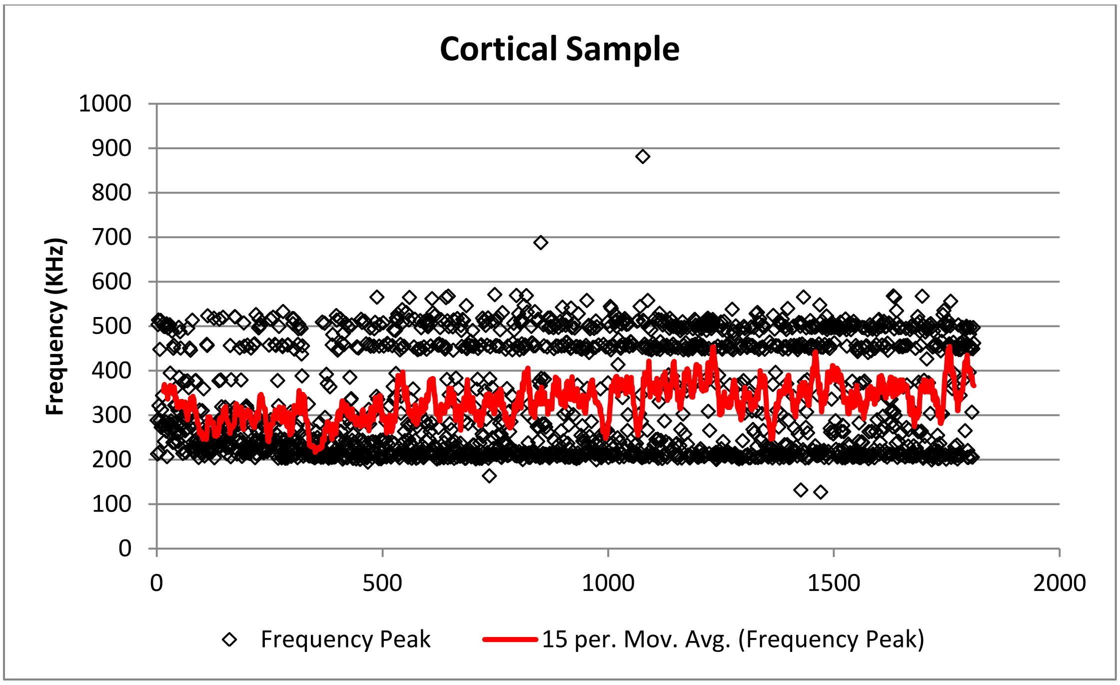

Fig. 3.23 The compensated Peak Frequency for cortical sample from Test 1 with moving average.

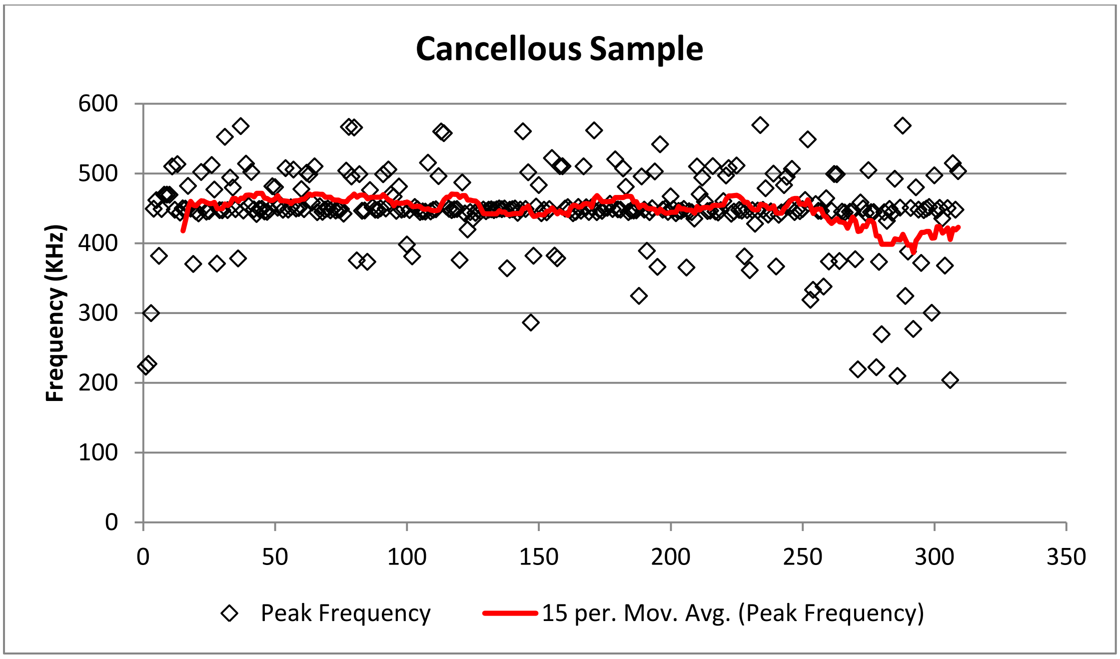

Fig. 3.24 The compensated Peak Frequency for cancellous sample from Test 1 with moving average.

3.5 Test 3 – Distinguishing Cortical Bone from Cancellous Bone

Aim: To test the acoustic emission characteristics of cortical and cancellous bone to determine which acoustic characteristics can be used to distinguish them.

Materials and Methods:

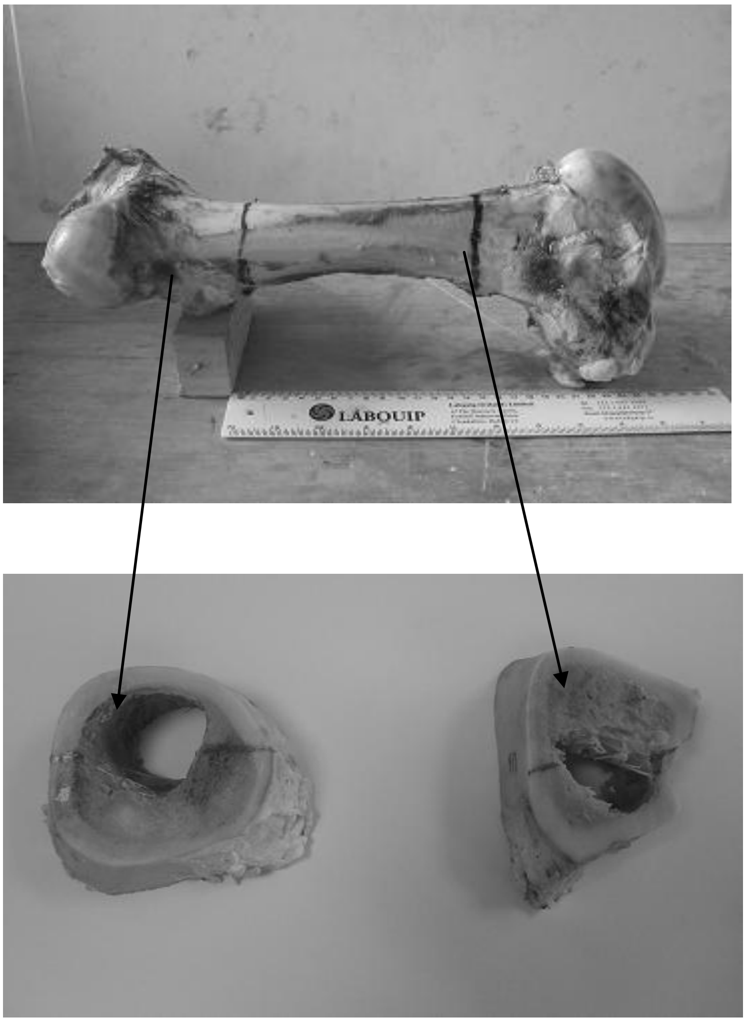

Fig . 3.25 Preparing cortical and cancellous samples for Test 3.

1. Three femora were taken from a local butcher (Grange, Co. Sligo) and the epiphyses were cut off using a band saw and distilled water to keep the bone

cool. The proximal cut was made immediately distal of the lesser trochanter while the distal cut was made 30 mm proximal of the proximal most point of the lateral epicondyle.

2. A cross sectional sample of bone was cut from both epiphyses. These samples are between 10 mm and 15 mm in thickness.
3. Then a pure cancellous sample was taken from both the proximal and distal epiphysis sections. A low speed diamond saw was used to cut the cancellous sample from the sections. There are six samples, two from each femur.
4. These cancellous samples are loaded longitudinally in compression and the AE data is used to characterise cancellous bone.
5. As it is difficult to decide when cancellous bone has fractured due to its porous and soft nature, the six cancellous samples were loaded until they were compressed by 3 mm. Then the Materials Testing Machine and AE recording systems were stopped. Both the load data of force versus displacement and the AE data were recorded for later analysis.

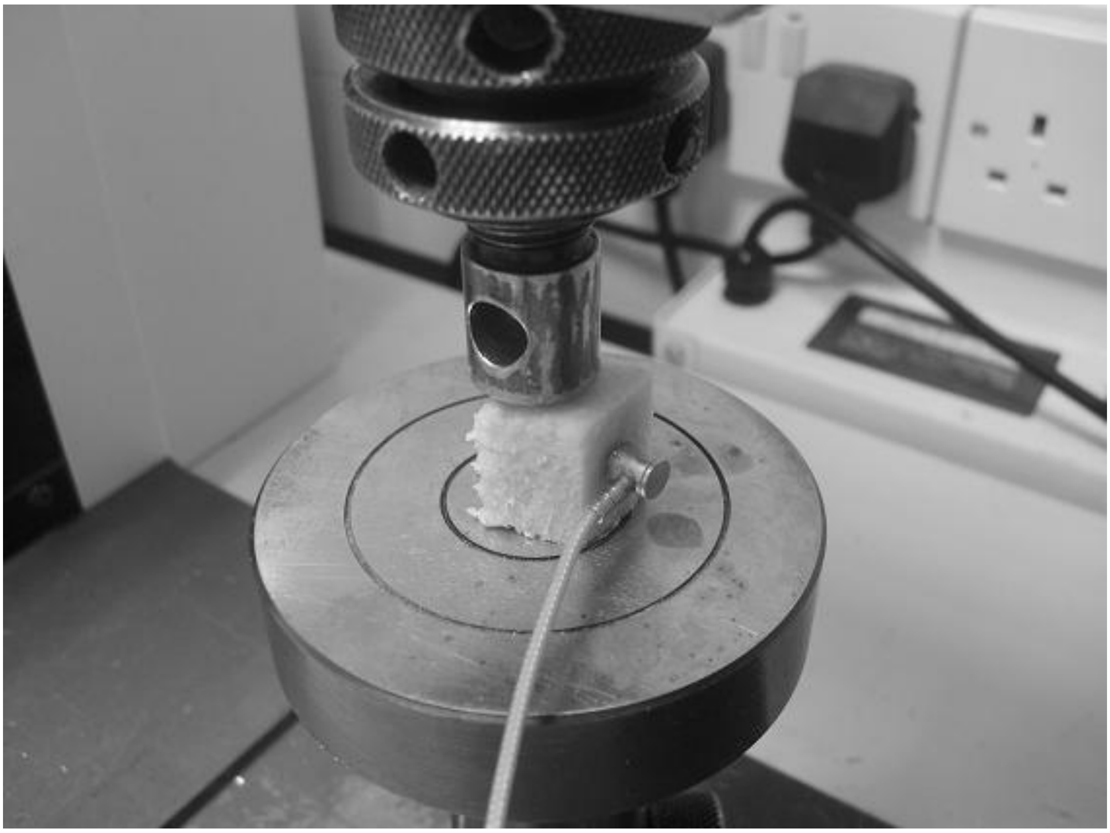

Fig. 3.26 Cancellous sample being loaded in compression and an AE sensor adhered to the sample to detect AE signals.

Experiment Setup – Cancellous Bone

Materials Testing Machine – *Tinius Olsen*

Load Range	5,000 N
Displacement Range	5 mm*
Speed	0.5 mm/minute
Extend until	5 mm*
Approach Speed	5 mm/minute
Preload	50N
Auto Return	OFF
AE system turned on at	50 N

AEwin Settings for PAC AE System

AE Channels	1
Threshold	30 dB
Preamplifier Gain	40 dB
Analog Filter	100 kHz – 1 MHz

Sampling Frequency	40 MHz
Pre – trigger	30
Acquisition length	8000 samples
PDT	120 µs
HDT	120 µs
HLT	150 µs
Max Duration	1 ms
Front End Filters	5 – 1000 counts

AE sensor	PICO Z s50
Peramplifier	PAC 2/4/6 (preamp 1)

*Even though the displacement range was set to 5mm, when the cross head had moved over 3mm the test was stopped.

Experiment Setup – Cortical Bone:

Cortical Bone Experiment

1. After the cancellous sections have been removed from the mid diaphysis a 10 mm thick ring of cortical bone is harvested with the band saw such as the sample displayed in Figure 3.27. However there is some cancellous bone in this sample and it must be removed to ensure all sample AE hits are cortical in origin.
2. Normally the low speed diamond saw would be used to cut a sample, but due to the cancellous bone residing within the cortical ring this is impossible, so instead a Deep Frame Tile Saw from Vitrex was used. This type of saw is typically used to cut curves into tiles somewhat similar to a coping saw for cutting curves in wood. Water is used to keep the bone cool during the cutting.

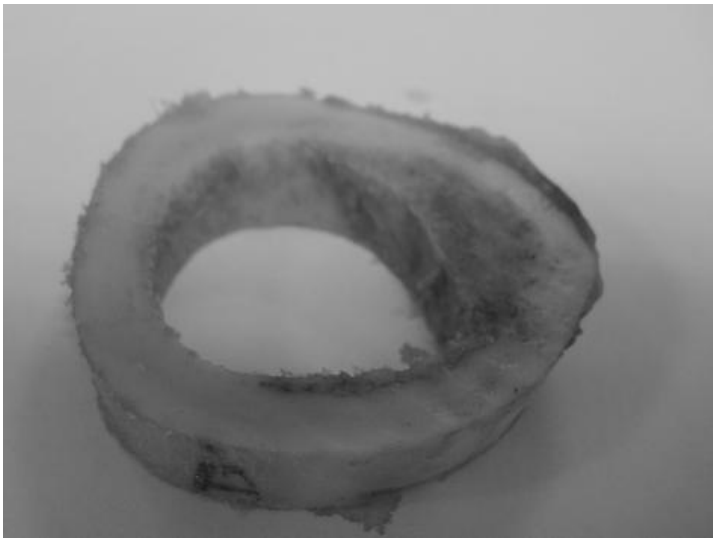

Fig. 3.27 Ring of cortical bone with some cancellous bone.

Fig. 3.28 Ring of cortical bone with the cancellous bone removed.

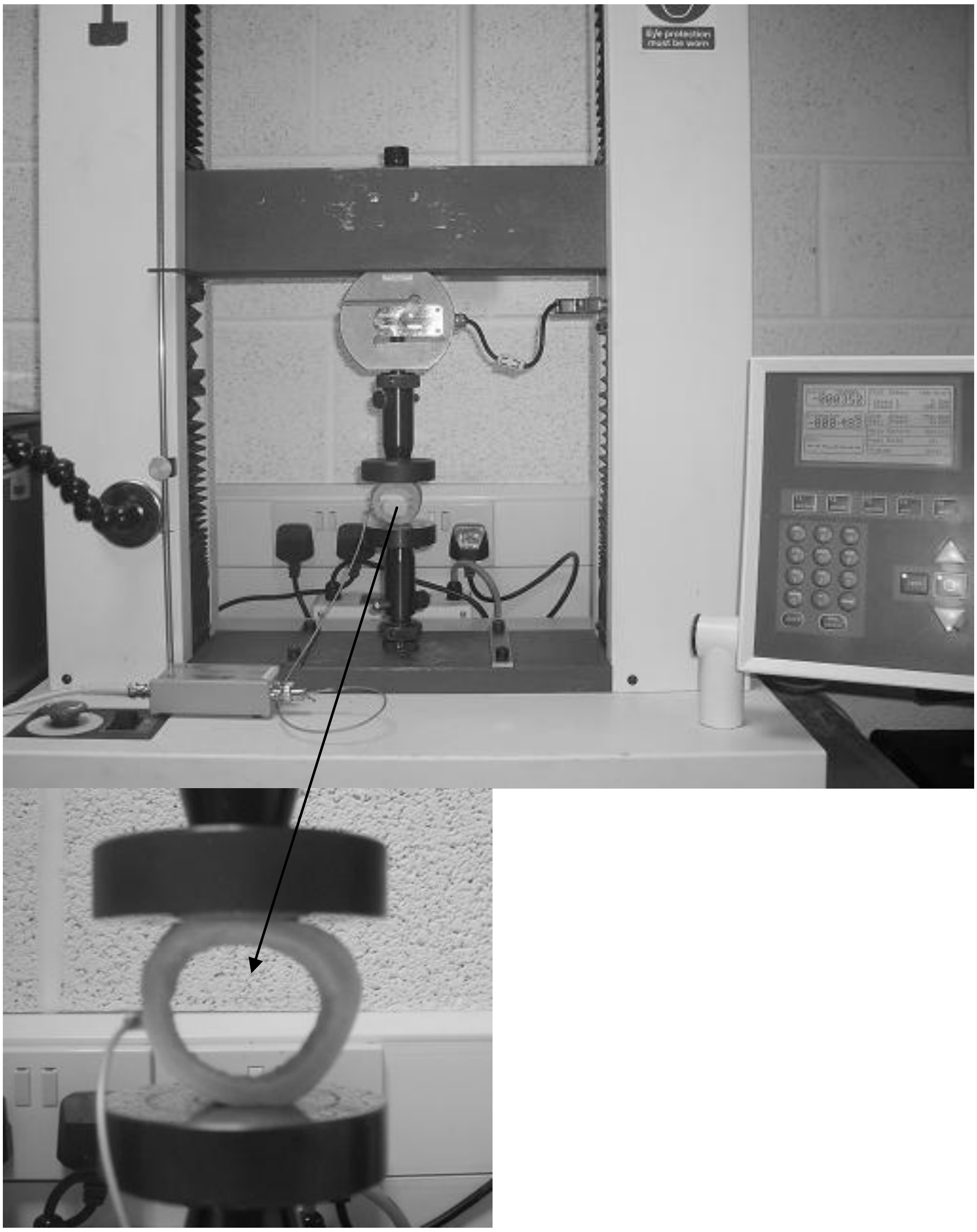

Fig. 3.29 Loading cortical ring of bone in a compression test.

<u>Materials Testing Machine – *Tinius Olsen*</u>

Load Range	5,000 N
Displacement Range	5 mm*
Speed	0.05 mm/minute
Extend until	6 mm*
Approach Speed	5 mm/minute
Preload	50 N
Auto Return	OFF
AE system turned on at	50 N

AEwin Settings for PAC AE system

AE Channels	1
Threshold	30 dB
Preamplifier Gain	40 dB
Analog Filter	100 kHz – 1 MHz
Sampling Frequency	40 MHz
Pre – trigger	30
Acquisition length	8000 samples
PDT	120 µs
HDT	120 µs
HLT	300 µs
Max Duration	1 ms
Front End Filters	5 – 1000 counts

AE sensor	PICO Z s50
Peramplifier	PAC 2/4/6 (preamp 1)

*Even though the displacement range was set to 5 mm, the bone sample broke well before this and the test was stopped when the sample broke.

3.6 Test 3 – Results

In order to analyse the data it is necessary to determine if the data is normal or not. The Shapiro-Wilk test reported the data to be not normal for cortical data - femur 2, proximal sample and Femur 3 proximal sample) at 10% significance and for the cancellous data - F1p (Femur 1, proximal sample), F1d (Femur 1, distal sample), F2p, F2d, F3p and F3d. Therefore medians and IQR need to be used instead of means and standard deviations. The following table shows the medians and the IQR's of the four frequency AE parameters which proved interesting in Tests 1 and 2. These results resemble those acquired in Test 1, in that the cortical results tend to be at a lower frequency than the cancellous results. This makes sense as the same sensor s50 was used and therefore it seems to suggest that though the sensor is the explanation of the differing frequency responses between Test 1 and Test 2, it does not show why the frequency compensation did not change this.

Cortical Frequency Results for Test 3

Femur		**A-FRQ (kHz)**	**R-FRQ (kHz)**	**I-FRQ (kHz)**	**P-FRQ (kHz)**
Femur1Prox	Median	160.5	188	198	429
	IQR	253.5	271.75	330	39
Femur1 Dist	Median	286	250	500	468
	IQR	118	115	314	78
Femur2Prox	Median	167	131	333	117
	IQR	48	32	103	39
Femur2Dist	Median	204	166	461	312
	IQR	187.5	156.5	404	312
Femur3Prox	Median	146	125	272	117
	IQR	62	61	200	39
Femur3Dist	Median	263	214	500	429
	IQR	148	120	272.25	312

Cancellous Frequency Results for Test 3

Femur		**A-FRQ (kHz)**	**R-FRQ (kHz)**	**I-FRQ (kHz)**	**P-FRQ (kHz)**
Femur1Prox	Median	333	300	666	429
	IQR	126	125	429	39
Femur1Dist	Median	316	294	600	429
	IQR	118	123.5	564	117
Femur2Prox	Median	333	307	600	429
	IQR	127.5	135	500	78
Femur2Dist	Median	333	294	600	468
	IQR	125	132	500	39
Femur3Prox	Median	324	291	545	429
	IQR	106.5	131	238	195
Femur3Dist	Median	353.5	313.5	633	468
	IQR	108	116.5	500	39

Table 3.6 Analysis of Cortical and Cancellous bone frequency parameters for test 3

Analysing the peak frequency first, all cancellous samples had a median of approximately 450 kHz. The cortical samples gave a more mixed set of results. Samples F2p and F3p had a median of 117 kHz while the other four samples had medians similar to the cancellous samples. The other three frequency parameters showed better, more consistent separation between cortical and cancellous samples. On visual inspection the reverberation frequency seemed to show the best separation. Next the Reverberation frequency was plotted against displacement with the load in newtons plotted with it. The six graphs are available in the Appendix. A typical cortical graph is reproduced in Figure 3.31

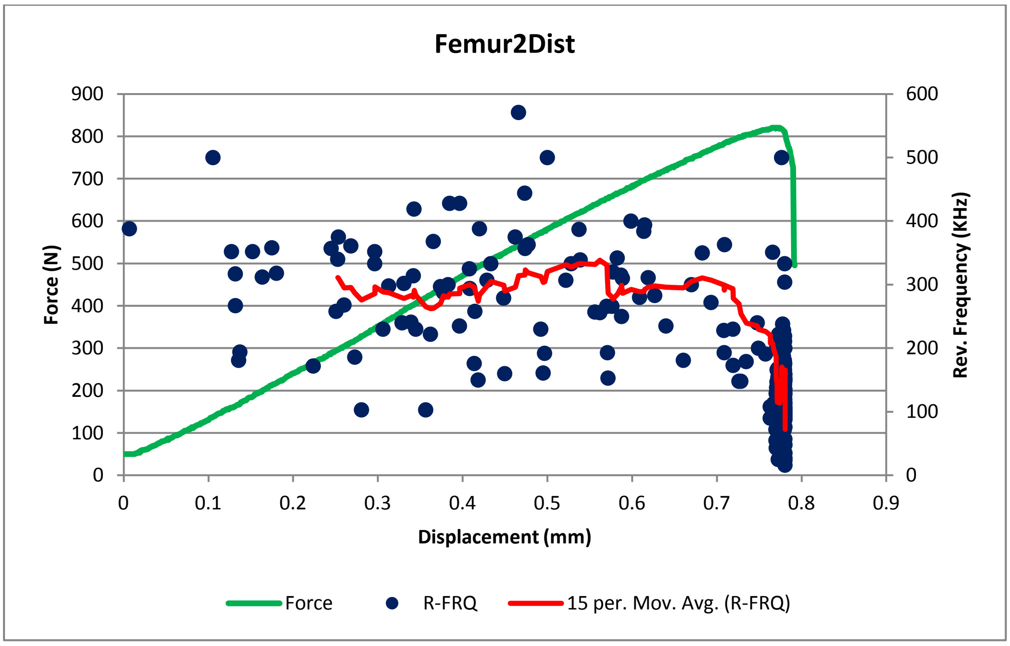

Fig. 3.30 The fracture of cortical sample Femur2Dist showing the reverberation frequency plotted with force (N) against displacement (mm).

The force gradually increases in a linear fashion until near fracture. Then it decreases at an increasing rate before a sudden drop at fracture point. Before peak force the moving average of the frequency of the AE hits are between 300 kHz and 550 kHz. But as the force starts to reduce, just before fracture, these AE hits reduce their average frequency to between 100 kHz and 200 kHz. The moving average gives a very good representation of this trend. While this result is somewhat evident in the fracture of all six cortical samples, this is the best example. The reverberation frequency of all six samples reduced to approximately 200 kHz or less just before fracture. Sample Femur2Prox reported only one AE hit before peak force. It was located between 250 kHz and 300 kHz. Sample Femur1prox reported all its AE hits at or very close to fracture point, but looking closely there is drop of frequency within this limited range of AE hits as the fracture progressed.

Each sample can tell its own story as to how it fractured. Some had no reported microcracking until just before facture, giving very little warning, while others give more advance warning with a drop in reverberation frequency before fracture. While these results point at an approach that may be useful at predicting fracture it is far from consistent and warrants more investigation.

While the cancellous samples showed a median reverberation frequency of 300 kHz, they do not show the same pattern as the cortical samples do leading up to the fracture point. The plot in Figure 3.31 is typical of the cancellous results. The moving average remains fairly consistently around 300 kHz. The other 5 samples gave very similar results. There is no evidence of a reduction of reverberation frequency before or at fracture point in any of the samples. Since all the cancellous results are very consistent unlike in the case of Test 2, it shows that the cortical shell may have had an effect on the cancellous samples in Test 2. Test 3 also shows that it is seems to be very difficult to distinguish cancellous bone AE hits from benign cortical bone AE hits.

However facture causing cortical AE hits tend to be at a lower AE frequency in particular the reverberation frequency. The other frequency parameters when examined showed similar patterns. While in the early stages of fracture the frequency of the AE hits of the cortical samples were similar to that of the cancellous samples, the frequency parameters dropping quite steeply just before and as fracture occurred.

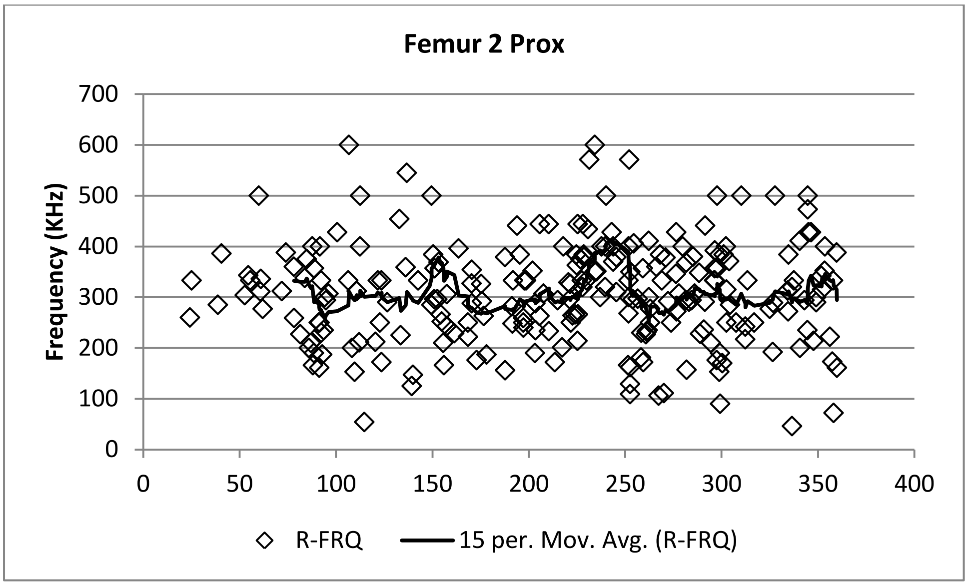

Fig. 3.31 The reverberation frequency of cancellous sample Femur2Prox with the moving average plotted against hit number.

3.7 Discussion

In summary this section started out with the aim of finding acoustic emission parameters that reliably distinguish cortical bone from cancellous bone. While Test 1 suggested it might be possible to distinguish them by looking at the moving average of a number of frequency parameters including the average frequency and the peak frequency, Test 2 refuted this suggestion showing that these changes were inconsistent and not always very clear. Test 3 used pure cancellous samples and cross sectional rings of cortical bones and elucidated a different way to predict fracture.

Observing the reverberation frequency of the individual AE hits as the cortical samples were loaded, the moving average for the most part was between 400 kHz and 600 kHz. However just before the fracture of most of the samples this moving average fell quite quickly towards 200 kHz. There is clearly some mechanical change occurring in the structure of the bone causing this reduction of frequency. While this does not explain this change, it does plot the change as it occurs. It might provide a way to predict fracture just before it occurs, or at the least signal its real time occurrence. Looking at the data that is contained in the Appendix, it is clear in samples Femur1Dist and Fermur2Dist that fracture could have been predicted by monitoring the moving average of the reverberation frequency. It is less clear in the other samples. However whole bone should produce more AE hits and probably fracture more gradually and therefore the pattern may be more evident. Even if it is not practical to predict fracture at a reasonable amount of time before the event so a surgeon could avoid the fracture entirely, it appears that the surgeon could be confident that a fracture has just taken place and he could then stop applying stress to the bone to minimise the damage. A hairline fracture is a lot less traumatic than a displacement fracture. Indeed there is some evidence that a hairline fracture in the THA procedure is beneficial as it promotes bone re-growth which helps to solidify the union between the bone and the prosthesis. The moving average of the cancellous samples was reported to be between 200 kHz and 400 kHz, interestingly this is lower than the pre fracture cortical AE hits. So it shows that perhaps the pre-fracture cortical AE hits may be distinguishable from the cancellous AE hits using the moving average method. While the fracture AE hits of the cortical samples may not be so distinguishable from AE hits of the cancellous samples on the basis of frequency, they will be on the basis of amplitude or energy. This is because cortical bone is much harder and stronger than cancellous samples.

The next logical step in this research would be to test fracture prediction with a sample consisting of both cortical and cancellous bone. One such example of a bone is the femur. So it was decided to undertake a simplified simulation of a total hip arthroplasty and see if the frequency components of AE hits predict fracture by reducing just before fracture occurs and determine what sort of warning period, if any, a surgeon could expect to have before it was too late.

4. Fracture Prediction: Simulating Total Hip Arthroplasty

4.1 Introduction

There are two parts of Total Hip Arthroplasty: The femur part where an artificial femoral head replaces the diseased natural one and the acetabular part where an artificial implant is inserted into the acetabular socket. This work relates to the femoral aspect as this is where most intra-operative fractures occur. In the preparation of the femur for an implant, the existing femoral head is removed and then a hole is reamed out of the femur. This involves the smallest broach being inserted into the medually canal (where the marrow resides). A surgical mallet is used to impact the broach until it is fully inserted. Next the broach is retracted by impacting it out using a special fixture and the mallet. Then a broach one size larger is impacted into the femur and retracted once the broach has reached its collar. This process is repeated until a broach the same size as the final prosthesis has been inserted and retracted. Since the prosthesis is the same size as the final broach, it is unlikely that the prosthesis will cause an intra-operative fracture. Normally it is the larger of the broaches that will cause the fracture. While there are a number of ways the broach can cause fracture during impaction, a common way is using a broach that is too large for the femur in question, as explained in Chapter 1. The surgeon may have a relatively large broach fully inserted and deem it to be a fairly good fit, but maybe the next size up would be a tighter fit and reduce the chances of the implant loosening post surgery. So the surgeon removes the current broach and impacts in the larger broach. However in doing so, he places too much stress on the femur and fractures occurs. While the surgeon cannot see any warning signs of fracture they do occur and if they could only be detected in time would allow the surgeon to avoid fracture. When a broach that is too large in its cross-sectional-area is forced into the femur it will stretch the femur in the radial (outward) direction causing the circumference to increase and this strain will attempt to tear the bone material apart. Thus microcracks will form and eventually coalesce into a larger crack causing a fracture. The aim is therefore to be able to detect these microcracks as they occur. Currey (2006) has shown that these microcracks occur towards the later stages of fracture and therefore detecting even a few would indicate imminent fracture. The difficulty is discerning the dangerous cortical microcrack AE from all the other sources of AE.

As was discussed in Chapter 1, there are three possible sources of acoustic emission in THA: cortical bone microcracking and fracture, cancellous bone microcracking due to it being compressed and removed, and the acoustic signature of the mallet hitting the broach. While it is reasonable to expect friction to be generated between the broach and the interior surfaces of the bone (both cortical and cancellous) as it is pushed in and that this friction will produce some acoustic emission, it is assumed that this source of AE will be small in amplitude allowing a simple threshold level to eliminate this AE. Furthermore the marrow which permeates the cancellous bone material will lubricate the interaction between broach and bone and thus minimize this friction. Due to time constraints this dissertation leaves the AE source associated with the mallet impacting the broach to further work. To push the broach into the femur without impaction, a Materials Testing Machine (Tinius Olsen) is used to gradually push the implant into the femur. While this approach does not replicate the real surgery exactly it achieves an approximation to it. Ignoring the impaction acoustics at this stage allows more in depth work on the development of a fracture prediction technique. The previous chapter shows that attempts to separate cancellous bone and cortical bone are far from easy. However loading cortical bone alone in bending and analyzing its frequency did yield a promising method to predict fracture. Whether this method will work in the presence of cancellous bone microcracking is yet to be determined. This chapter aims to determine this. The approach involves detecting the onset of cortical bone microcracking (using the frequency AE parameters) amongst the ongoing cancellous bone microcracking. A threshold level will be determined at which sufficient amount of cortical bone microcracking has occurred to give a fracture warning.

To validate this method, an independent way to determine when exactly fracture has occurred is needed. Relying on an audible bang or visual observation is not sufficient as a hair line fracture may occur without audible sound or visual clue and timing of the exact fracture time would not be possible using this approach. If pure cortical bone was being tested the force input to the Materials Testing Machine would supply the secondary sensory indicator, however with cancellous bone the force or load would not prove a very reliable indicator of when fracture occurs. This is because if cancellous bone suddenly compresses the applied load would also suddenly reduce. This is a typical indicator of fracture. However this is only due to cancellous bone compressing in steps. It may be difficult to distinguish cortical bone load reduction from the cancellous bone load reduction. For this reason a different method was chosen. Strain gauges are attached to the cortical shell of the femur at sites close to where facture is likely to occur. This sensor will only respond to strains on the cortical bone and so should give a very obvious and precise indication of when fracture occurs. It is expected that the strain should increase gradually as the broach is pushed into the femur. When fracture occurs the bone which is being stretched will suddenly be released from the stretching and as a result the strain should reduce spontaneously and dramatically.

4.2 Test 1 – Predicting Cortical Fracture

Aim:

To test the use of strain to verify time of fracture and understand how cortical bone behaves in a THA setting.

Materials and Methods:

1. The previously unused unloaded distal end of a bovine femur is used in this test. Its distal epiphysis is cut with a band saw so that a flat surface is created to allow the femur specimen to stand vertically as in Fig. 4.1.
2. A hole is drilled down the medullary canal of the femur removing much of the marrow and the central cancellous bone at the distal epiphysis.
3. Two pieces of wood are screwed together on which the femur stands as can be seen in Figure 4.1. This allows the femur to stand upright on it and the implant can be pressed through the femur and down into a hole drilled in wood below.
4. The broach which is drill drift no. 5 & 6 is inserted into the hole in the femur. It is manually pushed into the bone until it stays upright without support. Then

the compression platen of the Materials Testing Machine is brought down and it applies a small preload of 100 N.

5. Two AE sensors are glued to the femur: one on the side of the femur facing the wide side of the implant and the other facing the narrow side of the implant.
6. Two strain gauges are also mounted on the femur at the same horizontal location as the AE sensors but vertically higher, that is closer to the cut edge of the femur.
7. Load rate was started at 0.50 mm/minute. This arbitary rate was chosen to get an understanding of how the strain gauges responded to the strain on the bone.
8. The AE system and strain recorder was started when load was 100 N.
9. Both the AE system and strain recorder were started at the same time by pressing a key on each keyboard at the same time. This ensured that both systems started their acquisition clocks within 1 second of each other. Since the sample rate of the strain recorder is 1 second, this synchronization accuracy is sufficient.
10. Due to inactivity from the AE system (no AE hits were being detected), the test was stopped, the load speed was increased to 1 mm/minute and the test was resumed. This change in load speed happened at an applied load of 500 N, 13 minutes after the start of the test.

AE settings:

Channels:	*1, 2*
Preamp:	*3, 4*
Sensors:	*46 (ch. 1), 50 (ch. 2)*
Threshold:	*28 dB*

Premaplifier Gain: 40 dB
Analog Filter: 100 kHz – 1 MHz
Pre-trigger: 30 us
Hit length: 8000 samples
PDT: 120 us
HDT: 120 us
HLT: 150 us
Max Duration: 1 ms
Front End Filters: 10 - 1000 counts

Strain Gauges:
2 channels: 1, 2
Sample Rate: 1 sample/second
Ch1 facing narrow edge of implant
Ch2 facing wide edge of implant

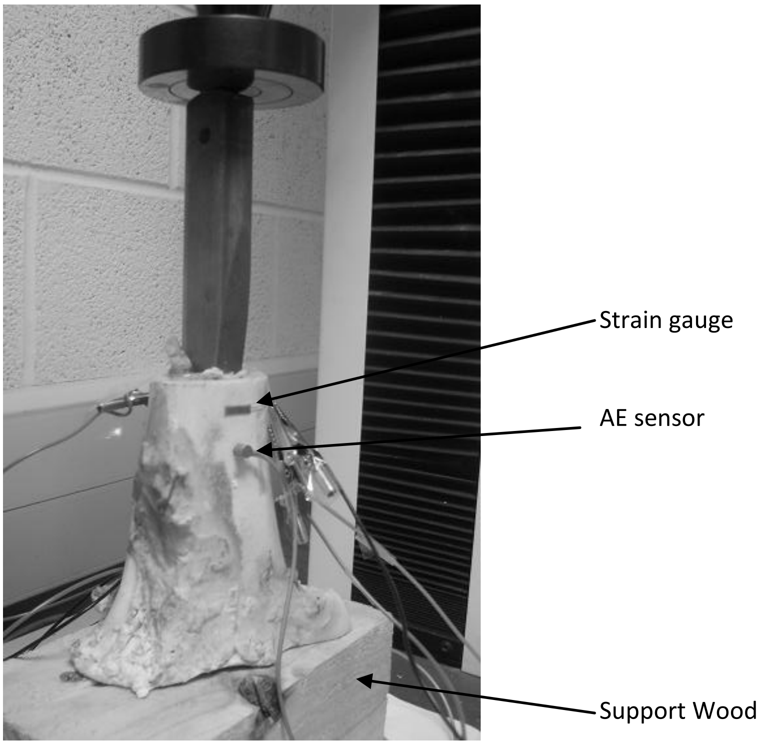

Fig. 4.1 Testing of strain gauge and Cortical THA fracture prediction. Two pieces of wood are screwed together to support the bone sample. A hole is drilled through the centre of the wood over which the bone sample is mounted. This allows the broach to project down into the hole in the wood as it is being pressed into the bone sample.

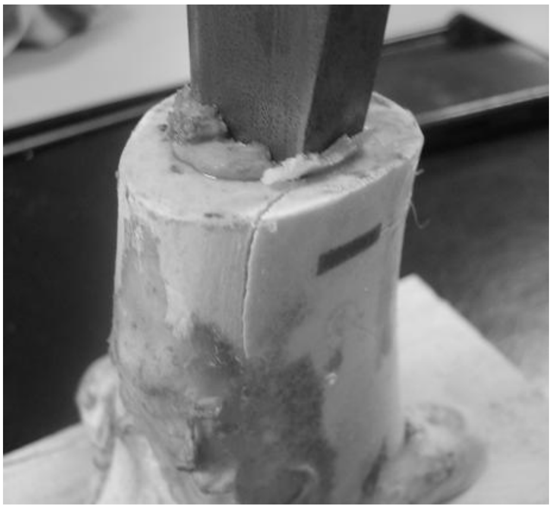

Fig. 4.2 Distal femur fracture

Results

After 1400 seconds the femur fractured with a very audible sound, Figure 4.2. The strain was observed to fall very quickly and a large number of AE hits were detected in a short space of time. The Materials Testing Machine, the strain gauge and the AE system were immediately stopped. The strain from the two gauges and the AE hits are plotted on a single graph in Figure 4.3. The peak strain of strain gauge 1 occurred at the same time as the largest AE hit at just under 8000 mV. While strain gauge 1 experienced tensile strain (inferred from the positive strain values) gauge 2 experienced compression (negative strain values). Two AE hits were detected just before 400 seconds and one just before 1000 seconds. At about 1050 seconds the main cluster of AE hits started occurring. The momentary dip in strain at 800 seconds is due to the Materials Testing Machine being stopped and restarted to facilitate load rate change. Just before fracture the strain increased more quickly. This was accompanied by higher amplitude AE hits. The strain of gauge 2 which had up to now been decreasing now levels off and increases. Just before 1400 seconds both strains fall instantly towards zero. This is a very clear indicator of fracture.

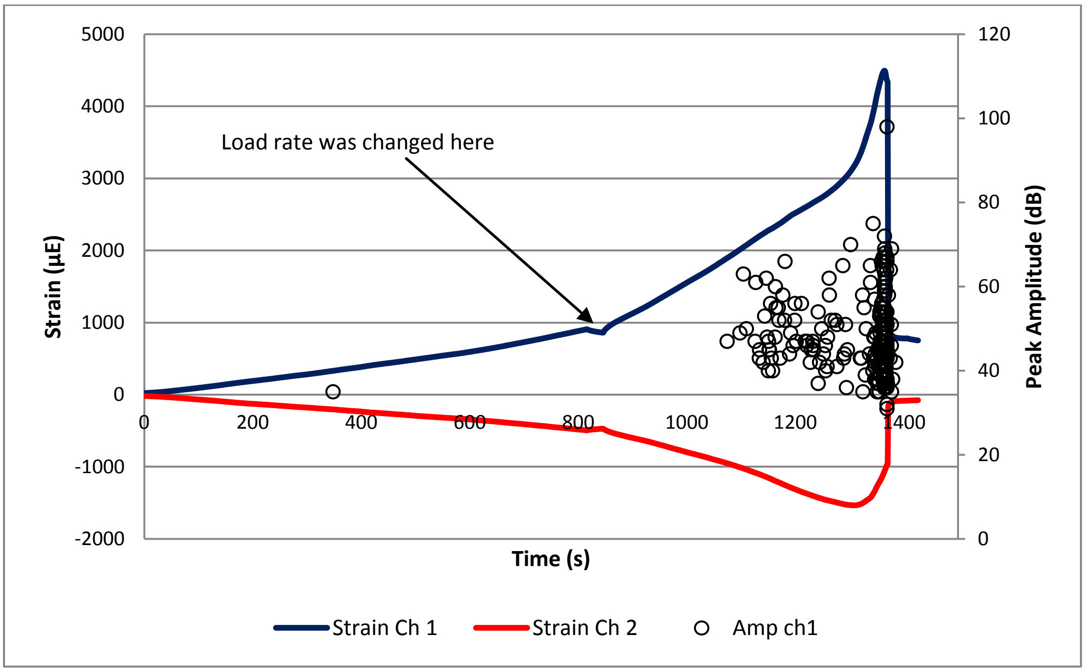

Fig. 4.3 Strain gauges are very effective at determining the exact time of fracture. Strain gauge channel 1 drops instantly at the same time as the largest detected AE hit occurs at 98dB. Strain gauge 2, while it is in compression (negative strain) also increases instantly at the time of fracture.

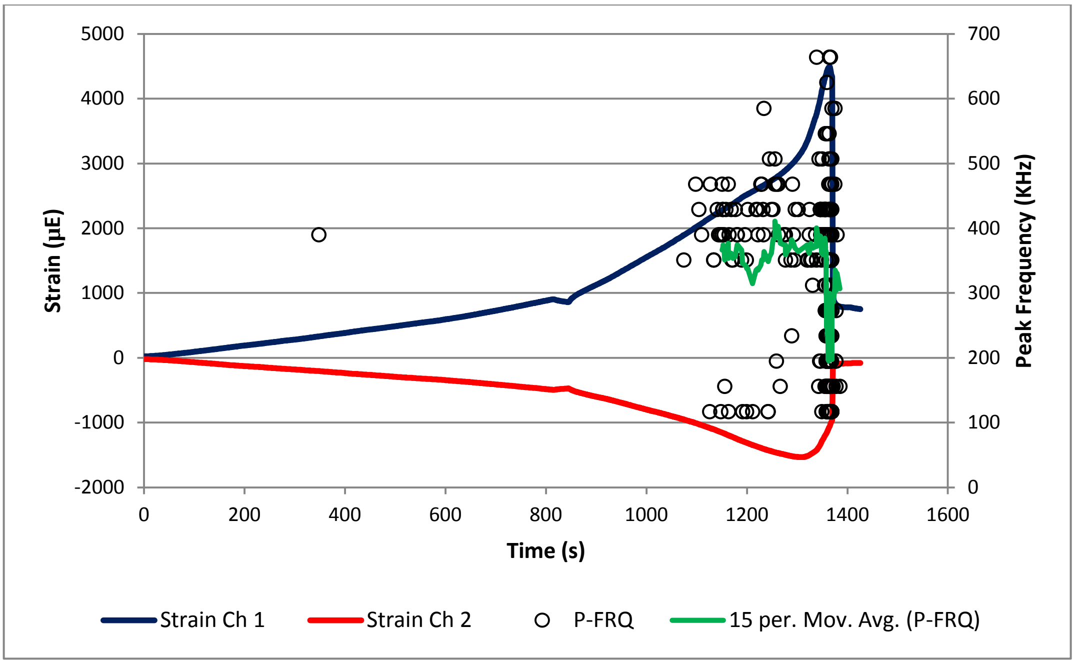

Fig. 4.4 The peak frequency of most of the AE hits start around 400 kHz but just before fracture it drops dramatically to between 200 and 300 kHz.

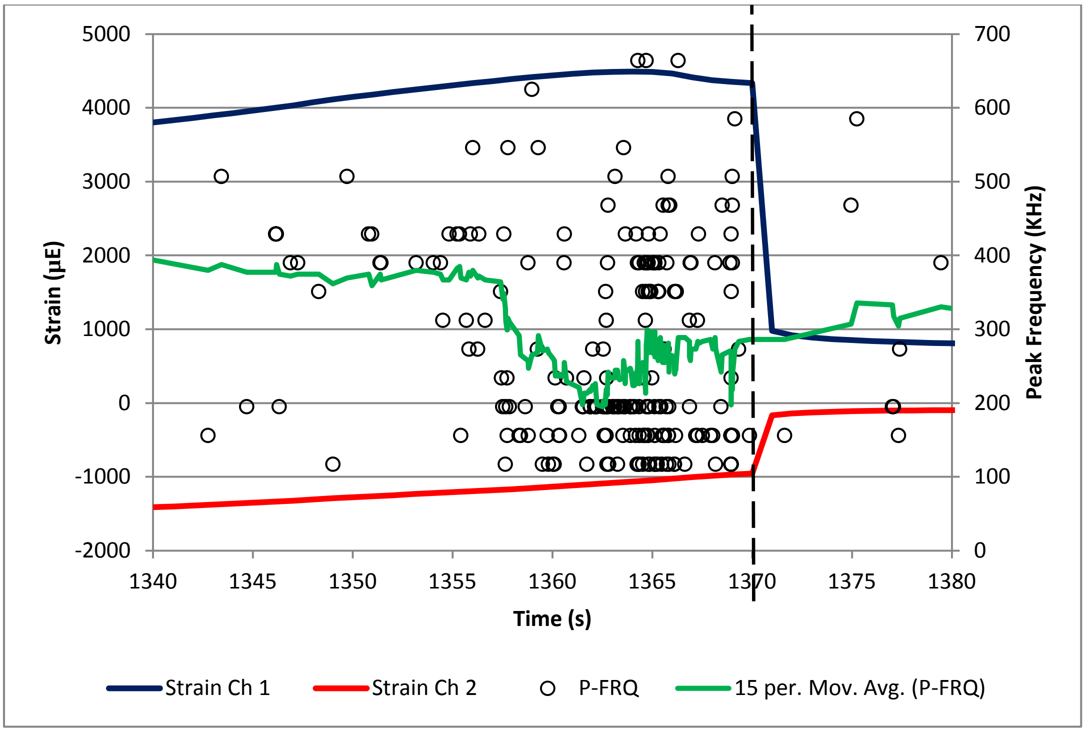

Fig. 4.5 A closer look at the peak frequency of the AE hits shows clearly that the moving average of the peak frequency drops quite spontaneously 12 seconds before fracture occurs. The dashed vertical line represents time of fracture.

Discussion:

This test showed that friction contributed almost no AE hits for most of the test. It is unknown if friction is responsible for some of the AE hits that start occurring around 1,100 seconds into the test. Importantly the test also shows that strain can give a very decisive indicator of when fracture occurs. Plotting the peak frequency of the AE from sensor 1's perspective gave a very interesting result. About 12 seconds before fracture the moving average of the peak frequency dropped from a fairly constant 400 kHz to between 250 kHz and 300 kHz. This is shown in Figure 4.4 and more clearly in Figure 4.5. This agrees very well with the results of Test 3 in Chapter 3 where cross-sectional rings of cortical bone were loaded in a radial direction in static compression. Interestingly there were 12 seconds between the onset of a frequency drop and the fracture event. This is more than enough time for a surgeon to halt impaction and evaluate the situation.

4.3 Test 2 – Predicting Fracture in Simulated THA – Femora 1 and 2

Aim:

The aim of this experiment is to test if the Peak Frequency or the Frequency Centroid of detected AE hits can be used to determine the onset of cortical bone microcracking and hence predict if and when the femur will fracture. The Materials Testing Machine (Tinius Olsen) is used to simulate the surgeon impacting the broach.

Methodology:

1. Two fresh femora are acquired from a local butcher's (Burns Butcher's, Grange, Co. Sligo) for this test and immediately frozen.
2. The day before the test they are cleaned of any adhering flesh and cartilage. Some cartilage surrounding the greater trochanter and the condyles is left attached as it will not affect the test and this cartilage is exceedingly difficult and laborious to remove. The femoral head is removed using a band-saw. A slow cutting speed is maintained and ultra pure water (de-ionised) is used to keep the femora cool during cutting.
3. Then the distal end of the distal epiphysis is removed to permit the femur to stand vertically during testing as shown in Fig. 4.7.
4. A 12 mm auger bit is used to ream the femur. This involved using a cordless drill to slowly twist the auger bit down through the centre of the medullary canal of the femur as accessed from where the femoral head has been removed. The auger bit is removed when it has reached the mid diaphysis of the femur.
5. As the drill drift (a steel wedge shaped tool) used in Test 1 is too small to ensure the femora fracture in every test a new mock broach is fabricated. This is made from 10 mm thick mild steel. Figure 4.6 presents the dimensions. This broach is intentionally oversized to ensure that fracture will occur.

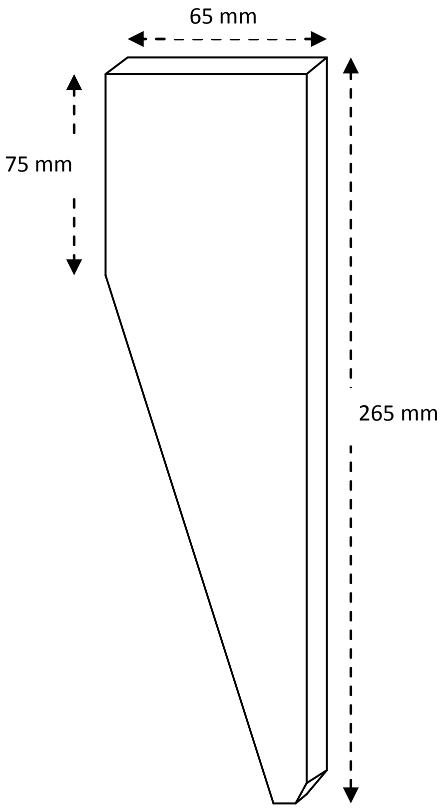

Fig. 4.6 The mock broach made from 10 mm thick mild steel with dimensions shown.

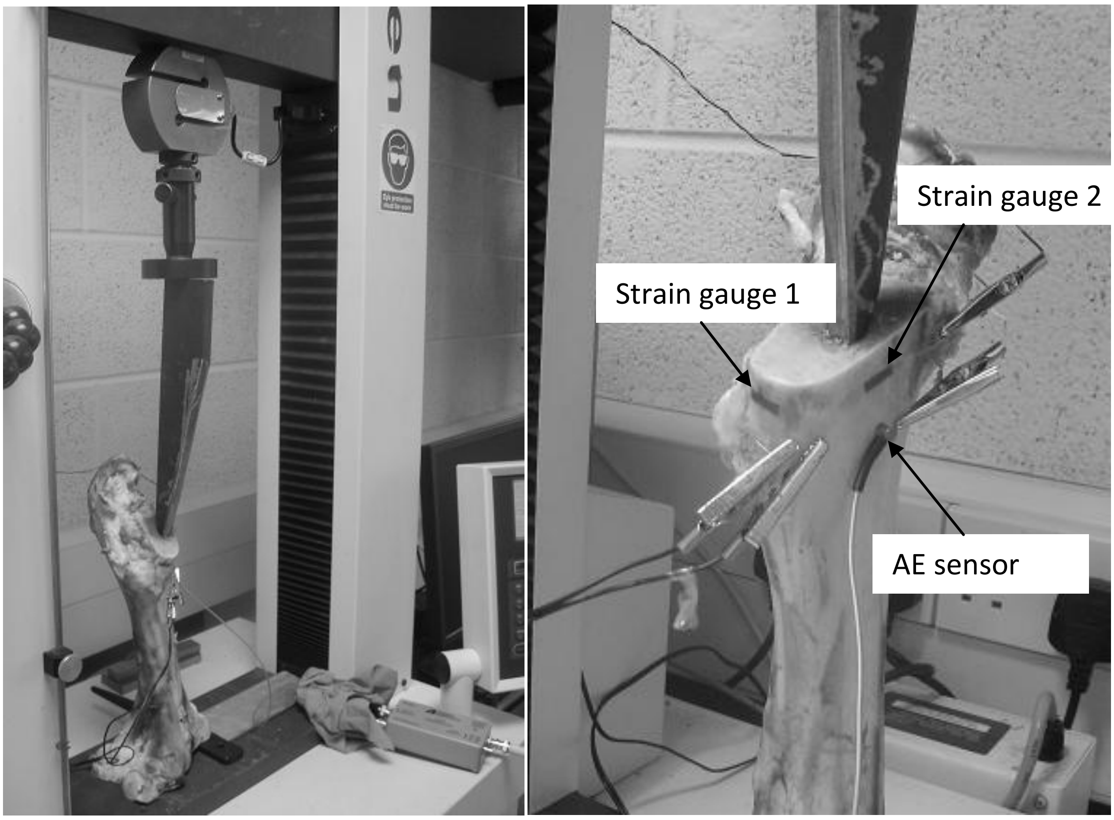

Fig. 4.7 A mock broach is used to simulate a THA intra-operative fracture. The left image shows where the distal end of the epiphysis have been sawn through perpendicular to the long axis of the bone permitting the femur to stand upright during the test. The compression platen is used to push the mock broach into the femur. The image on the right shows the placement of the AE sensor and the strain gauges.

6. The mock broach is inserted into the reamed pilot hole. The femur with broach is placed in the Materials Testing Machine as shown in Figure 4.7 and the compression platen is used to push the broach into the femur when the test is started. One AE sensor (61) and two strain gauges are mounted on the femur as shown in Figure 4.7. Super glue is used to attach the sensors. The strain gauges 1 and 2 are mounted on the medial and anterior aspects of the femur respectively.

7. The P3 Strain Indicator and Recorder from Vishay Micro-Measurements was used to record the strain from the two strain gauges. A Quarter Bridge setup was used on the strain gauge.
8. The ADLink PXI 9846 digitizer with LabVIEW program "AE Data Acquisition" was used to record the AE waveforms, as the PCI-2 AE system from Physical Acoustics Corporation was malfunctioning at this time. The AE settings are listed in Table 4.2.

AE Settings:	
No. of Samples	10,000
Sampling Rate	40 Million Samples per second
Channel	3
Preamplifier	4
AE sensor	61
Trigger	External Digital Trigger
Trigger voltage	6 mV
Post Trigger	8,500 samples
Pre Trigger	1,500 samples
Materials Testing Machine:	
Cross head speed (femur 1)	5 mm per minute
Cross head speed (femur 2)	2.5 mm per minute
Strain Recorder:	
Channels	1 and 2
Sampling Rate	1 sample per second

Table 4.1 Equipment settings for Test 2, Femora 1 and 2.

9. In order to compare the AE data and the strain data, both the AE system and the strain recorder are started at the same time to allow synchronization. This is achieved by manually clicking start button at the same time on the two computers. Since the sampling rate of the strain recorder is one sample per second and the human hand can easily press two keys simultaneously with a resolution less than 1 second, this approach was deemed sufficiently accurate.

10. The Materials Testing Machine pushed the mock broach into the femur until fracture was heard. Then the Materials Testing Machine, the strain recorder and the AE system were all stopped.
11. The two femora were tested in the same manner except that femur 2 was loaded at cross head speed of 2.5 mm/minute instead of 5 mm/minute as was used for femur 1. This was done to determine if speed of fracture would have any effect on the frequency parameters of the AE hits.

Results:

Both femora fractured successfully. Both fractures propagated parallel to the long axis of the bone and were located between the medial and the anterior aspects of the femora as in Figures 4.8 and 4.9. As in Test 1 strain was shown to indicate very clearly the time of fracture by dropping instantaneously. In contrast to the pure cortical bone in Test 1, the strain did not increase smoothly to a maximum before fracture but rather had a more jagged response. Unfortunately some of the strain data was lost during recording in Femur 1, but enough is seen to give a very good indication of the strain gauge’s behavior and importantly signals the time of fracture. Both peak frequency and frequency centroid were analyzed and while Femur 2 showed the same dramatic drop in frequency before fracture observed in Test 1, Femur 1 in this Test did not.

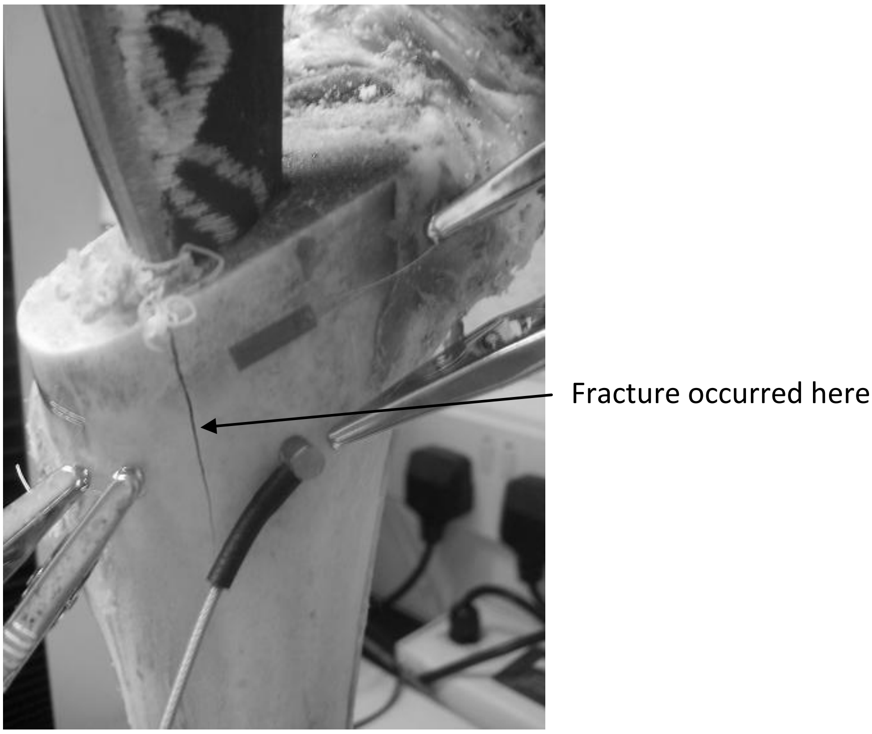

Fig. 4.8 Femur 1 fracture.

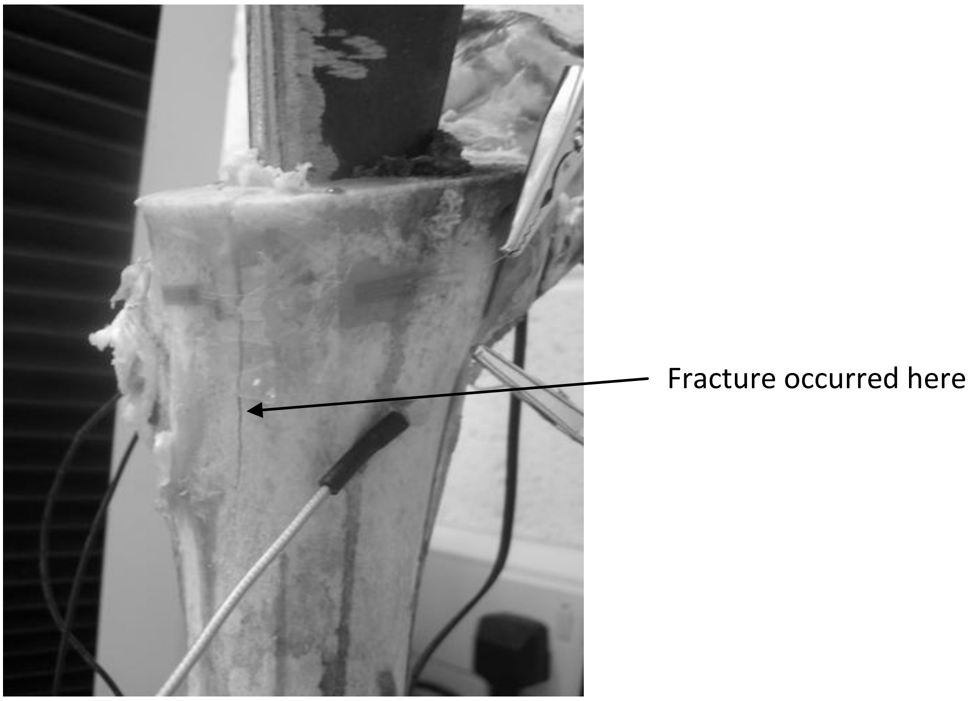

Fig. 4.9 Femur 2 Fracture.

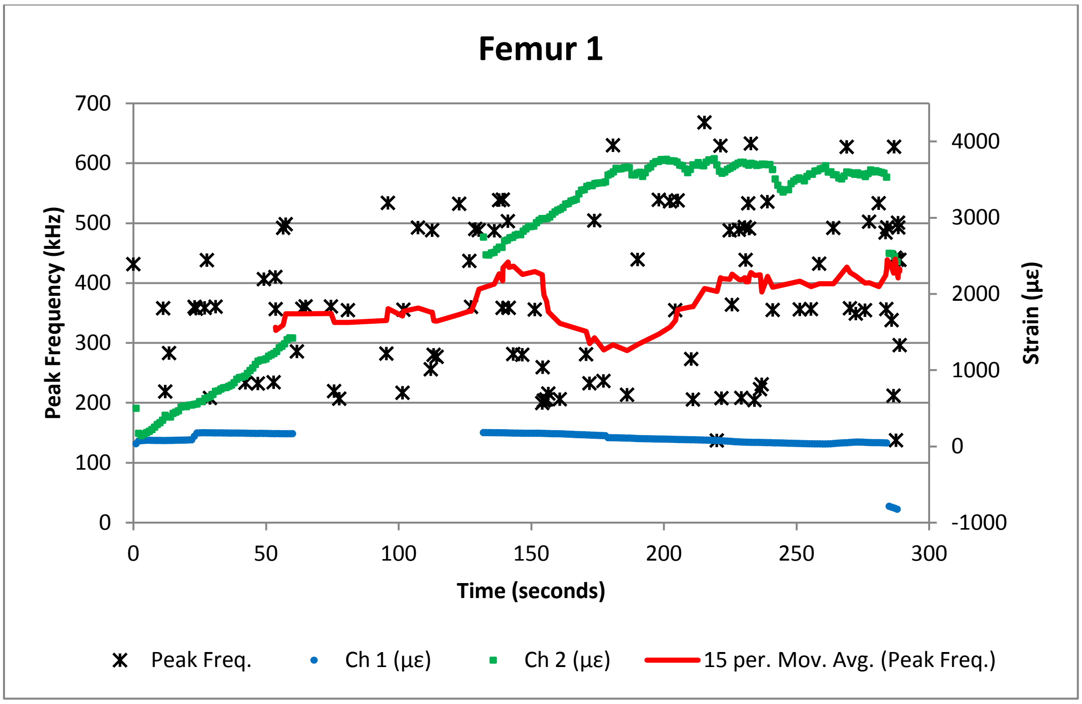

Fig. 4.10 Peak frequency of AE hits over time for Femur 1. Strain is plotted too. Strain channel 2 gives a good indication of the fracture event.

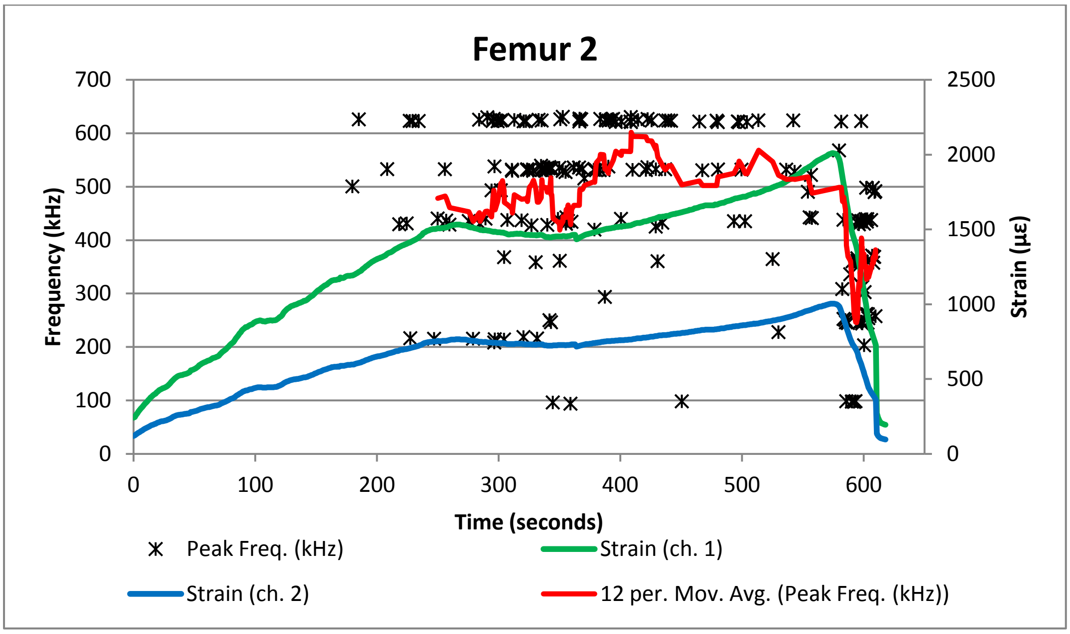

Fig. 4.11 Peak frequency of AE hits over time for Femur 2. Strain is also plotted. Both Strain channels give a good indication of the time of fracture.

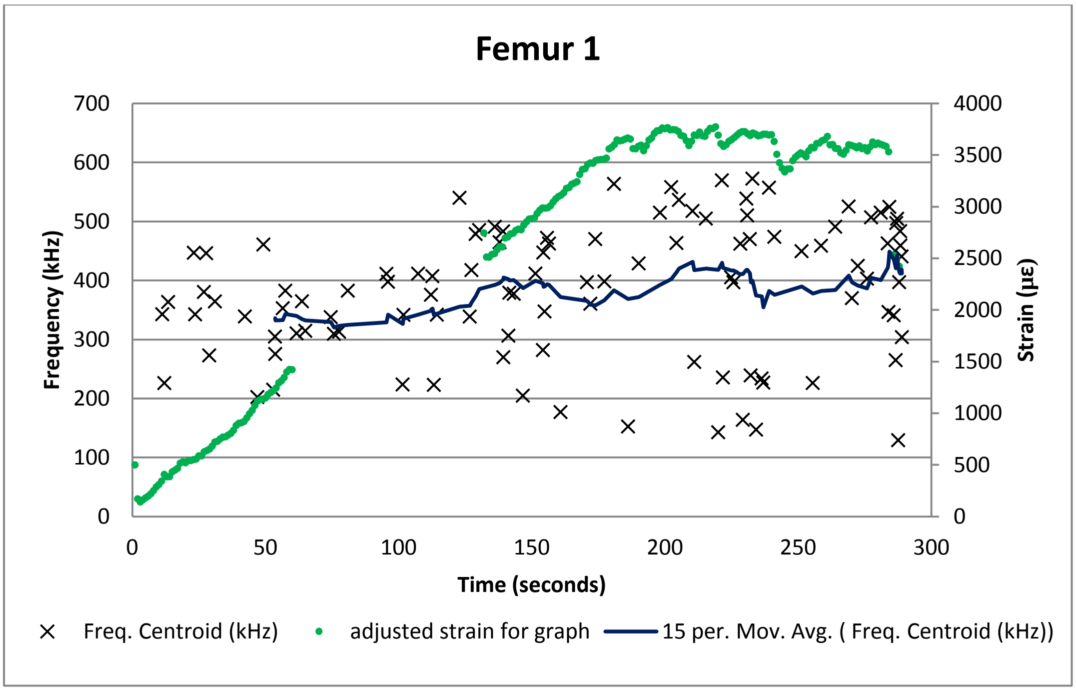

Fig. 4.12 Frequency Centroid of the AE hits over time for Femur 1.

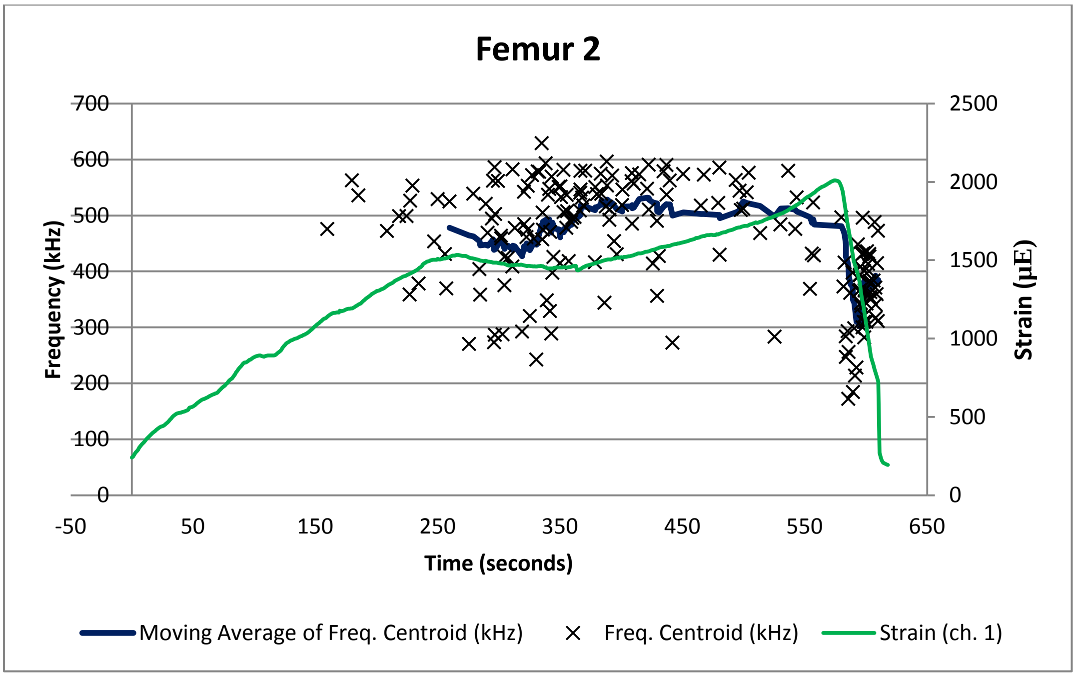

Fig. 4.13 Frequency Centroid of the AE hits over time for Femur 2.

Discussion

The results from Test 2 showed that strain gives a very clear indicator of when fracture occurs. The complete femur (that is with cancellous bone included) has a more irregular strain response but at the instant of fracture the strain changes dramatically. This is normally a decrease in strain value but as seen in Test 1 it can also be a sudden increase, depending on the location of the fracture and where the strain gauges are mounted. There was no obvious drop in the moving average in Femur 1. However Femur 2 did show the same peak frequency (moving average) drop that was observed in Test1 of this chapter and Test 3 in chapter 3. The cross head speed was not the same for all three tests. Test 1 had a relatively slow cross head speed of 0.5 mm/minute for first part of the test and then a still relatively slow 1 mm/minute for the second part of the test. In contrast Femur 1 in Test 2 had a cross head speed of 5 mm/minute and finally femur 2 of the same test had a cross head speed of 2.5 mm/minute.

It may be suggested that the faster cross head speed in Test 2 femur 1 did not allow sufficient time for the frequency to drop as was observed in the other tests. The strain response in femur 2 of Test 2 shows that the strain starts dropping at around the same time as the frequency drops. The gradual reduction in strain on two gauges located on either sides of the fracture, would suggest that final fracture is already occurring albeit gradually, when the frequency peak starts to drop. While it could be argued that if final fracture has started it is already too late to prevent fracture, this is not necessarily the case. Firstly, in phase 2 of fracture the bone material is yielding but has not yet failed. This yield would cause a drop in strain felt on the strain gauge, as the material immediately surrounding impending fracture site would stretch (yield) allowing material a little further away (where the strain gauges are mounted) to relax somewhat. Then when the final fracture event occurred the material would relax completely. This would explain the steep fall off in strain in Femur 2 before the abrupt drop at fracture point. Probably because of the faster load rate in Femur 1 the femur may have passed directly from phase 1 into phase 3 thus this drop off was not experienced. The compression of the cancellous bone would account for the AE hits prior to fracture as phase 1 in cortical bone does not typically produce much AE. Furthermore if the surgeon stops impaction when they have caused just a hairline fracture, it is far better than a displacement fracture as a hairline fracture may need no repair and some studies have shown that a non displaced fracture can actually improve bone ingrowth making for a more stable and long lasting artificial hip. More similar tests have to be conducted to determine if this frequency drop is really an indicator of impending fracture or if it is just a blip in the data.

4.4 Test 3 – Predicting Fracture in Simulated THA – Femora 3 to 8

Aim:

The aim of this experiment is to predict bone fracture during THA operation using AE feature data. This test sets out to determine if the moving average of the peak frequency of the AE hits can be used to indicate when fracture becomes imminent and has occurred. While Tests 1 and 2 showed some promising results in predicting intra-operative fracture in a Total Hip Arthroplasty setting, more samples and a better analysis of these are required to determine the value of this approach to fracture detection and prediction. Six femora are acquired and their attributes measured. The linear measurements of bone are based on a system developed for archaeological sites (Von Den Dreisch 1976).

Bone Attributes:

Linear Dimension:

Dimension	Femur 3 (mm)	Femur 4 (mm)	Femur 5 (mm)	Femur 6 (mm)	Femur 7 (mm)	Femur 8 (mm)
GL	400	405	375	390	386	374
GLC	375	385	355	358	360	345
BP	152.5	155	131	147	144	137.5
BD	120	118	105	116	115	109.5
SD	46.5	47.4	39.4	44.7	44.6	39.8

GL = Greatest Length (lateral aspect)

GLC = Greatest length from caput femoris (head) (medial aspect)

Bp = (Greatest) breath of the proximal end

Bd = (Greatest) breath of the distal end

SD = Smallest breath of diaphysis

Mass:

Measured using a science scales

Femur	Test 1 (kg)	Test 2 (kg)	Test 3 (kg)	Average (kg)
3	2.2889	2.2870	2.2860	2.2870
4	2.4339	2.4820	2.4624	2.4594
5	1.6785	1.6800	1.6843	1.6809
6	2.1481	2.1481	2.1481	2.1481
7	2.1125	2.1124	2.1125	2.1125
8	1.7039	1.7041	1.7041	1.7040

Volume:

Measured using Archimedes' principle

Femur	Test 1 (cm^3)	Test 2 (cm^3)	Test 3 (cm^3)	Average (cm^3)
3	1818	1816	1820	1818
4	1865	1868	1871	1868
5	1367	1366	1369	1367
6	1725	1728	1721	1725
7	1672	1679	1669	1673
8	1379	1383	1385	1382

Density = Mass/Volume

Femur	Test 1 (g/cm^3)	Test 2 (g/cm^3)	Test 3 (g/cm^3)	Average (g/cm^3)
3				1.258141
4				1.316613
5				1.229352
6				1.245516
7				1.26243
8				1.232722

Femur Preparation:

1. One of the six measured femurs is taken from the freezer.
2. The femur is positioned with the anterior aspect facing up and using wooden blocks it is supported so that the anterior surface is parallel to the ground. A spirit level is used to determine this. The femoral head and the greater trochanter are also ensured to be parallel to the ground. See Figure 4.12.

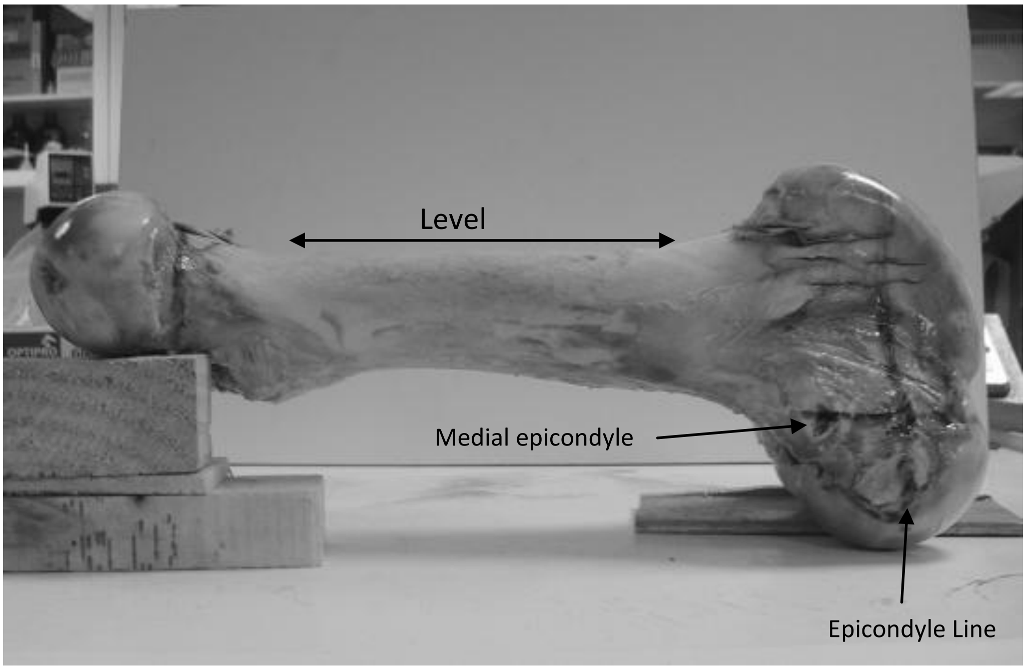

Fig. 4.14. The femur is supported so that the anterior aspect faces the ceiling of the lab. The wooden block supports were adjusted until the anterior diaphysis is level. The view here is the medial aspect.

3. **Distal Cut:** Next the distal cut lines are marked out. A line is marked from the medial epicondyle distally parallel to the ground. The mid-point on this line is marked and a perpendicular line is brought vertically up and down. This is the epicondyle line.
4. Using a square and vernier calipers a line is marked on the anterior aspect of the distal epiphysis that is perpendicular to the long axis of the femur. In doing this the Anterior Reference Line is also marked out. This line is drawn parallel to the bone long axis and divides it in half as viewed from the anterior. See Fig. 4.13.

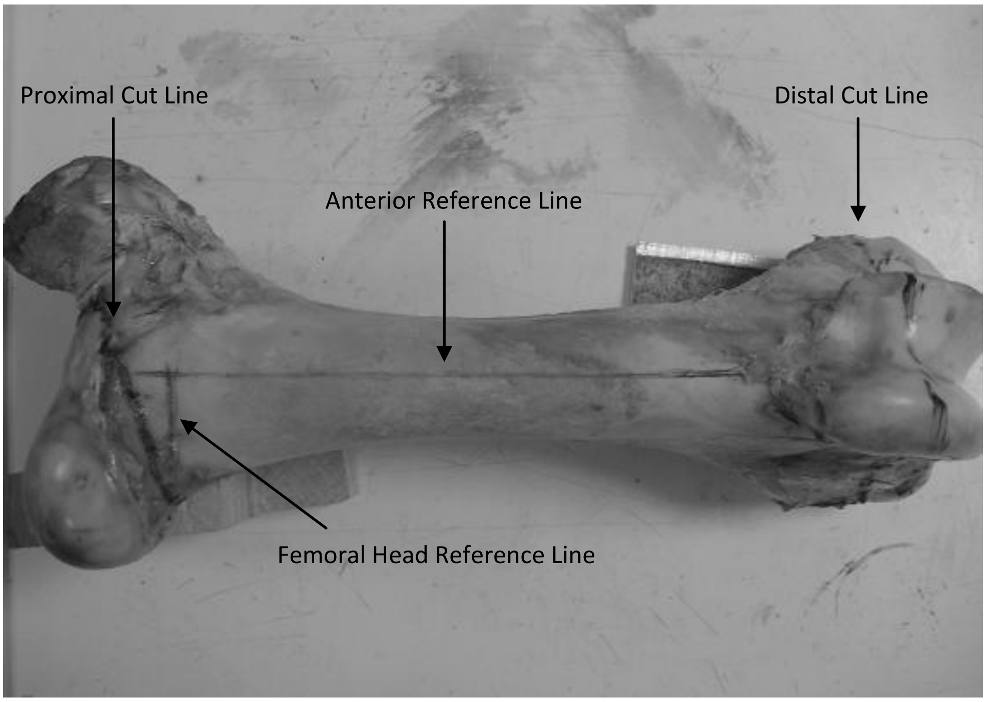

Fig. 4.15 Anterior reference line showing the drawn distal and proximal cut lines (viewed from the anterior aspect).

5. **<u>Proximal Cut:</u>** The Femoral Head Reference Line is drawn next. This intersects the Anterior Reference Line and is perpendicular to it. It is located just below the femoral head as shown in Fig 4.13.
6. The Proximal Cut Line is drawn from the medial extent of the Femoral Head Reference Line at an angle of 25° as far as the greater trochanter. This is done on both the anterior and the posterior aspects of the femur. On reaching the greater trochanter the angle changes from 25° to 90° (parallel to long axis of the bone), as in Fig 4.13.
7. **<u>Cutting:</u>** To carry out the Distal and Proximal cuts, the femur is mounted horizontally in a vice on a work bench. It is important to tighten the vice sufficiently to avoid movement of the femur during cutting but not too tight to

cause damage to the femur. A hack saw is used to cut the femur. A slow even speed is maintained and water from a spray can is used to keep the bone cool and for lubrication during the sawing process. Extreme care is taken to follow the cut lines for both the Distal and Proximal cuts.

8. **Reaming:** To create a pilot hole for the broach a cylindrical hole is reamed (drilled) down the centre of the femur. The surgeon normally uses a hand drill. A similar affect is achieved by drilling slowly with a cordless drill being conscious of keeping the drill hole vertical with respect to the femur.
9. To mark out the location of the drill hole: The proximal cut surface is divided into two halves with a pencil line as in Fig 3.15. Another line is taken from the point where the Anterior Reference Line meets the Proximal cut surface and drawn in the posterior direction. This line crosses the Proximal cut surface line at a somewhat oblique angle.
10. The centre point of the reaming (drilling) is marked on the Proximal Cut surface line 6 mm medial of the Anterior Posterior intersector as shown in Figure 4.14.
11. Figure 4.15 shows the location of the AE sensors and the strain gauges. AE sensor 1 (50) is centered on the intersection of the Anterior Reference Line and the Femoral Head Reference Line. AE sensor 2 (63) is centered on the Anterior Reference Line 30 mm distal of sensor 1. Strain gauge 1 is centered 10mm below and 10 mm in the medial direction of AE sensor 1. Strain gauge 2 is centered on the medial aspect of the femur 10 mm below the medial aspect of the cut surface.

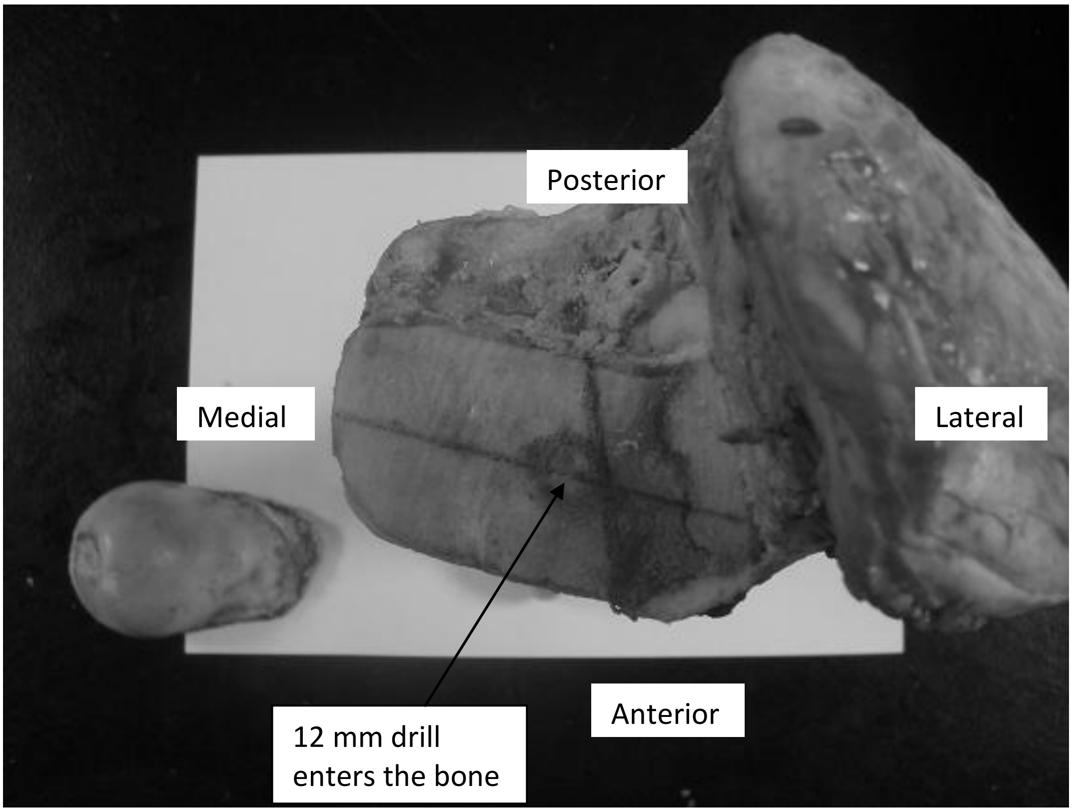

Fig. 4.16 Cut surface marked out to find the drill coordinates.

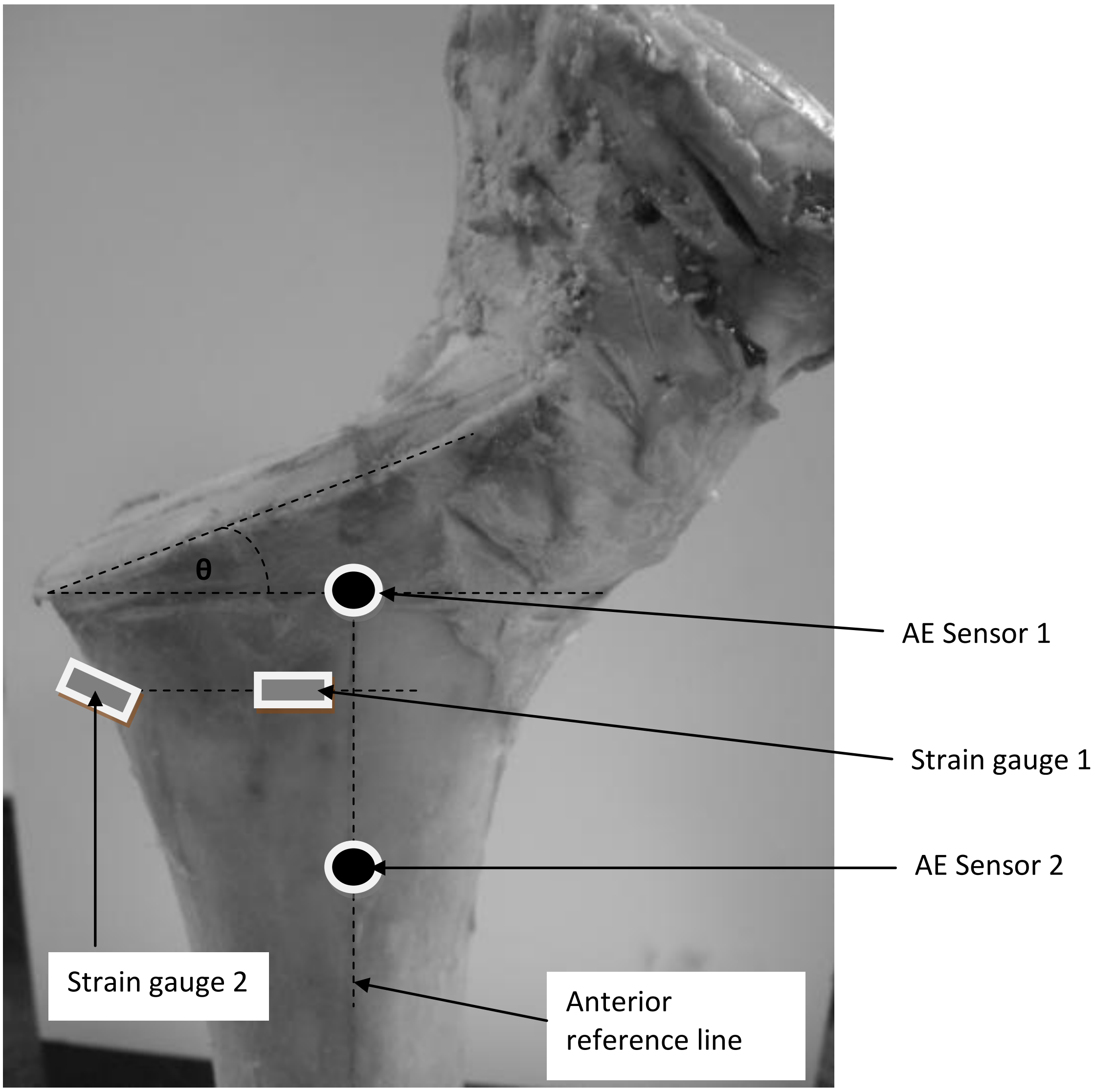

Fig. 4.17 The anterior view of a prepared femur. The two AE sensors and the two strain gauges are marked relative to the Anterior Reference Line and the Femoral Head Reference Line.

Acoustic Emission Settings using Physical Acoustics PCI-2 system

Channels: *1, 2*
Threshold: *30 dB*
Analog Filter: *100 kHz – 1 MHz*
Sampling Rate: *40 MSPS (Except femur 7 which is 5MSPS)*
Pretrigger: *100*
Hit Length: *10 K samples*
PDT: *120 µs*
HDT: *200 µs*
HLT: *200 µs*
Max Duration: *1 ms*
Front End Filter: *counts 10 to 1000*
Sensor 1: *sensor 50, preamp 1 and ch. 1*
Sensor 2: *Sensor 63, preamp 2 and ch. 2*

Test Procedure:

Figure 4.16 gives a good illustration of the sample loading setup. After the AE sensors and strain gauges have been mounted, the mock broach is inserted into the pilot hole of the femur. The top end of the broach is clamped in the jaws the Materials Testing Machine. The jaws hold the mock broach vertical. This is to ensure that each of the femora is loaded in the same manner. Next the AE sensors are connected to the AE system and the strain gauges are connected to the strain recorder. Tests are carried out to ensure all sensors are operational. The Materials Testing Machine was set to load the sample at a displacement rate of 2.5 mm per minute. Synchronising the three systems was done manually. The Materials Testing Machine was started first. When the preload reached 50 N, the AE system and the strain recorder were started simultaneously. As the maximum sample rate of the strain recorder is 1 sample per second, starting both systems by hand is sufficient. The test was run until a fracture was visually seen. The strain gauges would indicate when fracture actually occurred. Figure 4.17 shows the fracture in Femur 7.

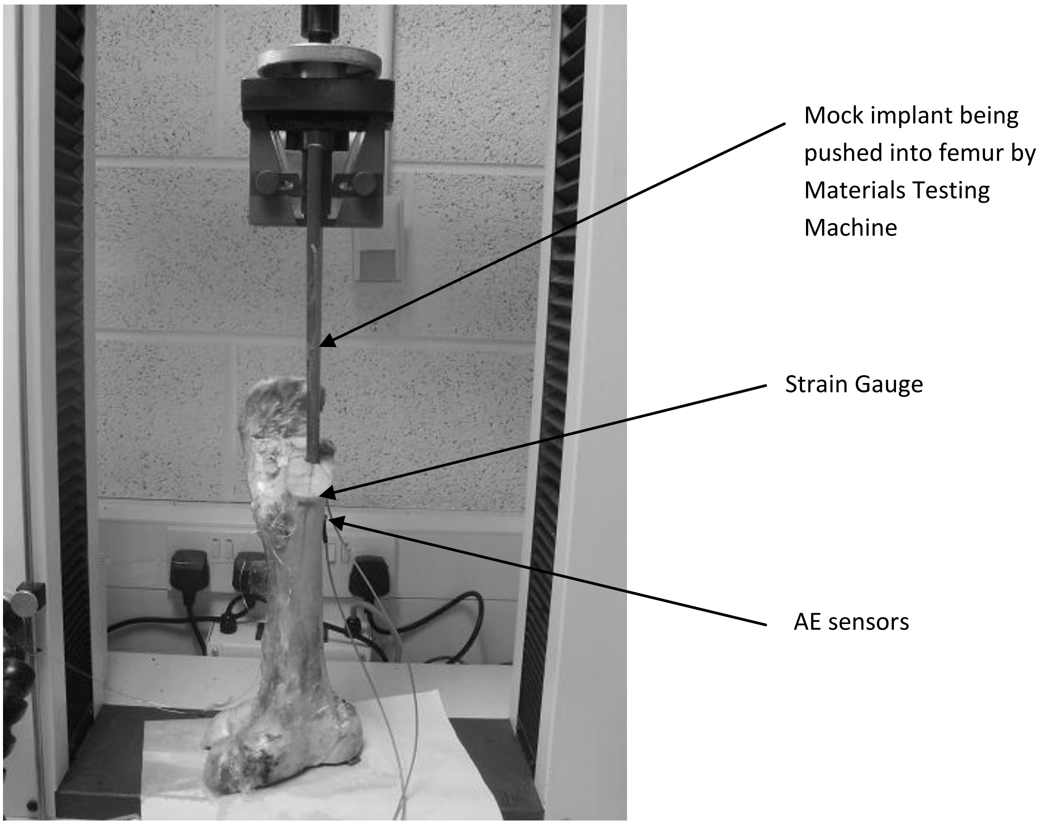

Fig. 4.18 Femur 7 mounted in Materials Testing Machine ready to start testing.

Fig. 4.19 Fracture of Femur 7.

4.4.1 Frequency Analysis

There are 6 femora in this test. Both the peak frequency and the centroid frequency were examined. Figure 4.20A through to Figure 4.20F show peak frequency and strain against time on the X axis. The moving average of the peak frequency is also plotted. A reduction in frequency coming up to and in particular just before fracture occurs is evident. The moment of fracture is signified by the vertical change in strain values. In these cases the change is in the negative direction. This is because as a fracture opens up the strain gauge which is to one side of this fracture, will suddenly return to its non strained position as the stretched bone relaxes after fracture. The strain results for femora 3 and 5 show two sudden drops before the main drop. These could indicate a smaller initial fracture before the major visually detected fracture. Inspecting these femora post test does show two fractures, one relatively small. However it is unknown whether these two fractures occurred simultaneously or successively as the strain is indicating. In all femora, a frequency drop is evident leading up to the fracture point. It is most clearly evident in femora 6, 7 and 8.

The frequency centroid was also plotted for femora 3 through 8. The 15 point moving average of the centroid frequency was plotted for each femur. However the reduction in frequency just prior to final failure that was observed with peak frequency was not evident here. The scatter graphs are included in the appendix. Therefore peak frequency is the preferred AE characteristic.

In order to determine if a fixed threshold could be used for all six femora, the 15 point moving average of the peak frequency for each femur is plotted on the same scatter graph - Figure 4.21. On each trace only the data points that lead up to and include the final failure are plotted. Any data points after that were not plotted. The point in time of the final failure is determined by the sudden change in strain that coincides with largest energy AE hit in the whole data set.

Also plotted is a critical threshold at 150 kHz. For each femur the moving average dips below this threshold at least once before final fracture. In every case it occurs close to the end of the trace. This result clearly shows that a reduction in peak frequency occurs just before final fracture. It is noted by examining the scatter graph that the traces for femora 3 and 7 came close to crossing the threshold before the final dip just before final failure. This may be a weakness and only further work can determine the robustness of this technique.

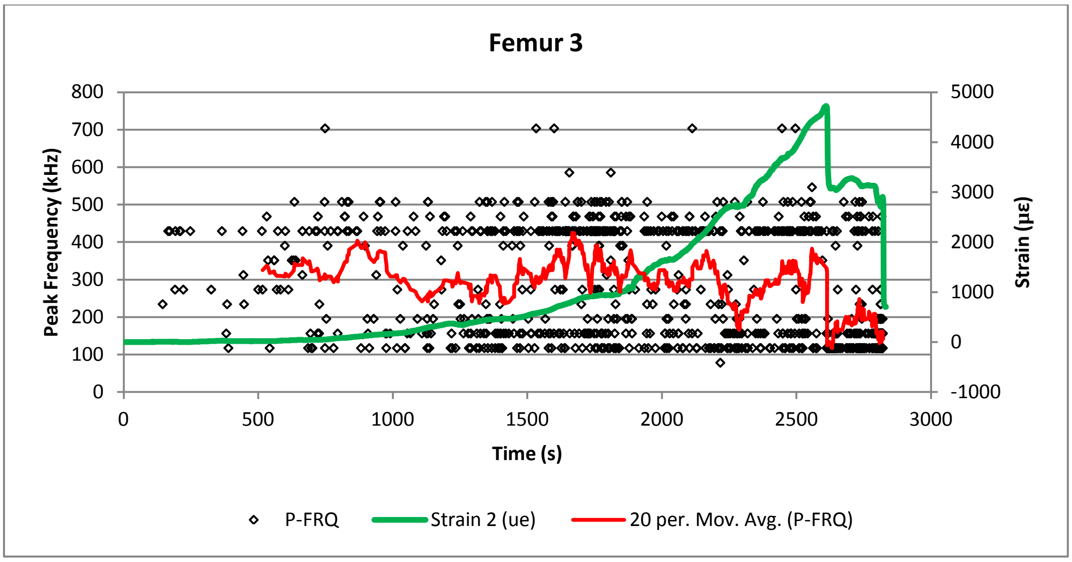

Fig. 4.20A Peak Frequency analysis of Femur 3.

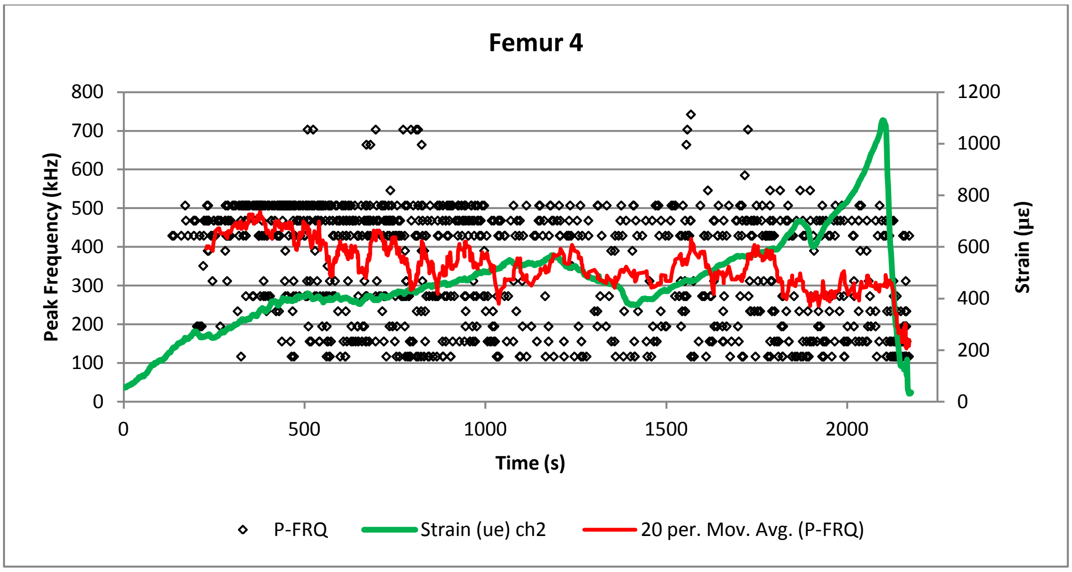

Fig. 4.20B Peak Frequency analysis of Femur 4.

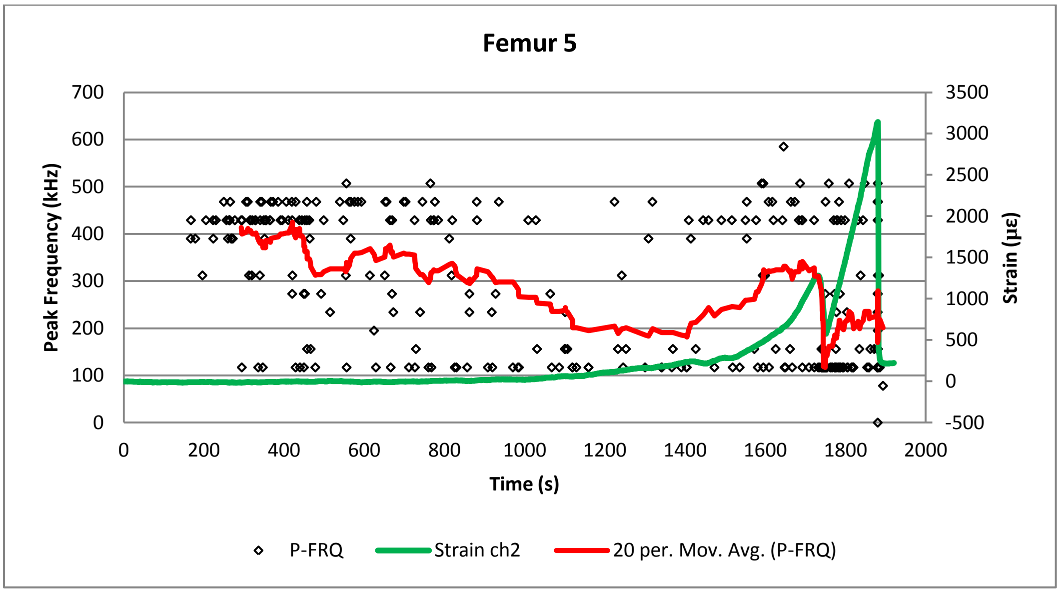

Fig. 4.20C Peak Frequency analysis of Femur 5.

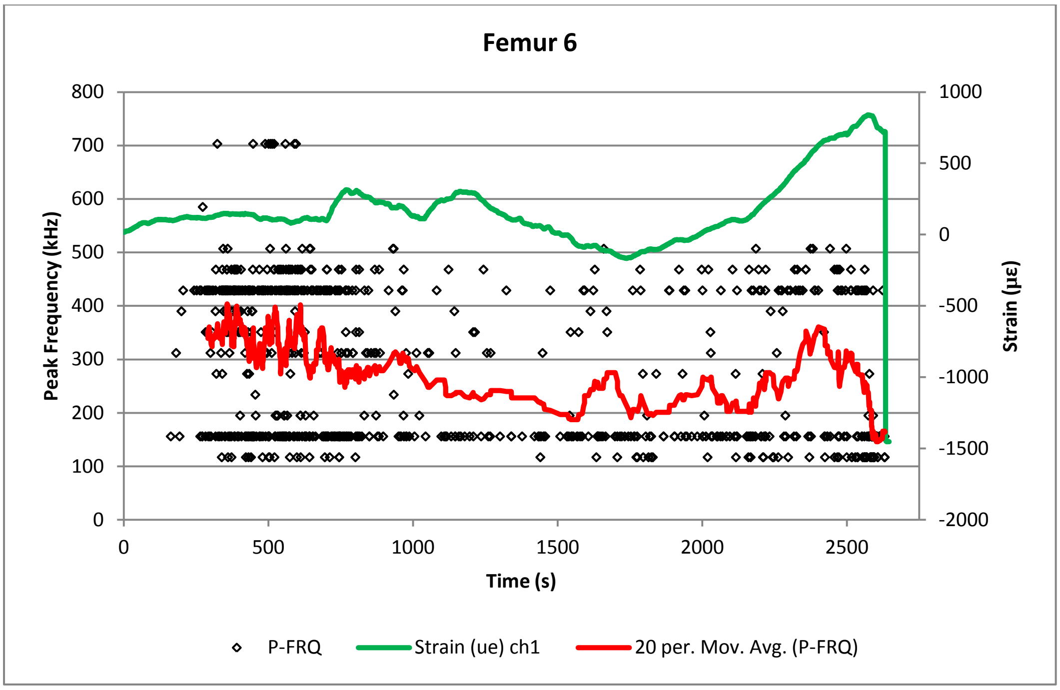

Fig. 4.20D Peak Frequency analysis of Femur 6.

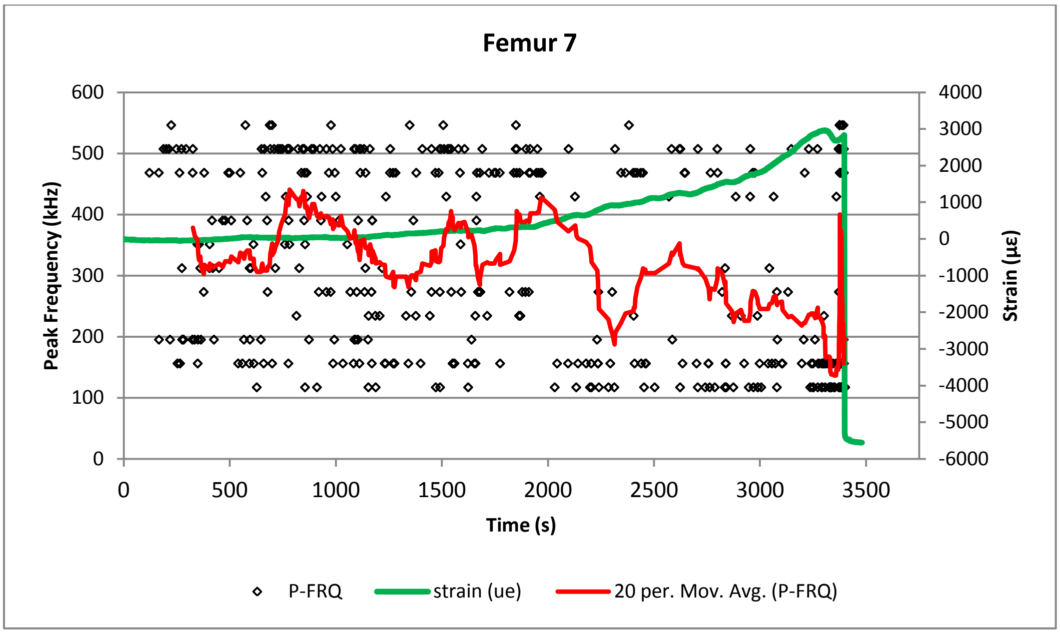

Fig. 4.20E Peak Frequency analysis of Femur 7.

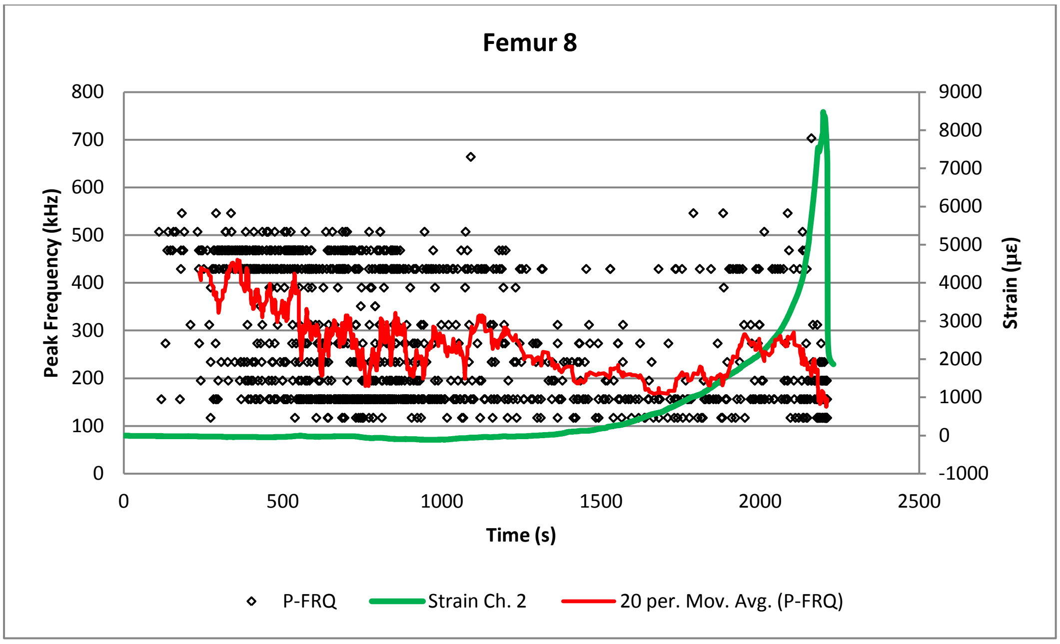

Fig. 4.20F Peak Frequency analysis of Femur 8.

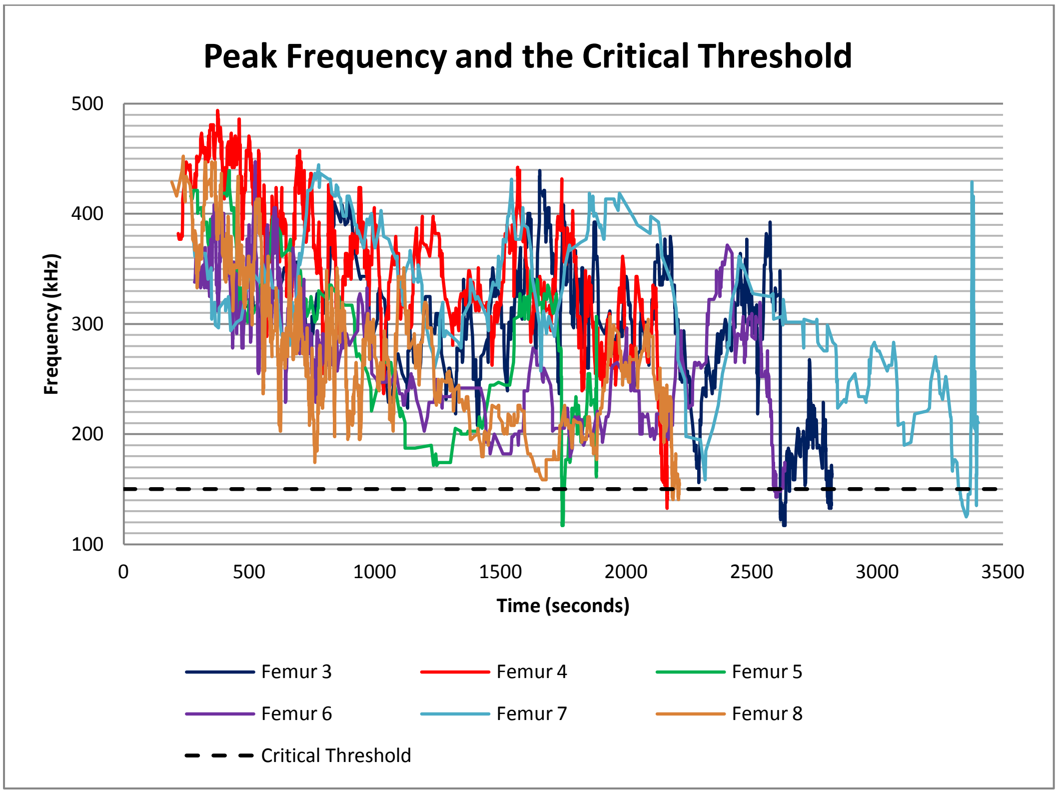

Fig. 4.21 The moving average of the peak frequency for femora 3 through 8 showing that all samples exhibit a reduction in frequency to below 150 kHz before final failure happens.

4.4.2 Energy Analysis

The use of an energy based AE parameter was rejected in chapter 3 because the AE waves attenuate as they propagates from their source to the AE sensor and if the distance travelled is unknown the amount of attenuation is unknown. Therefore it is not possible to determine the source energy. The energy detected from a distant large crack could be smaller than the energy measured from a closer smaller crack.

While it is impossible to determine the true AE energy of any one microcrack, if the energy of a large number of AE hits are added together, their accumulative energy may have some correlation with the energy released by the fracture process. Therefore instead of using any one AE hit or series of AE hits to indicate a critical stage in the fracture process, the accumulated AE energy is used to determine a critical level of energy released that warns of impending failure. A similar approach has been used by previous researchers (Yu 2011). They found a relationship between cumulative AE absolute energy and crack growth rate in steel samples representative of components in bridges. They showed how this relationship could be used to predict the fatigue life and when the crack growth reaches a critical stage. Similarly in this work cumulative absolute energy of the AE hits is used to try and predict when the THA femora reach a critical stage in their fracture process. Note that crack growth is not examined in the current work. It is expected however that THA bone samples will prove more difficult as the loading mode is more complex and there is more variations between samples. Scatter graphs showing the cumulative absolute energy of the AE hits for femora 3 through 8 are presented in Figure 4.21. The strain is also plotted to indicate the time of failure. Results from femora 1 and 2 are not included in this study because the relevant data was not collected.

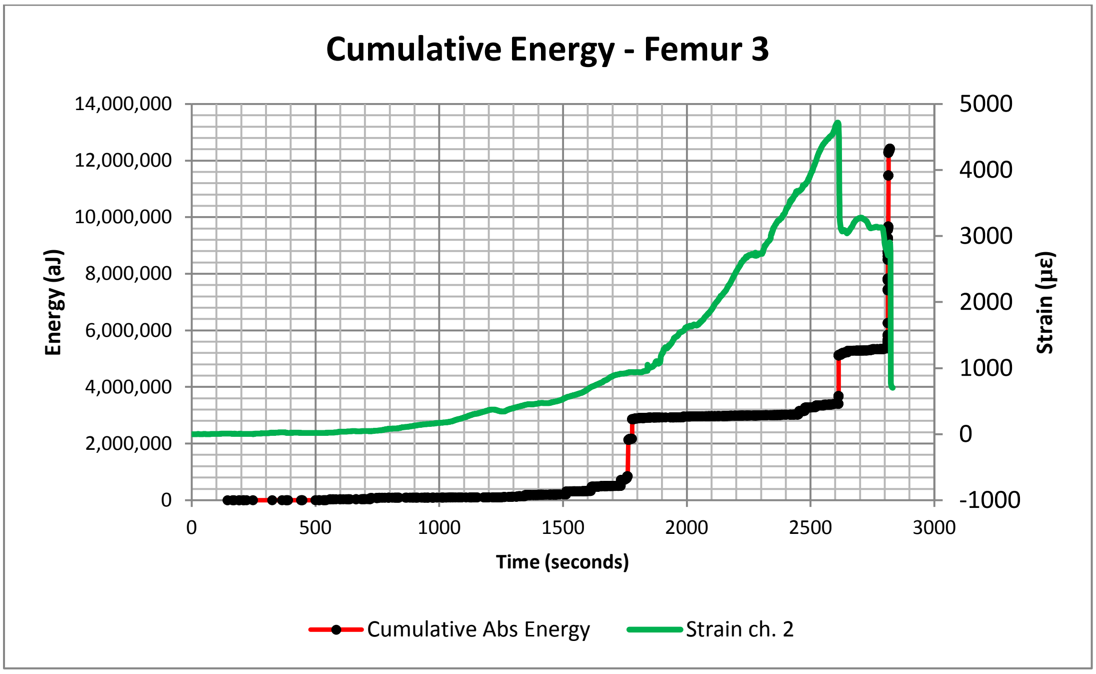

Fig. 4.22A Plot showing cumulative absolute energy for femur 3. Strain is also presented showing a large increase in absolute energy in the AE hits at the point of failure (sudden decrease of strain).

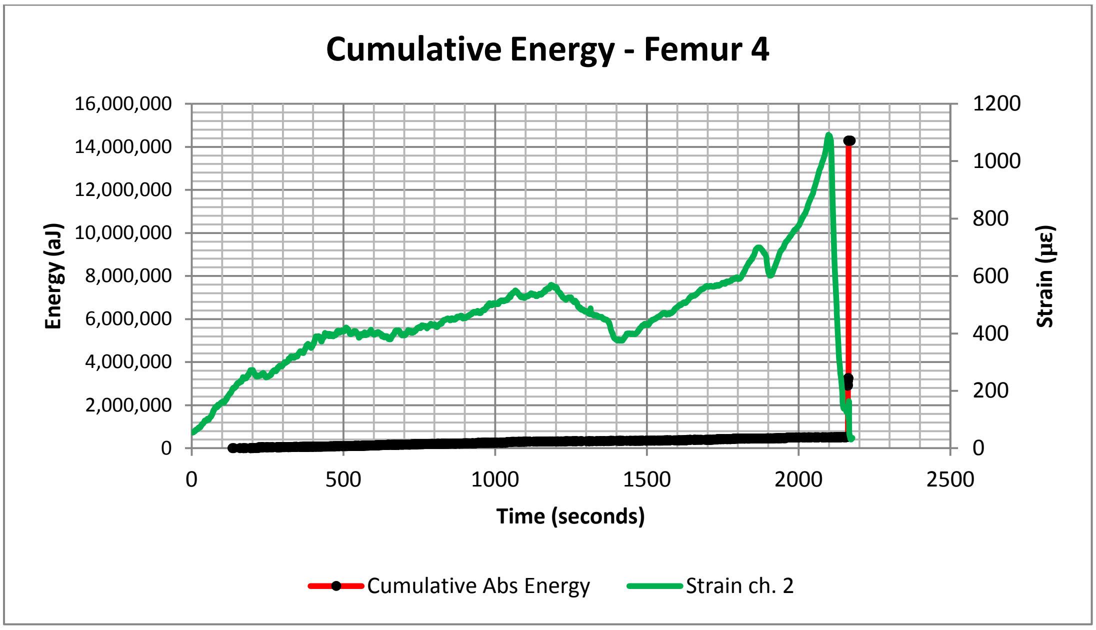

Fig. 4.22B Plot showing cumulative absolute energy for femur 4. Strain is also presented showing a large increase in absolute energy in the AE hits at the point of failure (sudden decrease of strain).

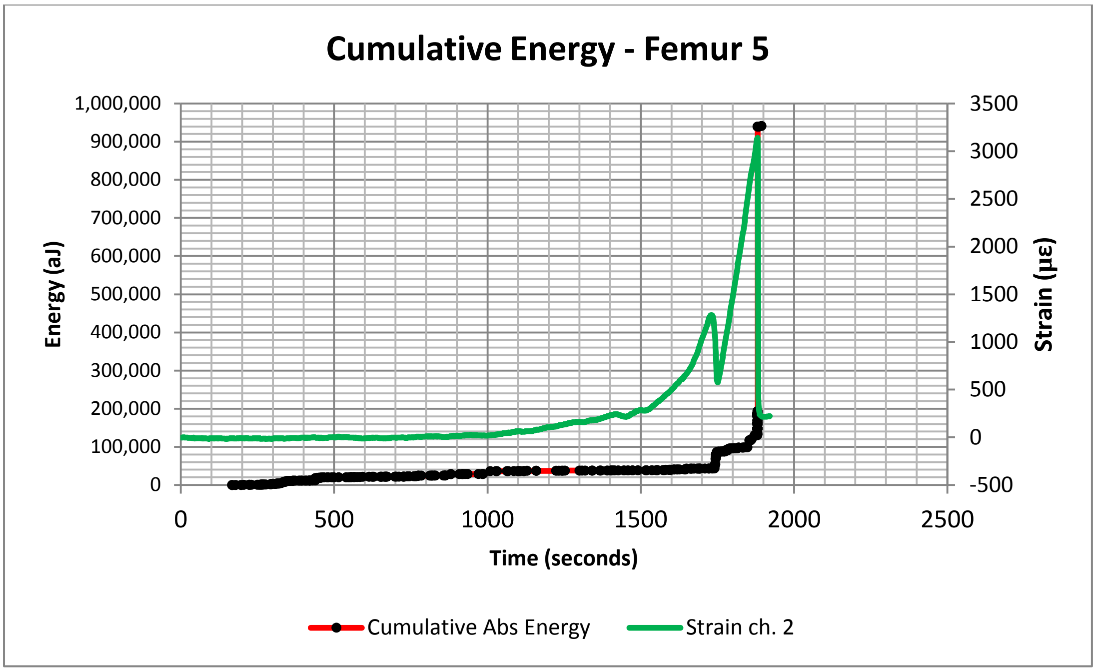

Fig. 4.22C Plot showing cumulative absolute energy for femur 5. Strain is also presented showing a large increase in absolute energy in the AE hits at the point of failure (sudden decrease of strain).

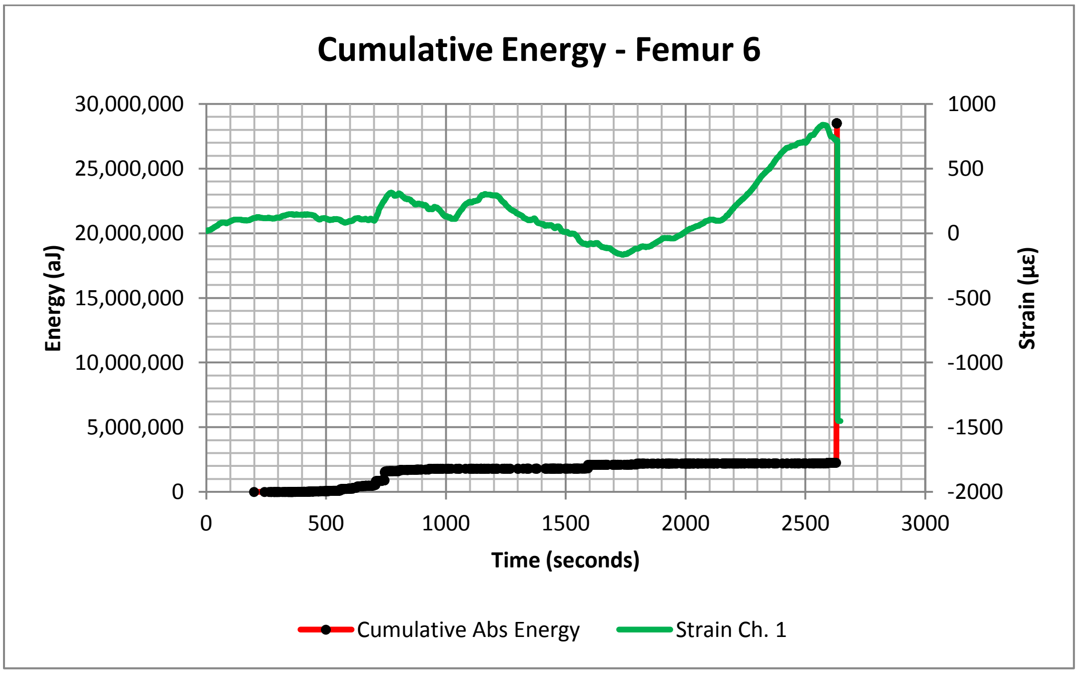

Fig. 4.22D Plot showing cumulative absolute energy for femur 6. Strain is also presented showing a large increase in absolute energy in the AE hits at the point of failure (sudden decrease of strain).

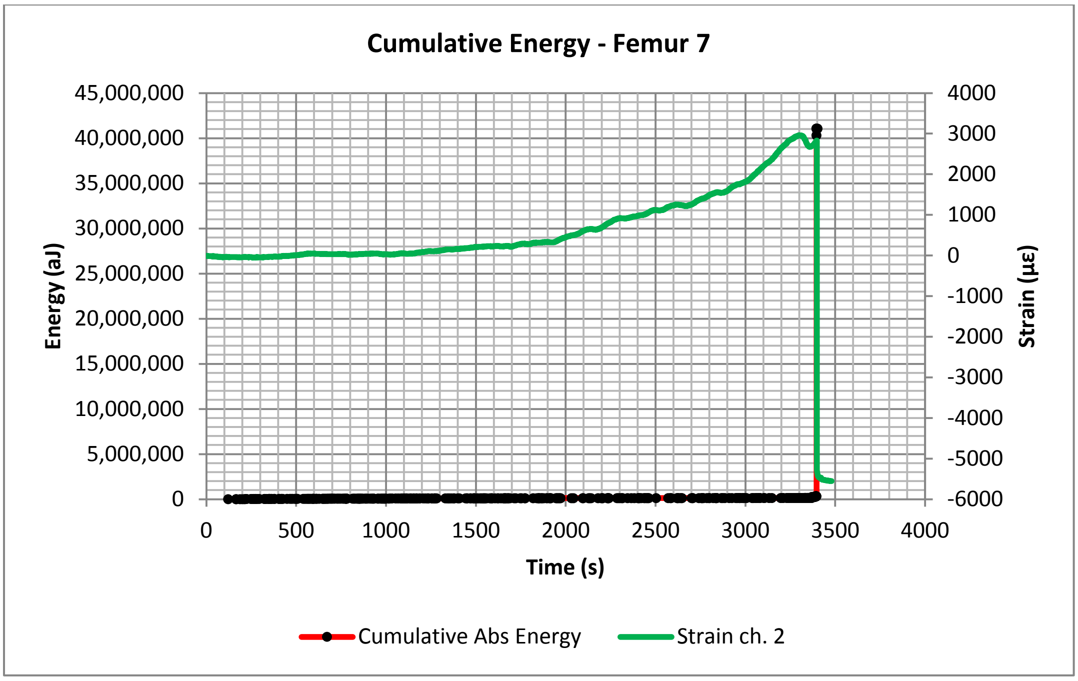

Fig. 4.22E Plot showing cumulative absolute energy for femur 7. Strain is also presented showing a large increase in absolute energy in the AE hits at the point of failure (sudden decrease of strain).

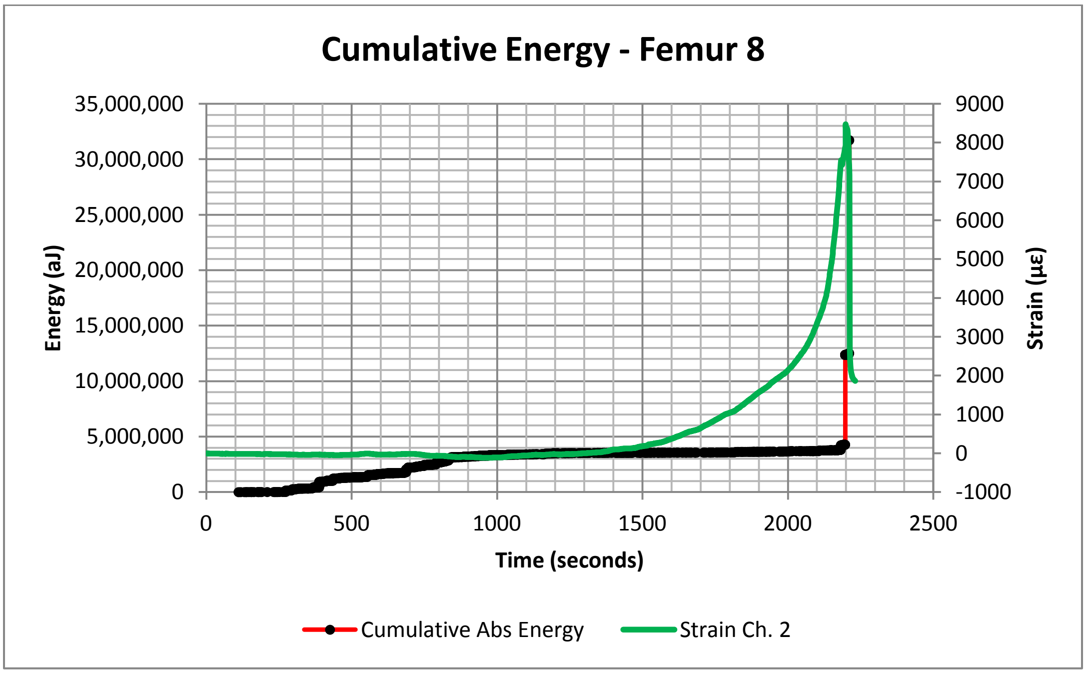

Fig. 4.22F Plot showing cumulative absolute energy for femur 8. Strain is also presented showing a large increase in absolute energy in the AE hits at the point of failure (sudden decrease of strain).

Examining the scatter graphs it is obvious that most of the energy is released in the final stages of fracture. Furthermore the total accumulative AE energy measured varies widely between samples. Attempts were made to correlate this variation with various characteristics of the bones measured in section 4.4. Figure 4.22 shows that there is no correlation between mass of the different bones and the accumulated AE energy measured up to bone failure. Next an attempt is made to correlate the mass of the bones with the accumulated energy up to 90% of the final failure time. This would be the same as the up to 90% of the displacement of the mock broach as it is pushed into the medullary canal of the femur. This is because the cross head speed of the materials testing machine is constant at of 2.5 mm per minute. Again no correlation was found between the mass of the femora and the accumulated absolute AE energy as can be seen in Figure 4.23. The other bone characteristics that were measured in section 4.4 were also compared with accumulated energy but correlations were not found. The results of these tests are in the appendix.

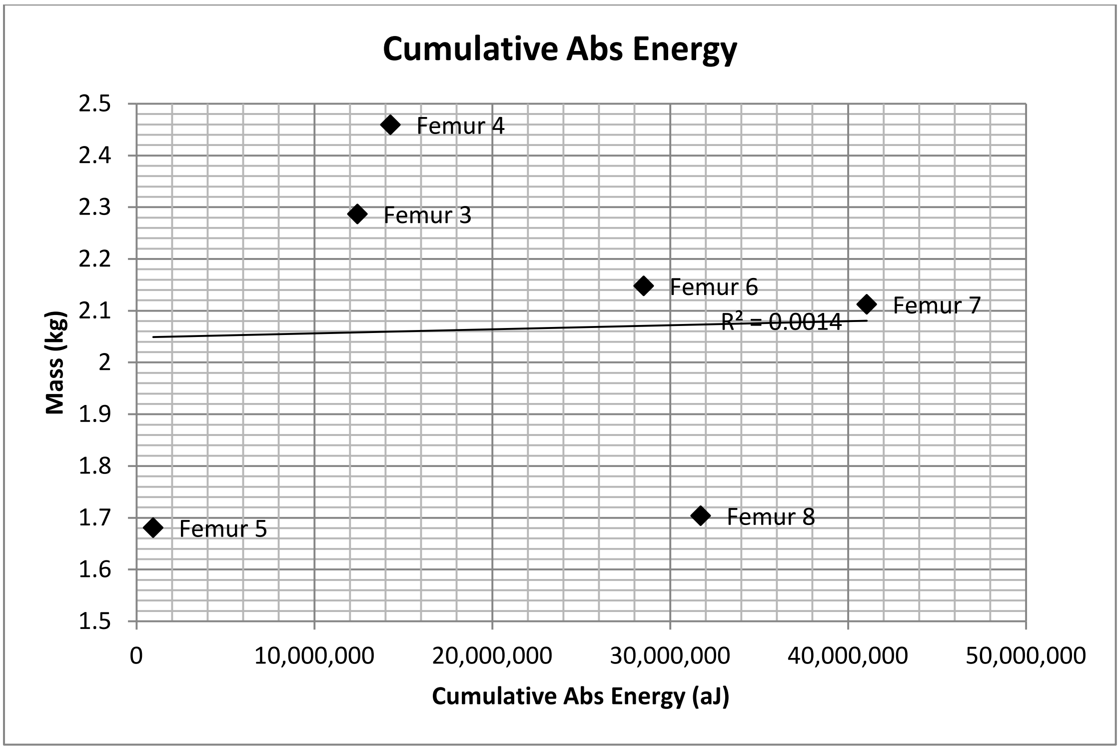

Fig. 4.23 The mass of femora 3 through 8 plotted with their respective AE hit cumulative absolute energy at the point of failure. No correlation was observed.

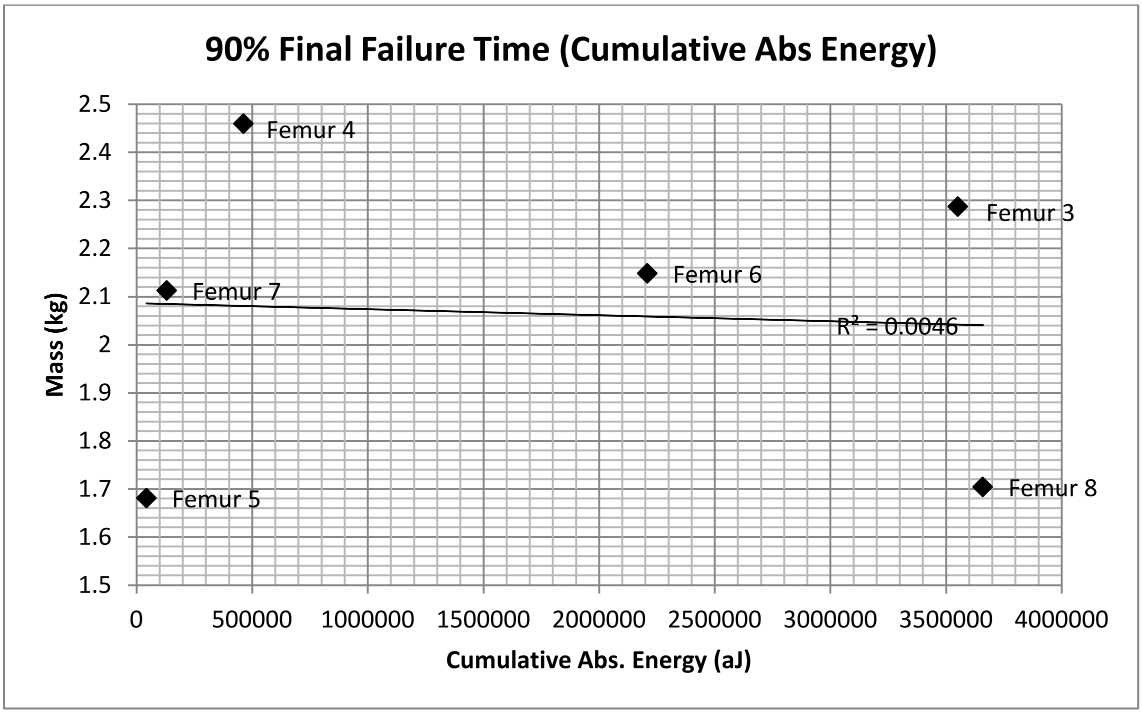

Fig. 4.24 The mass of femora 3 through 8 plotted with their respective AE hit cumulative absolute energy at 90% of time to failure. No correlation was observed.

4.5 Discussion

This peak frequency approach yielded interesting positive results. Seven out of eight femora showed at least some reduction before fracture. Femur 1 which showed no frequency reduction pre fracture was loaded at a faster rate than the others and this may have contributed to this result. Little work has been gleamed from the literature regarding frequency analysis to predict fracture. Sakai et al. (2011) did achieve a similar result but instead of using acoustic emission he used a microphone which took in air borne sounds including the hammering of the implant in a THA simulation experiment. These results warrant more work in determining at what exact level of fracture that this frequency reduction occurs. Also tests would have to be carried out to determine whether it would be feasible for a surgeon to stop impaction once he is alerted to the fall off in frequency. Unfortunately the use of the accumulated AE absolute energy did not reveal a method that could be used to warn a surgeon of impending femur fracture.

While this work does show promise for a technique that could be used to warn the surgeon of impending fracture during THA, it is still in the very early stages of development and therefore has many limitations. Some of the challenges that would need to be overcome include:

1. The experiments carried out were merely a simulation of real THA surgery. The broach used was not a real broach but a piece of mild steel roughly in the shape of a broach. The method of inserting the broach into the femora was a controlled constant displacement of the broach in a downward direction. In real surgery a surgical mallet is used to impact the broach. This could introduce

other sources of AE that may interfere with the signals of interest. Also the final failure may occur quicker than in these experiments and so give the surgeon less warning of the fracture.

2. Only bovine bone was used in this work. There is a risk that human bone would not exhibit the same reduction in peak frequency before fracture. Furthermore most patients that undergo THA surgery are elderly and their bones tend to be more brittle than younger people especially if osteoporosis is a factor. Brittle bones tend to fracture more abruptly and thus the surgeon may not get sufficient warning if any.
3. This peak frequency reduction technique would need to be made sufficiently reliable so that a surgeon could be confident that a fracture is really imminent. A predicted fracture that did not materialize may threaten the introduction of the technique. Too many false predictions may render the technique less than beneficial.
4. A suitable method to attach the sensor to the femur would need to be devised. This work does not investigate this. Superglue was used in the current work. A medical alternative would have to be sourced. The sensor and the associated sensor cable would have to attached and routed so as not to obstruct the surgeon's work.
5. A method to sterilize the sensor would need to be realized. Perhaps a wireless sensor could be used.
6. Even if the technique could be validated and proved beneficial, the surgeons themselves would have to be won over. They may not want to rely on a piece

of technology when they are used to using their own intuition and experience.

This is why trainee surgeons may be more open to using this technique.

5. AE Source Location

5.1 Literature Review

To be able to find the location of individual microcracks in bone has numerous benefits. One is the understanding of bone fracture that it affords. It is impossible to see into a solid material either with the naked eye or though other visual aids such as a microscope or by slowing down time with a high speed camera. While visible light does not travel through solid materials like bone other physical forces do, in this case acoustic waves. Acoustics can be deployed in two main ways: active through the use of ultrasound and a passive approach using acoustic emission. This project uses the later.

While analysis and classifying AE (acoustic emission) parameters gives information about how fracture is occurring and when it is reaching a critical stage as seen in the previous sections of this dissertation it does not show where fracture is occurring or where the microcracks are forming. This localization of microcracks could be extremely useful in understanding the areas of bone that are likely to initiate a fracture. The source location of microcracks could also have a use in preventing intra-operative fracture during Total Hip Arthroplasty as alluded to in Chapter 1. If the surgeon knows where an impending fracture is likely to occur he can re-orient the implant or broach so that the stress that is causing this impending fracture is relieved and by redirecting the implant, a stable position can be attained without causing fracture. A review of the current literature of source location using AE with special reference to bone follows.

While a large number of researchers: Fischer et al. (1986), Wright et al. (1981), Rajachar et al. (1999A) Rajachar et al. (1999B) and Akkus et al. (2000) use acoustic emission to detect and characterize microcracks in bone, there is very little work on trying to find the location of microcracks in bone. Rajachar et al. (1999A) did use a general purpose AE system to locate cracks in bone for the purposes of microdamage characterization. However, very little detail is given in his paper. Because of the lack of previous work in AE source location of microcracks in bone, it was necessary to look into literature on AE acoustic emission localisation in other materials.

The simplest AE source location approach is the zone technique. It works on the principle that the sensor closest to the source will have the largest amplitude and the second closest sensor will have the second largest amplitude. So by recording which sensors have the largest and second largest amplitudes the possible location of the source can be reduced to a specific zone (Baron and Ying 1987; Ge 2003A). However to get a precise location this approach would require a very large number of sensors. Another AE source location method is the Triaxial Sensor Approach (Ge 2003A). It uses a composite sensor consisting of at least 3 sensor elements. By determining the sequence that the sensor elements detect the passing AE wave, the approach angle can be determined. The difference in time between the P wave (primary or compressional wave) and S wave (secondary or shear wave) can be used to determine the distance from the source. Horn (1996) and Holler et al. (1991) used similar methods but they traced the approach angle of the AE waves at two composite sensors back towards their sources. At some point the two traces intersect giving the source location.

The most common approach is Hyperbolic Source Location, also known as Hyperbolic Positioning. This technique uses the Time Difference Of Arrival (TDOA) of the acoustic emission wave at a set of 2 sensors and the AE wave velocity to develop the equation of a hyperbola on which the source must lie. A second set of two sensors can be used to create a second hyperbola on which the source must also lie. The definitive source location is the intersection of the two hyperbolae. This technique depends on the AE wave travelling in a straight line at constant velocity to all sensors and the recording of the exact time the wave reaches each of the sensors. Baron and Ying (1987), Ge (2003A) and Ge (2003B) give some instruction of how Hyperbolic Source Location is achieved. Generally with this technique it is necessary to solve two or three hyperbolic equations depending on whether the goal is two dimensional or three dimensional source location. However the equations are non-linear, so the problem is generally solved using numerical approximation techniques. Qi et al. (2000) used first order Taylor expansions to linearise the equations and then solved. Lee et al. (2006) used the Newton-Raphson Method to solve three non-linear equations representing the difference in time of arrival at four sensors in three dimensional location.

There is a less well known and less used approach to AE source location on complex structures which automatically takes the nature of the structure under test into account. This is the use of multiple regression. Artificial AE sources are created on the bone surface at points in a grid format. The TOA (time of arrival) is recorded at each sensor and TDOA (Time Difference Of Arrival) are computed by subtracting a set of two TOA's. Using regression analysis it is determined which values of the TDOA's correlate to which values of the location coordinates. This correlation is used to develop regression equations, which when given new TDOA's will output the corresponding location coordinates. Even locations between the points on the grid can be located as the regression equations can interpolate. Given another sample of the same type of bone the regression equations should still give accurate location coordinates. Some work has been carried out on similar approaches when locating AE sources on aerospace components. Baxter et al (2007) used an algorithm called Delta T which consists of using an artificial AE source to acquire TOA data at each sensor and analysis of delta T (TDOA) is used to draw a map of contour lines with equal delta T's. Then future AE data can be overlaid on this map and its location can be identified. This approach was found to be particularly useful when dealing with bent AE wave paths. Hensman et al. (2010) used a regression type algorithm known as Gaussian Processes to learn the relationship between the TDOA's and the location of artificially created AE sources and is able to predict new AE sources when given the relevant TDOA's.

Both the Hyperbolic source location and the Regression source location techniques have potential in the AE localization of microcracks in bone. So the two techniques are developed for bone samples and tested. Because whole bone is complex and irregular, small rectangular samples were harvested from bovine femora used in for following experiments. The same samples are used for both Hyperbolic Source Location and Regression source location

5.2. Preparing Bovine Bone Samples for AE Localization

While materials like steel, concrete, or composites can be formed or machined to most conceivable dimensions, bones have greater restrictions. The femur is the most massive and thickest long bone in the bovine skeleton. A typical adult bovine femur is approximately 45 mm from the lateral to medial and 53 mm from posterior to anterior at the mid diaphysis. The thickness of the cortical wall is at maximum 8 – 10 mm, but this thickness is only at particular parts of the femur. Other parts of the femur wall might be around 5 or 6 mm thick. After measuring and cutting up various femora, the following dimensions of rectangular samples were decided upon: 55 - 65 mm long (proximal distal direction) by 20 – 25 mm wide (tangential to the proximal distal direction) and 5 – 6 mm thick (periosteum to endosteum). The sample is taken from the mid diaphysis of the lateral aspect of the femur.

Two batches of bone samples were acquired and prepared. The two batches were taken from a local butcher (Burns' Butcher, Grange, Co. Sligo, Ireland). Batch one consisted of 10 bovine femora and the butcher supplied the following information on them: Each bone was acquired from cattle from north Co. Sligo, Ireland. Each sample was female. The animals were 2 years old plus or minus six months. The breeds were a mixture of Limousin cross, Belgium Blues, Charolais cross and Simmental. Unfortunately, the particular breed of each individual sample was not acquired. However the breed of each of the samples in Batch 2 was recorded and all the details are presented in Table 5.1. Batch 2 consisted of 5 femora.

Sample No.	*Breed*	*Sex*	*Age*	*Femur*	*Locality*
Sample 1	Limousin cross	Female	2 yrs	Right	North Sligo
Sample 2	Belgian Blue	Female	2 yrs	Left	North Sligo
Sample 3	Limousin cross	Female	2.2 yrs	Left	North Sligo
Sample 4	Charolais cross	Female	2 yrs	Left	North Sligo
Sample 5	Charolais cross	Female	2 yrs	Right	North Sligo
Sample6	Belgium Blue	Female	2 yrs	Right	North Sligo

Table 5.1 Details of samples from Batch 2.

Extracting Bone Samples from Bovine Femora:

1. The femora were acquired fresh from the butcher and they were delivered to the work area in one hour and during the transportation they were kept wrapped in a plastic bag to retain moisture in the bones.
2. Auto-Touch-Up paint (as used for scratches on cars) was used to label the posterior, anterior, medial and lateral sides of the bones. The distal and proximal ends were also marked. This paint was chosen as it was thick enough to remain on damp bone. Still, care was needed so it would not rub off.
3. The two epiphysis were sawed off with a carpenters hand saw as illustrated in Figure 5.1

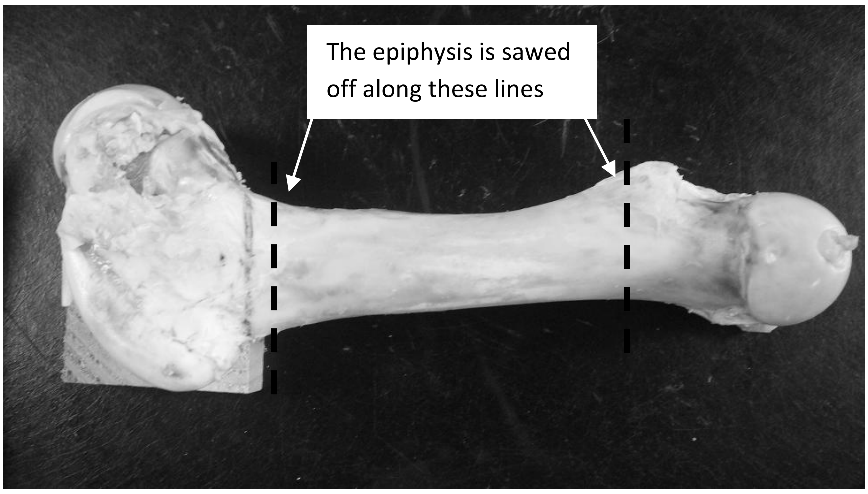

Fig. 5.1 Both the distal and the proximal epiphysis are cut off each of the femora.

4. The epiphyses were disposed of and the remaining femur was cleaned of any surface flesh and the marrow was removed.

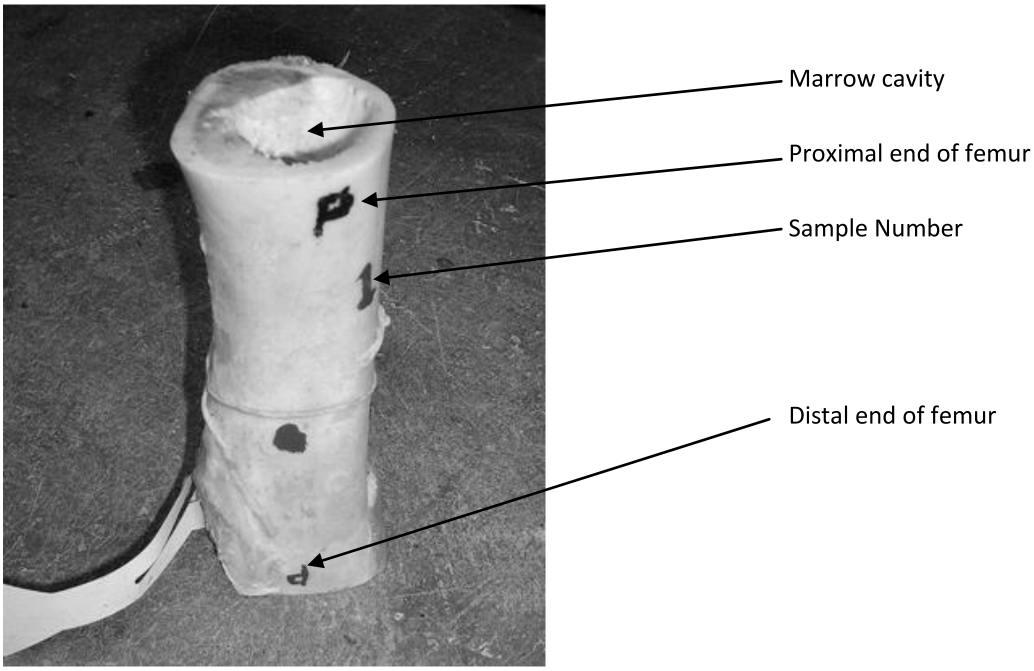

Fig. 5.2 The mid diaphysis of a femur cleaned of flesh and marrow. The Markings on the bone are indicated.

5. Using a band saw the lateral side is cut from the femur. The mid piece is then cut from this lateral side as in Figure 5.3. Water was used to keep the bone cool during the cutting process.

6. Then the lateral mid diaphysis sample was taken to a milling machine which is used to cut the final rectangular sample.

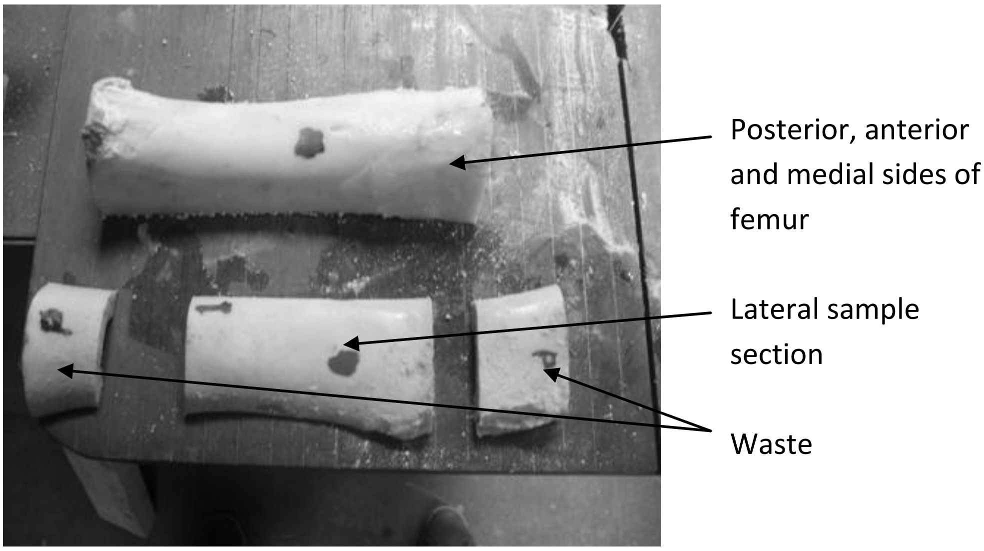
Posterior, anterior and medial sides of femur

Lateral sample section

Waste

Fig. 5.3 Cutting the bone sample from the femur.

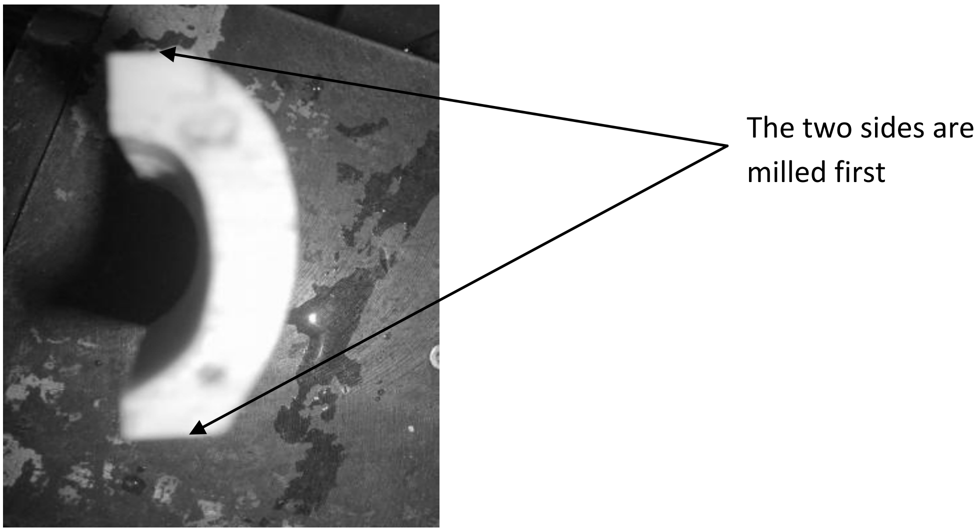
The two sides are milled first

Fig. 5.4 The edges of the bone sample are milled first.

7. First the sides of the sample are milled flat and parallel. Next the top and bottom (periosteum and endorsteum) are cut flat and parallel to each other.

Finally the ends are cut flat. The way the sample is mounted in the milling machine allows all surfaces to be cut at right angles to each other.

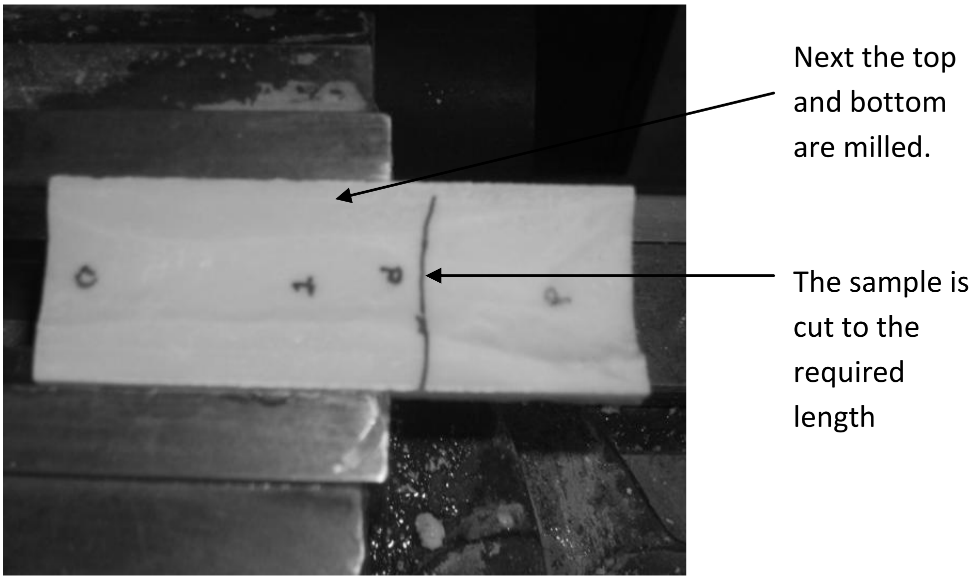

Next the top and bottom are milled.

The sample is cut to the required length

Fig. 5.5 The top and bottom surfaces of the bone sample are milled.

8. After all the samples were cut to rectangles some were a little larger than others, so to get them all the exact same size, they were all reduced to the dimension of the smallest sample whose dimensions turned out to be 65 mm x 22 mm x 5.5mm. Batch 1 initially consisted of 10 samples, but one proved to be unacceptably small so it was discarded. Therefore nine samples of the above dimensions were achieved. Batch 2 consisted of 5 samples initially but two were damaged during the preparation process so three samples of the same dimensions were formed.
9. In order to reliably and repeatedly mount AE sensors and create AE sources, a reference grid system must be developed. Although various schemes were looked into and tested, a simple pencil grid was used in the end. A small engineering square, a precise 15 mm steel ruler and a mechanical pencil with a

0.3 mm 2H lead were used to create the grid. First lines 2.5 mm apart were drawn parallel to the long axis of the sample, as in Fig. 5.6. (The lines closest to the sample edge were 1 mm from the edge). Then another set of lines also 2.5 mm apart were drawn parallel to the width of the sample. This created a complete grid as shown in Fig. 5.7. The positions of the four sensors are also marked in red at the four corners of the sample.

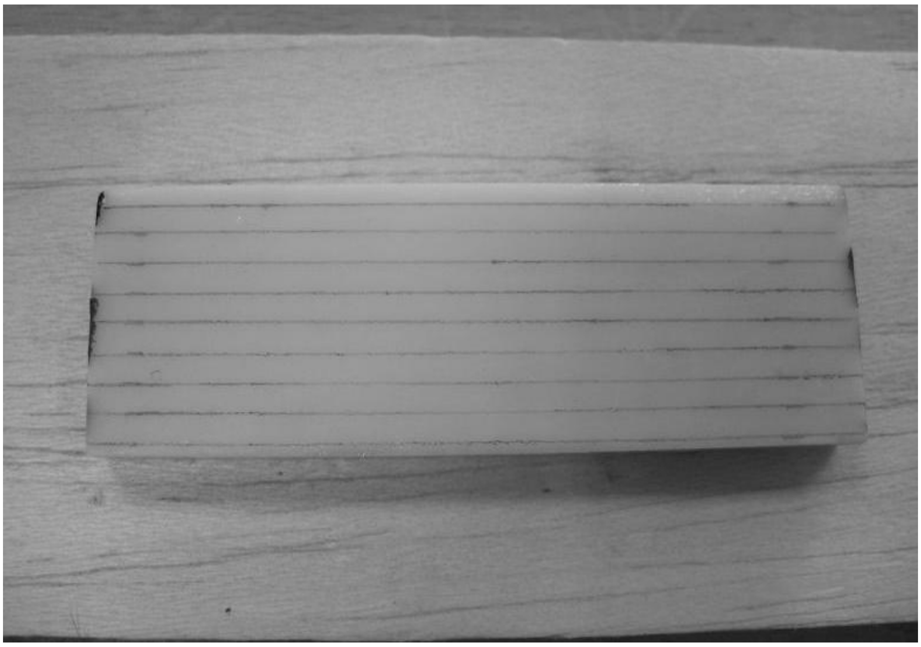

Fig. 5.6 A 0.3 mm lead pencil is used to draw lines parallel to the length of the sample.

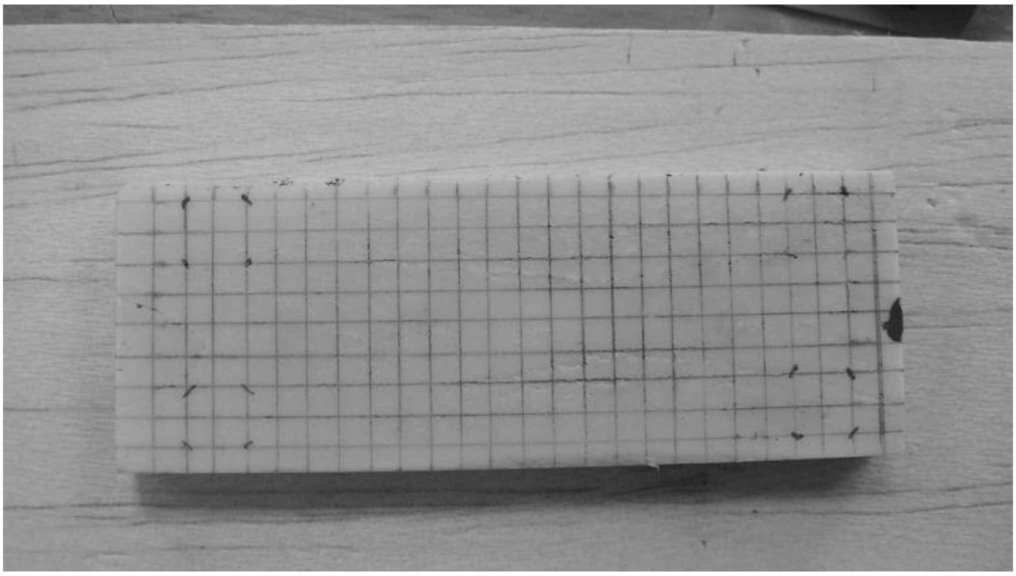

Fig. 5.7 Lines drawn parallel to the short axis of the sample complete the grid on the sample. The positions of the sensors are also marked in at the four corners.

6. Hyperbolic Source Location Algorithm

As the bone samples are rectangular and relatively thin (5.5 mm), two dimensional source location (also known as planar source location) is used. The aim of this algorithm is quite simple: to find the location in terms of X and Y coordinates of the AE hit. The AE hit will be detected at three or more sensors. The AE acquisition device records the AE waveforms from all sensors to a common time base, meaning that the Time Of Arrival (TOA) at each of the sensors is available as an input parameter to the source location algorithm. The velocity of the AE wave as if propagates from the AE source to the respective AE sensors is also available. However the AE wave velocity has a different value depending on its direction through the bone. Kann et al. (1993) found that AE wave velocity propagates 29% faster in the longitudinal direction compared to the transverse direction in pig bones. The variation has to be taken into account in the hyperbolic algorithm. The coordinates of the AE sensors are also available for use in the algorithm.

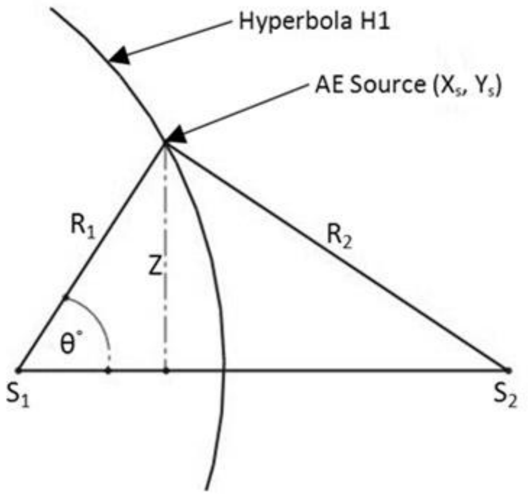

Fig. 6.1 The TDOA between two sensors describe a hyperbola on which the AE source must lie.

Figure 6.1 presents two sensors S_1 and S_2 and an AE source on an infinite plane. An AE wave travels from the AE source (X_s, Y_s) to each of the sensors. This wave covers distances R_1 and R_2 to sensors S_1 and S_2 respectively. The times taken are t_1 and t_2 respectively. Subtracting t_1 from t_2 gives the TDOA between sensor 2 and sensor 1 and this quantity is called TDOA 2-1. The AE wave arrives at sensor 1 first, so the TOA at this sensor is recorded as zero. The TOA at sensor 2 is equal to zero plus the time difference. If this time difference is multiplied by the AE wave velocity, the result is a distance difference. This distance difference describes a hyperbola (H_1) on which the source must lie.

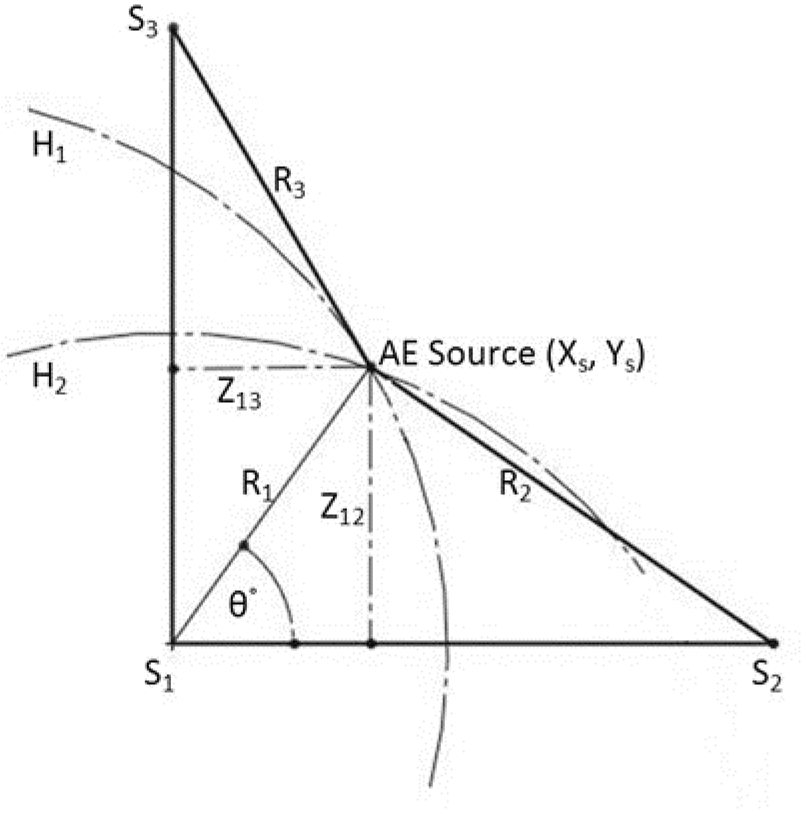

Fig. 6.2 The addition of a third sensor allows a second hyperbola to be drawn. The AE source is at the point of intersection of the two hyperbolae.

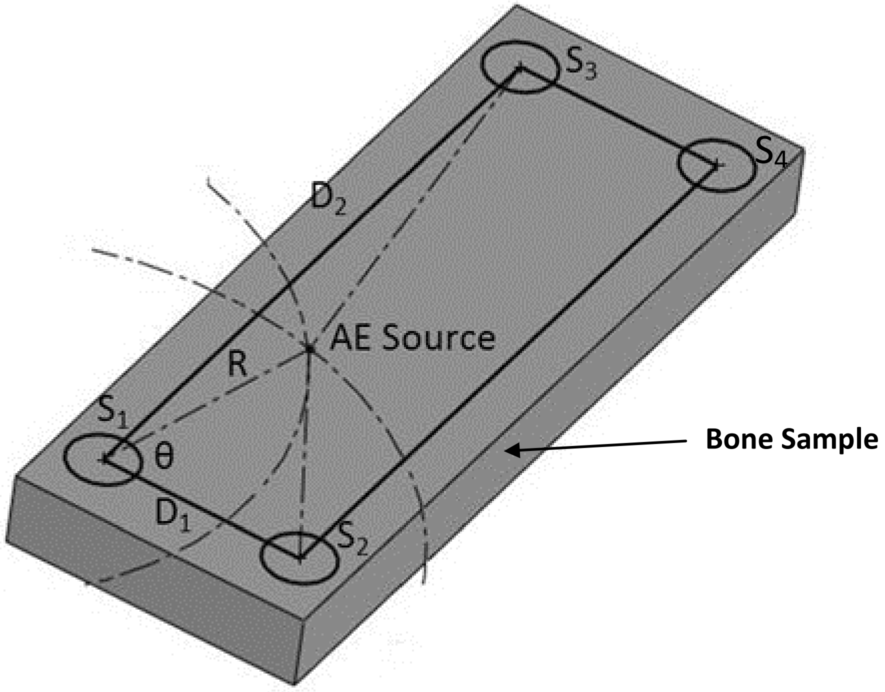

Fig. 6.3 The hyperbolic source location setup is implemented on a bone sample with the addition of a fourth sensor.

Next a third sensor S_3 is brought into the problem and this allows for a second time difference TDOA 3-1, as in Figure 5.9 The corresponding distance difference describes another hyperbola (H_2) on which the source must also lie. The intersection of the two hyperbolae is the AE source. Referring to Figure 6.3, two equations (Eq. (3) and Eq. (4) below) will be derived in terms of R_1 and θ.

$$R_1 - R_2 = t_1V_1 - t_2V_2 \tag{1}$$

so $R_1 = R_2 + (t_1V_1 - t_2V_2)$.

Hence $Z_{12} = R_1 \sin(\theta) = [R_2 + (t_1V_1 - t_2V_2)]\sin(\theta)$.

Considering the triangle with hypotenuse R_2 gives

${Z_{12}}^2 = {R_2}^2 - (D_{12} - R_1\cos(\theta))^2$. Thus

$$R_1{}^2\sin^2(\theta) = R_2{}^2 - \left(D_{12}{}^2 + R_1{}^2\cos^2(\theta) - 2D_{12}R_1\cos(\theta)\right)$$, so

$$R_1{}^2\sin^2(\theta) + R_1{}^2\cos^2(\theta) = R_2{}^2 - D_{12}{}^2 + 2D_{12}R_1\cos(\theta)$$ and hence

$$R_1{}^2 = R_2{}^2 - D_{12}{}^2 + 2D_{12}R_1\cos(\theta) \qquad (2)$$

Now Eq. (1) gives $R_2 = R_1 - (t_1V_1 - t_2V_2)$

So Eq. (2) implies

$$R_1{}^2 = [R_1 - (t_1V_1 - t_2V_2)]^2 - D_{12}{}^2 + 2D_{12}R_1\cos(\theta) \quad \Rightarrow$$

$$R_1{}^2 = R_1{}^2 + (t_1V_1 - t_2V_2)^2 - 2R_1(t_1V_1 - t_2V_2) - D_{12}{}^2 + 2D_{12}R_1\cos(\theta) \quad \Rightarrow$$

$$R_1[2(t_1V_1 - t_2V_2) - 2D_{12}\cos(\theta)] = (t_1V_1 - t_2V_2)^2 - D_{12}{}^2 \quad \Rightarrow$$

$$R_1 = \frac{(t_1V_1-t_2V_2)^2-D_{12}{}^2}{2(t_1V_1-t_2V_2)-2D_{12}\cos(\theta)} \qquad (3)$$

Similarly, considering R_1 and R_3 we can derive

$$R_1 = \frac{(t_1V_1-t_3V_3)^2-D_{13}{}^2}{2(t_1V_1-t_3V_3)-2D_{13}\cos(90°-\theta)} \qquad (4)$$

Note that Baron and Ying (1987) derived equations similar to Eq. (3) and Eq. (4), but under the assumption of constant velocity.

Now equate Eq. (3) and Eq. (4) to get

$$\frac{(t_1V_1 - t_2V_2)^2 - D_{12}{}^2}{2(t_1V_1 - t_2V_2) - 2D_{12}\cos(\theta)} = \frac{(t_1V_1 - t_3V_3)^2 - D_{13}{}^2}{2(t_1V_1 - t_3V_3) - 2D_{13}\cos(90° - \theta)}$$

Multiplying by 2 and taking reciprocals gives

$$\frac{(t_1V_1 - t_2V_2) - D_{12}\cos(\theta)}{(t_1V_1 - t_2V_2)^2 - {D_{12}}^2} = \frac{(t_1V_1 - t_3V_3) - D_{13}\cos(90° - \theta)}{(t_1V_1 - t_3V_3)^2 - {D_{13}}^2}$$

Next define

$$A = \frac{(t_1V_1 - t_2V_2)}{(t_1V_1 - t_2V_2)^2 - {D_{12}}^2}$$

$$B = \frac{D_{12}}{(t_1V_1 - t_2V_2)^2 - {D_{12}}^2}$$

$$C \ = \frac{(t_1V_1 - t_3V_3)}{(t_1V_1 - t_3V_3)^2 - {D_{13}}^2}$$

$$D = \frac{D_{13}}{(t_1V_1 - t_3V_3)^2 - {D_{13}}^2}$$

Hence

$$A - B\cos(\theta) = C - D\cos(90° - \theta)$$

So $$-B\cos(\theta) = C - A - D\cos(90° - \theta)$$

and therefore $$B\cos(\theta) = A - C + D\cos(\theta - 90°).$$

Thus $$B\cos(\theta) = A - C + D\,[\cos\theta\cos(90°) + \sin\theta\sin(90°)]$$

$$= A - C + D\sin(\theta)$$

which implies $$\cos(\theta) = \frac{A-C}{B} + \frac{D}{B}\sin(\theta).$$

Next define $\alpha = \frac{A-C}{B}$ and $\beta = \frac{D}{B}$ to get

$$\cos(\theta) = \alpha + \beta \sin(\theta)$$

and hence

$$\alpha + \beta \sin(\theta) - \cos(\theta) = 0 \tag{5}$$

θ can be found by solving Eq. (5) using the Newton-Raphson method and then subsequently R_1, X_S and Y_S can be calculated. Assuming constant velocity, $V_1 = V_2 = V_3$. The initial value used for θ in the Newton-Raphson method was 45°.

AE Wave Velocity

The velocity of the AE wave is a critical input variable of Hyperbolic Source Location algorithms. However as discussed earlier, bone is anisotropic meaning velocity value varies considerably depending on the direction the AE wave is propagating in relation to the bone orientation. First the AE velocity was measured along the long axis of the bone sample. This is the same direction as the long axis of the whole bone from which the sample is taken and will be termed the longitudinal velocity (LV). Then the velocity was measure across the bone sample and this velocity is called the transverse velocity (TV). As the direction of travel through the bone is not known in any give test until after the location has been computed neither the longitudinal nor the transverse velocities are very reliable. Some average of the two could give an approximation to the real velocity in all cases. A weighted mean of the two velocities was used. It was based on the ratio of the length (L) of the sample to the width (W) of the sample. As the bone sample is longer than it is wide, the velocity equation is weighted towards the longitudinal direction and is presented below.

$$V = \frac{\mathrm{L}(LV)+\mathrm{W}(TV)}{(\mathrm{L}+\mathrm{W})} \tag{6}$$

LV and TV were measured experimentally by creating an AE source at one end of the sample and measuring the time of arrival of the AE signal at two sensors placed at different distances along the line joining the two sensors and the AE source. A pencil lead break was used as the AE source. This involves breaking the 0.3 or 0.5 mm diameter 2H lead of a specially adapted pencil at the desired AE source position, Kalyanasundaram (2007) and Evans (1997). Then the time difference between the two TOA's at the two sensors is divided into the distance between them to give a velocity value. Both the LV and the TV velocity measurements were repeated 15 times for each sample to get a more reliable average for each sample.

Variable Velocity Model

The above algorithm assumes the AE signal velocity is constant for all locations and the weighted velocity value was used. However due to this value being an estimate of the true velocity value for any given path, there will be a certain level of error introduced. In an effort to avoid this source of error, a different velocity value is used in relation to the AE wave travelling from the source to each sensor. These velocity values are altered depending on the location coordinates. The variable velocity algorithm is conducted in the steps outlined below. In the first iteration of the algorithm, velocity values for each sensor are the same, but in subsequent iterations, velocities are different. In the equations that follow, “i” represents the iteration number the algorithm is currently executing. The value of the velocity in the first iteration is noted by “${}_0V$” and the subscripts after the variables represent the relevant sensor.

1. Set ${}_0V_1 = {}_0V_2 = {}_0V_3 = {}_0V$ where ${}_0V = \frac{D_{13}(LV)+D_{12}(TV)}{(D_{13}+D_{12})}$

2. Solve: $\frac{\left((TOA_1-TOA_2)\ {}_0V\right)^2-D_{12}{}^2}{2\left((TOA_1-TOA_2)\ {}_0V\right)-2D_{12}\cos(\theta)} = \frac{\left((TOA_1-TOA_3)\ {}_0V\right)^2-D_{13}{}^2}{2\left((TOA_1-TOA_3)\ {}_0V\right)-2D_{13}\cos(90°-\theta)}$ The Newton Raphson Method is used to get the first estimate of the location of the AE source (${}_0X_s$, ${}_0Y_s$).

3. Get velocities (${}_1V_1$, ${}_1V_2$, ${}_1V_3$) based on the first estimate (${}_0X_s$, ${}_0Y_s$) :

$$ {}_1V_1 = \frac{{}_0Y_S LV + {}_0X_S TV}{{}_0Y_S + {}_0X_S},\quad {}_1V_2 = \frac{\left({}_0Y_S\right)LV + \left(D_{12} - {}_0X_S\right)TV}{\left({}_0Y_S\right) + \left(D_{12} - {}_0X_S\right)},\qquad {}_1V_3 = \frac{\left(D_{13} - {}_0Y_S\right)LV + \left({}_0X_S\right)TV}{\left(D_{13} - {}_0Y_S\right) + \left({}_0X_S\right)} $$

4. Get the distances (R_1, R_2, R_3) from the estimated location of the source to each of the respective sensors

$R_1 = \sqrt{\left({}_0X_s - X_1\right)^2 + \left({}_0Y_s - Y_1\right)^2}$ (X_1, Y_1) are the coordinates for sensor 1

$R_2 = \sqrt{\left({}_0X_s - X_2\right)^2 + \left({}_0Y_s - Y_2\right)^2}$ (X_2, Y_2) are the coordinates for sensor 2

$R_3 = \sqrt{\left({}_0X_s - X_3\right)^2 + \left({}_0Y_s - Y_3\right)^2}$ (X_3, Y_3) are the coordinates for sensor 3

5. Get the times t_1, t_2, t_3 which the AE wave takes to reach the sensors based on the distances and the original velocity ${}_0V$.

   $t_1 = \frac{{}_0R_1}{{}_0V_1}$, $t_2 = \frac{{}_0R_2}{{}_0V_2}$, $t_3 = \frac{{}_0R_3}{{}_0V_3}$.

Let $i = 1$:

6. Solve $\frac{\left(t_1\ {}_iV_1 - t_2\ {}_iV_2\right)^2 - D_{12}{}^2}{2\left(t_1\ {}_iV_1 - t_2\ {}_iV_2\right) - 2D_{12}\cos(\theta)} = \frac{\left(t_1\ {}_iV_1 - t_3\ {}_iV_3\right)^2 - D_{13}{}^2}{2\left(t_1\ {}_iV_1 - t_3\ {}_iV_3\right) - 2D_{13}\cos(90° - \theta)}$ to get $({}_iX_s, {}_iY_s)$.

7. Find further improved velocity values:

   ${}_{i+1}V_1 = \frac{{}_iY_sLV + {}_iX_sTV}{{}_iY_s + {}_iX_s}$, ${}_{i+1}V_2 = \frac{\left({}_iY_s\right)LV + \left(D_{12} - {}_iX_s\right)TV}{\left({}_iY_s\right) + \left(D_{12} - {}_iX_s\right)}$, ${}_{i+1}V_3 = \frac{\left(D_{13} - {}_iY_s\right)LV + \left({}_iX_s\right)TV}{\left(D_{13} - {}_iY_s\right) + \left({}_iX_s\right)}$

8. Use these improved velocities to acquire a further improved source location $({}_{i+1}X_s, {}_{i+1}Y_s)$ using ${}_{i+1}V_1$, ${}_{i+1}V_2$, ${}_{i+1}V_3$ and t_1, t_2, t_3 .

9. Increment i. If $i < 20$ then go to Step 6. Otherwise stop. For each iteration use the latest velocities and always the same times t_1, t_2, ${}_1t_3$. Note that 20 iterations are conducted.

The aim of this algorithm is that the velocity values should converge to the correct values for the given input data. As a result the location coordinates should also converge to the correct values for the given input data.

AE Source Location using Four Sensors

The previous sections describe how source location is achieved with the use of three sensors arranged in a triangular shape. But the bone sample is in the shape of a rectangle, as in Figure 5.7. While the Hyperbolic Source Location technique will locate sources in the entire rectangle, it is reasonable to assume that its accuracy will diminish for locations near sensor three and particularly those near sensor four. To improve the accuracy of source location in these regions, a fourth sensor is added as shown in Figure 6.3. The Hyperbolic Source Location algorithm was designed to use data from three sensors. So to make use of this fourth sensor, it is first determined whether the source is closer to sensor 1 or sensor 3. If the source is closer to sensor 1 the source location algorithm is not altered in any way. However if the source is closer to sensor 3, the source location is determined from the point of view of sensor 4. In practice this involves using the TOA data from sensor 4, 3 and 2 instead of 1, 2 and 3. The distances D_{12} and D_{13} will remain the same. Some adjustments will also have to be made to compute the X and Y coordinates from the θ and R values. Otherwise the algorithm remains the same. The sensor closest to the source is determined by observing which TOA is the smallest.

Treatment of Outlier Locations

All located AE sources should ideally reside within the bone sample boundaries. If not, the location coordinates contain some sort of error. Small errors can be expected with any location algorithm, so if the computed location lies inside the sample boundaries it is reasonable to assume that the true location is somewhere in the vicinity of that computed location, however if the computed location is outside these boundaries, it is impossible to have any confidence as to where the true location lies. For this reason the computed locations that lie within or close to the sample boundaries are termed successful location attempts while those far outside the sample boundaries are termed failed location attempts. Note that the successful location attempts will contain some error. The sample boundaries are defined as: -2.5 mm < X < 17.5 mm and 2.5 mm < Y < 47.5 mm where the location of sensor 1 is treated as x = 0, y = 0.

6.1 Test 1 - Testing the Source Location Algorithm

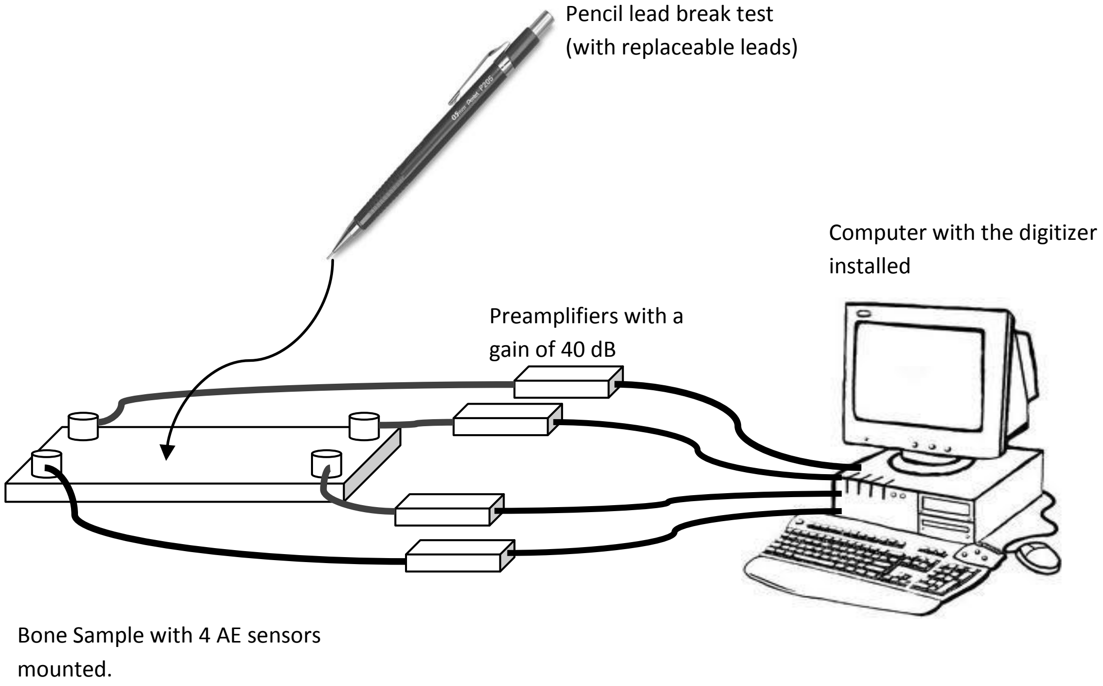

Fig. 6.4 Test 1 setup: a pencil lead break is used to create AE sources at any desired location on the bovine bone sample.

Four AE sensors were adhered onto the bone samples as presented in Figure 6.4 using super glue (UHU GmbH & Co.). The Frequency response of these sensors ranged from 100 to 900 kHz, refer to the Appendix for their calibration charts. The AE signals were amplified with 2/4/6 preamplifiers from (Physical Acoustics Corporation) by factor of 100 or 40 dB. The amplified AE signals were then fed into a digitizer (PXI 9846 from Adlink). Details of this AE system are given in *2 AE Instrumentation.* A threshold voltage level of 3 mV was used to determine when an AE hit was detected. This level was sufficiently high above the noise floor to avoid false triggers from noise spikes yet low enough to pick up small AE hits resulting from small microcracks. A software package known as NI LabVIEW was used acquire the AE signals and save them to disk in as text files. Then a separate LabVIEW program was written to analyse the waveforms and compute the source location. A copy of these LabVIEW programs can be located in the Appendix.

A pencil lead break was used to create AE sources at 24 evenly spaced locations on the top (periosteum) surface of each of the nine samples. The pencil lead break was repeated five times at each location. The TOA's and the weighted mean AE constant velocity specific to each sample was used to compute each AE source for each sample. Three sensor source location was first attempted on samples 1, 2, and 3. Next four sensor source location was attempted on all 9 samples. The constant velocity algorithm was employed for both tests.

Next the variable velocity model was tested using the data from all 9 samples and employing four sensors.

6.2 Test 2 - Predicting Final Fracture Location in Bone

In Test 1, a pencil lead break was used to simulate microcracks on bone samples and both constant and variable velocity hyperbolic source location were used to find the AE sources. Now the variable velocity source location algorithm is used to locate real microcracks and thus predict where final fracture will occur. To do this three bone samples from batch 2 are loaded in Three Point Bend tests which bends the sample gradually. As the bone sample bends, small microcracks occur and the location of these small microcracks should indicate where the final fracture will occur. The sample is loaded until it fractures and then the location of the final fracture location is compared with the located microcracks to see how well these microcracks predicted the location of the final fracture. The variable velocity location algorithm was used to find the microcracks in this Test. After the test the computed location of the microcracks can be compared to the actual fracture line to determine whether they predicted where the bone sample would fracture.

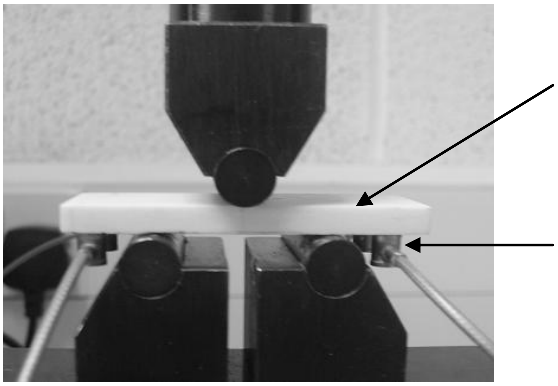

Bone sample with the AE sensors mounted on the surface of the sample that experiences tensile forces. This is also the outside surface of the bone (periosteum)

AE sensors

Fig. 6.5 Bovine bone sample loaded in Three Point Bend testing to induce microcracks and ultimately cause fracture

To determine the error between the computed location and the real location a quantity referred to as Distance Error is used. It takes into account both the X and Y errors. The Distance Error is the straight line distance between the point at which the AE source was actually created and where the algorithm computed it to be. The mean Distance Error is calculated according to equation below.

$$\frac{\sum_{i=1}^{n} D}{n} = \frac{\sum_{i}^{n}\left((X_{cal}-X_{act})^{2}+(Y_{cal}-Y_{act})^{2}\right)^{\frac{1}{2}}}{n} \tag{7}$$

Where:

D = distance error for one location attempt
cal = location calculated by the algorithm
act = the actual location where the AE source was created or known to have originated.
n = the sample number (in terms of location attempts in a test)

6.3 Test 1 Results

AE Velocity:

15 longitudinal and 15 transverse velocity measurements were conducted for each of the 9 samples. An Inter-quartile Range (IQR) Test was performed to determine outliers. The IQR test is commonly used in clinical studies to reject data points. Data more than 1.5 times the IQR above the third quartile or more than 1.5 times the IQR below the first quartile are regarded as outliers. The longitudinal velocity data (135 data values) had 10 outliers while the transverse velocity data (135 data values) had 33 outliers. These outlier data values were removed and Figures 6.6 show the results of the AE velocity testing. The Shapiro-Wilk test was used in SPSS to determine whether or not the data was normal. Several of the data sets were found to be non-normal, so medians and IQRs are reported rather than means and standard deviations. The median velocity values of 4030 m/s and 3165 m/s and IQRs of 113 m/s and 120 m/s were found for the Longitudinal and Transverse velocities respectively.

Source Location Algorithms:

The three sensor Constant Velocity algorithm yielded a median distance error of 1.89 mm (IQR 1.45 mm) across nine samples, as in Figure 6.7. When the four sensor approach was employed these results improved slightly to give a median distance error of 1.78 mm (IQR 1.51 mm) across nine samples, as in Figure 6.8. The number of failed locations was 10.2% for the three sensor approach, while it was 5.1% for the 4 sensor approach. Figure 6.9 shows the results from the Variable Velocity algorithm. It shows significant improvement in terms of the median distance error of 0.70 mm across the nine samples. Furthermore the IQR was 0.79 mm, considerably lower than with the Constant Velocity approach. The number of failed locations was much lower at 1.9%. The means and standard deviations may also be of interest: the four sensor Constant Velocity data has a mean error of 1.92 mm (standard deviation 1.29 mm) while the Variable Velocity data has a mean error of 1.04 mm (standard deviation 1.54 mm).

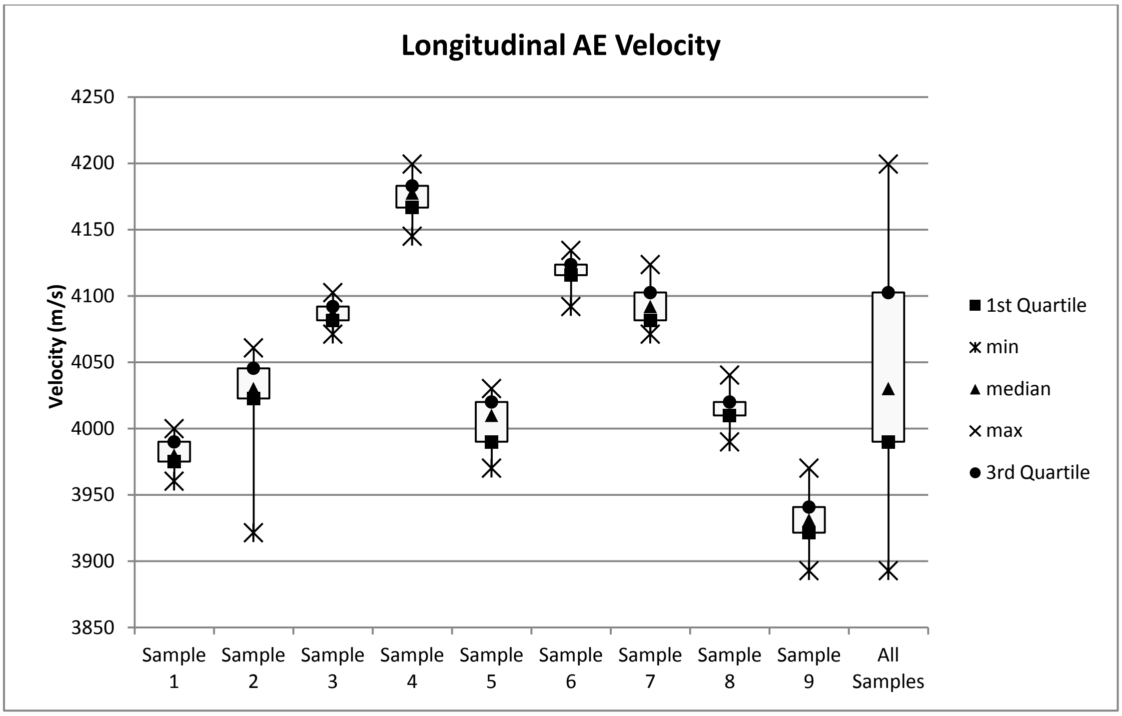

(A)

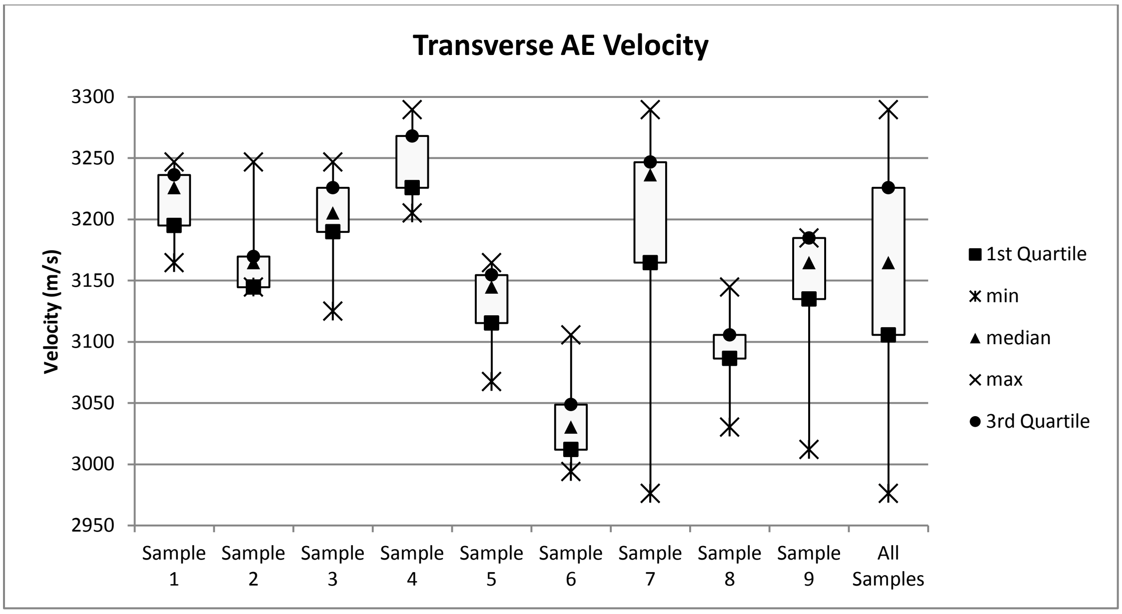

(B)

Fig. 6.6. (A) Longitudinal AE Velocity quartile analysis, after the outliers have been removed. (B) Transverse AE velocity quartile analysis, after the outliers have been removed.

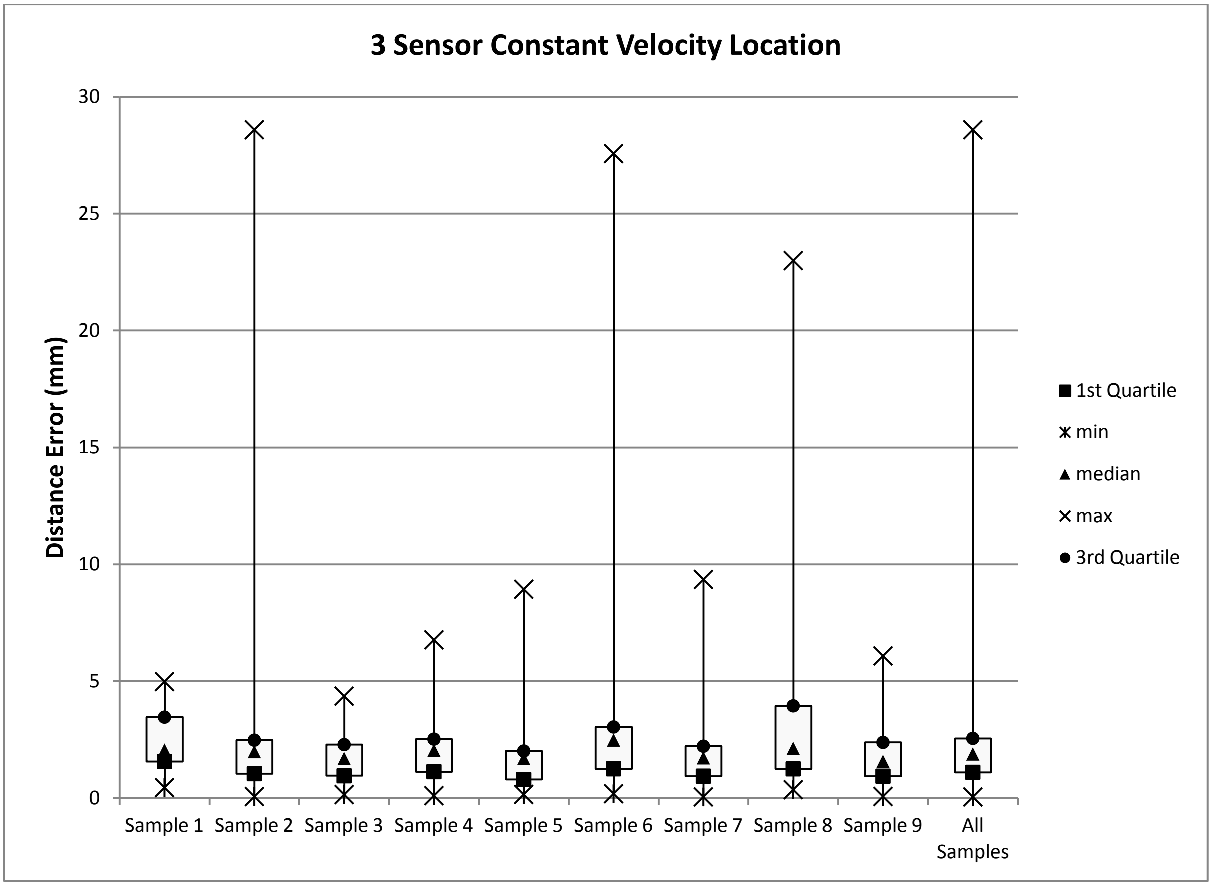

Fig. 6.7 The error analysis of three sensor constant velocity location showing the quartiles.

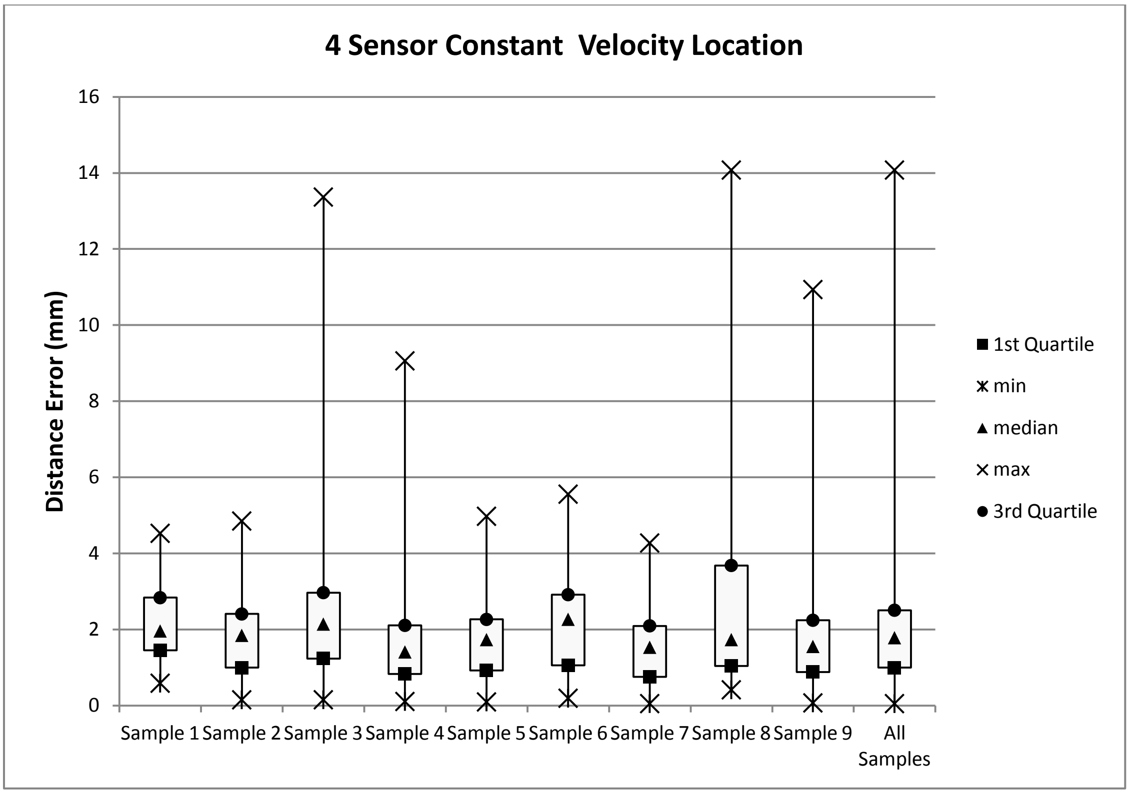

Fig. 6.8 The error analysis of four sensor constant velocity location showing the quartiles.

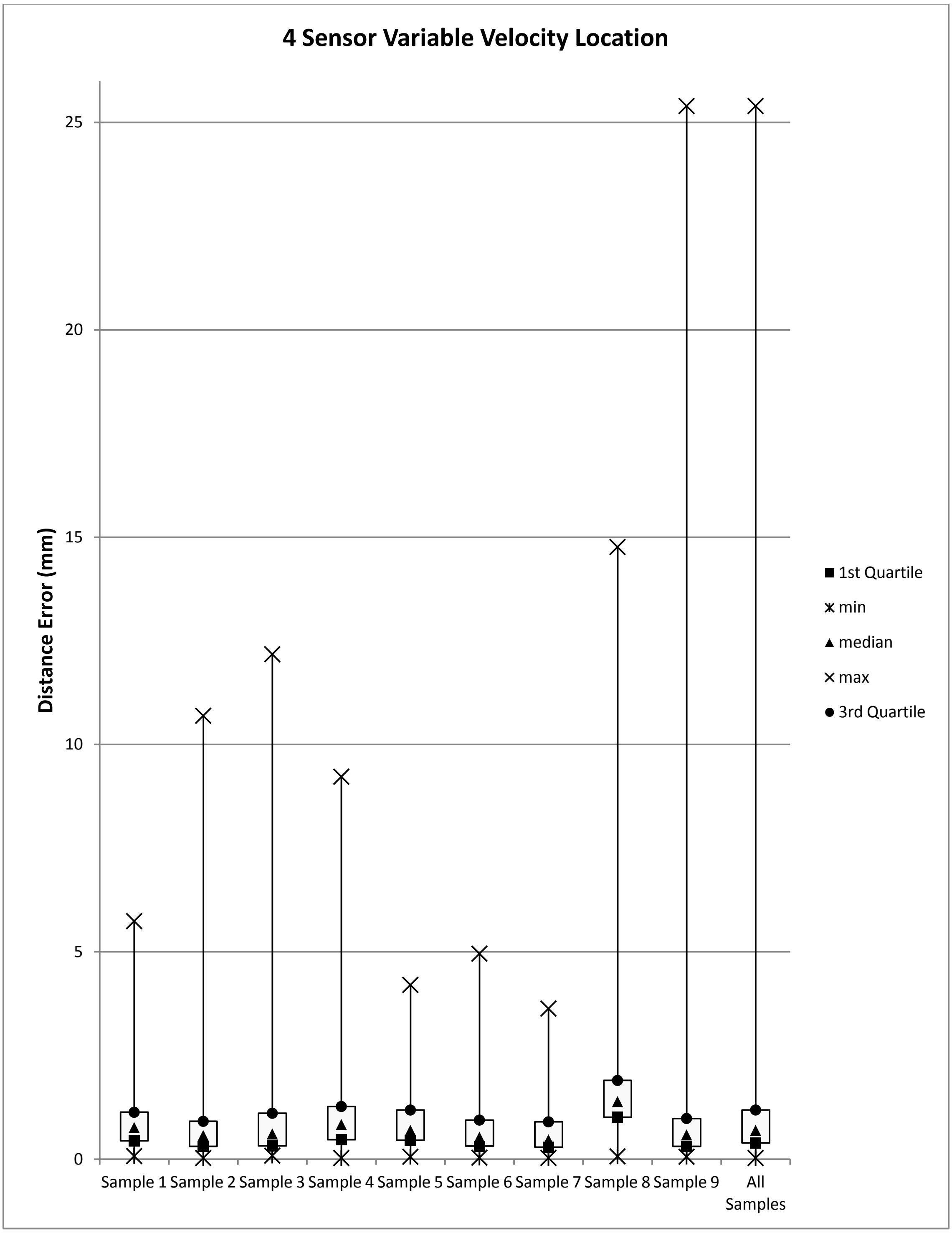

Fig. 6.9 The error analysis of four sensor variable velocity location showing the quartiles.

6.4 Test 2 Results

Figure 6.10 shows the computed microcrack locations as dots with their respective peak amplitudes. The solid black line represents the final fracture line on the compressive (upper) surface and the dashed black line represents the final fracture line on the tensile (lower) surface of the samples. The sensors are marked along with their coordinates. The support pins for the three point bend test are also indicated in Figure 6.10. Comparing the located microcracks which predict where the bone sample would fracture to where the bone actually fractures confirms a close correlation. Figure 6.11 shows the displacement of the middle point (y = 25 mm) of Sample 1 plotted against the amplitude of the AE hits. The final fracture event is signified by the AE hit with the peak amplitude of 1000 mV. The graph shows that many AE hits were detected before this and several of them were also located. While only Sample 1 was graphed, the other samples showed similar patterns.

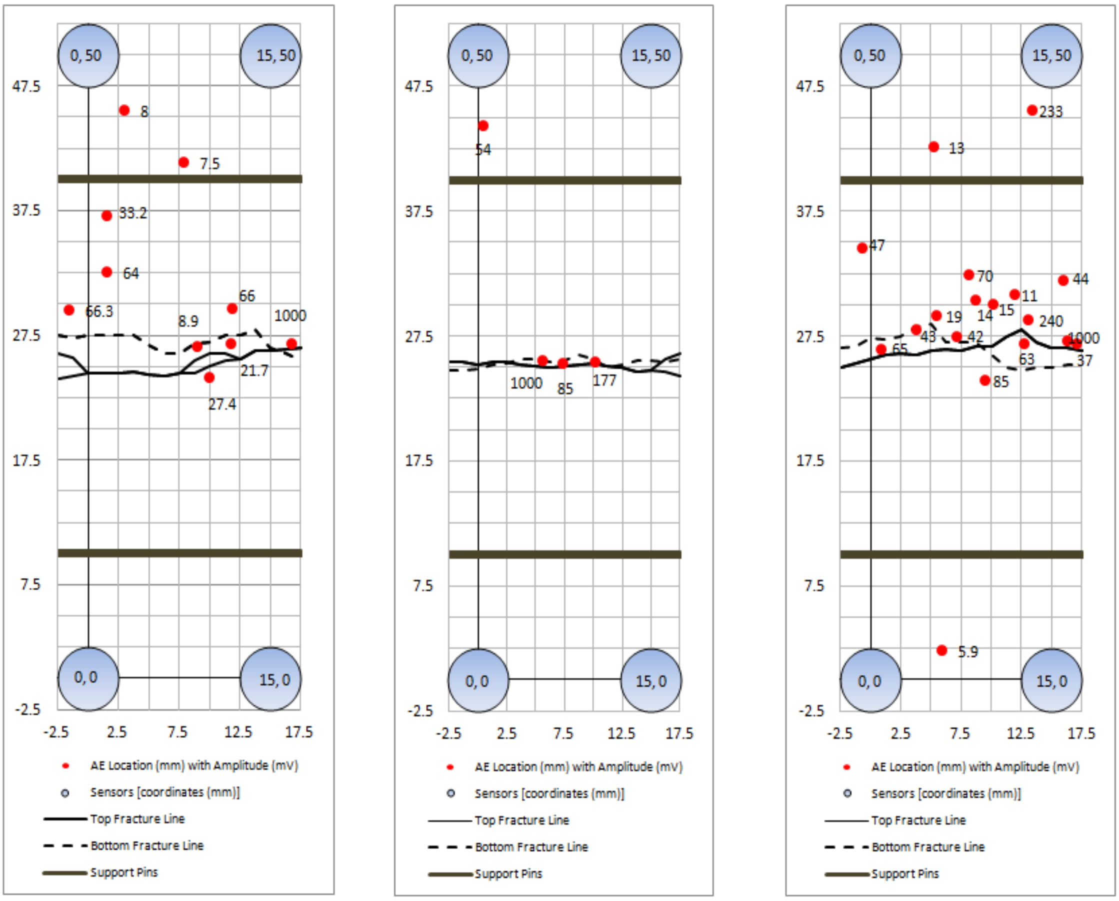

Fig. 6.10 Load induced microcrack source location on bone samples 1, 2 and 3 from left to right. The middle pin of the three point bend test is positioned at 25 mm on the vertical axis and is not shown as it would obscure other data.

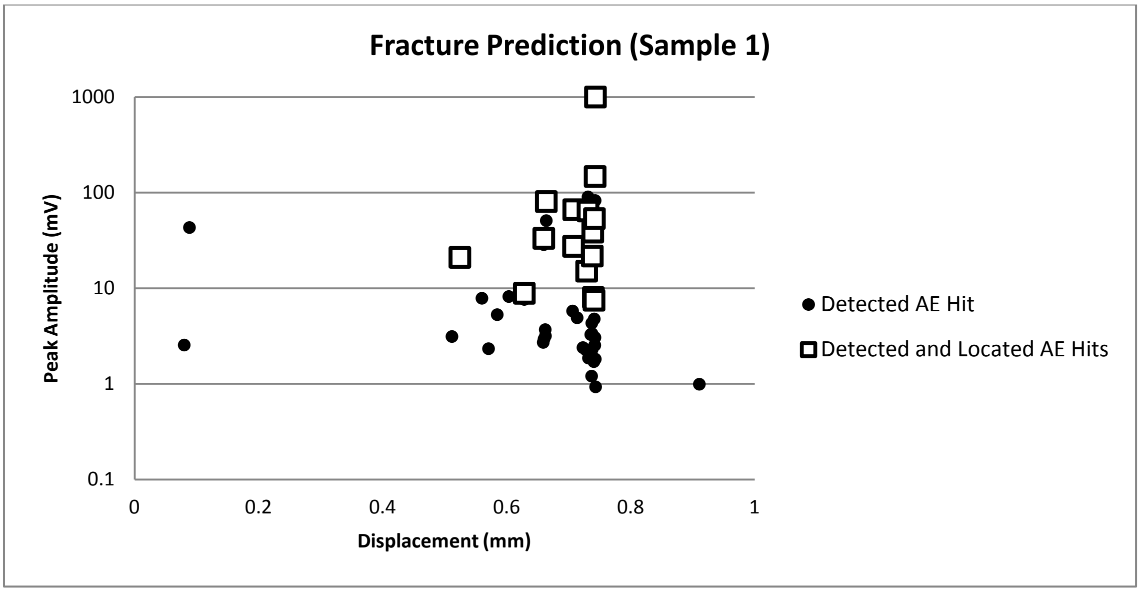

Fig. 6.11 The AE hits detected and located for sample 1 during the three point bend test. The plot shows that not alone are AE hits detected before the sample fractures but that some are also located, predicting the fracture location

6.5 Discussion

The AE velocity in bovine bone was found to be similar with what Kann et al. (1993) found in pig radii. This work shows AE velocity to be 27% greater in the longitudinal direction than in the transverse direction. Kann et al. (1993) reported ultrasound velocities to vary by 29%.

Although three sensor source location gave reasonably accurate localization, the results indicate that adding a fourth sensor does reduce the median error. However both algorithms used an estimated AE velocity value and not the real velocity values, meaning that a significant error still remained. The Variable Velocity algorithm addressed this shortcoming by iteratively converging on the best mix of longitudinal and transverse velocity values for each wave path. This gave a significantly improved median error, IQR and number of failed locations. Levene's homogeneity of variance test was conducted in SPSS and indicates that the variances are not equal for the four sensor Constant Velocity data and the Variable Velocity data. A t-test was conducted and indicates a significant (p=0.05) difference in the mean errors. Using the median or the mean as the measure of centrality shows that the error is reduced in the Variable Velocity model compared with the 4 sensor Constant Velocity model. Measuring the dispersion of the data is more complicated: if the standard deviation is used to measure dispersion then the Variable Velocity data is more dispersed, whereas if the IQR is used to measure dispersion (this is the better measure for this non-normal data) then the dispersion is reduced for the Variable Velocity model compared with the 4 sensor Constant Velocity model.

In Test 2, most of the located AE hits were found to lie close to or on the measured fracture lines confirming that the algorithm can locate real microcracks as well as pencil lead break AE sources. The few AE sources located far from the fracture lines have two possible explanations. Firstly, these are microcracks that did occur, but did not propagate to final fracture at that location, or secondly, errors in the TOA input data caused incorrect source location. While friction between the three point bend supports and the bone may have accounted for some of the smaller AE hits increasing the threshold for an acceptable AE source location from 3 mV to 7mV should minimise this source of AE. Furthermore very little if any friction would be experienced at the middle pin as the sample does not move relative to it.

Figure 6.11 shows that some AE hits were successfully located before the sample fractured confirming that the source location algorithm can predict where fracture will occur before the fracture event happens.

7. Regression Source Location Algorithm

7.1 Regression

Regression can be used to predict the value of a variable given the value of another variable. A regression equation is used to do this prediction and the predictor variable is substituted into the regression equation to give the value of the predicted variable. In order to develop the regression equation, data must be collected. So a number of values for the predictor variable are collected and a number of values for the predicted variable are collected. The regression equation is formed and then when given new values of the predictor variable the regression equation will produce values for the predicted variable.

TDOA label	Description
TDOA 1-2	TOA at sensor 1 – TOA at sensor 2
TDOA 3-4	TOA at sensor 3 – TOA at sensor 4
TDOA 1-3	TOA at sensor 1 – TOA at sensor 3
TDOA 2-4	TOA at sensor 2 – TOA at sensor 4
TDOA 2-3	TOA at sensor 2 – TOA at sensor 3
TDOA 1-4	TOA at sensor 1 – TOA at sensor 4

Table 7.1 A list of possible predictor variables for the regression equations to predict AE source location.

In the AE source location problem, the X and Y coordinates of the located AE source are the predicted variables. The TOA at respective sensors could be the predictor variables but the TOA at the sensor closest the source would have a TOA of zero. A better predictor variable would be the difference between arrival times at two sensors – TDOA. Using four sensors at the four corners of the bone sample, there are six possible TDOA's. Figure 7.1 shows the layout of the sensors on the bone sample and Table 7.1 lists the six possible TDOA's.

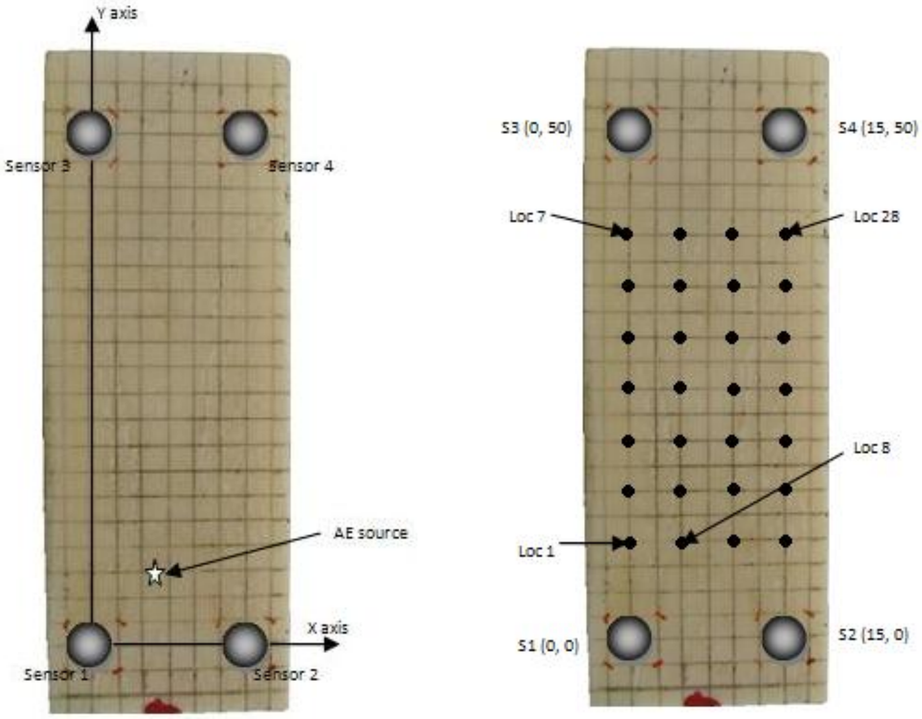

(A) **(B)**

Fig. 7.1 (A) shows the locations of the 4 AE sensors in relation to the X and Y axis. (B) shows the 24 evenly spaced locations where at the artificial AE sources are created as training data to build the regression equations. Several locations are indicated for later reference.

The next step is to determine which TDOA's can be used to predict the X coordinate, and which can be used to predict the Y coordinate. When an AE signal is produced at the AE source in Figure 7.1, the AE signal will take more time to reach sensor 2 than sensor 1. So the TDOA(1-2) will give a negative value. Now if the AE source occurred further to the right but still closer to sensor 1 than sensor 2 the TDOA(1-2) will give a lower magnitude negative value. At exactly halfway between both sensors the TDOA(1-2) will give a zero value (assuming isotropy) and closer to sensor 2 a positive value. So as the X coordinate of the AE source moves from sensor 1 to sensor 2, the TDOA(1-2) will change gradually from a maximum negative value to zero and finally to maximum positive value. It is easy to see that TDOA(1-2) would be a good predictor for the X coordinate. The same would apply to TDOA(3-4) but what about TDOA(1-3). As the X coordinate of the AE source moves left (X increases) the time to reach the sensors would change but the difference between the two TOA‘s would remain the same. This means that TDOA(1-3) would not be useful to predict the X coordinate. However TDOA(1-3) would be useful to predict the Y coordinate because as the AE source moves along the Y axis the TDOA(1-3) changes from a negative value, to a smaller negative value, to zero and then to a positive value. Similarly TDOA(2-4) would be useful to predict the Y coordinate. While TDOA(2-3) and TDOA(1-4) should be somewhat useful in predicting both the X coordinate and the Y coordinate, they provide no real additional value as they are dependent on the other four predictors. Since more than one TDOA is used to predict each of the coordinates, the regression is called multiple regression.

In order to develop the regression equations data needs to be collected. Artificial AE sources are created at known locations across the surface of the sample. A pencil lead break (HSU-Nielsen Source) is used to create these sources (Kalyanasundaram et al. 2007; Evans 1997). A grid is created on the bone sample using a fine tip pencil as can be seen in Figure 7.1. The reference point of the grid (0, 0) is fixed to the coordinates of sensor 1. AE sources are created at selected nodes on the grid as shown in Figure 7.1B. Each grid square has a side length of 2.5mm. So the first location (Loc 1) has coordinates (0, 10). For each AE source created the TOA of the AE signal is recorded at each of the 4 sensors. The TOA’s are subtracted to produce TDOA’s as in Table 7.1. The predicted variables are the location coordinates X and Y. The TDOA’s are the predictors. Next a scatter plot is drawn to show how well each of the TDOA's predicts their respective coordinates. Then the errors are examined to identify outliers that may be affecting the accuracy of the regression equation. When a sufficient number of the more extreme outliers have been removed the data can be regarded as accurate. Outliers here are due to experimental errors. To verify this, the regression equations are tested on new data and if they perform better, then the hypothesis that the outliers were due to experimental errors is confirmed.

7.2 Test 1 – Developing the Regression Equations

The set of nine bovine bone samples from batch 1 were used in this Test and they were called training samples as the data collected from them were used to train or develop the regression equations. They were the same samples as used with the Hyperbolic algorithm in chapter 6. Super glue (UHU GmbH & Co. KG, Buhl, Germany) was used to attach the sensors onto their locations as shown in Figure 7.1. A pencil lead break was used to create an AE source at each of the locations shown in Figure 7.1. As with hyperbolic algorithm, the PXI 9846 digitizer programmed with LabVIEW was used to acquire the AE data, compute the TOA at each of the four sensors and save to text files. The AE source was repeated 5 times at each location to minimise the effect of experimental errors. There were a total of 1,260 AE sources executed across the 9 samples. Microsoft Excel was used to analyse the data. The first step was to calculate the TDOA's by subtracting the TOA's.

To visually confirm that there was a relationship between the X and Y coordinates and their respective predictors, scatter plots of the coordinate against the relevant predictor variables were produced in Excel. Figure 7.2 shows that as the X coordinate of the AE source increased from 0mm to 15mm, the TDOA between sensor

1 and 2 and between sensor 3 and 4 increased from approximately -2µs to + 2µs with a few outliers. A positive correlation was evident in the plot. Similarly in Figure 7.3 as the Y coordinates increased from 10 mm to 40 mm, the TDOA between sensors 1 and 3 and between sensors 2 and 4 increased from approximately -7µs to +7µs (excepting a few outliers). Again the data shows a positive correlation. Data from sample one only was plotted for the sake of clarity, but similar relationships were found across all samples.

While these two plots indicated that there was a relationship between the TDOA's and the location coordinates, it is difficult to see how strong these relationships are. A numerical value determining how well the TDOA's predict the location coordinates would be useful. Regression analysis provides such a number. It is R^2 in simple regression and Adjusted R^2 in multiple regression. Regression analysis was performed in Excel and it returned an Adjusted R^2 of 0.21 and 0.70 for the X and Y coordinate respectively. These values confirm the relationships observed but also that the relationship between the Y coordinate and its respective predictors is much stronger than the relationship between the X coordinate and its respective predictors. The regression equation was constructed using the Intercept (a constant), and two coefficients – a coefficient for each predictor variable. The regression analysis tool in Excel also produced these. The regression equations produced for the X and Y coordinates were:

$$X = 7.17 + 365{,}884*(TDOA1\text{-}2) + 428{,}008*(TDOA3\text{-}4) \quad (1)$$

$$Y = 24.68 + 510{,}315*(TDOA1\text{-}3) + 510{,}315*(TDOA2\text{-}4) \quad (2)$$

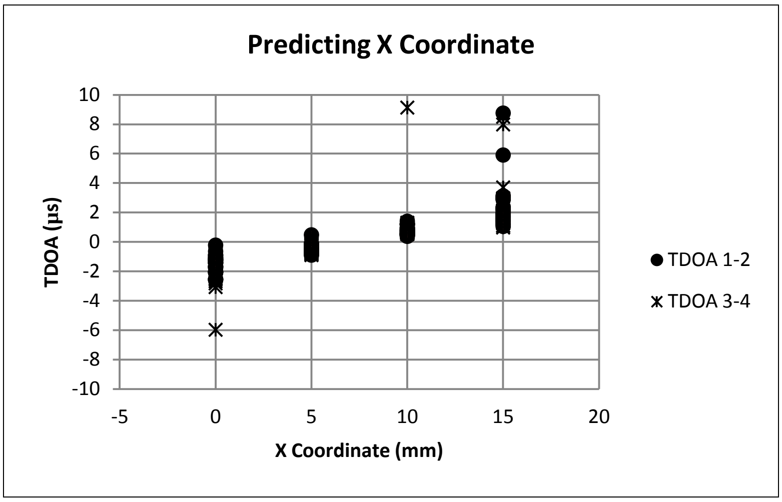

Fig. 7.2 Scatter plot showing how the X coordinate is related to TDOA 1-2 and TDOA 3-4 (sample 1 data).

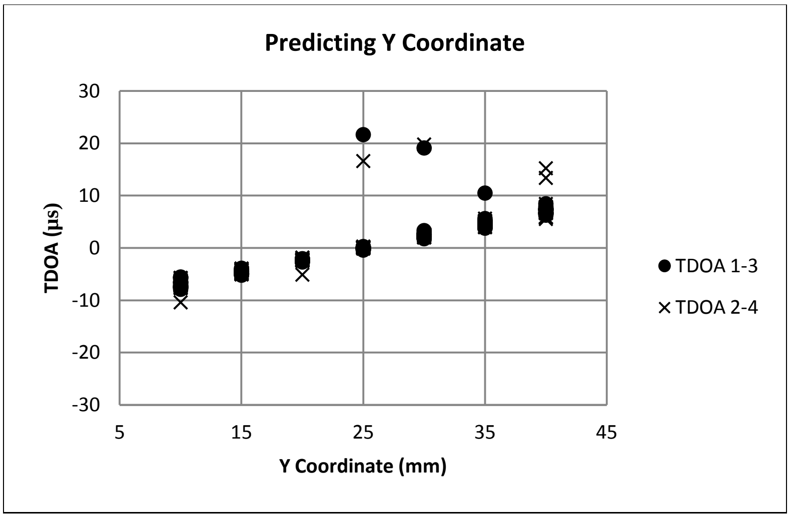

Fig. 7.3 Scatter plot showing how the Y coordinate is related to TDOA 1-3 and TDOA 2-4 (sample 1 data).

Based on the Adjusted R^2 the regression equation for the Y coordinate should perform well while the regression equation for the X coordinate should perform poorly. To understand the actual accuracy of these regression equations a simple test was undertaken. Equations (1) and (2) were used in Excel to compute the actual locations they were modeled on. The absolute error between the location coordinate where the pencil lead break was executed, and the location coordinate predicted by the regression equation gave an indication of the performance of the regression equations. When tested on the complete set of training data, the mean of the absolute X errors was 4.21mm and the mean of the absolute Y errors was 3.68mm. The differences in the observed mean errors reflect the Adjusted R^2 of each regression analysis. Given the surface dimensions of the bone sample (60mm by 20mm), a mean error of up to 4.21mm indicates a poor location accuracy.

A few outliers were observed (Figures 7.2 and 7.3). As was previously proposed, discarding these should improve the regression relationships and tests will be conducted on new data to confirm this approach. Deleting the outliers presented in the scatter graphs (Figures 7.2 and 7.3) would be tedious and not a very precise process. So the absolute values of the test errors were plotted and the data points which had an error larger than the main group of data were deleted. The X and Y errors were plotted on scatter plots – Figures 7.4 and 7.5 (data from sample 1 shown). The magnitude of most of the errors was less than 8mm in each plot so all TDOA's and their respective location coordinates with errors greater than or equal to 8mm were deleted from the data set. Regression analysis was then carried out on the remaining data. The new Adjusted R^2 was 0.73 and 0.97 for the X coordinate and the Y coordinate respectively. Using the new regression equations the mean absolute X error and the mean absolute Y error was recalculated giving 1.84 mm and 0.77 mm respectively. While this is a significant improvement, when the errors were examined again it was possible to remove some more outliers.

New plots of the absolute X errors and the absolute Y errors were produced in Figures 7.6 and 7.7 (data from sample 1 shown) respectively. All absolute X errors greater than 5mm and all absolute Y errors greater than 2mm were classified as not helpful in the regression equations. So the related data was deleted. The regression analysis was redone. The new Adjusted R^2 was 0.968 and 0.997 for the X and Y coordinates respectively and the new regression equations were:

$$X = 6.63 + 2{,}132{,}552 * (TDOA1\text{-}2) + 2{,}176{,}893 * (TDOA3\text{-}4) \qquad (3)$$

$$Y = 24.93 + 1{,}182{,}049 * (TDOA1\text{-}3) + 995{,}881 * (TDOA2\text{-}4) \qquad (4)$$

The new mean absolute X error was 0.68mm and the new mean absolute Y error was 0.37mm. This was a much improved performance. With this mean absolute error the user could expect the true location to be within 1 mm of the predicted location. While this process of removing the outliers could be repeated for further iterations, there is a risk that too much data would be lost, compromising the regression equations. It turned out that data pertaining to 79 source locations were deleted as outliers. That is 6.27% of the total 1,260 source locations.

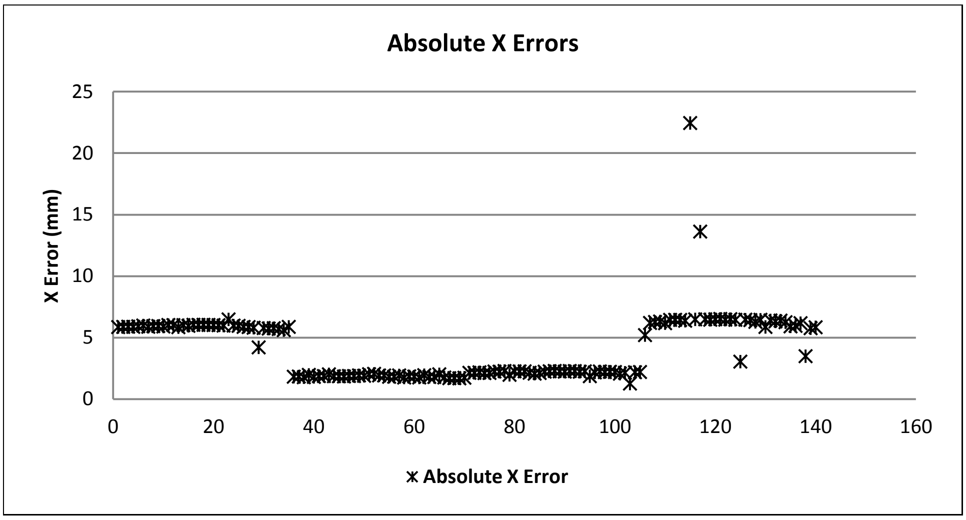

Fig. 7.4. X error analysis – data from sample 1. Any outlier with an error greater than 8 mm was removed from the data set.

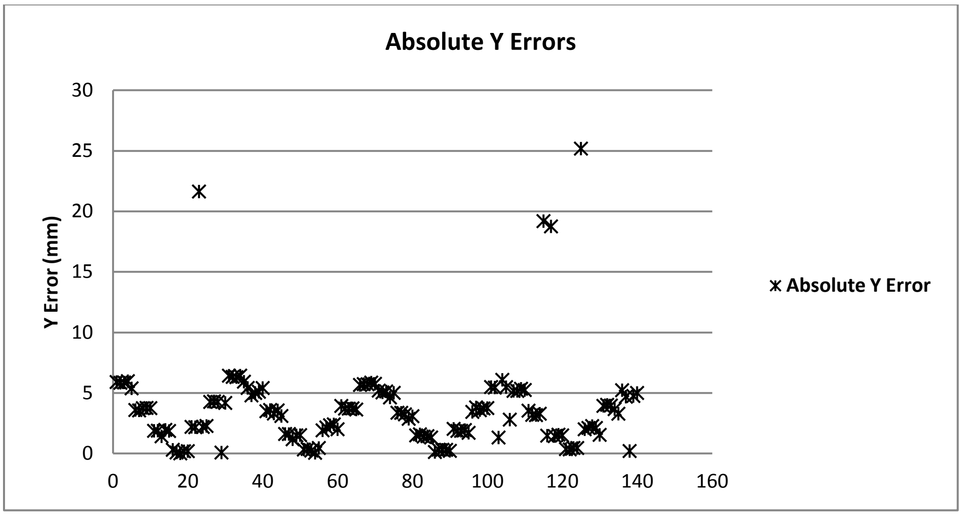

Fig.7.5 Y error analysis – data from sample 1. Any outlier with an error greater than 8 mm was removed from the data set.

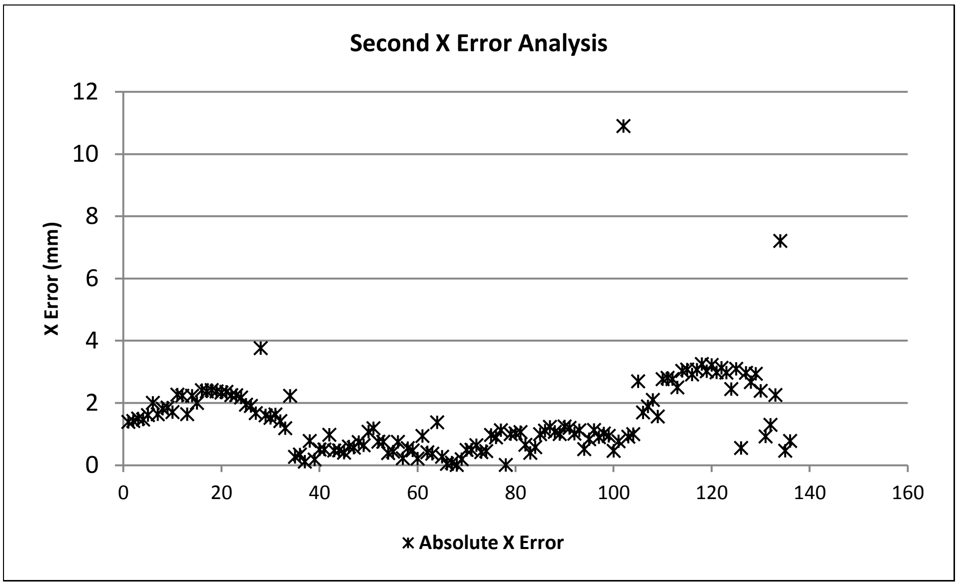

Fig. 7.6 X error analysis with first round of outliers removed – data from sample 1.

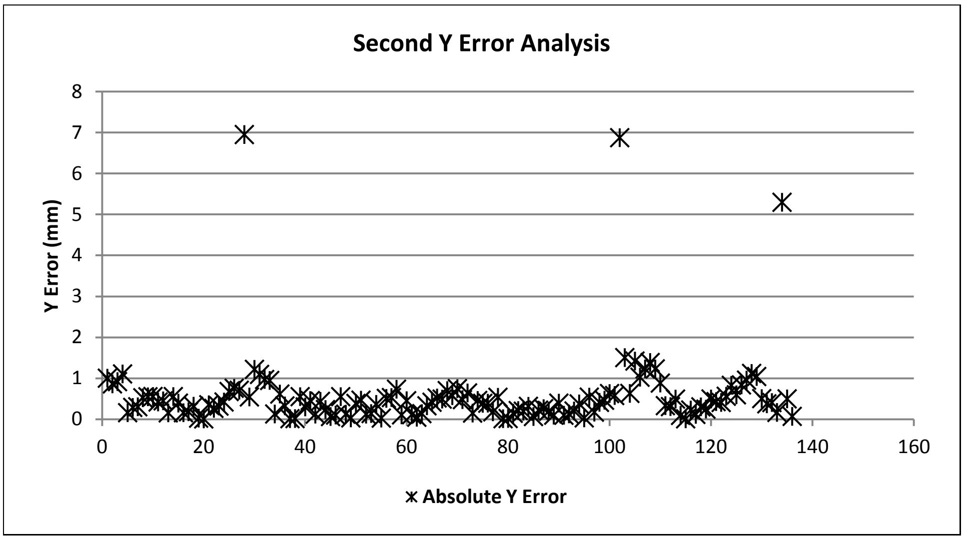

Fig. 7.7 Y Error analysis with first round of outliers removed – data from sample 1.

7.3 Test 2 – Testing the Regression Equations on New Samples

This Test involves testing the regression equations on three new samples (test samples). These were taken from batch 2 as described in section 5.2 preparing Bovine Bone Samples for AE Source Location. As in Test 1, AE sources were created with pencil lead breaks, the AE waveforms were acquired and the TOA's computed using the PXI 9846 with LabVIEW. A separate LabVIEW programme, Regression Source Location.vi, was written by the author, which used the regression Equations (3) and (4) to compute the source location when TOA data is input. This LabVIEW program is included in the Appendix. Two sets of locations were tested. One set used the same pencil lead break locations as the training samples – training locations. The second set of pencil lead break locations used, were interspersed between the training locations and called test locations. The average error of both sets gave a good indication of the expected error in any random location attempt on these type of samples. Figure 7.8A shows the training locations and Figure 7.8B shows the test locations used in this Test. Firstly, AE sources were created at each of the training locations. Then AE sources were created at each of the test locations. This gave two data sets for each of the three samples. The predicted X and Y coordinates were compared with the actual coordinates of X and Y to compute the errors.

Incorrect input data can introduce large errors in the location coordinates and these errors are not due to the failings of the source location algorithm. In an effort to more fairly quantify the accuracy of the algorithm all location outcomes were classified as either successful or failed. The successful outcomes would have a certain level of error but fall within the sample boundaries. Failed location outcomes are those which fall outside the sample boundary. All error statistics were calculated with the successful locations only. The sample boundaries used were: -5 < X <20mm and 0 < Y < 50mm with reference to Figure 7.8B.

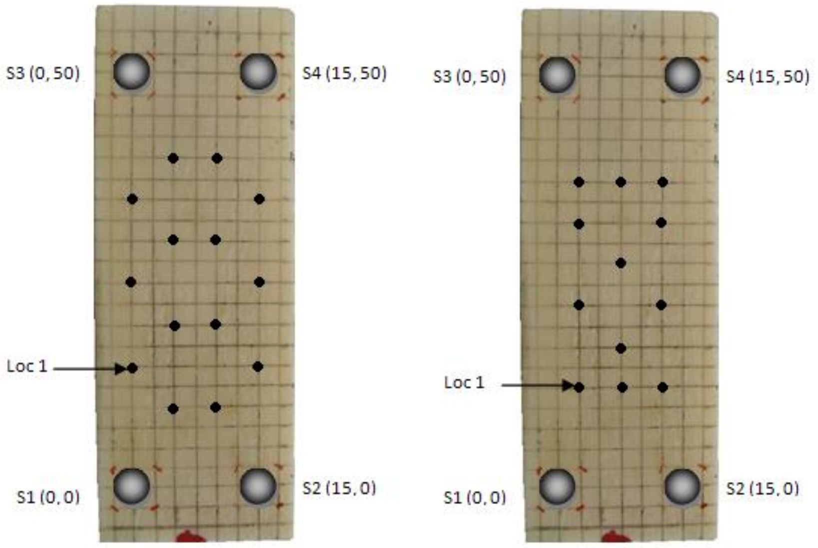

(A) **(B)**

Fig. 7.8 (A) shows the training locations. Notice these are the same as were used on Batch 1 samples (training data) (B) shows the test locations. These are interspersed between the training sample locations and are designed to test the ability of the regression to interpolate between the points at which it was modeled.

7.4 Test 3 – Locating Load Induced Cracks

As with the Hyperbolic Source Location algorithm the goal is to locate real cracks in bone samples and this is done by locating the source of the AE signal emanating from these cracks. So far the regression equations are tested on artificial AE sources – pencil lead breaks. This is very useful as this type of AE is similar to the AE from a real crack with the added benefit of the amplitude of the pencil lead breaks being relatively consistent. Furthermore sources can be created on demand at any desired location which is essential for building regression equations. However the AE produced by real cracks are somewhat different. They can be so small as to just rise above the threshold and indeed be completely obscured by noise or alternatively be large enough to saturate the instrumentation. Because of this variation in amplitude the TOA could be slightly different for different sized AE hits.

For these reasons this Test aims to test the Regression Source Location technique with the detection and location of actual microcracks. The Test Samples from batch 2 were loaded in three point bend tests with a slow cross head speed until they fractured. During the test the TOA of the AE signal from each detected AE event was recorded at each of the four AE sensors. Subsequent to the test, TDOA's were computed and these TDOA's entered into the regression equations developed in Test 1 to give predicted X and Y coordinates. The location of the actual fracture line was then compared to the predicted crack locations to determine how well the located cracks predicted the fracture line. A Material Testing Machine was used to load the samples. The cross head speed was set to 0.2 mm/minute up to an applied force of 1000 N and then the speed was reduced to 0.1 mm/minute until the samples fractured.

As with first regression Test the PXI 9846 with LabVIEW was used to acquire the AE waveforms and compute the TOA's. As in Test 1, the LabVIEW programme Regression Source Location.vi was used to find the location of each AE source. At the point of fracture both the Materials Testing Machine and the AE system (PXI 9846) were stopped manually. As can be seen in Figure 7.9 the bone sample was positioned so that the ideal fracture line is halfway along the long dimension of the bone sample at Y = 25 mm. The regression equations only work when the acoustic signal is detected at all four sensors. The threshold level used to determine when the AE signal has arrived is 2 mV. To ensure that the first arrived wave (or as close as possible to the first arrived wave) is detected and not just the peak amplitude, a minimum peak amplitude of 7 mV is required. So in this Test a successful location is only accepted when the peak amplitude of the AE waveform is at least 7 mV at all four sensors and the computed location falls within the sample boundaries. These boundaries are the same as those used in Test 2: -5 < X < 20 mm and 0 < Y < 50 mm. The time from the first successfully located AE event to the last is also recorded. This allows the fracture to be plotted in time.

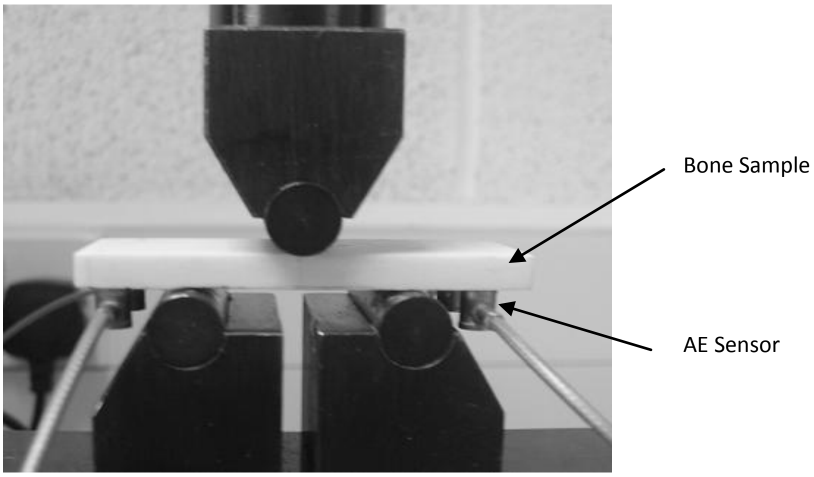

Fig. 7.9 Samples loaded in three point bending.

7.5 Results

Test 1

Nine bovine bone samples were tested in this Test. That gives 1,260 AE sources on all nine samples of which 6.27% (79) were not used in the final regression equations because they were removed as outliers. A mean absolute distance error across the 9 samples of 0.83mm, standard deviation 0.74mm was achieved. Considering that the bone samples were 60mm long, 22mm wide and 5.5mm thick this is a very good result. The mean of the absolute distances errors were calculated according to Equation (5).

$$\frac{\sum_{i=1}^{n} D}{n} = \frac{\sum_{i}^{n}\left((X_{cal}-X_{act})^2 + (Y_{cal}-Y_{act})^2\right)^{\frac{1}{2}}}{n} \tag{5}$$

Where:

D = distance error for one location attempt
cal = location calculated by the algorithm
act = the actual location where the AE source was created or known to have originated.
n = the sample number (in terms of location attempts in a test)

Table 7.2 shows that the mean absolute Y error (0.37mm) was much smaller than the mean absolute X error (0.68mm). A suggested reason for this discrepancy is that there were 7 values of Y used to build the Y regression equation while only 4 values of X were used to build the X regression equation. Given the size and shape of the bone sample it was impractical to take more values for the X value. Another consideration to be taken from these results is that each AE source was created by hand meaning that the execution of the actual AE sources introduced some error. It is quite possible that on occasion, this error could be as large as the mean location error.

Training Samples (1 through 9)	
Mean of Absolute X Errors (mm)	0.68
Mean of Absolute Y Errors (mm)	0.37
Mean of Absolute Distance Errors (mm)	0.83
Standard Deviation of the Absolute Distance Errors (mm)	0.74
Percentage of AE sources discarded as outliers (%)	6.27

Table 7.2 Testing regression equations on the AE data used to develop them (Training Samples).

Test 2

Three new bone samples were tested in this Test. The regression equations (3) and (4) developed in Test 1 were used. Two sets of AE locations were tested. One set are called the training locations and are the same locations as those used in Test 1. The other set are interspersed between the training locations and are called test locations. A mean absolute distance error, across the 3 Test Samples, of 1.15mm (Table 7.4) was achieved for the training locations, while the test locations gave a mean absolute distance error of 1.03mm (Table 7.4). These results indicate that regression equations can work with samples other than those they were modelled on and at locations other than those at which it was modelled on. In contrast to Test 1, this Test yielded very similar mean absolute X and Y errors (Table 7.3).

As the three Test Samples were harvested from three different bovine breeds, it can be seen that the regression equations are able to locate AE sources on the bone of a variety of different bovine breeds. This suggests some robustness in the regression equations which would be useful in a practical application. It must be noted however that all samples were taken from the mid diaphysis of bovine femora. Samples taken from different parts of a femur or indeed different bovine bones may exhibit different acoustic characteristics and thus these regressions equations may not perform as well.

Test Samples	Sample 1	Sample2	Sample3	3 Sample Mean
Mean of Absolute X Errors (mm)	0.62	0.71	0.75	0.69
Mean of Absolute Y Errors (mm)	0.70	0.71	0.79	0.71
Mean of Absolute Distance Errors (mm)	1.02	1.11	1.16	1.10
Standard Deviation of Absolute Distance Errors (mm)	0.76	1.23	1.24	1.03
Failed Location as a Percentage of Total Locations (%)	6.15	3.08	4.62	4.62

Table 7.3 Testing regression equations on new bone samples.

Test Samples	Sample 1	Sample2	Sample3	3 Sample Mean
Training Locations:				
Mean of Absolute Distance Errors (mm)	1.10	1.17	1.19	1.15
Test Locations:				
Mean of Absolute Distance Errors (mm)	0.92	1.04	1.12	1.03

Table 7.4 Testing regression equations on new bone samples separated into training locations and test locations.

Test 3

The same three Test Samples used in Test 2 were used in this Test. As can be seen in Figure 7.10 the AE sources produced by the regression equations were superimposed on an image of a bone sample. The actual fracture line of the sample is also superimposed on the image. The solid line is the top fracture line and broken line is the bottom fracture line. This gives a clear view of how well the located microcracks correlate with the actual fracture line. As can be seen there is a good spatial correlation in each case. Some of the located sources of AE that are not very close to the fracture line may still be caused by a microcrack as not all microcracking zones lead to fracture. In each case the largest amplitude AE event is the actual sample fracture event. Since the AE acquisition system also recorded the amplitude of the recorded AE events, this largest AE event could be checked to see how close it was situated to the fracture line. These are marked with an arrow on Figure 7.10 and in each case are on the fracture line.

The time between the first successfully located AE event, (microcrack), to the largest AE event (bone fracture) was recorded. This time was over 2 minutes in the case of sample 1 and 2. In Sample 3 the largest amplitude event happened early on. It was actually the second successfully located AE event and it occurred 30.52 seconds after the first located AE event. While the largest amplitude AE event happened early on, the sample did not fully fracture until over 2 minutes after the first located AE event. These results indicate that this Regression Source Location Algorithm can be used to determine where a fracture will take place on a bone sample well before the event actually occurs. It must be noted however that this time is very dependent on the rate at which the sample is loaded.

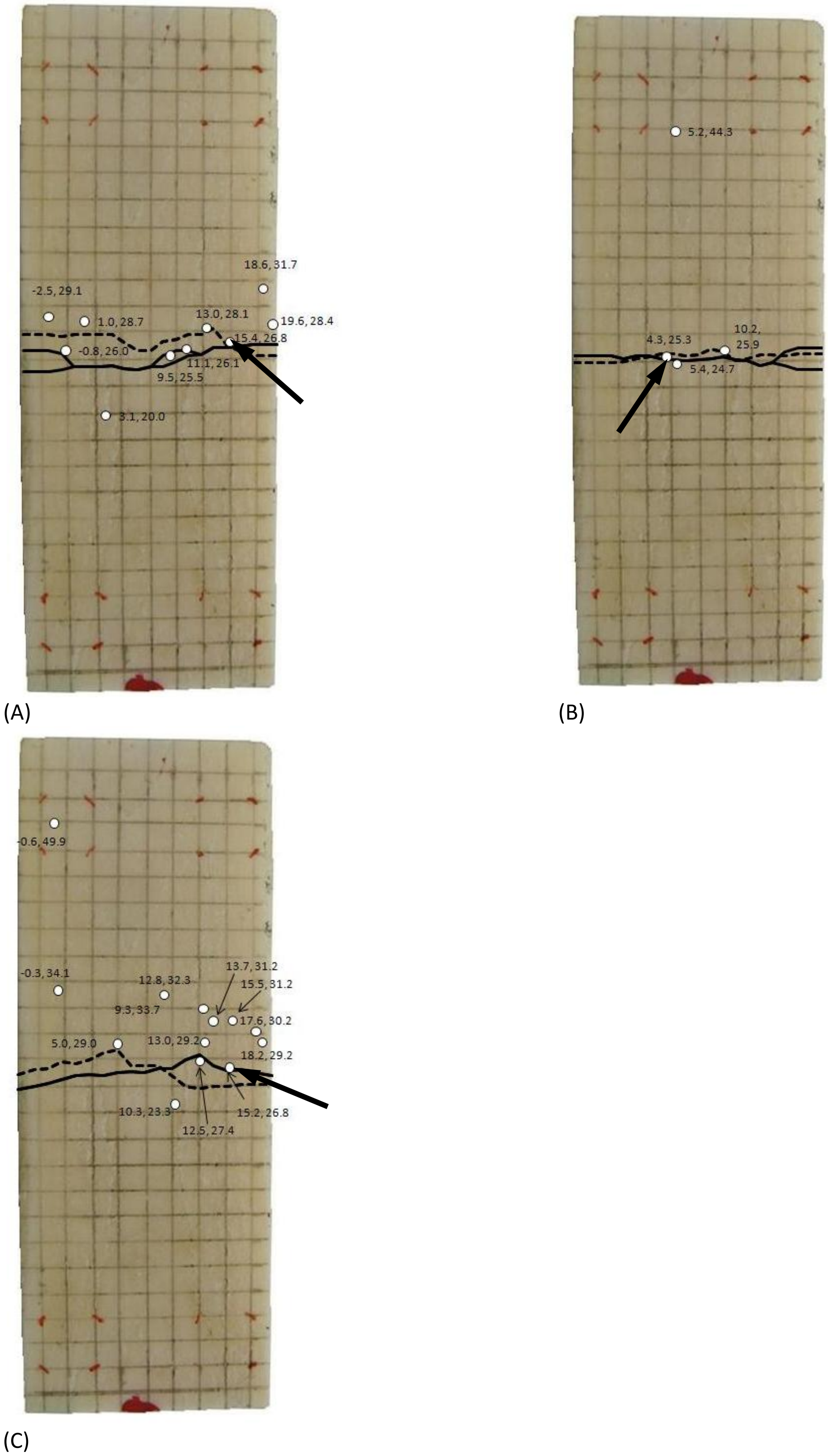

Fig. 7.10 (A) Locating microcracks in sample 1. (B) Locating microcracks in sample 2. (C) Locating microcracks in sample 3. The black arrow indicates the location of the final facture event.

7.6 Discussion

The regression algorithm proved very effective at locating AE sources from pencil lead breaks (Test 2) and from real microcracks (Test 3). While it was necessary to simulate AE sources in a grid fashion across the surface of the sample, it was not necessary to measure AE velocity throughout the sample as was the case with more conventional hyperbolic source loaction. Test 2 showed that the regression approach is effective on similar samples from different bones and different breeds of animals. This is very useful as it suggests that once the tedious testing of Test 1 were completed, AE source location on any similar sample was achievable using just the two regression equations and TOA data from the new sample. Test 3 shows that, not alone does AE indicate the imminence of fracture, but also that it is possible to predict where on the sample this fracture will take place before it occurs.

The main limitation of this work is that it was performed on two dimensional samples while whole bone is a three dimensional structure. Simulating microcracks within a solid material would prove more difficult. However the cortical layer of bone is relatively thin and this is where microcracks are most likely to occur, so it may not be necessary to simulate AE sources from within the bone. Also the bone samples were relatively small compared to whole bone. Larger distances would cause more attenuation of the AE signal making location of the smaller microcracks more difficult. Using the approach to understand fracture in bone samples or indeed whole bone could be useful due to the accuracy that is achieveable. However using this approach to locate microcracks in a Total Hip Athroplasty operation would prove quite difficult as a large range of types and sizes of bone may have to be modeled. Consider osteoporotic bone, different races, male/female and one gets an idea of the challenges involved. But it may just be possible with a large but manageable range of samples. Another challenge to AE source location on femora during THA surgery is the limited space available to mount the sensors. A minimum of three AE sensors would be required.

8. Concluding Discussion

The major themes of this dissertation are acoustic emission, bone fracture and intra-operative fracture during Total Hip Arthroplasty. Acoustic emission is a phenomenon that can be used to learn about the fracture process. The author firmly believes that it has wide ranging application and has yet to reach its full potential in research into bone fracture. He uses it to track fracture in a spatial as well as a temporal manner. The hypothesis is that the details of what is happening in the fracture event are in the acoustic signature and it is up to the researcher to decode this information from the acoustic puzzle.

While much is understood about bone fracture, there is yet an enormous amount to learn. Most of what is known is in relation to a few common animals. There is perhaps an unfathomable quantity of understanding, insight, inspiration for future engineering abilities to be gained from not alone understanding more fully the bones and bone fracture of common animals but also those of the more unfamiliar and obscure animals (for example fish bones and elephant bones which are solid the whole way through and prehistoric bones, about which we know even less). What countless problems has nature solved which we currently face or will face in the future? This is why practical learning about this amazing biological material is so important.

The author undertook this research with one particular medical application as a goal. This is to add some technology to the art of Total Hip Arthroplasty. It is the incorporation of a sensor that would give some feedback as to the state of the femur under operation. This sensor is of course the AE sensor. While a complete system to warn the surgeon is far from complete, the fundamentals have been put in place. A method to predict fracture with the use of a single sensor has been tentatively uncovered. The principle of locating microcracks in real time has been devised and validated on small bovine bone samples. Whether source location of microcracks will be ultimately used in the proposed warning system is unknown. But in the process of getting to this system the use of the location technique will be quite beneficial. In addition there are other uses of such a location technique not least the ability to “see” inside bone to see the fracture process unfold and thus understand more of what is actually occurring.

What this research does above all else is open up new possibilities: the possibility of predicting fracture using a relatively simple frequency analysis and the possibility of plotting fracturing over time in a very spatial way. These research avenues will be explored by other researchers in the on-going quest to understand more about bone fracture.

References

1. Akkus, O., Jepsen, K.J., and Rimnac, C. M. (2000). Microstructural aspects of the fracture process in human cortical bone, *Journal of Materials Science*, Vol. 35, PP: 6065-6074.
2. Baron, J. A., and Ying, S. P., (1987). *Acoustic Emission Testing: Nondistructive Testing Handbook,* Columbus: American Society for NDT, pp. 135-154.
3. Egle, D., (1987). *Acoustic Emission Testing: Nondistructive Testing Handbook,* Columbus: American Society for NDT, pp. 91-120.
4. Baxter, M.G., Pullin, R., Holford, K.M., and Evans, S.L. (2006). Delta *T* source location for acoustic emission. *Mechanical Systems and Signal Processing*, 21, pp.1512-1520.
5. Bharati, S., Sinha, M. K., Basu, D., (2005). Hydroxyapatite coating by biomimetic method on titanium alloy using concentrated SBF. *Bulletin of Materials Science*, 28 (6), pp. 617-621.
6. Cowin, S. (2001) *Bone Mechanics Handbook*. 2nd ed. Florida: CRC Press.
7. Currey, J. D. (2006) *Bones: Structures and Mechanics*. New Jersey: Princeton University Press.
8. Davidson, D., Pike, J., Garbuz, D., Duncan, C. P., and Masri, B. A. (2008). Intraoperative Periprosthetic Fractures During Total Hip Arthroplasty. Evaluation and Management. *Journal of Bone and Joint Surgery*, 90, pp: 2000-2012.

9. Evans, M. (1997). *The Use of Diffuse Field Measurements for Acoustic Emission*, Unpublished PhD Thesis, Imperial College of Science, Technology and Medicine, University of London, London, UK.
10. Fischer, R. A., Arms, S. W., Pope, M. H., and Seligson, D. (1986). Analysis of the Effect of using Two Different Strain Rates on the Acoustic Emission in Bone. *Journal of Biomechanics*, 19(2), pp. 119-127.
11. Ge, M., (2003A). Analysis of Source Location Algorithms. Part1: Overview and non-iterative methods. *Journal of Acoustic Methods*, 21, pp.14-28.
12. Ge, M., (2003B) Analysis of Source Location Algorithms. Part2: Iterative Methods. *Journal of Acoustic Methods*, 21, pp.14-28.
13. Gupta, H. S. and Zioupos, P. (2008) Fracture of Bone Tissue: The 'hows' and the 'whys'. *Medical Engineering and Physics*, 30 (10), pp.1209-1226.
14. Hensman, J., Mills, R., Pierce, S. G., Worden, K., and Eaton, M., (2010). Locating Acoustic Emission Sources in Complex Structures using Gaussian Processes. *Mechanical Systems and Signal Processing*, 24(1), pp. 211-223.
15. Holler, P., Klein, M., Waschkies, E. and Deuster, G. (1991). New approach for location of continuously emitting acoustic emission sources by phase-controlled probe arrays. *Nuclear Engineering and Design*, 128, pp.79-82.
16. Horn, M. (1996). Acoustic Emission Source Location by Reverse Ray Tracing. *US patent No. 5,528,557*.
17. Kalyanasundaram, P., Mukhopadhyay, C. K., and Subba Rao, S. V., 2007*,* *Practical Acoustic Emission*, Oxford: Alpha Science International, pp. 51-52.

18. Kann, P., Schulz, U., Nink, M., Pfützner, A., Schrezenmeir, J., and Beyer, J., (1993). Architecture in Cortical Bone and Ultrasound Transmission Velocity. *Journal of Clinical Rheumatalology*, 12(3), pp. 364-367.
19. Khan, M., A., and O'Driscoll, M. (1977). Fractures of the Femurs during Total Hip Replacement and their management. *The Bone and Joint Journal,* 59-B (1), pp.36-41.
20. Lannocca, M., Varini, E., Cappello, A., Cristofolini, and L., Bialoblocka, E., (2007). Intra-operative evaluation of cementless hip implant stability: a prototype device based on vibration analysis. *Medical Engineering Physics*, Vol. 29 (8), pp. 886-894.
21. Lee, D., Jo, M., Lee, S., and Ko, H., (2006). Implementation of the Position Location System in a Underwater Channel Environments. *WESPAC IX 2006 - The 9th Western Pacific Acoustics Conference,* Seoul, Korea, June 26-28, 2006.
22. Marby, T. M., Cabanela, M. E., and Hannssen, A. D. (2006). Intra-operative Fractures During Primary Total Hip Arthroplasty. *Orthropaedic Surgery Hip,* pp. 31-32.
23. Meek, R. M. D., Garbuz, D. S., Bassam A. Masri, B. A., Greidaanus, N., V., and Duncan, C., P., (2004). Intraoperative Fracture of the Femur in Revision Total Hip Arthroplasty with a Diaphyseal Fitting Stem. *Journal of Bone and Joint Surgery*, 86, pp.480-485.
24. Mavrogordato, M., Taylor, M., Taylor, A., and Browne, M., (2011). Real Time Monitoring of Progressive Damage during Loading of a Simplified Total Hip

Stem Construct using Embedded Acoustic Emission Sensors. *Medical Engineering and Physics*, 33, pp.395-406.

25. Net Doctor. (n.d.). *A history of hip replacement* [Online]. Available: http://netdoctor.privatehealth.co.uk/surgery-and-treatments/hip-replacement-surgery/guide/history-of-hip-replacement/ [Accessed 30 September 2012].
26. Qi, G., Pujol, J., and Fan, Z., (2000). 3-D AE Visualization of Bone-Cement Fatigue Locations. *Journal of Biomedical Materials Research*, 52(2), pp. 256-260.
27. Rajachar, R.M., Chow, D. L., Curtis, C. E., Weissman, N. A., and Kohn, D. H.(1999A). Use of Acoustic Emission to Characterize Focal and Diffuse Micriodamage in Bone. *Acoustic Emission: Standards and Technology Update*, ASTM STP 1353, S.J. Vahaviolos, Ed., American Society for Testing and Materials, West Conshohocken, PA, 1999.

28. Rajachar, R. M., Chow, D. L., and Kohn, D. H., (1999B). Determining Mechanisms of Microdamage Formation and Accumulation in Cortical Bone Using Acoustic Emission. *Proceedings of the 1999 Bioengineering Conference*, Big Sky, Montana, Vijay K. Goel, ed., American Society of Mechanical Engineers, 1999, BED Series Volume 42.
29. Rowlands, A., Duck, F. A., and Cunningham, J. L. (2008). Bone vibration measurement using ultrasound: Application to detection of hip prosthesis loosening. *Medical Enginneering and Physics*, 30 (3), pp. 278-284.

30. Sakai, R., Kikuchi, A., and Morita, T., (2011). Hammering sound frequency analysis and prevention of intra-operative periprosthetic fractures during total hip arthroplasty. *Hip International*, 21 (6), pp. 718-723.

31. Shiel, W., C. (n.d.). *MedicinNet.com (Total Hip Replacement)*. Available: http://www.medicinenet.com/total_hip_replacement/article.htm [Accessed: April 2010].

32. Thillemann, T. M., Pedersen, A. B., Johnsen, S. P., and Soballe, K. (2008). Inferior outcome after intraoperative femoral fracture in total hip arthroplasty. Acta Orthopaedica, 79(3), pp. 327-334.

33. Toen, C.V., Street, J., Oxland, T.R., and Cripton, P.A., (2012). Acoustic emission signals can discriminate between compressive bone fractures and tensile ligament injuries in the spine during dynamic loading. *Journal of Biomechanics*, 45, pp 1643-1649.

34. Von Den Dreisch, A. (1977). *A guide to the Measurement of Animal Bones from Archaeological Sites*. Cambridge: Harvard University.

35. Wright, T., Vosburgh, F., and Burstein, A. H., (1981). Permanent Deformation of Compact Bone Monitored by Acoustic Emission. *Journal of Biomechanics*, 14(6), pp. 405-409.

36. Yu, J., Ziehl, P., Zarate, B., Caicedo, J., (2011). Prediction of fatigue crack growth in steel bridge components using acoustic emission. *Journal of Constructional Steel Research,* 67, pp.1254-1260.

37. Zioupos, P., Currey, J.D., and Sedman, A.J. (1994). An examination of the micromechanics of failure of bone and antler by acoustic emission tests and

Laser Scanning Confocal microscopy. *Medical Engineering and Physics,* 16 (May), pp.203-212.

Appendix

A. Sensor Calibration Sheets

Pancom PICO-Z No 46 18 06 09

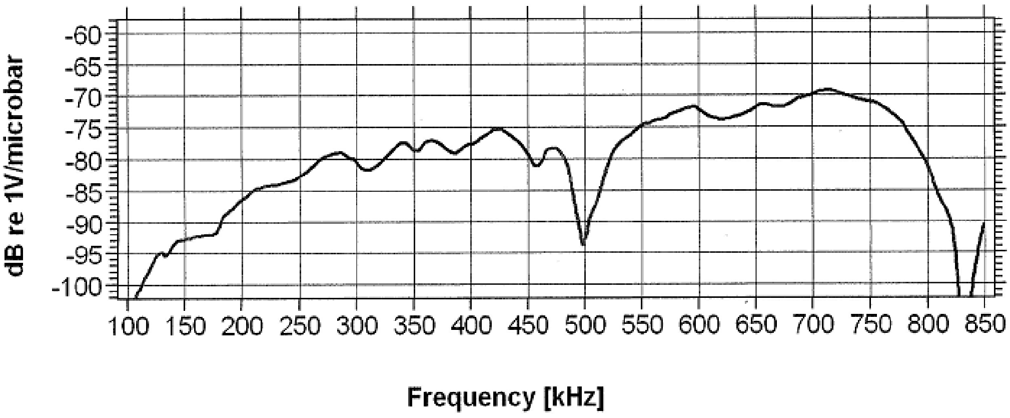

Calibration method based upon ASTM standard E976. Face to Face excitation : 0.1Vrms at V103 (No 546007) 50 ohm loaded , preampifier AEP4 gain 34dB, offset -148dB, Filter bandwidth bypass

Pancom PICO-Z No 47 18 06 09

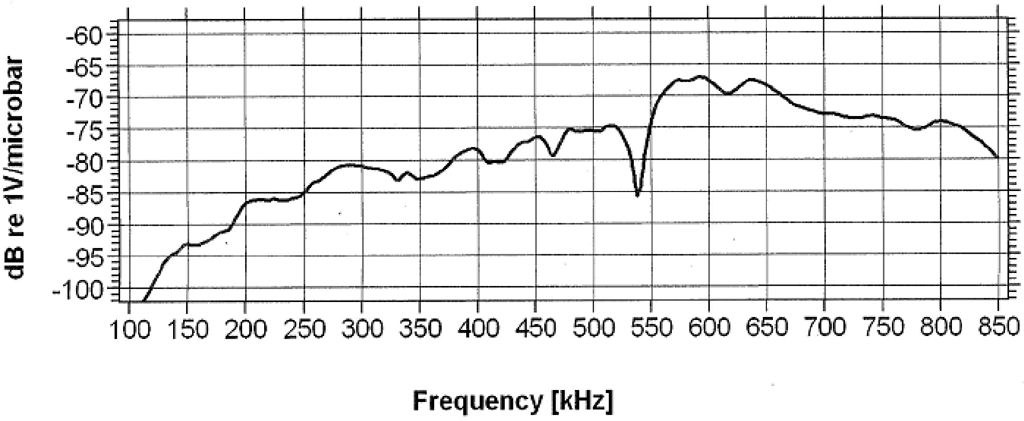

Calibration method based upon ASTM standard E976. Face to Face excitation : 0.1Vrms at V103 (No 546007) 50 ohm loaded , preampifier AEP4 gain 34dB, offset -148dB, Filter bandwidth bypass

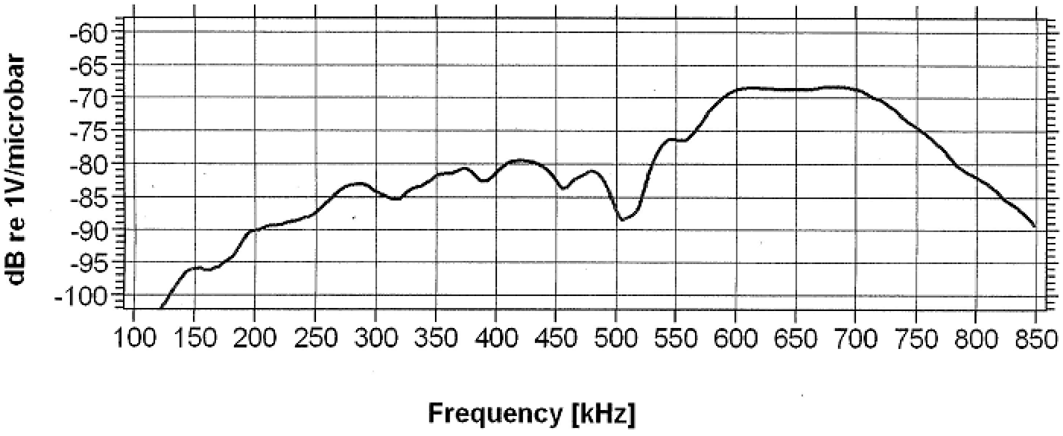

Pancom PICO-Z No 49 18 06 09

Calibration method based upon ASTM standard E976. Face to Face excitation : 0.1Vrms at V103 (No 546007) 50 ohm loaded , preampifier AEP4 gain 34dB, offset -148dB, Filter bandwidth bypass

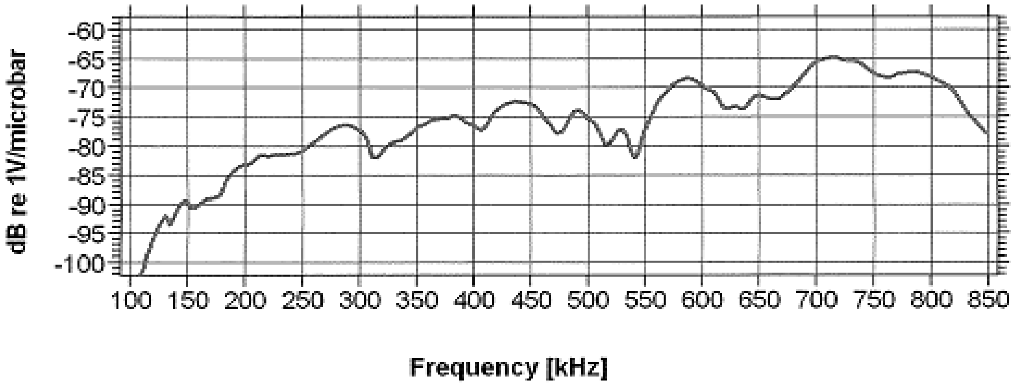

Pancom PICO-Z No 50 18 06 09

Calibration method based upon ASTM standard E976. Face to Face excitation : 0.1Vrms at V103 (No 546007) 50 ohm loaded , preampifier AEP4 gain 34dB, offset -148dB, Filter bandwidth bypass

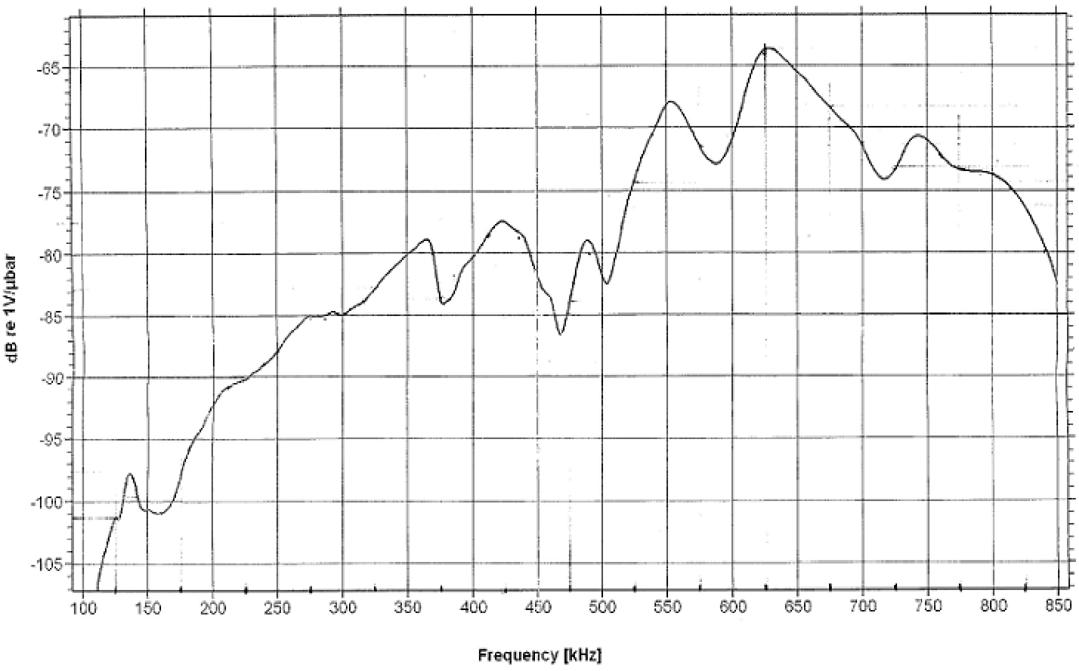

Calibration method based on ASTM standard E976. Face to face excitation: 0,1Vrms at V103 (50R). Offset -(114 + Gain)dB, coupling agent: light machine oil. For sensitivity to ANSI S1.2-1988 subtract 15dB.

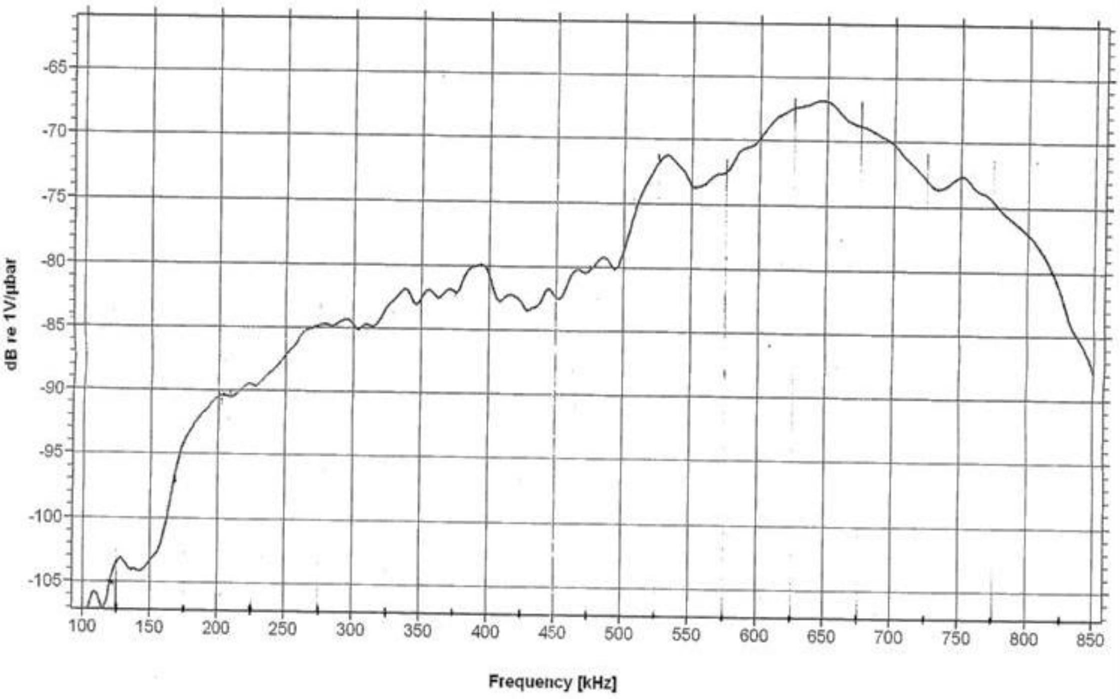

Calibration method based on ASTM standard E976. Face to face excitation: 0,1Vrms at V103 (50R), Offset -(114 + Gain)dB, coupling agent: light machine oil. For sensitivity to ANSI S1.2-1988 subtract 15dB.

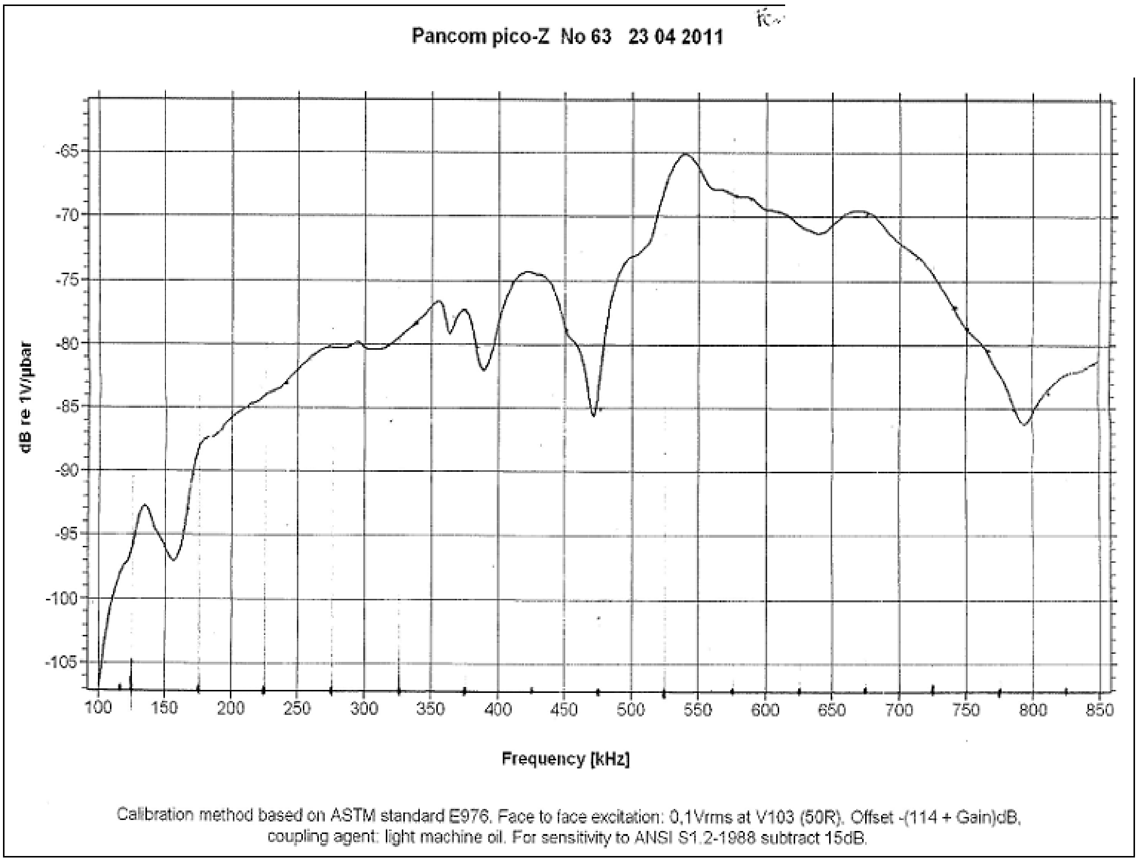

Pancom pico-Z No 63 23 04 2011

Calibration method based on ASTM standard E976. Face to face excitation: 0,1Vrms at V103 (50R). Offset -(114 + Gain)dB, coupling agent: light machine oil. For sensitivity to ANSI S1.2-1988 subtract 15dB.

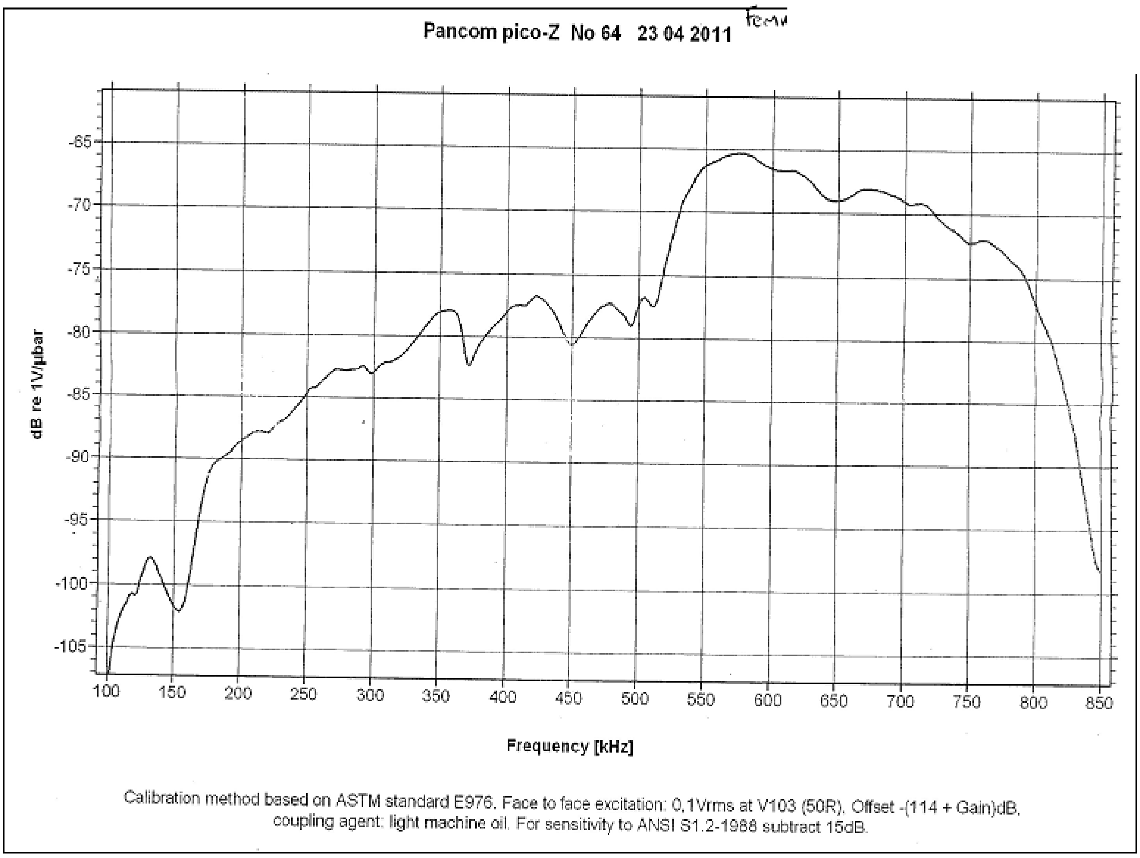

Pancom pico-Z No 64 23 04 2011 Fem

Calibration method based on ASTM standard E976. Face to face excitation: 0,1Vrms at V103 (50R). Offset -(114 + Gain)dB, coupling agent: light machine oil. For sensitivity to ANSI S1.2-1988 subtract 15dB.

B. Preamplifier Power Supply Circuit Diagram

This is an excerpt from the Vallen Acoustic Emission catalogue

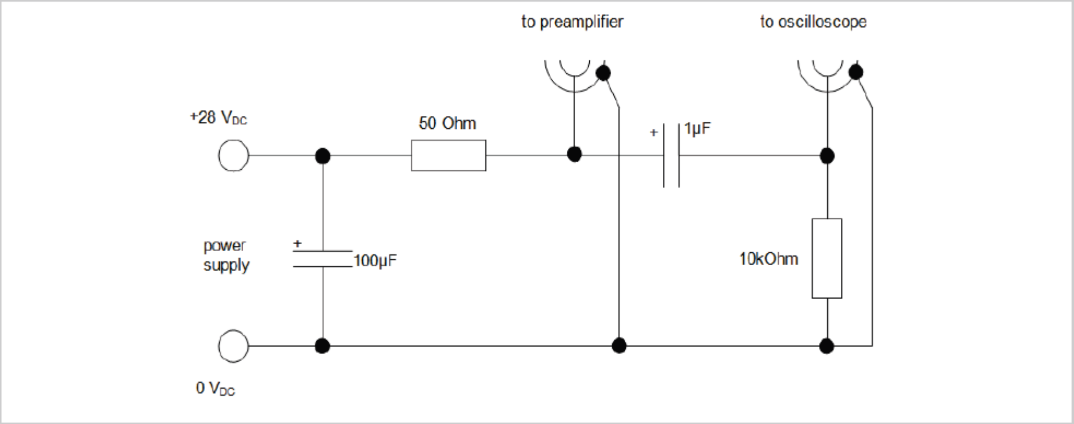

Figure 1: Principle electronic circuit to supply power to the preamplifier and decoupling AC component from the signal

C. ANOVA Table for Test 1 in Chapter 3

Rise Time

Anova: Single Factor

SUMMARY

Groups	*Count*	*Sum*	*Average*	*Variance*
Cortical	556	37479	67.40827338	29994.13752
Cancellous	91	3348	36.79120879	14192.21148

ANOVA

Source of Variation	*SS*	*df*	*MS*	*F*	*P-value*	*F crit*
Between Groups	73305.9	1	73305.91248	2.637926462	0.104828197	3.855916135
Within Groups	1.8E+07	645	27789.2176			
Total	1.8E+07	646				

P-value is not less than 0.05, therefore no significant difference could be concluded

Average Frequency

Anova: Single Factor

SUMMARY

Groups	*Count*	*Sum*	*Average*	*Variance*
200	555	134926	243.1099099	11985.65396
250	90	28618	317.9777778	17163.01074

ANOVA

Source of Variation	*SS*	*df*	*MS*	*F*	*P-value*	*F crit*
Between Groups	434076.9334	1	434076.9334	34.1731753	8.01999E-09	3.855961229
Within Groups	8167560.251	643	12702.271			
Total	8601637.184	644				

P-value is less than 0.05, therefore there is a significant difference

Root Mean Square (RMS)

Anova: Single Factor

SUMMARY

Groups	*Count*	*Sum*	*Average*	*Variance*
Cortical	556	1.3316	0.002394964	5.63396E-05
Cancellous	91	0.0444	0.000487912	1.86863E-06

ANOVA

Source of Variation	*SS*	*df*	*MS*	*F*	*P-value*	*F crit*
Between Groups	0.000284405	1	0.000284405	5.835263925	0.015984953	3.855916135
Within Groups	0.031436643	645	4.8739E-05			
Total	0.031721047	646				

P-value is less than 0.05, therefore there is a significant difference

Average Signal Level (ASL)

Anova: Single Factor

SUMMARY

Groups	*Count*	*Sum*	*Average*	*Variance*
Cortical	556	10990	19.76618705	85.42991769
Cancellous	91	1176	12.92307692	31.51623932

ANOVA

Source of Variation	*SS*	*df*	*MS*	*F*	*P-value*	*F crit*
Between Groups	3662.005242	1	3662.005242	47.00478181	1.65971E-11	3.855916135
Within Groups	50250.06586	645	77.90707884			
Total	53912.0711	646				

P-value is less than 0.05, therefore there is a significant difference

Reverberation Frequency

Anova: Single Factor

SUMMARY

Groups	Count	Sum	Average	Variance
Cortical	556	123743	222.5593525	7178.636111
Cancellous	91	28428	312.3956044	13126.44176

ANOVA

Source of Variation	SS	df	MS	F	P-value	F crit
Between Groups	631124.6625	1	631124.6625	78.80623571	6.72979E-18	3.855916135
Within Groups	5165522.8	645	8008.56248			
Total	5796647.462	646				

P-value is less than 0.05, therefore there is a significant difference

Initiation Frequency

Anova: Single Factor

SUMMARY

Groups	Count	Sum	Average	Variance
Cortical	556	278047	500.0845324	64963.75681
Cancellous	91	60262	662.2197802	67598.10672

ANOVA

Source of Variation	SS	df	MS	F	P-value	F crit
Between Groups	2055733.356	1	2055733.356	31.46626627	3.01305E-08	3.855916135
Within Groups	42138714.63	645	65331.34051			
Total	44194447.99	646				

P-value is less than 0.05, therefore there is a significant difference

Peak Frequency

Anova: Single Factor

SUMMARY

Groups	*Count*	*Sum*	*Average*	*Variance*
Cortical	556	207534	373.2625899	20589.58137
Cancellous	91	42202	463.7582418	14368.51868

ANOVA

Source of Variation	*SS*	*df*	*MS*	*F*	*P-value*	*F crit*
Between Groups	640423.6012	1	640423.6012	32.47332876	1.83868E-08	3.8559161
Within Groups	12720384.34	645	19721.52611			
Total	13360807.94	646				

P-value is less than 0.05, therefore there is a significant difference

D. Cortical Bone Results from Test 3 Chapter 3

Cortical Samples Reverberation Frequency analysis:

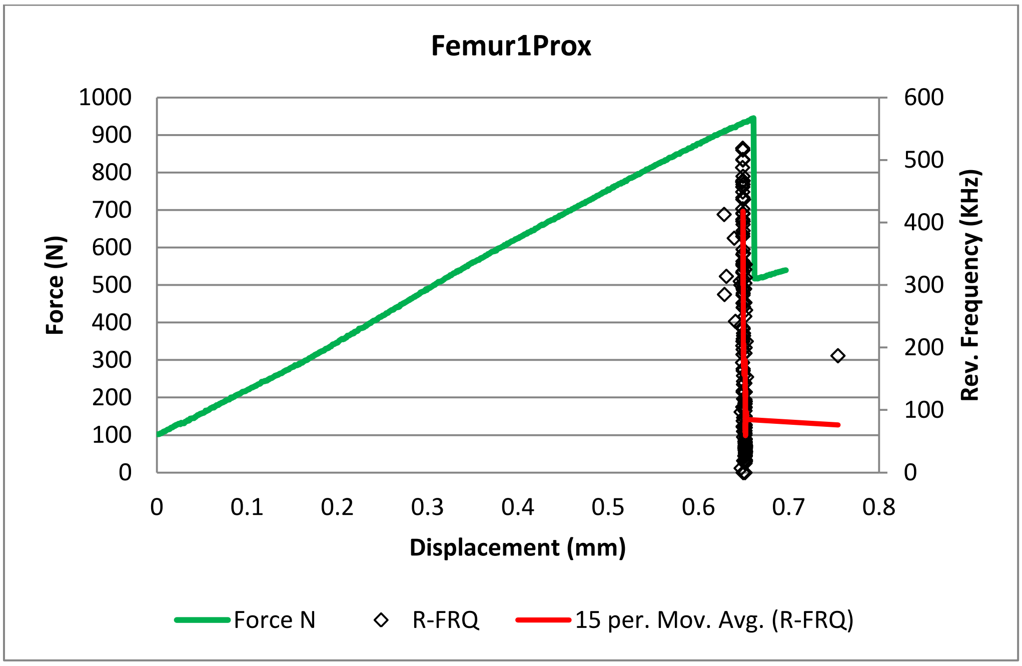

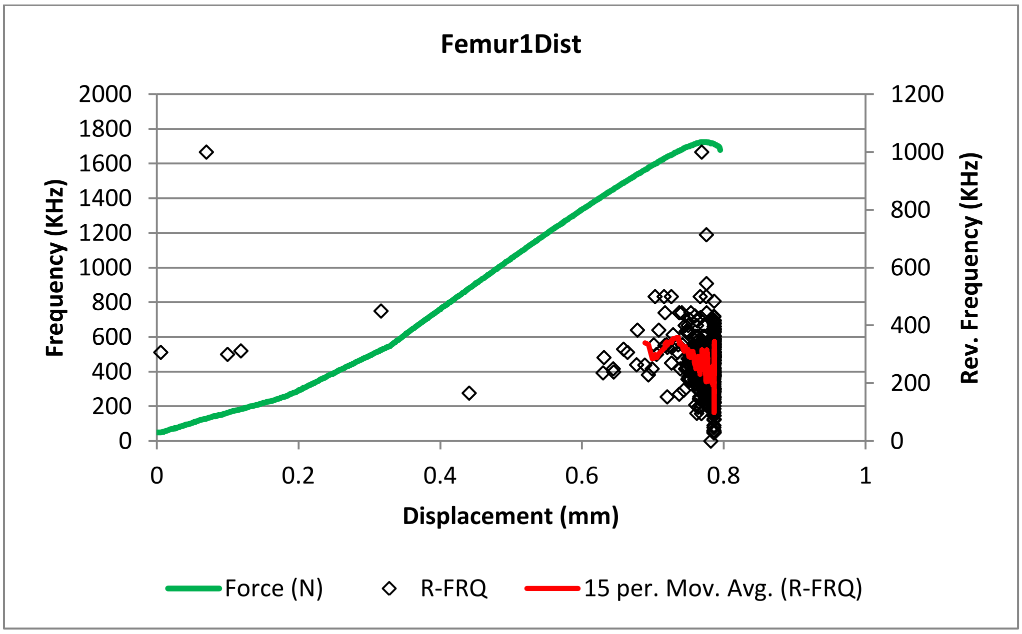

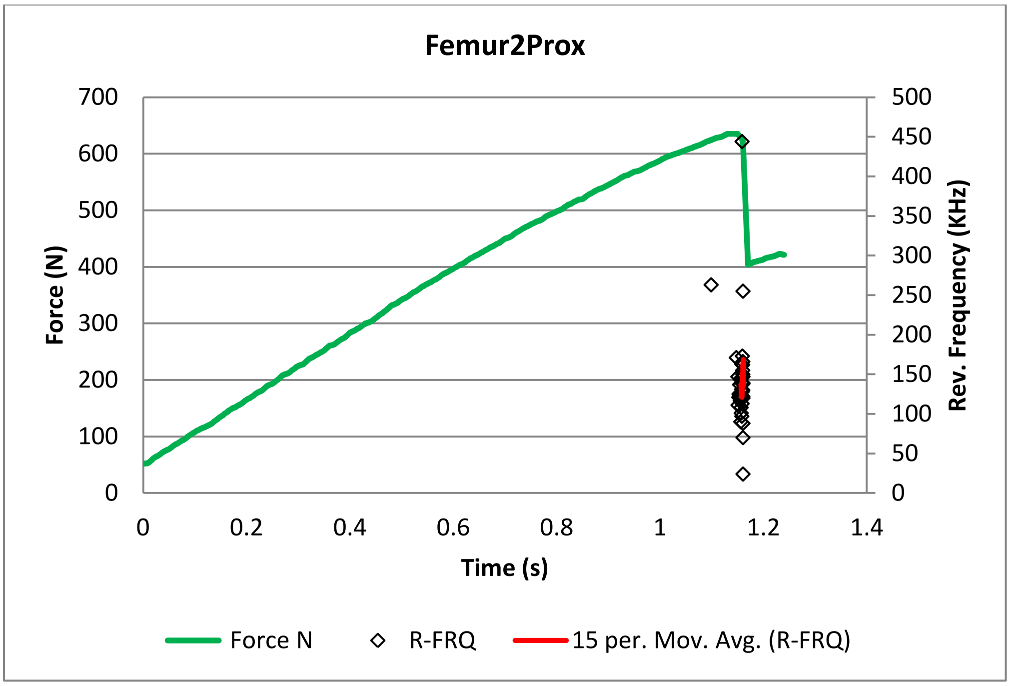
Femur2Prox
Force (N)
700
600
500
400
300
200
100
0
Rev. Frequency (KHz)
500
450
400
350
300
250
200
150
100
50
0
0
0.2
0.4
0.6
0.8
1
1.2
1.4
Time (s)
Force N
R-FRQ
15 per. Mov. Avg. (R-FRQ)

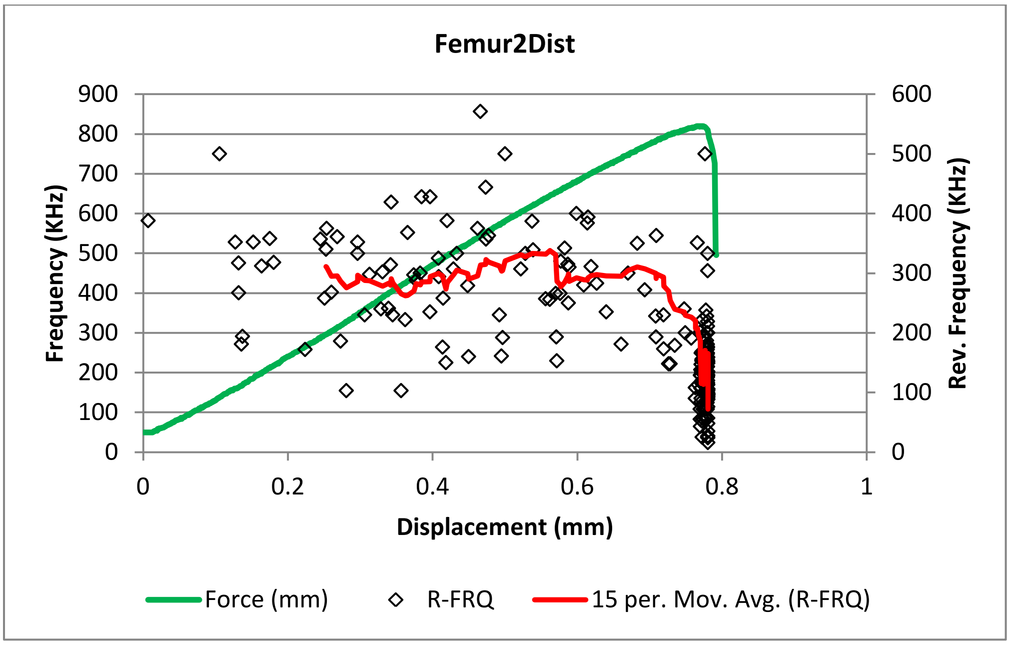
Femur2Dist
Frequency (KHz)
900
800
700
600
500
400
300
200
100
0
Rev. Frequency (KHz)
600
500
400
300
200
100
0
0
0.2
0.4
0.6
0.8
1
Displacement (mm)
Force (mm)
R-FRQ
15 per. Mov. Avg. (R-FRQ)

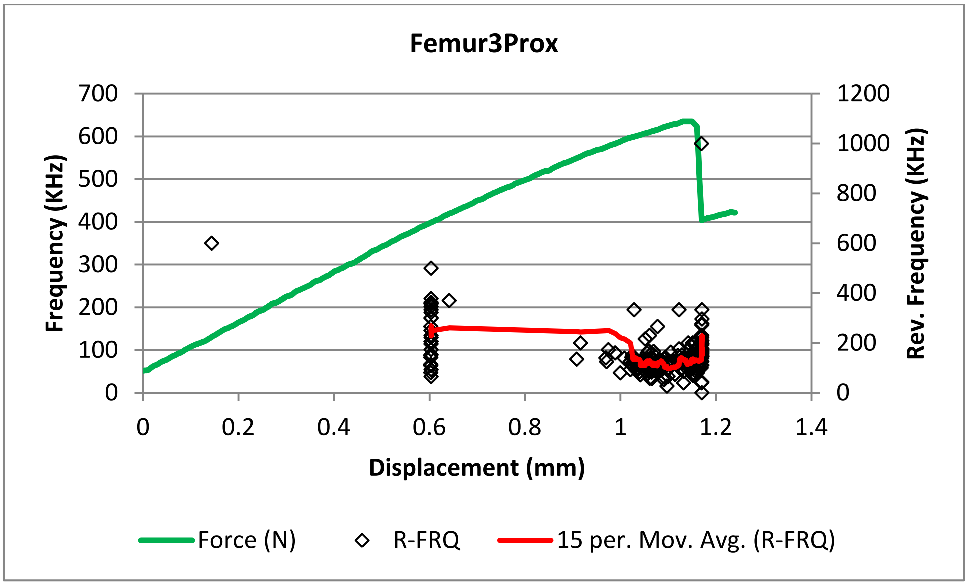
Femur3Prox
Frequency (KHz)
700
600
500
400
300
200
100
0
Rev. Frequency (KHz)
1200
1000
800
600
400
200
0
0
0.2
0.4
0.6
0.8
1
1.2
1.4
Displacement (mm)
Force (N)
R-FRQ
15 per. Mov. Avg. (R-FRQ)

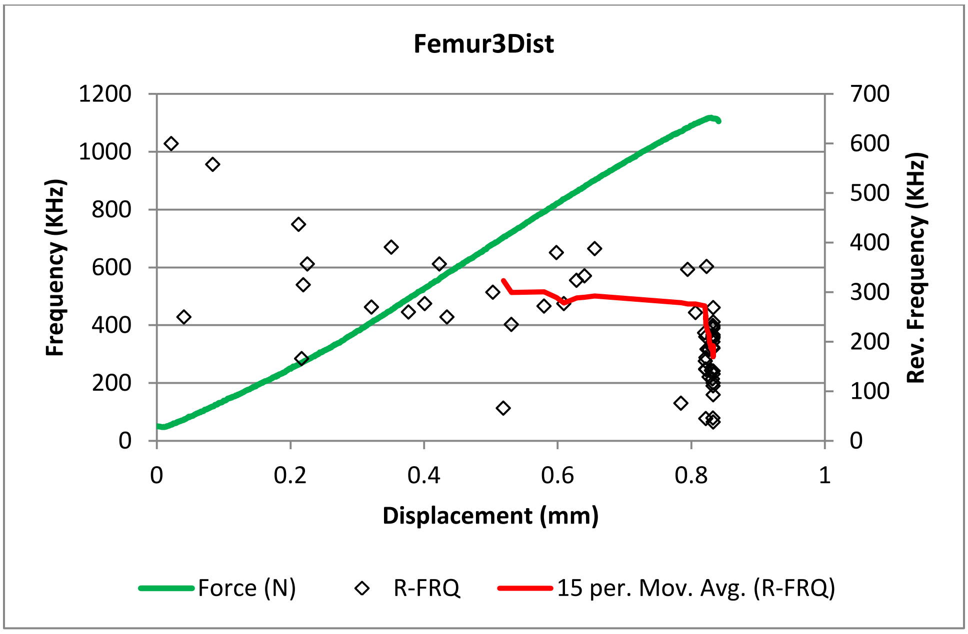
Femur3Dist
Frequency (KHz)
1200
1000
800
600
400
200
0
Rev. Frequency (KHz)
700
600
500
400
300
200
100
0
0
0.2
0.4
0.6
0.8
1
Displacement (mm)
Force (N)
R-FRQ
15 per. Mov. Avg. (R-FRQ)

E. Cancellous Bone Results from Test 3 Chapter 3

Samples Reverberation Frequency analysis:

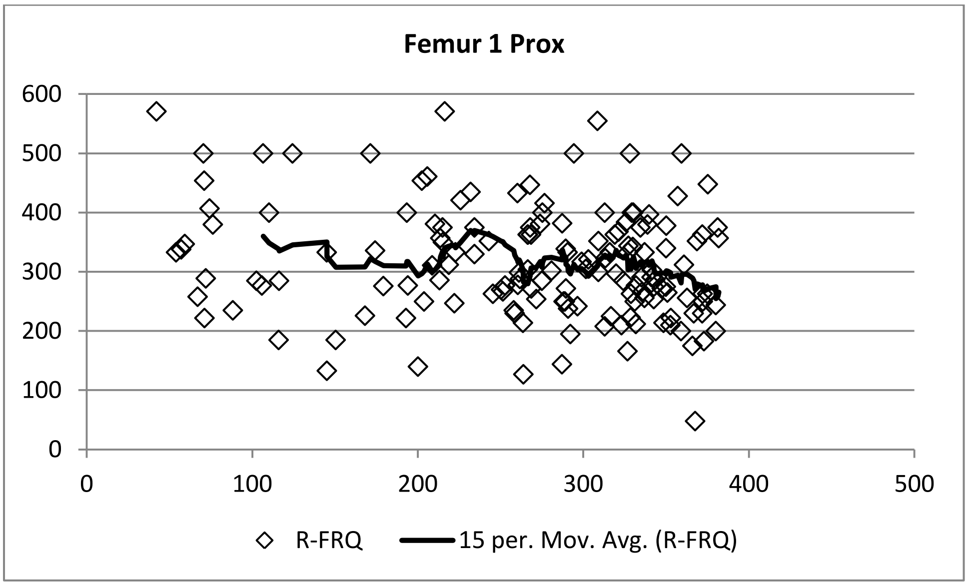

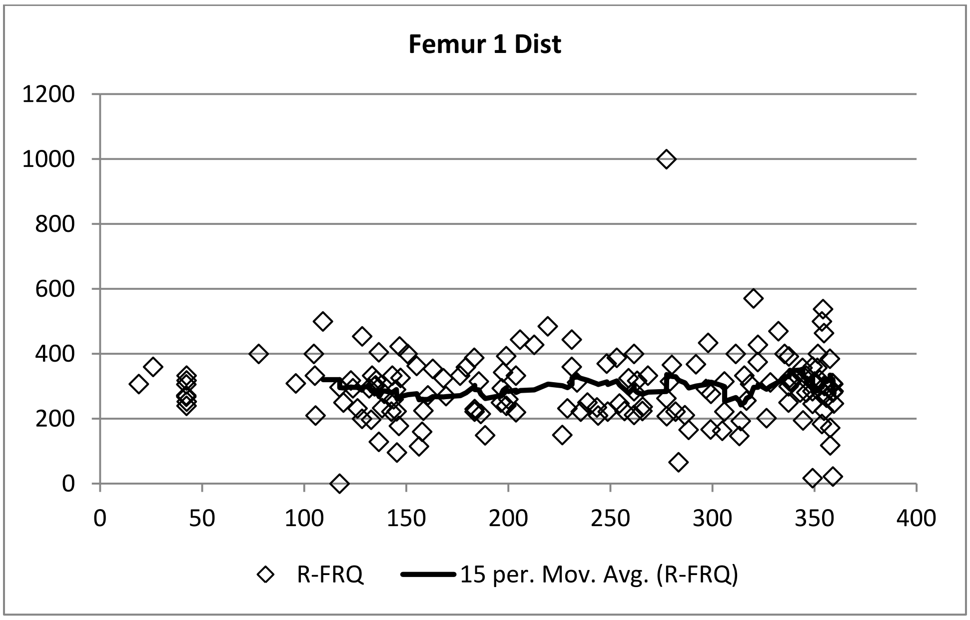

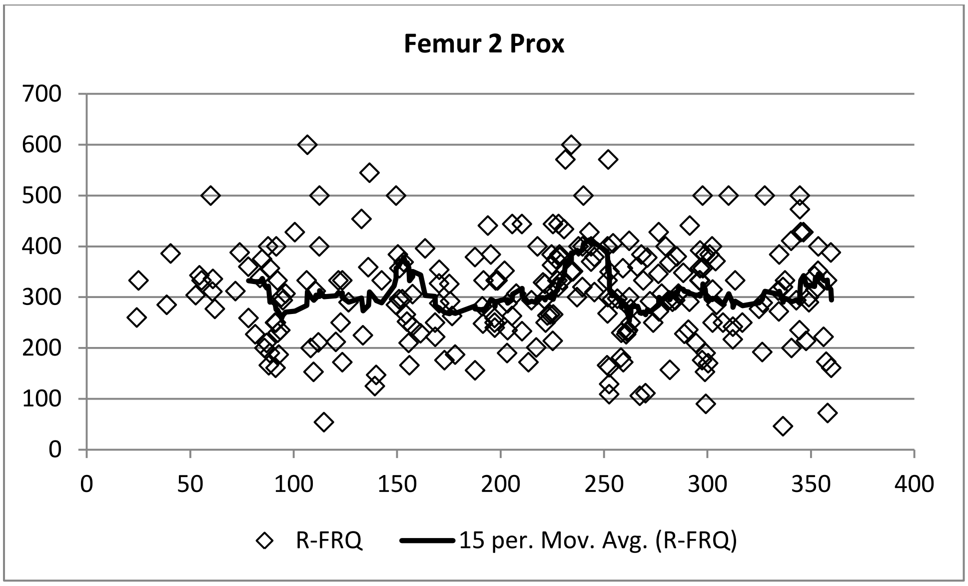
Femur 2 Prox
700
600
500
400
300
200
100
0
0
50
100
150
200
250
300
350
400
R-FRQ
15 per. Mov. Avg. (R-FRQ)

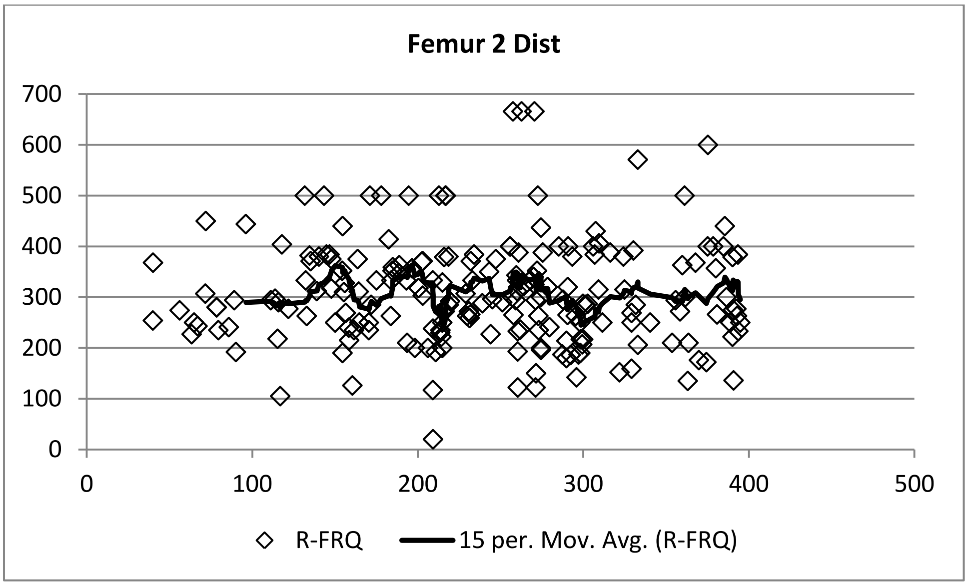
Femur 2 Dist
700
600
500
400
300
200
100
0
0
100
200
300
400
500
R-FRQ
15 per. Mov. Avg. (R-FRQ)

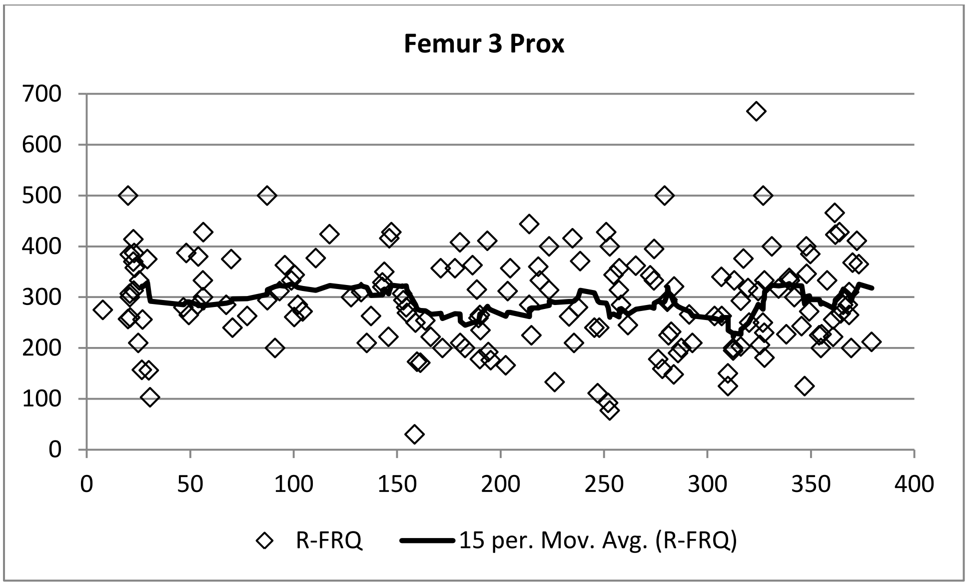
Femur 3 Prox
700
600
500
400
300
200
100
0
0
50
100
150
200
250
300
350
400
R-FRQ
15 per. Mov. Avg. (R-FRQ)

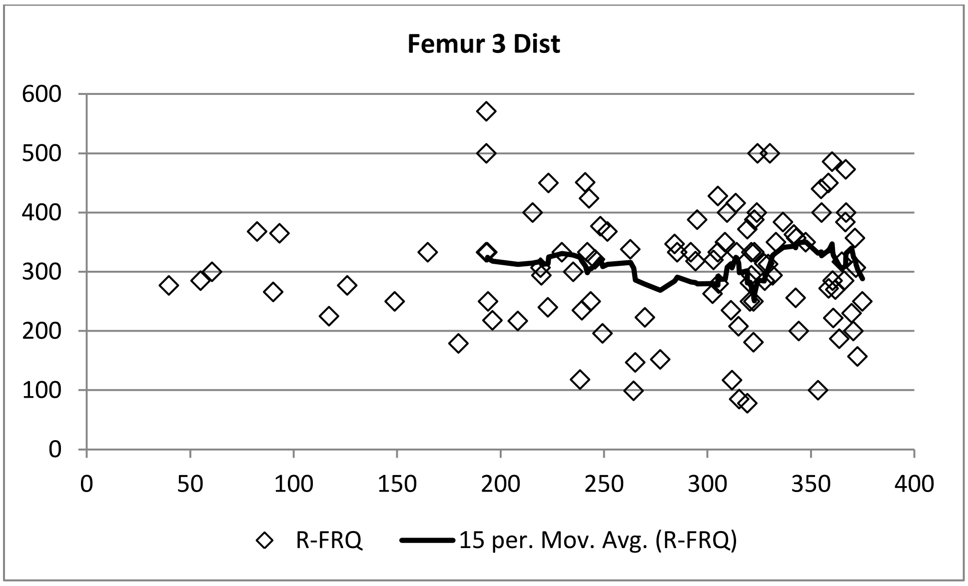
Femur 3 Dist
600
500
400
300
200
100
0
0
50
100
150
200
250
300
350
400
R-FRQ
15 per. Mov. Avg. (R-FRQ)

F. Centroid Frequeny Analysis scatter graphs for femora 3 through 8 from Test 3 Chapter 4

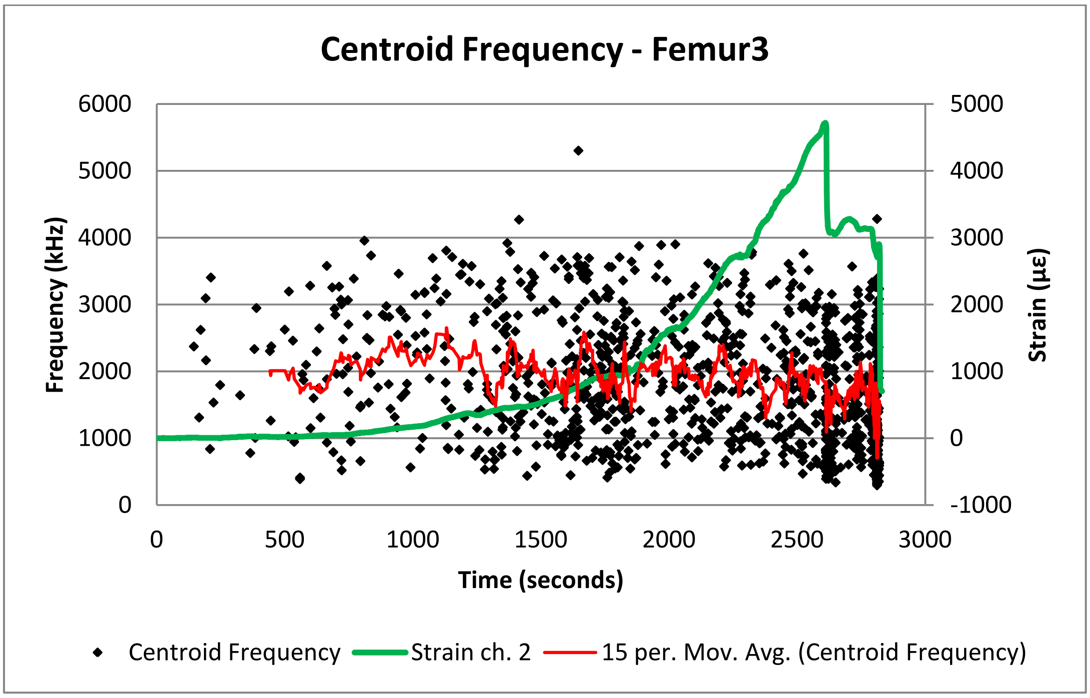

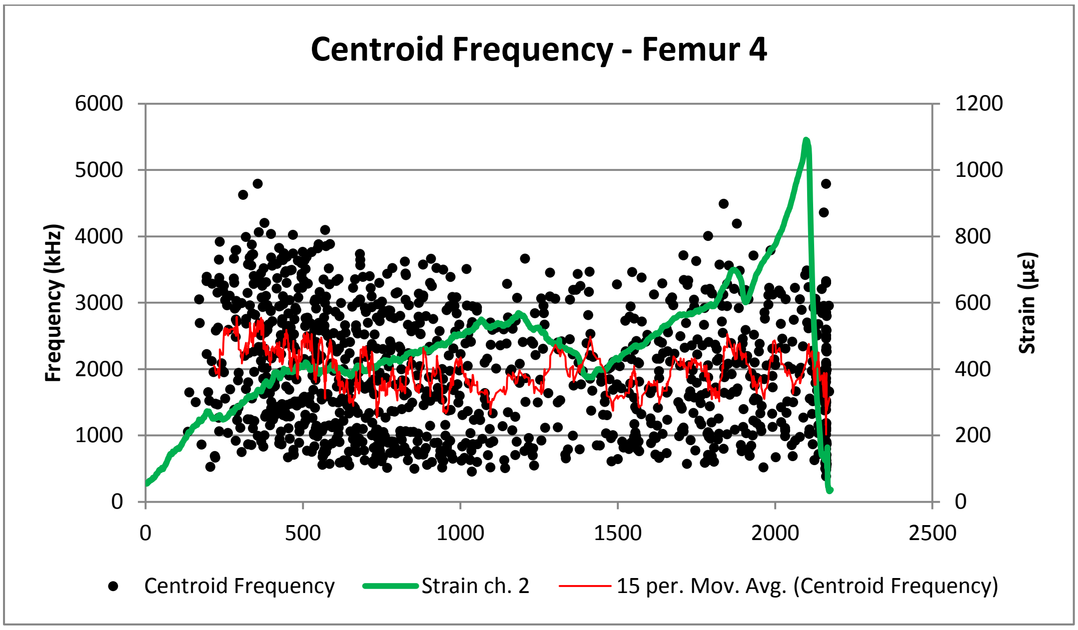

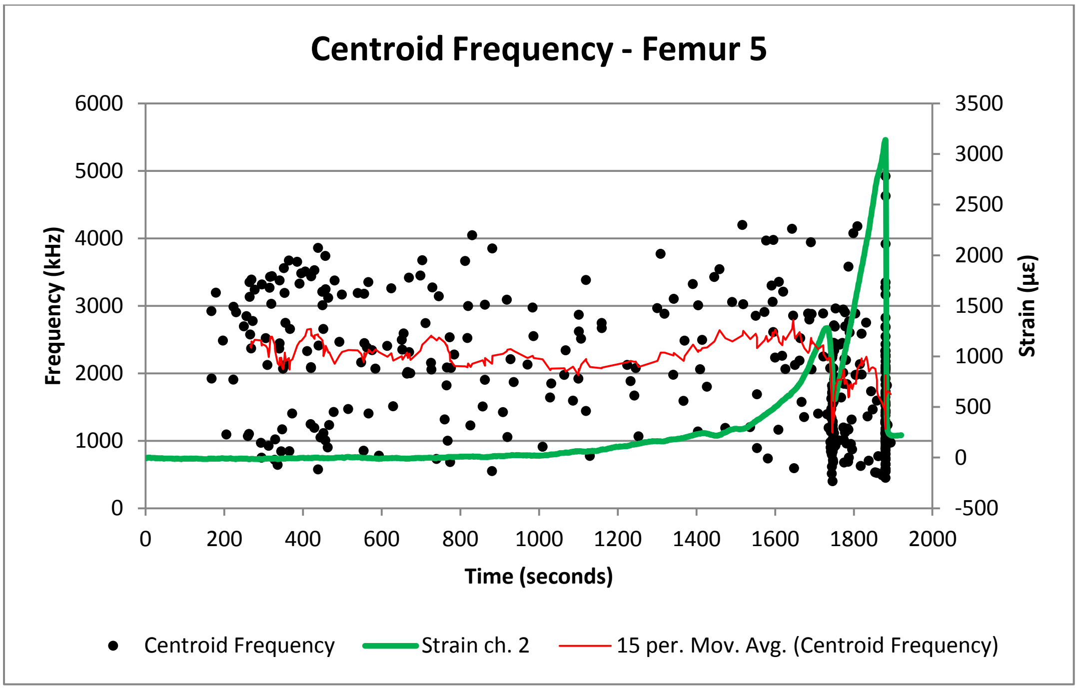
Centroid Frequency - Femur 5
Frequency (kHz)
6000
5000
4000
3000
2000
1000
0
Strain (με)
3500
3000
2500
2000
1500
1000
500
0
-500
Time (seconds)
0
200
400
600
800
1000
1200
1400
1600
1800
2000
● Centroid Frequency
Strain ch. 2
15 per. Mov. Avg. (Centroid Frequency)

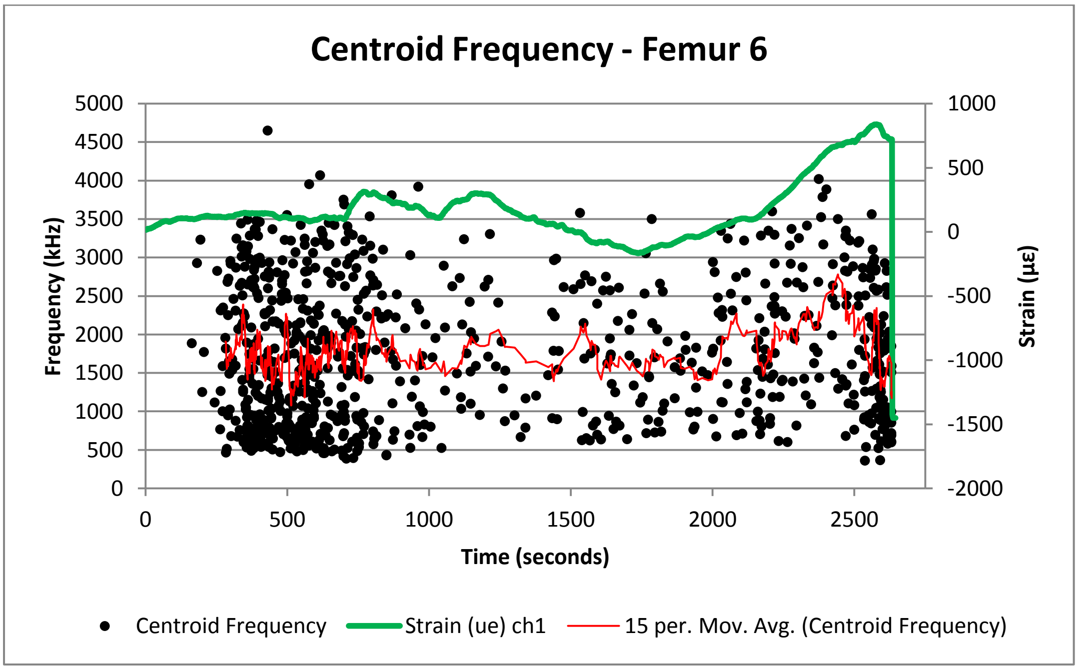
Centroid Frequency - Femur 6
Frequency (kHz)
5000
4500
4000
3500
3000
2500
2000
1500
1000
500
0
Strain (με)
1000
500
0
-500
-1000
-1500
-2000
Time (seconds)
0
500
1000
1500
2000
2500
● Centroid Frequency
Strain (ue) ch1
15 per. Mov. Avg. (Centroid Frequency)

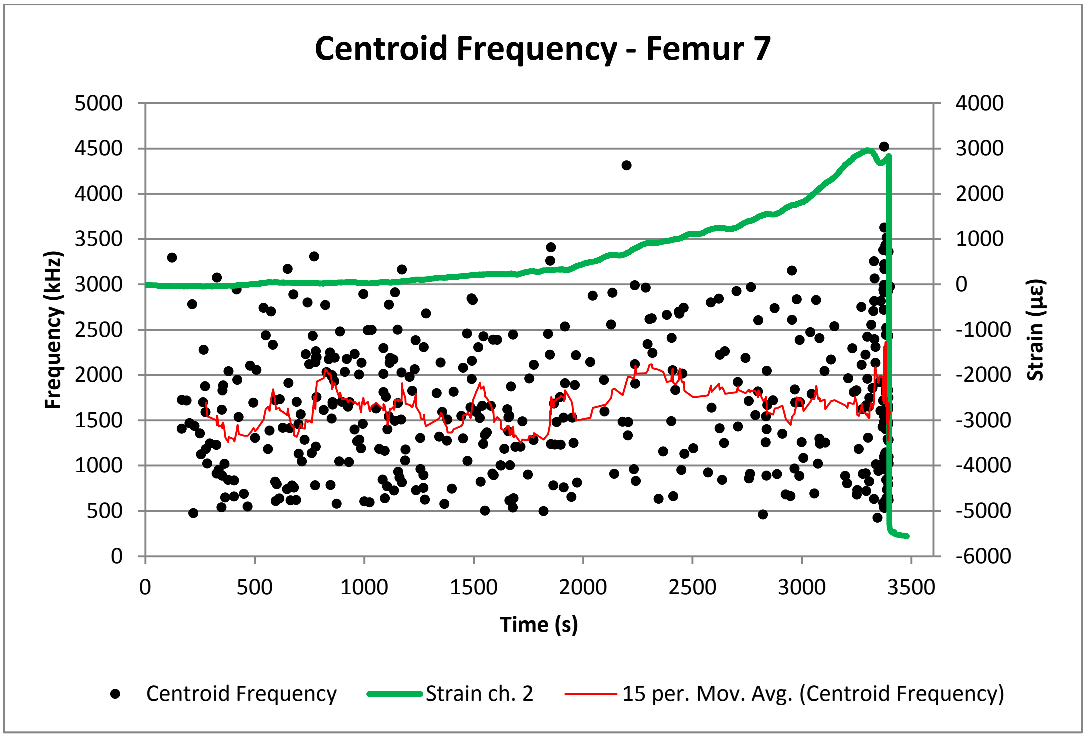
Centroid Frequency - Femur 7
Frequency (kHz)
5000
4500
4000
3500
3000
2500
2000
1500
1000
500
0
Strain (με)
4000
3000
2000
1000
0
-1000
-2000
-3000
-4000
-5000
-6000
0
500
1000
1500
2000
2500
3000
3500
Time (s)
● Centroid Frequency
Strain ch. 2
15 per. Mov. Avg. (Centroid Frequency)

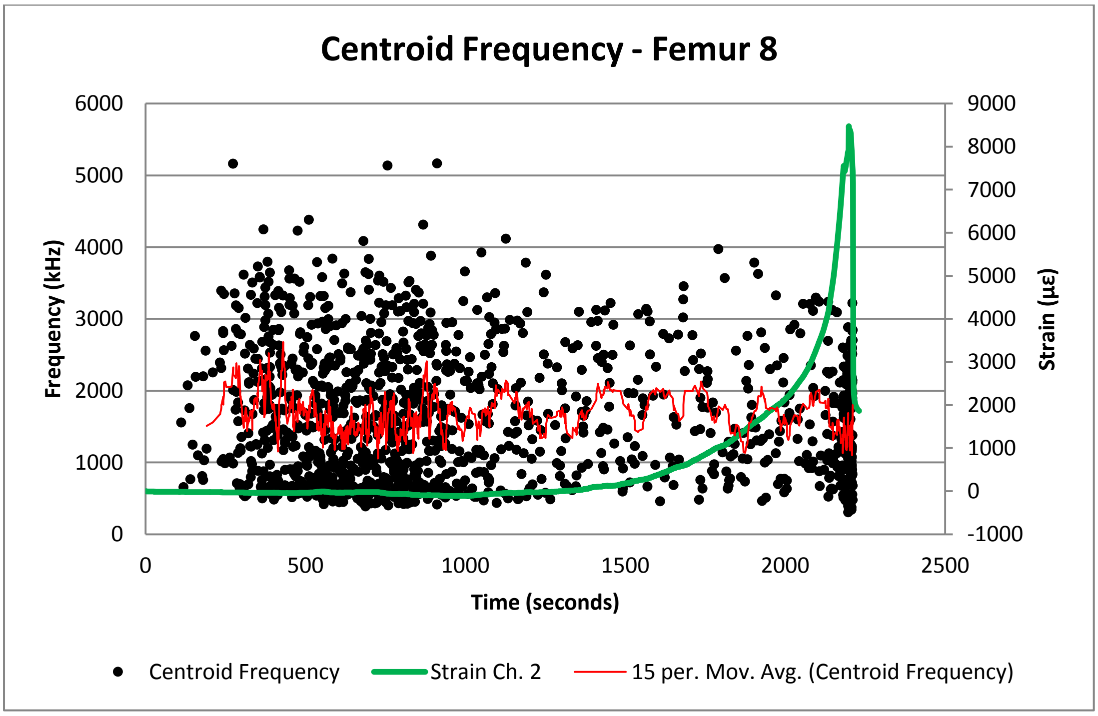
Centroid Frequency - Femur 8
Frequency (kHz)
6000
5000
4000
3000
2000
1000
0
Strain (με)
9000
8000
7000
6000
5000
4000
3000
2000
1000
0
-1000
0
500
1000
1500
2000
2500
Time (seconds)
● Centroid Frequency
Strain Ch. 2
15 per. Mov. Avg. (Centroid Frequency)

G. Correlation between measured bone properties and accumulated absolute energy at Final Fracture time and at 90% of final fracture time from Test 3 Chapter 4

Femur	Cumulative Energy (aJ)	90% of Final Time (aJ)	Mass (kg)	Volume (cm^3)	Density (g/cm^3)	GL (mm)	GLC (mm)	BP (mm)	BD (mm)	SD (mm)
5	941,193	43193	1.681	1367	1.229	375	355	131	105	39.4
8	31,721,550	3,659,069	1.704	1382	1.233	374	345	137.5	109.5	39.8
7	41,057,113	130,828	2.113	1673	1.262	386	360	144	115	44.6
6	28,517,269	2,208,728	2.148	1725	1.246	390	358	147	116	44.7
3	12,426,773	3,551,257	2.287	1818	1.258	400	375	152.5	120	46.5
4	14,280,010	462,702	2.459	1868	1.317	405	385	155	118	47.4
Correlation coefficient (R^2) between Cumulative energy and the bone property:			0.0014	0.0036	0.0016	0.0199	0.1264	0.0095	0.0461	0.0071
Correlation coefficient (R^2) between 90% of the Cumulative energy and the bone property:			0.0046	0.0000	0.0106	0.0000	0.0412	0.0267	0.0606	0.0008